

Lecture Notes in Engineering

The Springer-Verlag Lecture Notes provide rapid (approximately six months), refereed publication of topical items, longer than ordinary journal articles but shorter and less formal than most monographs and textbooks. They are published in an attractive yet economical format; authors or editors provide manuscripts typed to specifications, ready for photo-reproduction.

The Editorial Board

Managing Editors

C. A. Brebbia
Dept. of Civil Engineering
University of Southampton
Southampton SO9 5NH (UK)

S. A. Orszag
Dept. of Applied Mathematics
Rm 2-347, MIT
Cambridge, MA 02139 (USA)

Consulting Editors

Chemical Engineering:

J. H. Seinfeld
Dept. of Chemical Engg., Spaulding Bldg.
Calif. Inst. of Technology
Pasadena, CA 91125 (USA)

Earthquake Engineering:

A. S. Cakmak
Dept. of Civil Engineering, Princeton University
Princeton, NJ 08544 (USA)

Electrical Engineering:

P. Silvester
Dept. of Electrical Engg., McGill University
3480 University Street
Montreal, PQ H3A 2A7 (Canada)

Geotechnical Engineering and Geomechanics:

C. S. Desai
College of Engineering
Dept. of Civil Engg. and Engg. Mechanics
The University of Arizona
Tucson, AZ 85721 (USA)

Hydrology

F. Pinder
School of Engineering, Dept. of Civil Engg.
Princeton University
Princeton, NJ 08544 (USA)

Laser Fusion – Plasma:

R. McCrory
Lab. for Laser Energetics, University of Rochester
Rochester, NY 14627 (USA)

Materials Science and Computer Simulation:

S. Yip
Dept. of Nuclear Engg., MIT
Cambridge, MA 02139 (USA)

Mechanics of Materials:

F. A. Leckie
College of Engineering
Dept. of Mechanical and Industrial Engineering
Univ. of Illinois at Urbana-Champaign
Urbana, IL 61801 (USA)

A. R. S. Ponter

Dept. of Engineering, The University
Leicester LE1 7RH (UK)

Nonlinear Mechanics:

K.-J. Bathe
Dept. of Mechanical Engg., MIT
Cambridge, MA 02139 (USA)

Fluid Mechanics:

K.-P. Holz
Inst. für Strömungsmechanik,
Universität Hannover, Callinstr. 32
D-3000 Hannover 1 (FRG)

Structural Engineering:

J. Connor
Dept. of Civil Engineering, MIT
Cambridge, MA 02139 (USA)
W. Wunderlich
Inst. für Konstruktiven Ingenieurbau
Ruhr-Universität Bochum
Universitätsstr. 150,
D-4639 Bochum-Querenburg (FRG)

Structural Engineering, Fluids and Thermodynamics:

J. Argyris
Inst. für Statik und Dynamik der
Luft- und Raumfahrtkonstruktion
Pfaffenwaldring 27
D-7000 Stuttgart 80 (FRG)

Lecture Notes in Engineering

Edited by C. A. Brebbia and S. A. Orszag

3

Computational Aspects of Penetration Mechanics

Proceedings of the Army Research Office Workshop
on Computational Aspects of Penetration Mechanics
held at the Ballistic Research Laboratory at Aberdeen
Proving Ground, Maryland, 27–29 April, 1982

Edited by J. Chandra and J. E. Flaherty



Springer-Verlag
Berlin Heidelberg New York Tokyo 1983

Series Editors

C.A. Brebbia · S.A. Orszag

Consulting Editors

J. Argyris · K.-J. Bathe · A.S. Cakmak · J. Connor · R. McCrory
C.S. Desai · K.-P. Holz · F.A. Lecki · F. Pinder · A.R.S. Pont
J.H. Seinfeld · P. Silvester · W. Wunderlich · S. Yip

Editors

J. Chandra
U.S. Army Research Office
Research Triangle Park
North Carolina 27709
USA

J. E. Flaherty
Department of Mathematical Sciences
Rensselaer Polytechnic Institute
Troy, New York 12181
USA

ISBN-13: 978-3-540-12634-8 e-ISBN-13: 978-3-642-82093-9

DOI: 10.1007/978-3-642-82093-9

Library of Congress Cataloging in Publication Data
Army Research Office Workshop on Computational Aspects
of Penetration Mechanics (1982 : Aberdeen Proving Ground, Md.)

Computational aspects of penetration mechanics.

(Lecture notes in engineering ; 3)

Workshop organized by the Mathematics Division of
the U.S. Army Research Office.

1. Penetration mechanics--Data processing--Congresses.

I. Chandra, J. II. Flaherty, J.E., 1943-

III. United States. Army Research Office. Mathematics Division.

IV. Title. V. Series.

TA354.5.A75 1982 620.1'126 83-12393

This work is subject to copyright. All rights are reserved, whether the whole
or part of the material is concerned, specifically those of translation, re-
printing, re-use of illustrations, broadcasting, reproduction by photocopying
machine or similar means, and storage in data banks.

Under § 54 of the German Copyright Law where copies are made for other
than private use, a fee is payable to 'Verwertungsgesellschaft Wort', Munich.

© Springer-Verlag Berlin Heidelberg 1983

P R E F A C E

A workshop organized by the Mathematics Division of the U.S. Army Research Office on the "Computational Aspects of Penetration mechanics" was held from April 27 to 29, 1982 at the Ballistic Research Laboratory at Aberdeen Proving Ground, Maryland. This book is an attempt to capture the essence of this active field and collects the contributions of several of the speakers at the workshop.

The major thrusts of the workshop were (i) to review the state of the art of computational methods and available computer codes that are relevant to penetration mechanics, (ii) to critically evaluate both existing and new constitutive relations and to point out the inadequacies in such models, and (iii) to propose new numerical methods that may be promising in solving impact and penetration problems.

Based on these interests and considerations, this book is divided into three parts, Part I is devoted to reviewing computational methods and computer codes that are being used in penetration mechanics, Part II deals with Physical modeling and constitutive laws, and Part III is concerned with some new and novel numerical methods that may be applicable to impact and penetration problems.

The opening Chapter of Part I is a discussion by R. E. Nichols and R. A. May on the use of the nonlinear elastic-plastic finite element code NIKE2D to analyze the resistance of radioactive shipping containers to puncture at low velocities. They use their computational analyses in conjunction with experimental results to determine the effects of geometry, material behavior and other considerations on failure. Indeed, they point out the difficulty of interpreting such experimental data without using computational models. Although the velocities that are involved in these calculations are much lower than ordnance velocities, their methodology is still applicable to problems at higher velocities. In Chapter 2, G. R. Johnson discusses the status of the two- and three- dimensional Lagrangian finite element codes EPIC-2 and EPCIC-3. In particular, he concentrates on a "nearest neighbor" Lagrangian formulation which allows nodal connectivity to change as the solution progresses and, thus, can tolerate large deformations and distortions without tangling of the grid. B. E. Ringers continues this discussion in Chapter 3, where she presents some new sliding surface techniques that enable EPIC-2 to solve deeper penetration and perforation problems. In Chapter 4, J. Mescall discusses some capabilities of the Lagrangian finite difference code HEMP, while at the same time, emphasizing the need for better material characterization. In the final Chapter of Part I, J. N. Reddy summarizes the properties and capabilities of several computer codes for impact and penetration studies and also surveys the literature and discusses available results on the behavior of laminated composite plates under

impact loading. Experimental and other theoretical investigations indicate that composites can offer substantially improved performance in penetration problems.

Chapter 1 of Part II contains a survey and a discussion by T. W. Wright of some of the simpler models and methods that are used to analyze impact and penetration problems involving long rods. These models offer reasonable results for only a modest amount of computation, and they can be valuable in preliminary design studies or in setting parameters for experimental investigations. M. E. Backman continues the spirit of this discussion in Chapter 2 where he explores the possibility of using computational schemes to construct engineering models of some impact events. In the third chapter, W. G. Hoover applies formulations based on nonequilibrium molecular dynamics to fluid and solid deformations, under both homogeneous and shock conditions, as well as to heat transport problems. These new nonequilibrium methods suggest novel formulations of thermodynamics in nonequilibrium systems and shed considerable light on the future of the principle of material frame indifference. In Chapter 4, G. Strang discusses some of the consequences of a loss of monotonicity in a constitutive law. In penetration problems this can occur, e.g., when adiabatic heating causes shear bands to form. While the analysis of shear banding is comparatively advanced, these problems of local instability with global stability are not well understood. In Chapter 5, J. T. Oden discusses three problem areas in the computer simulation of large scale penetration mechanics, namely, numerical instabilities due to incomplete integration of the momentum or continuity equations, constitutive modeling, and friction effects. In the final chapter, P. Le Tallec discusses a general framework for studying nonlinear problems in solid mechanics relevant to large deformations and plastic behavior. Specific applications described include numerical solution of equilibrium problems in incompressible finite elasticity and limit-load computations in plasticity.

The three chapters in Part III are all concerned with some modern numerical techniques that may be applicable to problems in penetration mechanics. In the first chapter, B. Plohr, J. Glimm, and O. McBryan present some results from validation tests of a two-dimensional front tracking code for gas dynamics. The structure of their code allows them to explicitly track shock and contact discontinuities and their interactions. In Chapter 2, R. Gelinas and S. K. Doss discuss a moving finite element method, where nodes are systematically moved to those locations which can yield the most accurate and stable solutions of partial differential equations. They apply their code to problems in blast wave gas dynamics and penetration mechanics. In the final chapter, T. Belytschko and W. K. Liu describe some improvements in the finite element formulation and time integration procedures that are used in penetration problems. Specifically, they emphasize mesh stabilization techniques for underintegrated elements.

Overall, we feel that the workshop and these proceedings accomplished their

stated goals. It is apparent from many of the papers in this book that even relatively simple penetration problems require a substantial computational effort to solve. Hence, we suggest that future workshops and proceedings concentrate more on adaptive methods and parallel computation, both of which can offer dramatic computational savings and greater reliability. One unique aspect of this book is that it contains ideas from several diverse fields. In doing this, we hope to encourage and stimulate interaction between groups of researchers that have very different backgrounds, but who may be able to benefit from each others expertise.

In closing, we must thank Dr. T. W. Wright and his staff at the Ballistic Research Laboratory for hosting the workshop, Ms. Sherry Duke, Ms. Frances Atkins, and Ms. Jeanne Clark of the Army Research Office for their expert secretarial support throughout the preparation of this book.

Jagdish Chandra

Joseph E. Flaherty

March 1983

TABLE OF CONTENTS

Part I Computer Codes and Computational Methods for Impact and Penetration Problems

1. Design of Radioactive Material Shipping Packaging for Low-Velocity Puncture Resistance 3
R. E. Nickell and R. A. May
2. Status of the EPIC Codes, Material Characterization and New Computing Concepts at Honeywell 24
G. R. Johnson
3. New Sliding Surface Techniques Enable Lagrangian Code to Handle Deep Target Penetration/Perforation Problems 36
B. E. Ringers
4. Materials Issues in Computer Simulations of Penetration Mechanics 47
J. Mescall
5. Impact on Laminated Composite Plates: A Review of Recent Computational Developments 63
J. N. Reddy

Part II Physical Modeling and Constitutive Laws

1. A Survey of Penetration Mechanics for Long Rods 85
T. W. Wright
2. Some Examples of the Use of Continuum Mechanical Computational Models in the Development of Engineering Models 107
M. E. Backman
3. Rheology via Nonequilibrium Molecular Dynamics 123
W. G. Hoover
4. Notes on Softening and Local Instability 137
G. Strang
5. Comments on Some Problems in Computational Penetration Mechanics 149
J. T. Oden
6. Augmented Lagrangians in Finite Elasticity and in Plasticity 166
P. Le Tallec

Part III Modern Numerical Methods

1. Application of Front Tracking to Two-Dimensional Gas Dynamics Calculations 180
B. Plohr, J. Glimm, and C. McBryan
2. The Moving Finite Element Method: Strong Shock and Penetration Applications 192
R. Gelineas and S. K. Doss
3. On Mesh Stabilization Techniques for Underintegrated Elements 210
T. Belytschko and W. K. Liu

PART I

**Computer Codes and Computational Methods
for Impact and
Penetration Problems**

Design of Radioactive Material Shipping
Packaging for Low-Velocity Puncture Resistance*

R. E. NICKELL

Technical Specialist
Electric Power Research Institute
Palo Alto, California 94304

R. A. MAY

Member of Technical Staff
Sandia National Laboratories
Albuquerque, New Mexico 87185

Introduction

Both the standards developed by the International Atomic Energy Agency (IAEA) and those contained in the U. S. federal regulations [1] stipulate that transport packagings containing large quantities of radioactive material, such as spent fuel from a nuclear power reactor or waste by-products from nuclear weapons programs, should be designed to resist a sequence of impact, puncture, fire, and water immersion conditions without harmful release of contents. A recent paper [2] has offered a perspective on the design of such packagings relative to the impact event - a 30-foot (9 m) drop onto an essentially unyielding target. In that paper, it was shown that modern tools of computational mechanics, incorporating elastic-plastic material response and finite strain kinematic descriptions, could be used efficiently for the iterative design of a monolithic steel containment system, including models for bolted closures, shear keys, and seals.

In this paper we address the second event in the accident design sequence - the 40-inch (1 m) drop of the packaging, after primary impact, onto a mild steel cylindrical punch. The regulations describe the geometry of the punch in some detail - 6 inches (15 cm) in diameter, at least 8 inches (20 cm) long, with the edges of the cylindrical punch at the top surface rounded to no more than a radius of 0.25 inch (6 mm). The length requirement is intended to insure that the "essentially unyielding" support surface for the punch does not make contact with the package until maximum penetration damage has taken place. The rounded

* Portions of this work were performed at Sandia National Laboratories and were supported by the U.S. Department of Energy under contract number DE-AC04-76DP00789 for the U. S. Department of Energy.

edge requirement is intended to ensure that shearing action at the punch periphery is reasonably severe.

The orientation of the punch is also described, in that the cylindrical punch must be vertical and perpendicular to the essentially unyielding support surface. Beyond the geometry and orientation of the punch, however, the designer is merely required to select an orientation for the packaging at which maximum damage is expected. Since satisfaction of this design requirement is usually demonstrated by testing, some analytical justification for the particular test orientations is needed in order to eliminate unnecessary testing expense.

Typically, the analytical methods have involved correlations based upon extensive laboratory-scale or field-scale experiments [3]. These correlations may be expressed as a normalized incipient puncture energy versus a dimensionless design parameter - such as thickness divided by punch diameter. A combination of design parameters could also be used, provided that the structural response and failure mechanisms are reasonably well understood. An example of the use of a rational failure criterion and the reasoning by which experimental data can be interpreted is provided by Johnson et al. [4, 5] in their studies of static and dynamic piercing of tubes by sharp indenters. Under some conditions, extensive plastic deformation is observed away from the punch, indicating a significant structural response. Under other conditions, the deformation is localized at the periphery of the punch.

In recent years, computational methods have been examined as a means to understand the structural response and failure mechanisms of penetration, in order to develop design procedures that avoid large test programs. In this paper we use a large deformation, inelastic finite element program to analyze laboratory experiments. These analyses enable us to properly determine the effect of geometry, constraint, and material behavior on the propensity to fail by plastic collapse, buckling (based upon the magnitude of the compressive stresses), and punching shear. Laboratory data can then be normalized in such a way as to provide the designer with direct information on the performance of puncture-resistant configurations.

In the next section we discuss the difficulties of interpreting existing experimental data without recourse to computational results. Then, the computational models that provide the interpretation are described. The computational results for a series of well-controlled

experiments on a simple geometry are then discussed, followed by the interpretation through a rational failure theory. Finally, the implications of this interpretation in terms of design rules are given.

Experimental Interpretation

A fairly complete summary of available experimental puncture data at low velocity has been published by Larder and Arthur [6], in a research program conducted for the U. S. Nuclear Regulatory Commission. The data is graphically displayed in Figure 1, and includes results from earlier studies in addition to that generated by the USNRC program. In an attempt to find a dimensionless representation of the data, the incipient puncture energy, E , is normalized by the static ultimate strength of the materials, σ_u , multiplied by the cube of the plate thickness, t . This scaled puncture energy, called \bar{E} , is plotted versus the punch diameter to plate thickness ratio, d/t . Two empirical data fits are also shown - a lower bound curve by Sakamoto et al. [3] given by

$$\bar{E} = 0.7e^{2t/d}(d/t)^{1.8} \quad , \quad (1)$$

and a data fit suggested by Nelms [7],

$$\bar{E} = 2.35(d/t)^{1.6} \quad . \quad (2)$$

The experimental puncture energies obtained by Larder and Arthur on lead-backed and uranium-backed stainless steel plates, in all cases, are higher than those obtained in the earlier investigations. The differences range from 20% to a factor of two. Dynamic versus static test comparisons indicate that more energy is absorbed prior to puncture in static tests. Larder and Arthur observed that their results were in substantial disagreement with the earlier work in two respects: (1) first, their puncture data averaged 60% higher than previous puncture predictors; (2) their data did not support the 30 to 60% increase in puncture energy that is normally observed in a dynamic test over that in a static test. The cause for these disagreements was felt to be the overall structural response of the plates.

Two analytical comparisons support this contention. Figure 2 shows an example of the deformed shape of a lead-backed stainless steel plate, as predicted by the two-dimensional, nonlinear finite element code NIKE2D

[8], and the experimentally-derived shape. The comparison is quite good, and indicates that the amount of structural deformation accompanying the puncture can be substantial. The amount of energy accommodated by this deformation, as opposed to the amount of energy absorbed locally around the periphery of the punch (see Figure 3 for a description of the punching shear distributions), was not calculated in the USNRC study. However, it is conceivable that the amounts could have been roughly equal, or even that the energy of structural deformation was greater. This might help to explain the differences in puncture energies from previous tests, which were conservative (i.e., virtually all of the drop potential energy goes into puncture). The dynamic energies were lower than the static energies, we surmise, because the structural deformation pattern is more localized around the punch. The inertia of the plate away from the punch prevents the deformation from being more global.

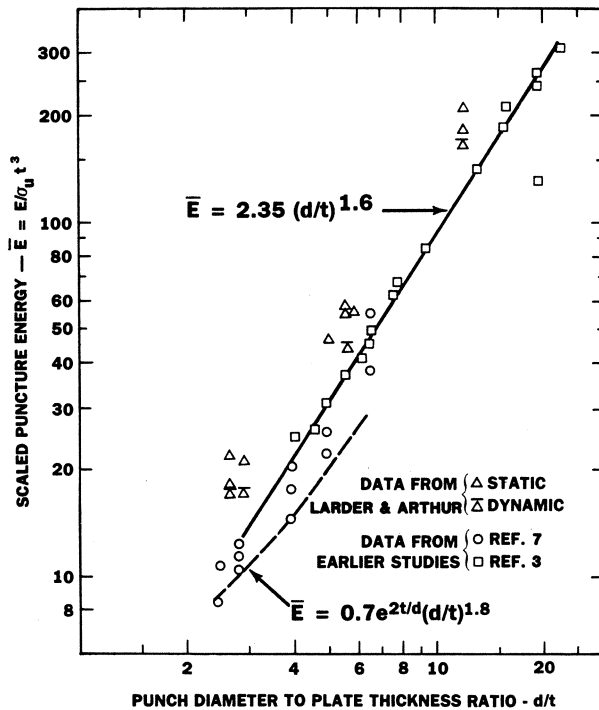


Figure 1. Scaled Puncture Energy Comparisons.

This observation is in agreement with the static/dynamic comparisons noted by Johnson et al. [5] in their experimental studies on

cylindrical tubes subjected to static and dynamic penetration loads. It was recognized prior to the experiments that localized static or dynamic loads from pointed objects might produce either gross structural deformation or local penetration, or even a combination of the two. The object of the study was to identify the parameters that control the material and structural response.

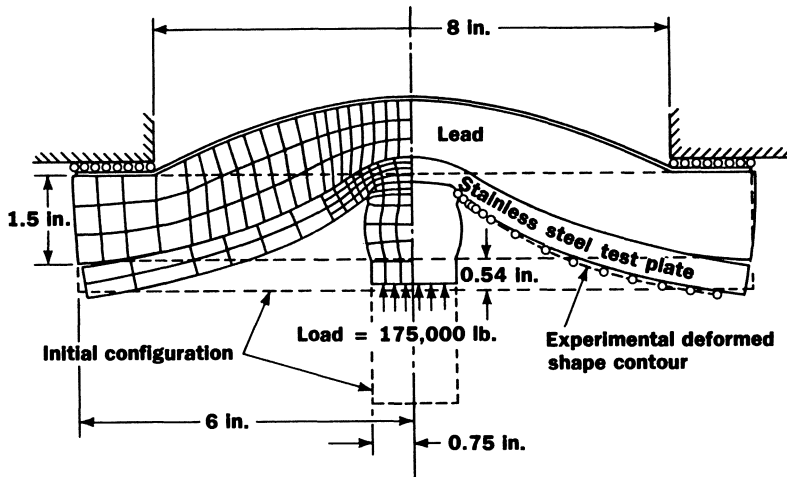


Figure 2. Comparison of Analytical and Experimental Plate Deformation at Failure.

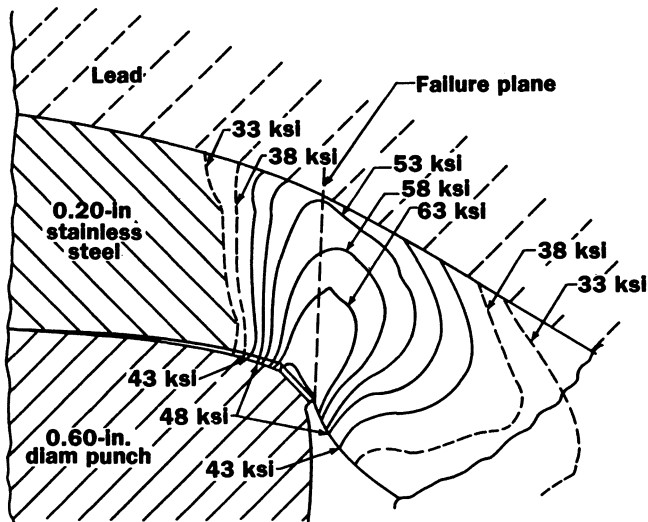


Figure 3. Typical Shear Stress Contours at Failure.

The materials investigated were mild steel, commercially pure copper, a heat-treated aluminum alloy, and a 70/30 brass. All the materials were cold drawn into 2-inch (50 mm) outside diameter tubes without any stress relieving. The penetrators were of two types - either pyramidal or conical, with a 30-degree apex angle, manufactured from hardened and tempered tool steel. Tube length-to-diameter ratios varied from 1/4 to 5. The dynamic experiments involved projectile velocities of about 540 ft/sec (165 m/sec). These velocities are considerably greater than those to be expected from the regulatory drop of 40 inches (1 m).

The principal findings from the comparisons between static and dynamic puncture were:

1. The nature of the structural deformation that accompanies penetration is different in the dynamic events from that in the static events; the dynamic deformation pattern does not exhibit distinct plastic hinge formation that is observed in static penetration tests; instead, plastic hinges appear to have traveled without appreciable slope discontinuities; dynamic structural deformation essentially disappears for long tubes (length to diameter of two or greater) because of the stiffening effect of adjacent material.
2. The dynamic failure mode associated with the conical punch appears to be a ductility exhaustion (strain) mode; penetration causes a lip to form on the inside surface of the tube which eventually fractures; this is a consequence of stretching of the tube material that conforms to the shape of the penetrator.

Because of the expense associated with nonlinear finite element analysis of this class of problems, numerous approximate techniques have been suggested. A sophisticated procedure of this type was described by Shieh [9] for spent fuel shipping casks, based upon partial success in modeling static and dynamic puncture experiments on circular stainless steel plates. The approximate solution is the upper-bound, rigid-perfectly-plastic, large deflection result obtained by Onat and Haythornthwaite [10], extended to include shear correction effects for thick plates, elastic strain contributions, and strain hardening. Inertial effects were not treated.

The essential features of the approach are as follows:

1. A deflected shape is assumed for either a clamped-edge boundary condition, a simply-supported edge condition, or a membrane model; the deflected shape has a single free parameter – the displacement at the center of the plate, which corresponds to the location of the applied punch;
2. The upper-bound solution gives the punch load as a function of this unknown central deflection;
3. An expression for the energy absorbed or stored by the plate in elastic and plastic deformation can be used to close the system of equations;
4. A punch failure criterion must be provided, in order to determine whether the potential energy of the 40-inch (1 m) drop is sufficient to cause penetration.

The two failure criteria suggested were: (i) a punching shear failure at the periphery of the six-inch-diameter punch, described by

$$\tau = 0.6\sigma_u, \quad (3)$$

where τ is the average shear stress across the thickness of the plate, and σ_u is the ultimate tensile strength of the plate material, or (ii) a ductility exhaustion limit, expressed as

$$\epsilon_u / \epsilon_a = 1 \quad (4)$$

where ϵ_u is the ultimate tensile strain for the plate material and ϵ_a is the radial membrane strain.

The procedure was tested on experimental data generated by Larder and Arthur [6]; through judicious use of strain hardening, boundary conditions, and strain rate parameters, a reasonable comparison with the experimental data was obtained. From detailed finite element calculations using NIKE2D, however, Larder and Arthur observed that the agreement was coincidental. Strain rate effects were not supported by either the analytical or the experimental results. We conclude that the deflected shape assumed for the upper bound solution will differ for static and dynamic puncture events, and the differences may be

substantial. Shieh attempted to compensate for the errors introduced by the static deflected shape assumption, but these compensations tend to obscure the phenomena of importance.

Computational Model

To assist in the design process of a new transport package it was necessary to qualify a capability to analytically predict the puncture behavior of various sizes and types of plate. Data from laboratory-scale puncture tests on thin, clamped edge circular plates conducted by Effects Technology Inc. (ETI) as part of the design process would be used to evaluate the adequacy of the predictions. The analytical predictions of deformation, stresses and strains in the circular plates were obtained using the HONDO II [11] computer code. HONDO II is a computer code designed to compute the time-dependent displacements, velocities, accelerations and stresses in two-dimensional plane or axisymmetric bodies. The code was developed to analyze problems where large deformations and inelastic behavior would be anticipated. Five material subroutines are available in the code, along with a sliding interface capability which allows interaction between two or more separate bodies.

The code uses an arbitrary quadrilateral mesh to define the geometry. The spatial discretization is generated by the Galerkin form of the finite element method. The motion is assumed to vary bilinearly over the element using isoparametric coordinates. The stress may be taken as constant, or variable over an element.

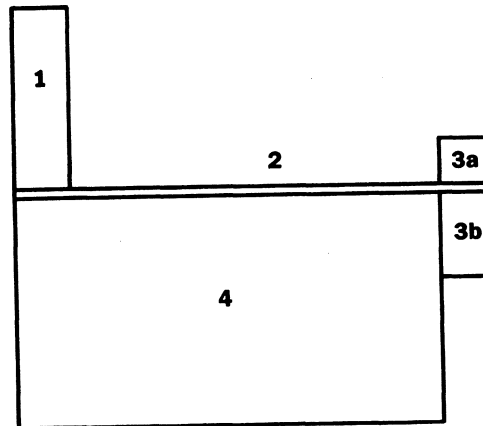
Using central difference expressions for velocity and acceleration the simultaneous equations are integrated. The integration procedure is conditionally stable with respect to the time step size, so a continuous monitor of the step size is used.

No stiffness matrices are constructed as the geometry is constantly changing and the material can be nonlinear in its response. Thus time and storage requirements are reduced. The process begins with the current stress and strain within each element. A new strain is calculated based on the time step determined by the code and then a new stress is computed. The numerical divergence of the stress field is used to obtain the nodal forces. These are accumulated for all the elements about a node and provide the new accelerations. New velocities and positions are obtained and the process is repeated.

Five material models are available in the code. These are Kirchhoff Large Rotation/Infinitesimal Strain, Finite Elastic Continuum Rubber, Finite Strain/Elastic-Plastic Strain Hardening, Finite Strain Soil and Large Rotation/Infinitesimal Strain Viscoelastic. However, other material models can be easily added due to the way the code is organized.

HONDO II output consists of both high-speed printer output and plot data. Nodal values of displacement, velocity and acceleration can be printed along with element stresses. The plot file can contain Cauchy stress and Signorini strain, the 2nd Piola-Kirchhoff stress and the Green-St. Venant strain or the Cauchy stress and Signorini strain where the bulk strain equals $\ln(\rho_0/\rho)$ depending on the option selected.

Axisymmetric analyses of the ETI puncture tests were carried out using HONDO II. Figure 4 illustrates the HONDO II representation of the ETI puncture tests. Part 1 represents the 2300-pound, 2.4-inch-diameter (1045 kg, 61 mm) puncture pin. The 18-inch-diameter, 0.060-inch-thick (457 mm, 1.52 mm) plate is shown as Part 2. Parts 3a and 3b represent the fixed steel clamping fixture and Part 4 is the polyurethane foam backing used in selected tests.



1 PUNCH
2 PLATE
3a UPPER FIXTURE
3b LOWER FIXTURE
4 FOAM (optional)

Figure 4. HONDO II Representation of the ETI Punch Tests.

Parts 1 and 3 were modeled as elastic materials. The density of the punch was adjusted to provide a weight equal to the weight of the punch and crosshead used in the ETI tests. The sliding interface option was used for the surfaces in contact between the punch and the plate, the fixture and plate and, when the foam was modeled, between the plate and the foam. Frictionless movement between the surfaces was assumed. The outer edge of the plate was fixed in the radial direction.

Various changes in the basic model were made in order to investigate the behavior of full scale puncture plates. These parameters are shown in Table I.

In order to reduce the computer time required for the analyses, a number of simplifications were made. First, the punch, which was expected to respond as a rigid body, was modeled with one element which resulted in a square edge instead of the 0.10 inch (2.54 mm) radius used in the ETI tests. This reduced the total number of elements required and also increased the time step allowed for computations by eliminating the smallest elements.

Second, the plate was modeled using only one 2x2 integration element through the thickness. This bilinear displacement element with four integration points per element does not exhibit keystoneing, which tends to be a problem with the one point integration element in problems of this type. By using only one element through the thickness the time step was again kept at a higher value and the number of elements reduced. Using one element through the plate thickness does have the effect of artificially increasing the bending stiffness of the plate slightly. However, with large deflections present, the primary load carrying mechanism is membrane action instead of bending, which can be captured using a single element through the thickness.

Another assumption was made in using the elastic-plastic material model rather than the soil material model for the foam backing material. Previous analyses have shown that the elastic-plastic model could be used with good success under similar conditions.

Analytical Results

The first three HONDO II analyses were used to ensure that the analytical model was valid and to determine the degree of correlation between the analytical results and the ETI experimental data.

TABLE I

Punch and Fixture

Material: Not Applicable*

Density: $0.3289 \text{ lb}_f\text{-sec}^2/\text{in}^4$ ($2.929 \times 10^5 \text{ kg/m}^3$) - 2300 lb. punch

$1.465 \text{ lb}_f\text{-sec}^2/\text{in}^4$ ($1.305 \times 10^6 \text{ kg/m}^3$) - 64000 lb. punch

Elastic Modulus: $30 \times 10^6 \text{ lb/in}^2$ ($2.1 \times 10^5 \text{ MPa}$)

Poisson's Ratio: 0.3

Plate

Material: 304 Stainless Steel

Density: $7.32 \times 10^{-4} \text{ lb}_f\text{-sec}^2/\text{in}^4$ (652 kg/m^3)

Elastic Modulus: $28 \times 10^6 \text{ lb/in}^2$ ($1.9 \times 10^5 \text{ MPa}$)

Poisson's Ratio: 0.265

Yield Strength: 44300 lb/in^2 (305 MPa)

Hardening Modulus: $35 \times 10^4 \text{ lb/in}^2$ (2400 MPa)

Backing

Material: Polyurethane Foam

Density: $5 \times 10^{-6} \text{ lb}_f\text{-sec}^2/\text{in}^4$ (4.5 kg/m^3)

Elastic Modulus: 1250 lb/in^2 (8.6 MPa)

Poisson's Ratio: 0.05

Yield Strength: 50 lb/in^2 (350 kPa)

Hardening Modulus: 10 lb/in^2 (69 kPa)

*Note: The punch and fixture were modeled as a totally elastic material since their response was not required. The density was chosen to give the punch the correct mass.

The first analysis used test conditions from the ETI Test SSD 605, which used an unbacked, clamped edge plate. The HONDO II analysis predicted a maximum deflection of 1.90 inches, (48.3 mm) which is within 8% of the 2.07 inches (52.6 mm) actually recorded in the test. The final deformed profile of the plate as shown by the computer graphics, Figure 5, is qualitatively similar to the tested plate.

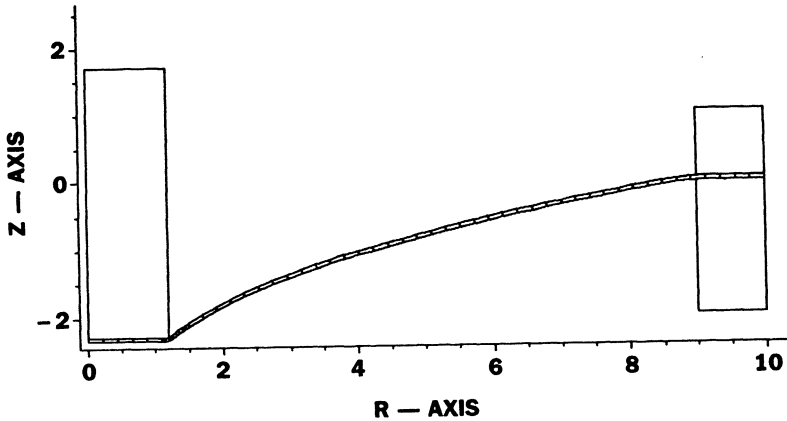


Figure 5. Final Profile of Test Plate SSD 605 as Generated by HONDO II.

The second analysis duplicated the test conditions of SSD 601. This test was identical to the previous test except for a higher initial velocity of the punch. Figure 6 shows both the analytically and experimentally determined plate profiles. The agreement between the two was quite good except in the immediate vicinity of the punch, possibly due to the relatively large mesh size in this area. The HONDO II analysis predicted a maximum deformation of 2.28 inches (57.9 mm) compared to the experimental value of 2.35 inches (59.7 mm).

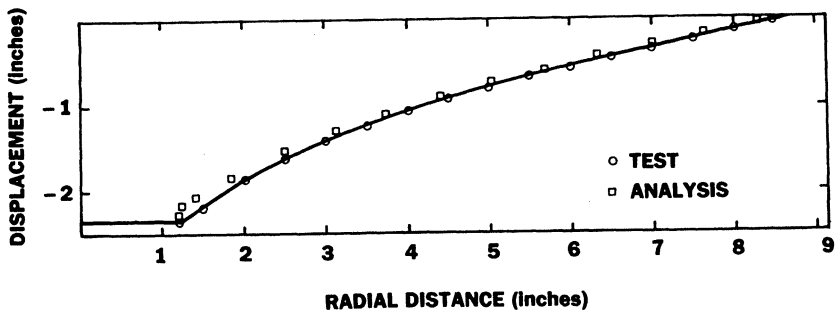


Figure 6. Comparison of HONDO II Results to ETI Test SSD 601.

The final test case duplicated test SSD 602F. In this case the circular plate was backed by 50 psi (350 kPa) polyurethane foam. Again the correlation between the analytical and experimental results is quite

good, as seen in Figure 7. The experimental results show a maximum deformation of 1.82 inches (46.2 mm) as compared to the analytically determined value of 1.96 inches (49.8 mm).

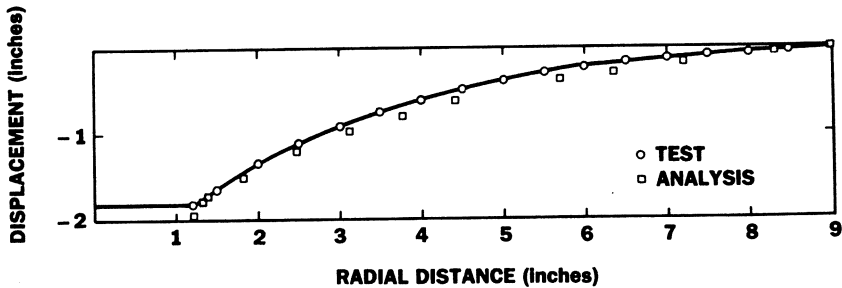


Figure 7. Comparison of HONDO II Results to ETI Test SSD 602F.

Based upon the excellent correlation between the laboratory-scale experimental results and the analytical results, similar analyses were used to determine the plate behavior for full scale puncture tests. The puncture plate envisioned for the packaging currently being designed was a large, ≈ 100 inches (2.5 m), rectangular plate whose thickness could be up to 0.50 inches (12.7 mm). This plate would be essentially unrestrained at the edges and backed by polyurethane foam. In addition, it was desired to design a fixture for a full scale test plate such that the behavior at the periphery of the punch duplicated that in the packaging. An additional constraint was that it was desired to test the smallest plate possible in order to minimize the costs and ease handling

It had been determined that a 60-inch-diameter (1.52 m) plate would be a reasonable size to work with if the puncture behavior adequately predicted the actual packaging behavior. To determine if this plate size was appropriate, four additional HONDO II analyses were carried out. The first two analyses modeled a 100-inch-diameter, 0.5-inch-thick (2.54 m, 12.7 mm) foam backed plate impacted by a 6-inch-diameter (152 mm) punch. The punch had a mass of 64000 pounds (29090 kg) and an impact velocity of 14.6 ft/sec (4.45 m/sec), closely approximating the full scale packaging impact conditions. Two edge conditions were modeled; guided, allowing radial movement but no vertical displacement, and free, allowing movement in the negative vertical direction as well as in the radial direction.

The results of these two analyses, shown in Figure 8, indicate that a 100-inch-diameter (2.54 m) plate approximates the behavior of an infinite plate. This conclusion is based on the observation that the behavior of the guided plate closely approximates that of the free plate. The boundary conditions have little effect on the plate profile. The behavior of the free plate model would be expected to be very close to the actual packaging puncture plate behavior.

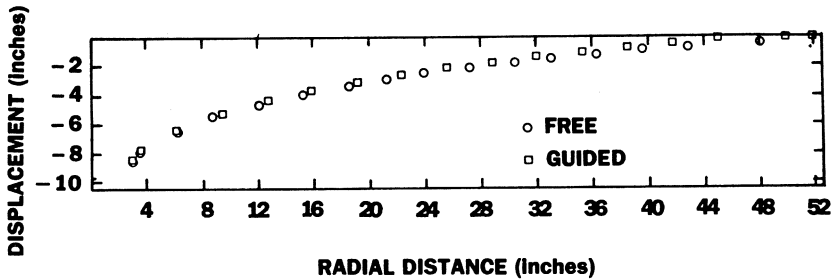


Figure 8. Results of the HONDO II Analyses of the 100 Inch Plate Having Free or Guided Edge Conditions.

Since a deflection of 2 inches (51 mm) was observed at a 30 inch (760 mm) radius, two more analyses were carried out to see what effect a fixture having a 60-inch-diameter (1.52 m) would have on the plate behavior. Again, a guided and a free plate edge were modeled. Figure 9 shows that the edge conditions for the smaller diameter plates can cause a large difference in the plate behavior. If the data is plotted with that data obtained from the 100-inch (2.54 m) plate, Figure 10, it can be seen that the profile of the plate having guided edges closely approximates that of the large plate out to a radius of 20 inches (510 mm). After that point the profile of the smaller plate is much steeper due to the enforced zero vertical displacement at the 60-inch (1.52 m) diameter. Although the 60-inch (1.52 m) plate with the free edge has a larger displacement over its entire surface, the curvature is very similar to that of the 100-inch (2.54 m) case over its diameter.

The results of these analyses indicated that a 60-inch-diameter (1.52 m) plate and fixture could be used for the full scale puncture tests. Because the actual puncture plates in the packaging will be loosely attached and are roughly 100 inches (2.5 m) wide, the free edge condition of the 100-inch (2.54 m) plate analyses should be a good approximation of the puncture behavior. The 60-inch-diameter (1.52 m)

plate having guided edges gives a good approximation of the actual behavior over most of the profile and gives a good indication of the amount of punch travel.

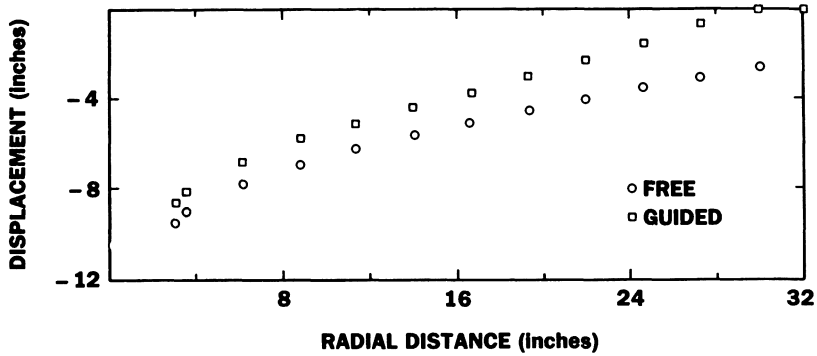


Figure 9. Results of the HONDO II Analyses of the 60 inch Plate Having Free or Guided Edge Conditions.

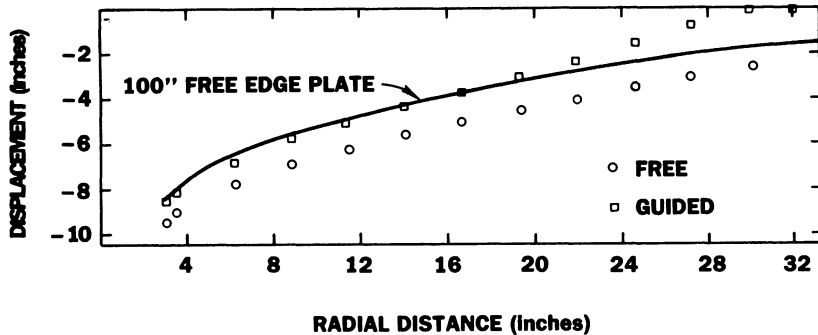


Figure 10. Comparison of the 60 inch Plate Results to the Results of the 100 inch Free Edge Plate.

Material Resistance to Puncture

With the HONDO II code successfully verified against experimental data, an exercise was conducted in order to determine a ranking system for material puncture resistance. The exercise consists of an estimation of the relative contribution to energy absorption by: (i) punching shear at the punch periphery; (ii) bending at the periphery of the punch, extending outboard a few punch diameters; and (iii) membrane stretching

over the region of deflection influence. Then, the parameters that control the magnitudes of these relative contributions can be identified and the resistance to puncture optimized.

For an ideally plastic material, with no strain hardening, the increment of plastic work is $dW = \sigma_y d\epsilon$, where σ_y is the yield stress and $d\epsilon$ the increment of effective plastic strain. When strain hardening is accounted for, as it must for austenitic stainless steels and other materials with large ratios of ultimate to yield strength, the plastic work is obtained by integrating the area under the elastic-plastic stress-strain curve. When the strains are large, the area under the true stress-true strain curve is appropriate. Table II shows the plastic work density (work per unit volume) for AISI 304 stainless steel. To use this table, we must integrate over a volume of known strain or stress level.

Simple estimates of energy absorption are found as follows. The final deflected shape from the HONDO II calculation is examined, and the plastic strains are computed from the deformed shape. The punching shear strain is observed to be concentrated near the periphery of the punch, as is the bending strain. Membrane strain in both radial and circumferential components is more global, with the circumferential membrane strain a strong function of the boundary fixity at the edge of the plate.

For ETI Test SSD 605, an unbacked clamped stainless steel plate being impacted by a 2.4-inch-diameter (61 mm) punch, the impact energy is represented by the kinetic energy of the punch (2300 lb., 78 in/sec), or 18,220 lbin (2059 J). The plate has a thickness of 0.060 inches (1.52 mm) and an effective clamping diameter of 18 inches (457 mm). The energy absorbed in punching shear is estimated to be between 730 lbin and 1,100 lbin (82-124 J); the energy absorbed by plastic work to form the slope discontinuity at the punch periphery is about 200 lbin (23 J); with virtually the entire remaining amount - about 17,000 lbin (1920 J) - being absorbed by membrane stretching of the plate.

From these estimates we conclude that: (1) the plates are so thin that little energy is absorbed in creating the plastic hinge at the edge of the punch or in plastic bending of the plate elsewhere - perhaps 1 to 2% of the impact energy; (2) the punching shear absorbs about 5% of the impact energy; and (3) membrane stretching absorbs between 90 and 95%. This implies that target plates undergoing significant structural

deformation, such as those in the Lawrence Livermore National Laboratory tests [6], should have substantially higher incipient puncture energies - perhaps by a factor of 10 - than very stiff target plates. Also, dynamic tests in which the response mode might tend to localize the deformation (e.g., a higher mode, with points away from the impact region lagging or out of phase with the points in the impact zone) will show substantially less energy absorption than will static tests.

TABLE II

True Strain	True Stress, Ksi (MPa)	Work Density, lbin/in ³ (MN•m/m ³)
.00826	29.8 (205)	123 (0.8)
.00932	35.4 (244)	158 (1.1)
.01424	38.9 (268)	340 (2.3)
.02153	41.8 (288)	635 (4.4)
.02955	44.3 (305)	980 (6.8)
.03742	46.5 (320)	1,337 (9.2)
.04486	48.4 (334)	1,690 (11.6)
.05316	50.5 (348)	2,100 (14.5)
.06044	52.7 (363)	2,476 (17.1)
.06781	54.6 (376)	2,872 (19.8)
.07549	56.4 (389)	3,298 (22.7)
.08354	58.3 (402)	3,760 (25.9)
.09157	60.2 (415)	4,235 (29.2)
.09935	62.0 (427)	4,711 (32.5)
.10785	63.6 (438)	5,244 (36.2)
.11532	65.1 (449)	5,725 (39.5)
.12332	66.8 (460)	6,253 (43.1)
.13110	68.5 (472)	6,779 (46.7)
.13908	70.0 (483)	7,331 (50.6)
.14723	71.3 (491)	7,907 (54.5)
.15450	72.6 (500)	8,430 (58.1)
.	.	.
.	.	.
.20	85.0 (586)	12,000 (82.7)
.40	130.0 (896)	33,500 (231.0)
.60	175.0 (1206)	54,000 (372.3)
.80	200.0 (1379)	91,500 (630.9)
1.00	225.0 (1551)	134,000 (923.9)

Since plastic membrane straining plays such a crucial role in determining the puncture resistance of relatively thin target plates, the analysis was extended slightly to investigate the performance of materials with better ultimate strength/yield strength characteristics than austenitic stainless steels. The most impressive candidate was a material designated as MAR-M918 steel, with low yield strength and high ultimate strength and ductility. The HONDO II code was then used to establish the degree of improvement to be expected.

A full-scale punch of a 0.5-inch-thick (12.7 mm) circular plate was modeled. The punch was given a mass of 64,000 lb (29090 kg) and an initial velocity of 175 in/sec (4.45 m/sec) corresponding to a drop height of 40 inches (1 m). For the stainless steel calculation, the elastic modulus was chosen to be 28×10^6 psi (1.9×10^5 MPa); Poisson's ratio equal to 0.265; yield strength equal to 44,000 psi (303 MPa); and a hardening modulus equal to 350,000 psi (2400 MPa). For the MAR-M918, $E = 30 \times 10^6$ psi (2.1×10^5 MPa); $\nu = 0.3$; $\sigma_y = 35,000$ psi (241 MPa); and the hardening modulus 127,000 psi (876 MPa). The failure criterion was selected to be punching shear, with the average shear stress at the punch periphery equal to $1/2 \sigma_u$. This is reasonably consistent with the results obtained in [6], where 60% of the ultimate strength was used as a failure threshold for the minimum shear stress at the edge of the punch.

In this case, failure in the 304 S.S. plate was predicted by the HONDO II calculation at a time of about 54 msec., with the punch having a remaining velocity of about 72 in/sec (1.83 m/sec). The energy absorbed was calculated to be 2×10^6 lbin (2.7×10^6 J). For the MAR-M918 calculation, the HONDO II results showed no failure, with the entire punch kinetic energy, 2.6×10^6 lbin (3.5×10^6 J), absorbed by the plate. Any decrease in plate thickness in order to promote failure in the MAR-M918 introduces additional flexibility and alters the proportion of energy absorbed in membrane stretching versus punching shear. The comparison was therefore made of the energy absorbed at the point where the average shear stress at the periphery of the punch reached $1/3 \sigma_u$, as an alternative.

In this case, the 0.5-inch (12.7 mm) MAR-M918 plate reached the point of incipient failure at the time when virtually all of the punch kinetic energy had been absorbed. The 0.5-inch (12.7 mm) 304 S.S. plate, on the other hand, failed at the point where approximately one-third of the

For the NABOR approach, on the other hand, it is necessary to develop a relationship between the nodal distance and the nodal force. Energy effects must also be included. One way to approach this relationship is to derive the forces on the basis of molecular physics. A strong argument for this approach is that this is the way real materials behave. Even if the forces are not derived in this manner, a strong argument for the basic approach remains; the simulation does on a larger scale what real material does on a much smaller molecular scale.

The primary disadvantage of this molecular approach is that more than the immediate six nearest neighbors contribute to the solution. Also, it is more convenient for most users if they can work with traditional equations of state, rather than molecular physics. Therefore, the approach which has been used is that of approximating the volumetric strain with a linear strain based on the distance between nodes.

The upper portion of Figure 4 shows a hexagonal close-pack configuration of nodes. If the grid is subjected to a uniform compressive pressure, all distances between the nodes are reduced uniformly as shown in the lower left portion of the figure. If D_0 and A_0 represent the initial distance between nodes and the initial area of each of triangles, then the compressed area is $A = A_0 (D/D_0)^2$, where D is the compressed distance between nodes. Furthermore, if $\mu = \rho/\rho_0 - 1$, where ρ_0 and ρ represent the initial and current densities, then μ can be expressed as a function of D_0 and D .

$$\mu = \rho/\rho_0 - 1 = V_0/V - 1 = A_0/A - 1 = (D_0/D)^2 - 1 \quad (3)$$

where the volumes, V_0 and V , are directly proportional to the areas, A_0 and A , for plane strain geometry.

Now it is possible to compute the hydrostatic pressure from the Mie-Gruneisen equation of state.

$$P = (K_1\mu + K_2\mu^2 + K_3\mu^3)(1 - \Gamma\mu/2) + \Gamma E_s(1 + \mu) \quad (4)$$

where K_1 , K_2 , and K_3 are material-dependent constants, Γ is the Gruneisen coefficient, and E_s is the internal energy per original unit volume.

The artificial viscosity, Q , is dependent on the volumetric strain rate which is given by

$$\dot{\epsilon}_v = 2\Delta V/D \quad (5)$$

where ΔV is the relative separation velocity between two nodes.

The resulting force due to the pressure and artificial viscosity can then be expressed as

$$F = (\sqrt{3}/2)(P + Q)D \quad (6)$$

primary, secondary, and peak categories - depending upon the degree to which their resultant is required to support applied loads. Applied loads, in this regard, should encompass body forces (e.g., inertial loads) as well as pressure. Second, the loading should be examined for its limiting characteristics; that is, does the deformation of the structure tend to mitigate the applied loads. Thus, based upon these two principles, the concepts of self-limiting stress and energy-limited load are seen to be complementary. If the energy potential of a load is large - such as that of internal pressure in a pressure vessel, the primary stresses are required to maintain equilibrium and must have the margin implied by this responsibility. Secondary stresses, in this case, will redistribute when strength limits are exceeded. On the other hand, when the energy potential of a load is limited - such as is the case for the puncture loading, the primary stresses become energy limited, although not self limited.

Therefore, rational design practice would indicate the following criteria for the containment boundary during the postulated puncture event:

- (1) The punching shear stresses and the membrane stretching stresses are considered primary;
- (2) the bending stresses are secondary;
- (3) the postulated puncture event should be considered a low probability event, and the margins should be those contained in Appendix F (Level D Service Condition Limits) of the ASME Boiler and Pressure Vessel Code, Section III;
- (4) the inertial loading from the postulated puncture event should be considered to be energy limited;
- (5) the limits on primary stress contained in Appendix F should be met;
and
- (6) membrane strain and peak strain limits should be considered as alternative criteria.

References

- 1 Title 10, Code of Federal Regulations, Part 7 (Jan. 1981).
- 2 Charman, C.M., Grenier, R.B., and Nickell, R.E., "Large Deformation Inelastic Analysis of Impact for Shipping Casks," to be published in Comp. Meth. Appl. Mech. Engr. (1982).
- 3 Sakamoto, et al., "An Experimental Study on Puncture Resistance of Spent Fuel Shipping Casks by Drop Impact Tests," Proceedings, 4th International Symposium on Packaging and Transportation of Radioactive Materials, September 22-27, 1974, Miami Beach, Florida, pp. 262-276.
- 4 Johnson, W., Ghosh, S.K., Mamalis, A.G., Reddy, T.Y., and Reid, S.R., "The Quasi-Static Piercing of Cylindrical Tubes or Shells," Int. J. Mech. Sci., Vol. 20, pp. 9-20 (1980).
- 5 Johnson, W., Reid, S.R., and Ghosh, S.K., "Piercing of Cylindrical Tubes," J. Press. Vessel Tech., Vol. 103, No. 3, pp. 255-260 (August 1981).
- 6 Larder, R.A. and Arthur, D., "Puncture of Shielded Radioactive Material Shipping Containers. Part I - Analysis and Results. Part II - Static and Dynamic Tests of Laminated Plates," NUREG/CR-0930, UCRL-52638, Lawrence Livermore Laboratory (December 1978).
- 7 Nelms, H.A., "Structural Analysis of Shipping Casks," Report No. ORNL-TM-1312, Vol. 3, Oak Ridge National Laboratory, Oak Ridge, Tennessee (1968).
- 8 Hallquist, J.O., "NIKE2D - An Implicit, Finite-Deformation, Finite Element Code for Analyzing the Static and Dynamic Response of Two-Dimensional Solids," UCRL-52678, Lawrence Livermore National Laboratory, (1979).
- 9 Shieh, R.C., "Analytical Puncture Study of Circular Metal Plates," Trans. ASME, J. Press. Vessel Tech., Vol. 102, No. 3, pp. 242-248 (August 1980).
- 10 Onat, E.T. and Haythornthwaite, R., "The Load-Carrying Capacity of Circular Plates at Large Deflections," Trans. ASME, J. Appl. Mech., Vol. 23, No. 1, pp. 49-55 (March 1955).
- 11 Key, S.W., Beisinger, Z.E., and Krieg, R.D., "HONDO II - A Finite Element Code for the Large Deformation Dynamic Response of Axisymmetric Solids," SAND78-0422, Sandia National Laboratories, Albuquerque, New Mexico (October 1978).

Status of the EPIC Codes, Material Characterization and New Computing Concepts at Honeywell

GORDON R. JOHNSON

Honeywell Inc.
Defense Systems Division
Hopkins, MN 55343

Summary

This paper presents the status of various aspects of computational penetration mechanics at Honeywell. The discussion includes references to previous work and a description of the work currently in progress. The status of the EPIC-2 and EPIC-3 computer codes for penetration computations is presented. The material characterization work considers both strength and fracture models. Large strain, high strain rate torsion data for a wide range of materials have been obtained for use with these models. A new computing concept has been developed, called the NABOR code, which involves a "nearest neighbor" Lagrangian formulation. This approach allows nodal connectivity to change as a solution progresses, thus allowing very severe distortions to be attained without "tangling" the Lagrangian grid.

EPIC Codes

The EPIC-2 and EPIC-3 computer codes are based on an explicit finite element formulation and are primarily used for problems involving intense impulsive loading. The two-dimensional triangular elements and three-dimensional tetrahedral elements used in these codes are well suited to represent the severe distortions which often occur under these loading conditions. A summary of the capabilities of the EPIC-2 and EPIC-3 codes has recently been presented [1].

Figure 1 shows an EPIC-3 simulation of a copper rod impacting a thin steel plate [2]. The nodes in the rod are designated "slave" and those on the surface of the plate are designated "master." In this problem the copper rod is allowed to erode while the master surface on the plate is held intact.

The erosion of the copper rod is accomplished by allowing the elements to fail completely at a specified plastic strain. When an element is completely failed, it cannot develop any stresses or pressures. It essentially disappears, except that mass is retained at the nodes. The "dots" in Figure 1 represent concentrated masses at nodes whose associated elements have completely failed. This approach is an approximation inasmuch as no allowance is made for the volumes of the completely failed elements. Such computations have been shown to give good results with experiments, however [1].

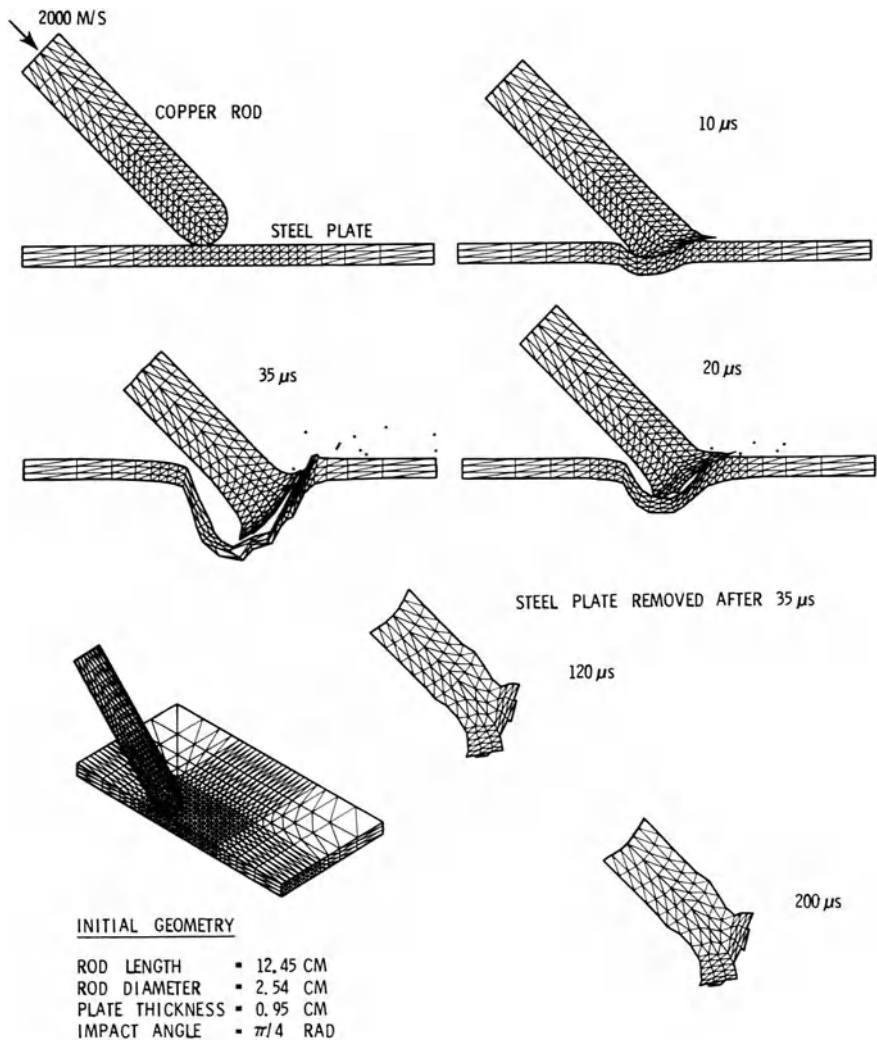


Figure 1. EPIC-3 Simulation of Oblique Impact of a Copper Rod onto a Steel Plate

For penetration into thick plates it is necessary to allow the projectile to break through the top surface of the plate. This can be accomplished by allowing the master plate to erode and be redefined as the solution progresses. Figure 2 shows examples where both the projectile and the target are allowed to erode. In these computations, a cylindrical volume in the target plate is specified as the eroded area. The master surface begins as a disk of nodes on the top surface of the target. As the projectile begins to penetrate, the elements containing master nodes are automatically monitored for plastic strain. When the specified strain values are exceeded, all elements in the disk of elements directly below the master surface are completely failed. Then the master nodes (excluding the outer ring) are designated as slave nodes, and the master surface is redefined as the disk (one layer below the original master surface), and a cylinder around the edge. No user intervention was required for either of these computations.

More work needs to be done to assess the effects of the associated approximations on the accuracy of such computations. An obvious improvement would be to have the master surface determined in a general manner instead of predetermining the eroded area as was done in the solutions of Figure 2. It is anticipated that this work will be performed in the future.

Material Characterization

An important aspect of numerical simulations is defining strength and fracture characteristics of materials. The work at Honeywell has consisted of defining these characteristics as functions of strain, strain rate, temperature, pressure, and stress, since these are the important variables commonly used in the computer codes. This work is being accomplished through a program of testing and analysis.

The model for the von Mises flow stress, $\bar{\sigma}$, is expressed as

$$\bar{\sigma} = [A + B \epsilon^n] [1 + C \ln \dot{\epsilon}^*] [1 - T^{*m}] \quad (1)$$

where ϵ is the equivalent plastic strain, $\dot{\epsilon}^* = \dot{\epsilon}/\dot{\epsilon}_0$ is the dimensionless plastic strain rate and T^* is the homologous temperature. The five material constants are A, B, C, n, m. The expression in the first set of brackets gives the stress as a function of strain for $\dot{\epsilon}^* = 1.0$ and $T^* = 0$. The expressions in the second and third sets of brackets represent the effects of strain rate and temperature, respectively. The basic form of the model is readily adaptable to most computer codes since it uses variables (ϵ , $\dot{\epsilon}^*$, T^*) which are available in the codes.

The data for the material constants are being obtained from torsion tests over a wide range of strain rates (quasi-static to about 400 s^{-1}), static tensile tests, dynamic Hopkinson bar tensile tests, and Hopkinson bar tests at elevated temperatures. The effects of strain hardening, strain rate hardening and thermal softening are clearly evident

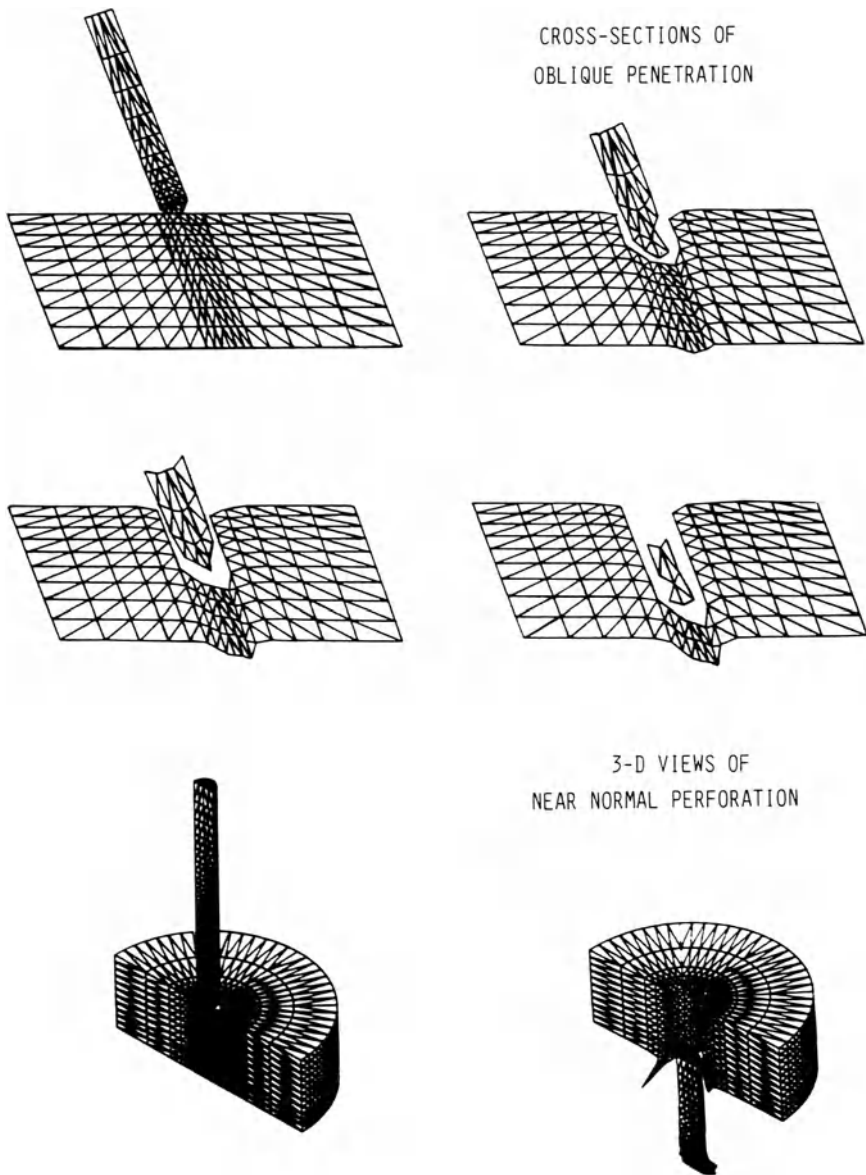


Figure 2. EPIC-3 Simulations Showing Capability for Eroding the Master and the Slave Surfaces

in all of the materials. The mode of deformation (tension vs. torsion) also has an influence on the resulting flow stress.

The torsion tester and the initial data are described in [3] and [4]. Torsional data and analyses for six very ductile materials (OFHC copper, cartridge brass, Nickel 200, Armco IF iron, Carpenter electrical iron, 1006 steel) are presented in [5]. Similar data and analyses for six less ductile materials (2024-T351 aluminum, 7039 aluminum, low alloy steel, S-7 tool steel, tungsten alloy, DU-0.75 Ti) are presented in [6]. The Hopkinson bar testing and analyses have not yet been completed.

A damage model for fracture has been developed and is currently being evaluated. It has the capability to take into account the effects of strain, ϵ , strain rate, $\dot{\epsilon}^*$, temperature, T^* , and dimensionless pressure, $\sigma^* = P/\bar{\sigma}$. It is path-dependent and requires only one storage variable per element. The expression for the strain at fracture is given by

$$\epsilon^f = [D_1 + D_2 \exp^{D_3 \sigma^*}] [1 + D_4 \ln \dot{\epsilon}^*] [1 + D_5 T^*] \quad (2)$$

for constant values of the variables (σ^* , $\dot{\epsilon}^*$, T^*). The five constants are $D_1 \dots D_5$. The damage to an element during an integration cycle is $\Delta D = \Delta \epsilon / \epsilon^f$, where $\Delta \epsilon$ is the equivalent plastic strain during that cycle and ϵ^f is the failure strain under the current conditions of σ^* , $\dot{\epsilon}^*$, T^* . The total damage is then $D = \Sigma \Delta \epsilon / \epsilon^f$ and failure occurs when $D = 1.0$.

Since this failure model is based on failure strains at constant σ^* , $\dot{\epsilon}^*$, and T^* , it is accurate under constant conditions. It is currently being evaluated for complicated loading paths. Although simple, the model is rational, and should provide a significant improvement over other failure models based only on plastic strain or the current condition of other variables.

The results obtained to date indicate that the fracture strain, ϵ^f , is highly dependent on the dimensionless pressure, σ^* . As σ^* goes from compression to tension, the corresponding fracture strain decreases rapidly. The strain rate and temperature have a much less significant effect on the fracture strain. The present study is scheduled for completion at the end of 1982. The detailed results of this work will be reported shortly thereafter.

New Computing Concept — The NABOR Code

The primary limitation of existing Lagrangian codes is their inability to represent very severe distortions. This limitation can essentially be eliminated by allowing for continuously changing nodal connectivity. Figure 3 shows a schematic representation of the main features of this new Lagrangian approach. The essential nature of this code is that each node is affected only by its "nearest neighbor" nodes. Using a flexible disk analogy for the nodes, it can be seen from Figure 3 that the maximum number of nearest neigh-

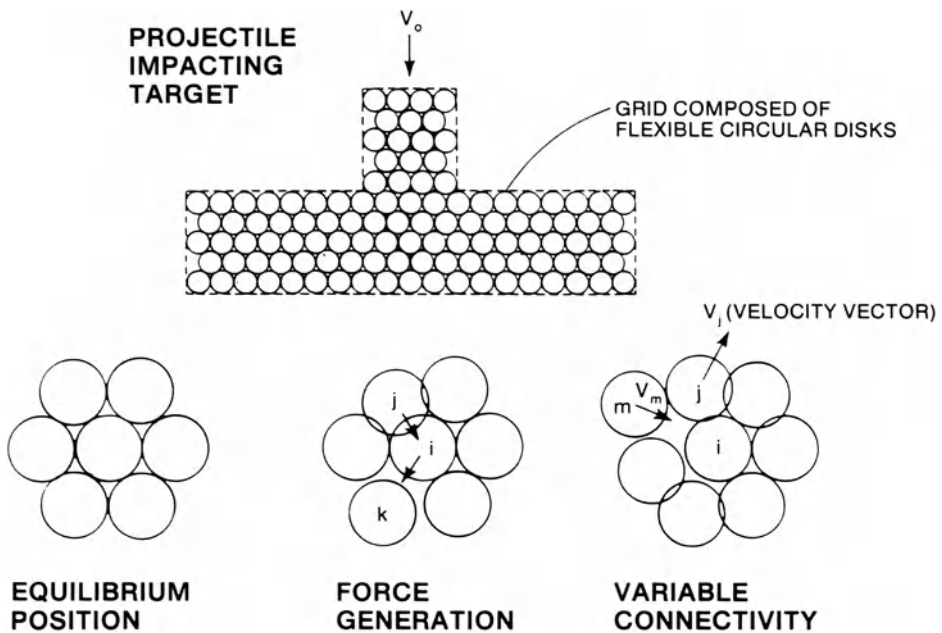


Figure 3. Schematic Representation of the NABOR Computational Technique

bors is six. As the nodes move closer than their equilibrium distance they generate compressive, repulsive forces. Conversely, when they move apart they generate tensile, attractive forces. Material strength effects can also be included. The key to this approach is that it is possible to have variable connectivity, i.e., a node can take on new nearest neighbors, thus allowing all forms of distortion. Based on the concept of nearest neighbors, the code has been called NABOR. Much of the NABOR work to date has been done by J.G. Dodd, Professor at Colgate University and consultant to Honeywell.

Another method of representing severe distortion is the particle-and-force method, developed at the Los Alamos Scientific Laboratory during the early sixties [7]. Although this method also makes use of variable connectivity, there are numerous differences; it does not include solids, it is not closely tied to six nearest neighbors, the search routines are different, and the force relationships are different.

The initial NABOR geometry for plane strain is shown in Figure 3. The nodes represent the centers of the flexible disks, arranged in a hexagonal close-pack configuration. If the initial disk radius is R_o , then the nodal spacing is $D_o = 2R_o$. Each internal node thus has six nearest neighbors. Although every node has the capacity to have six neighbors, the boundary nodes have fewer neighbors. After the grid is generated, the lattice is searched for each node to determine its six nearest neighbors. If two nodes are within a distance of

about D_0 then they are defined as neighbors and stored in the nearest neighbor array $NN(I,J)$; where $I = 1, N$ represents each node and $J = 1,6$ represents six "bond" positions for the node numbers of the nearest neighbor.

It is clear that it would not be computationally feasible to search the entire grid, for each node and for each cycle, to determine the appropriate nearest neighbors. Therefore, it is important that this portion of the technique be performed as efficiently as possible. The following three search criteria greatly reduce the time required for searching:

- If node i has six nearest neighbors in the node array, $NN(I,J)$, then the distances between node i and the six nearest neighbors are computed. If α is defined as a constant in the range of 1.2 to 1.4, and if the nodal distances, D , are all $D < \alpha D_0$, then the six nearest neighbors remain the same. This essentially says that if a node already has six close neighbors, there can be no room left for another. This check is a very quick one and represents the situation which exists the majority of the time.
- If the preceding check indicates that one (or more) of the neighbors has a distance $D > \alpha D_0$, then it is necessary to check if there is another node which has moved in to replace the existing neighbor. For example, when the distance between node i and node m becomes less than the distance between node i and node j , in Figure 3, then node m replaces node j as a neighbor to node i . The problem for the search routine is to find node m as quickly as possible. This is done by first checking the nearest neighbors of the departing node. In Figure 3 it can be seen that node m is, in fact, a neighbor of departing node j and can therefore be found very quickly. For those rare instances when this initial search does not produce another neighbor, then the entire grid must be searched.
- There will be some instances where a node will have less than six nearest neighbors. This will always be the case for boundary nodes. If a bond is vacant, then a search is made for the node that would, under the current velocity closing conditions at that cycle, first get within bonding distance ($D < \alpha D_0$). The time this will take to occur is converted to cycles using the current time increment. Some small fraction of this number of cycles is then stored as a negative number in that vacant bond position in the nearest neighbor array, $NN(I,J)$. This negative integer is incremented upward each cycle, and when zero, triggers another search for a neighbor at that position. If no new neighbor is found, the process is repeated. This process drastically reduces the search time for boundary nodes.

As two nodes move closer than the initial equilibrium distance to one another, compressive forces develop between the nodes, as shown in Figure 3. It is at this point that a difference exists between the NABOR approach and that used in traditional Lagrangian finite element and finite difference approaches. In the traditional approaches, the pressure is related to the volumetric strain in an element or a cell. The distance between adjacent nodes does not affect the pressure directly, but only indirectly through its affect on the volumetric strain.

For the NABOR approach, on the other hand, it is necessary to develop a relationship between the nodal distance and the nodal force. Energy effects must also be included. One way to approach this relationship is to derive the forces on the basis of molecular physics. A strong argument for this approach is that this is the way real materials behave. Even if the forces are not derived in this manner, a strong argument for the basic approach remains; the simulation does on a larger scale what real material does on a much smaller molecular scale.

The primary disadvantage of this molecular approach is that more than the immediate six nearest neighbors contribute to the solution. Also, it is more convenient for most users if they can work with traditional equations of state, rather than molecular physics. Therefore, the approach which has been used is that of approximating the volumetric strain with a linear strain based on the distance between nodes.

The upper portion of Figure 4 shows a hexagonal close-pack configuration of nodes. If the grid is subjected to a uniform compressive pressure, all distances between the nodes are reduced uniformly as shown in the lower left portion of the figure. If D_0 and A_0 represent the initial distance between nodes and the initial area of each of triangles, then the compressed area is $A = A_0 (D/D_0)^2$, where D is the compressed distance between nodes. Furthermore, if $\mu = \rho/\rho_0 - 1$, where ρ_0 and ρ represent the initial and current densities, then μ can be expressed as a function of D_0 and D .

$$\mu = \rho/\rho_0 - 1 = V_0/V - 1 = A_0/A - 1 = (D_0/D)^2 - 1 \quad (3)$$

where the volumes, V_0 and V , are directly proportional to the areas, A_0 and A , for plane strain geometry.

Now it is possible to compute the hydrostatic pressure from the Mie-Gruneisen equation of state.

$$P = (K_1\mu + K_2\mu^2 + K_3\mu^3)(1 - \Gamma\mu/2) + \Gamma E_s(1 + \mu) \quad (4)$$

where K_1 , K_2 , and K_3 are material-dependent constants, Γ is the Gruneisen coefficient, and E_s is the internal energy per original unit volume.

The artificial viscosity, Q , is dependent on the volumetric strain rate which is given by

$$\dot{\epsilon}_v = 2\Delta V/D \quad (5)$$

where ΔV is the relative separation velocity between two nodes.

The resulting force due to the pressure and artificial viscosity can then be expressed as

$$F = (\sqrt{3}/2)(P + Q)D \quad (6)$$

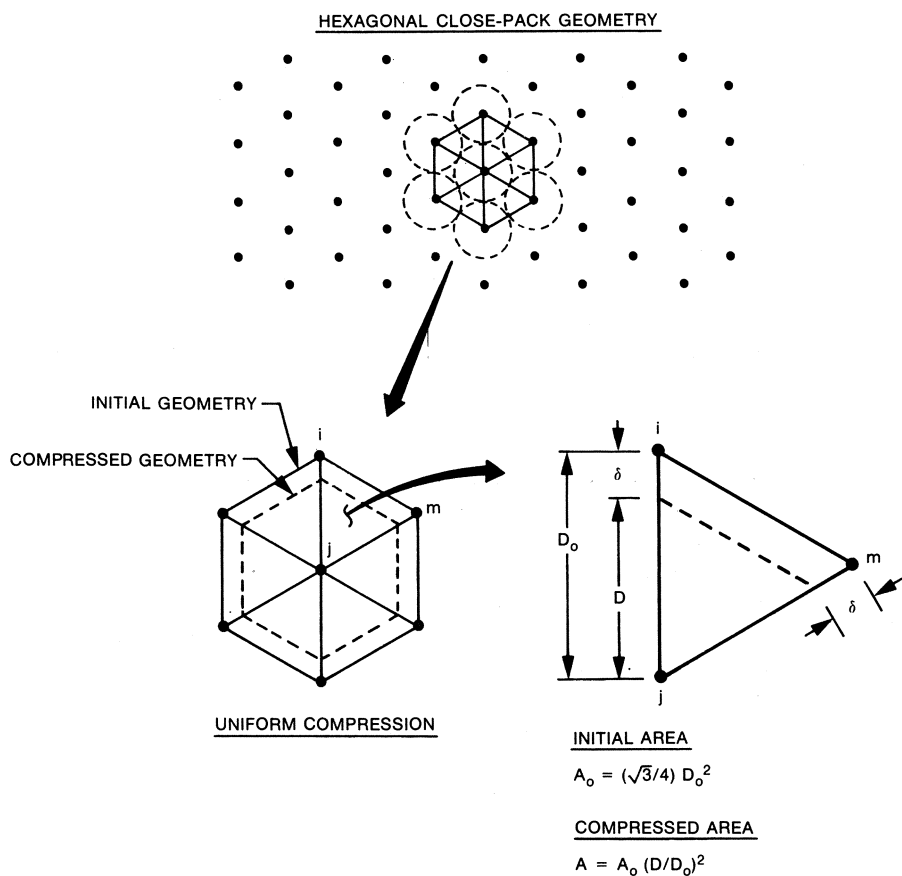


Figure 4. Volumetric Strain Relationships for the Hexagonal Close-Pack Nodal Geometry

Material strength effects can be added by utilizing triangular elements as shown in Figure 4. The forces due to shear and deviator stresses are also distributed to the nodes. After all forces are distributed, the equations of motion are updated in the usual manner.

A simplified version of NABOR has been developed and an example is shown in Figure 5. This involves a projectile impacting a deformable plate of the same material (copper with no strength) at a velocity of 1000 m/s. It can be seen that there has been significant swapping of nearest neighbor nodes and that large distortions have been generated.

Continued developed of the code is anticipated. The primary tasks consist of incorporating material strength effects, evaluating the accuracy, and assessing the computing time required for large simulations.

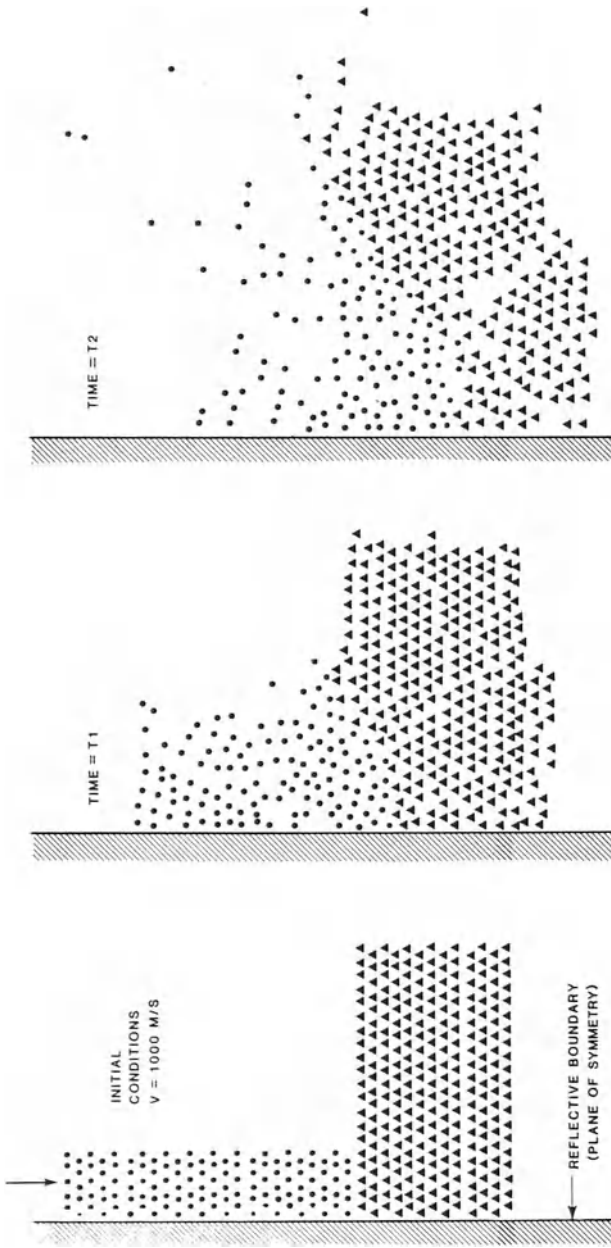


Figure 5. NABOR Simulation of a Copper Projectile Impacting a Copper Plate at 1000 m/s. Material strength effects not included.

If, eventually, it is determined that the computing time is too great or the accuracy is not sufficient for mild plastic flow, then another very interesting possibility could be examined. This is illustrated schematically in Figure 6, where a projectile is about to impact a target plate. Two different Lagrangian grids are used for this problem. In the areas which will be highly distorted, the NABOR grid is used. For the remainder of the geometry a traditional Lagrangian grid is used.

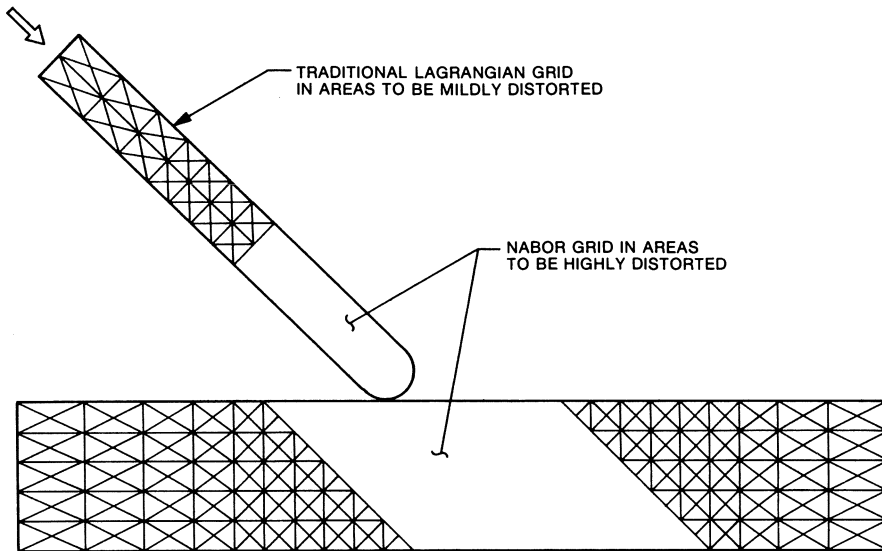


Figure 6. Schematic of the NABOR Computational Technique Coupled to a Traditional Lagrangian Computational Technique

By decreasing the number of NABOR nodes, the search time is reduced. Also, since the traditional Lagrangian approach is probably more accurate in the mildly distorted areas, the incorporation of this grid increases the accuracy of the solution. The coupling together of the two Lagrangian approaches would be much more straightforward than that of combining a Lagrangian code with a Eulerian code. The nodal equations of motion are identical for the NABOR and traditional Lagrangian approaches; both have concentrated forces acting on concentrated masses. There would be a separate element loop for the traditional Lagrangian approach with the output being nodal forces, and a separate loop for the NABOR nodes to generate nodal forces.

Referring again to Figure 6, another potential use of this approach can be envisioned. If the projectile is a steel penetrator, and it is impacting a concrete target, for example, then the projectile would see relatively little distortion and the concrete would be severely distorted. In this case the entire projectile could be composed of a traditional La-

grangian grid and the target could contain the NABOR grid as shown. The interaction between the projectile and the target would occur by allowing the NABOR nodes to be "slave" nodes to the "master" surface of the projectile. This general problem is of much interest at this time and there are currently no satisfactory computational approaches available.

References

1. Johnson, G.R., "Recent Development and Analyses Associated with the EPIC-2 and EPIC-3 Codes," *1981 Advances in Aerospace Structures and Materials*, AD-01, Wang, S.S. and Renton, W.J., eds. ASME, 1981.
2. Johnson, G.R., Colby, D.D. and Vavrick, D.J., "Three-Dimensional Computer Code for Dynamic Response of Solids to Intense Impulsive Loads," *International Journal for Numerical Methods in Engineering*, 1979.
3. Lindholm, U.S., Nagy, A., Johnson, G.R., and Hoegfeldt, J.M., "Large Strain, High Strain Rate Testing of Copper," *Journal of Engineering Materials and Technology*, ASME, October 1980.
4. Johnson, G.R., "Dynamic Analysis of a Torsion Test Specimen Including Heat Conduction and Plastic Flow," *Journal of Engineering Materials and Technology*, ASME, July 1981.
5. Johnson, G.R., Hoegfeldt, J.M., Lindholm, U.S. and Nagy, A., "Response of Various Metals to Large Torsional Strains over a Large Range of Strain Rates—Part 1: Ductile Metals," *Journal of Engineering Materials and Technology*, ASME, (in press 1983).
6. Johnson, G.R., Hoegfeldt, J.M., Lindholm, U.S. and Nagy, A., "Response of Various Metals to Large Torsional Strains over a Large Range of Strain Rates—Part 2: Less Ductile Metals," *Journal of Engineering Materials and Technology*, ASME, (in press 1983).
7. Daly, B.J., Harlow, F.H., Welch, J.E., Wilson, E.N., and Sanmann, E.E., "Numerical Fluid Dynamics Using the Particle-and-Force Method," LA-3144, Los Alamos Scientific Laboratory, 1965.

NEW SLIDING SURFACE TECHNIQUES ENABLE LAGRANGIAN CODE TO HANDLE DEEP TARGET
PENETRATION/PERFORATION PROBLEMS

B. E. RINGERS

Ballistic Research Laboratory
ATTN: DRDAR-BLT
Aberdeen Proving Ground, MD 21005

Summary

Sliding surface techniques were developed and incorporated into EPIC-2¹, a Lagrangian finite element impact code to accomplish the dynamic relocation of sliding surfaces and the automatic addition and processing of new sliding surfaces when warranted. This development was necessary in order to model ballistic impact situations involving deep penetration and/or perforation of targets.

The techniques were implemented and tested in an axisymmetric simulation of a kinetic energy penetrator versus a titanium target, the failure of which was considered to be plugging due to high strains.

This paper discusses the modifications involved, the results of the tests performed and the extrapolation of techniques to handle other failure mechanisms, plane strain simulations, and multi-target situations.

Geometrical Considerations

The impetus for this effort was the desire to model ballistic impact situations where the primary mode of target failure was plugging, whether due to high strains or adiabatic shear. In papers by Moss² and Zener and Holloman³ describing the results of punching experiments, the thicknesses of the shear bands measured were in thousandths of an inch; the velocities involved were in tens-of-feet/sec. Johnson⁴ noted that "the faster a punching operation is, the higher the strain rate and the larger the flow stress but the narrower the shear zone."

In modeling ballistic impacts with EPIC-2, triangular element sizes are typically measured in tenths or hundredths of an inch. Therefore, in simulating a region an order of magnitude smaller, it was decided to let splitting occur "between" elements when an element has attained a particular failure criterion.

In the original version of EPIC-2, material fracture is simulated by enabling elements which are not master surface elements to fail in two possible ways: 1) failure in shear and tension if the element exceeds specified equivalent or volumetric strain levels, 2) total failure if the element exceeds a specified equivalent strain level. In the first case the element is still able to withstand hydrostatic compression while in the second case all stresses, including pressure, are set equal to zero. Since the master sliding surface has to remain intact, only relatively moderate penetration problems can be handled before severe grid deformation essentially halts a calculation.

In this effort provision was made to totally fail any elements, including master surface elements, when they reached another, as yet unspecified, failure criterion. The rationale was that shearing should be simulated by splitting "between" elements and that eventually the levels of equivalent strain suffered by some elements would probably require total failure of those elements.

EPIC-2 initially had two-triangle element arrangements and the choice of orientation of the diagonal between the triangles was left to the user. Johnson⁵ recently recommended, however, due to the excessive stiffness of triangular elements in this arrangement, that future EPIC-2 simulations utilize crossed triangles (4 triangles in a quad) arrangement. (Note the element arrangement in Figure 1a.) The geometry generator for this arrangement was therefore utilized in this work.

Sliding Surface Techniques in EPIC-2

EPIC-2 utilizes sliding surfaces comprised of master and slave nodes to keep projectile and target materials separate. For each time increment, the equations of motion are applied to the master nodes (usually the target frontal surface) and the slave nodes (usually those on the projectile surface likely to interact with the target).

There were some problems with the original EPIC-2 sliding surface routines. Under certain conditions crossovers (interference) occurred between projectile and target materials⁶. Sliding surface routines written by Lambert⁷ which corrected these problems and increased efficiency were therefore utilized in place of the original sliding surface routines. A two-pass check is made for interference: slave nodes versus master surfaces, then master nodes versus slave surfaces. If there is interference in the first case the slave node is placed on the master surface in a direction normal to the master surface. Similarly an interfering master node is placed on the slave surface. Ensuring that translational and rotational momenta are conserved, the velocities of the interfering node and the two nodes comprising the surface involved are updated.

New Sliding Surface Techniques

This work primarily involved dynamically relocating the master surface in order to handle the modeling of target deep penetration and perforation. It is assumed that the slave surface resides on the projectile exterior and the original master surface specified by the user is the frontal target surface. (This is arbitrary and could readily be reversed.) When an element attains Criterion 1* indicating that fracture or "splitting" is to occur, a node is essentially split in two (Figure 1a, 1b.); the "split" node, that meeting Criterion 2*, also must be a master node or the element involved is rejected as causing "splitting". The direction of the split, determined by a third criterion*, establishes the "next" node, the node from which further splitting must occur.

(* Defined in the following section).

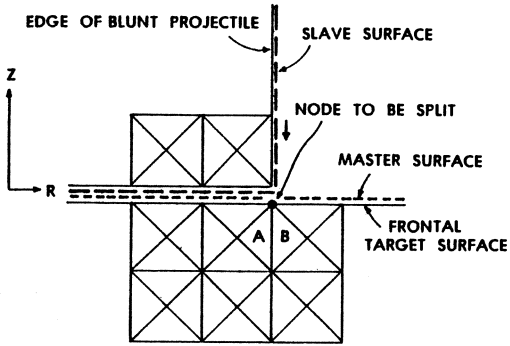


Figure 1a. Element A or B Meets Criterion 1

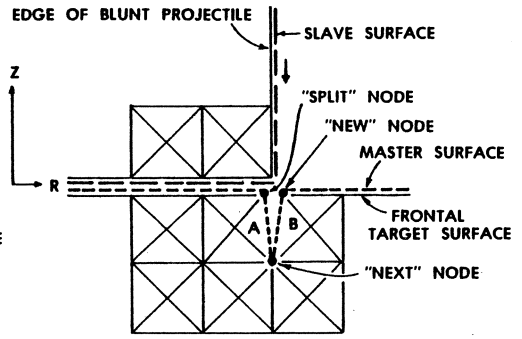


Figure 1b. "Split" Node Meets Criterion 2
Criterion 3 Establishes "Next" Node

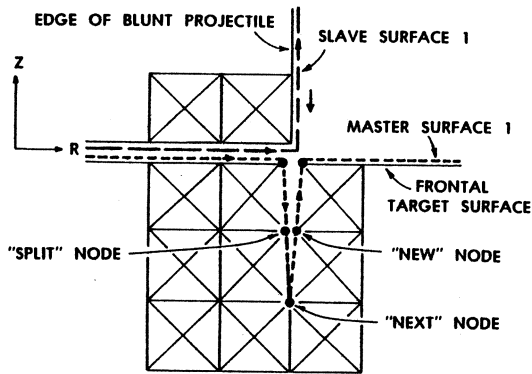


Figure 2a. Sliding Surface 1 Interactions

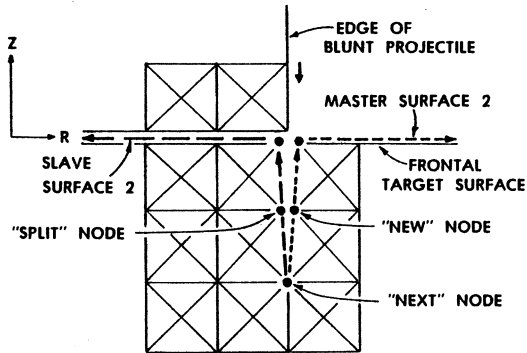


Figure 2b. Sliding Surface 2 Interactions

Once the "split", "new", and "next" nodes are determined, the elements involved are assigned the "split" or "new" node depending on which side of the split they reside. Both the "next" node and the "new" node are now inserted in the master surface after the original "split" node, thereby dynamically relocating this sliding surface. (See Figure 2a.) The "new" node is assigned the same coordinates, velocities and restraint properties as the "split" node. The masses assigned to the "split" and "new" nodes are based on which elements now share each node. The forces assigned the "split" and "new" nodes are based on the ratios of the newly assigned nodal masses to the original pre-split nodal mass.

Besides interference between the projectile (slave surface) and target (master surface) there must be concern about possible interference between the two sides of the split developing in the target. This is handled by establishing another set of master and slave surfaces whose mutual interference is checked identically to the first set. The second slave surface is considered to be the first master surface up to and including the original "split" node. The second master surface is considered to be the first master surface starting with the "next" node (the second node being the "new" node). (See Figure 2b.) This was also done arbitrarily in that the second master and slave surfaces could reverse positions and the result should be the same.

Interference between master and slave surfaces is based on the stipulation that the slave surface remains to the left of the master surface proceeding in the increasing direction of the sliding surface. A necessary addition to the sliding surface treatment was the consideration of an interposing surface between a supposed interfering slave or master node and a corresponding master or slave surface. (See Figure 3.) The master node M is to the right of slave surface S1 but it is also to the left of slave surface S2. M, therefore, appears to be interfering with S2 but surface S1 interposes so M does not validly interfere.

The split continues until either the projectile velocity reaches zero or until target perforation occurs. When the "next" node is positioned on the distal target surface, perforation is imminent; a discontinuity in the sliding surface enables complete separation of the plug from the remaining target material. There is no further test for elements reaching Criterion 1.

Simulation of Axisymmetric Plugging Failure

To test the techniques discussed, an experimental situation performed and discussed by Woodward⁸ was modeled. A blunt, hardened, roller bearing steel cylinder impacted a pure titanium (Ti 125) target. The expected energy to accomplish perforation resulted in a critical velocity of approximately 300 m/s. Various attempts detailed in Reference 9 involved a striking velocity of 350 m/s with various levels of critical equivalent strain utilized to initiate and further fracture. The case presented here was done primarily so that the problem would progress quickly, testing out the techniques developed and assuring perforation.

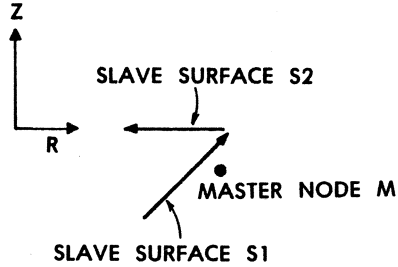


Figure 3. Interposing Surface

	<u>PROJECTILE</u>		<u>TARGET 1 (Ti 125)</u>
<u>MATERIAL</u>	<u>HARDENED, ROLLER BEARING STEEL</u>		<u>ROLLED & ANNEALED 99% PURE Ti</u>
SHAPE	BLUNT		50 mm SQUARE
MASS	3.34 g		—
LENGTH	25.4 mm	THICK	6.35 mm
DIAMETER	4.76 mm		—
DENSITY	$7.39 \times 10^3 \text{ kg/m}^3$		$4.51 \times 10^3 \text{ kg/m}^3$
YIELD σ_Y	2290 MPa		522.5 MPa
UTL σ_U	2500 MPa		600 MPa
ϵ_U	∞		.45 - .5
SPEC HEAT	$4.6 \times 10^2 \text{ J/kg } ^\circ\text{C}$		$5.1916 \times 10^2 \text{ J/kg } ^\circ\text{C}$
YOUNGS MOD	$1.93 \times 10^5 \text{ MPa}$		$1.158 \times 10^5 \text{ MPa}$

Table 1. Projectile and Target Characteristics

The parameters which were utilized to model this ballistic impact situation, except with a striking velocity of 500 m/s, are given in Table 1. The criteria utilized to model the fracture involved in the plugging failure and discussed in Reference 9 were as follows:

Criterion 1: An element initiates or furthers a split

- 1) when its equivalent strain reaches an assigned critical level, and
- 2) if furthering a split, is associated with the "next" node, and
- 3) its shear stress is greater than its deviatoric axial or radial stress, and
- 4) the direction of the split (Criterion 3) does not change by 90° or more.

Criterion 2: The node at which initial splitting occurs

- 1) must belong to the element meeting Criterion 1, and
- 2) must suffer the highest force of all three nodes belonging to the same element, and
- 3) must be a master node.

Criterion 3: The direction of the split is determined by the strain of the element meeting Criterion 1. If the axial strain is greater than the radial strain, splitting is to the nearer radial node. Otherwise, splitting is to the nearer axial node.

Since experimental evidence did not exist for the striking velocity involved in this calculation, the amount of possible projectile and target erosion was unknown. The conservative position was taken that elements would be totally failed only when a minimum time increment violation occurred. Deformation plots of the results are shown in Figure 4. The position of the elements which initiated or furthered splitting and the times at which they did so are shown in Figure 5. Target perforation was predicted to occur at $35.6 \mu\text{s}$. The projectile velocities and depths of penetration are shown through $45 \mu\text{s}$ in Figures 6a and 6b.

At $44.7 \mu\text{s}$ a minimum time increment violation for an element in the highly stressed target material to the right of the plug did occur. Modifications were subsequently made to automatically enable an element to be totally failed for a minimum time increment violation and the calculation was continued, primarily to prove that the procedure worked.

The residual velocity of the projectile stabilized at 237 m/s by $40 \mu\text{s}$ so at $45 \mu\text{s}$ the projectile and plug are essentially free of the remaining target material. If a second target were involved, it would now be reasonable to dispose of the non-plug target elements and address the problems involved in multi-target impact simulations discussed in the following section.

The deformation plots indicate large volumetric strains for the distal target elements at $15 \mu\text{s}$ and later. Woodward¹⁰ suggested that it might be due to a buildup of hydrostatic tension. The hydrostatic tension had been limited to one-third of the ultimate strength of the material in the calculation. The calculation was rerun

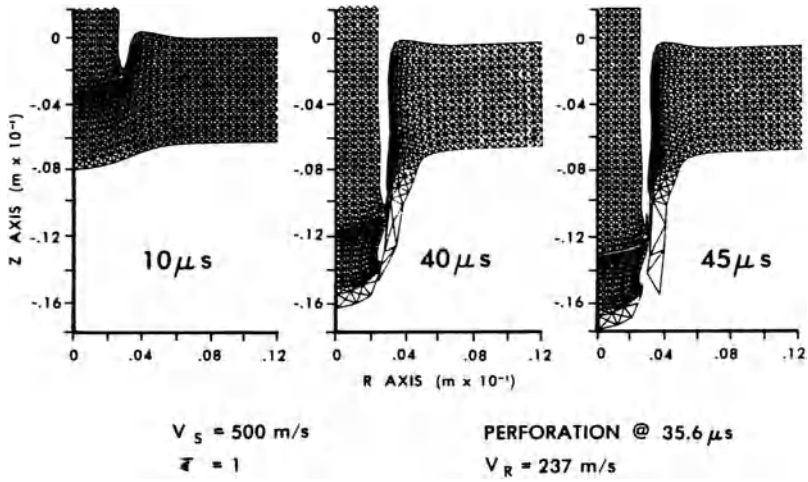


Figure 4. Deformation Plots Showing Progress of Calculation Simulating Steel Cylinder vs Ti 125 Target

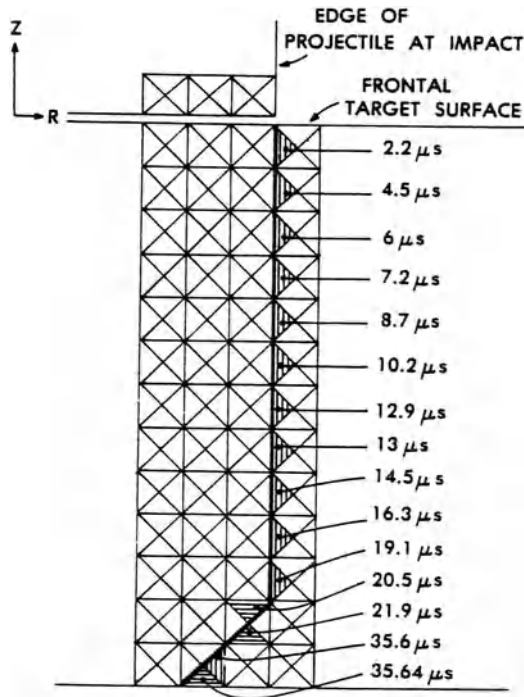


Figure 5. Pattern of Elements Which Initiated or Furthered Splitting

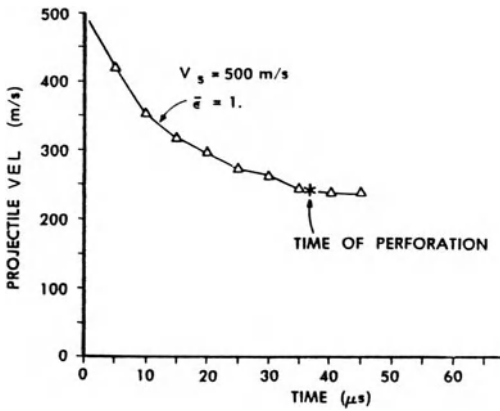


Figure 6a. Projectile Velocity History

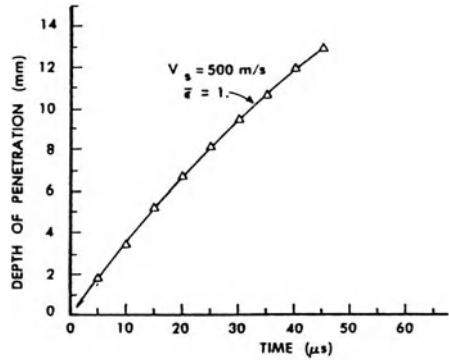


Figure 6b. Depth of Penetration History

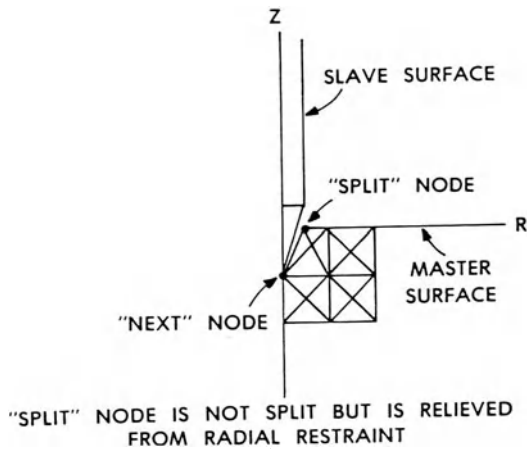


Figure 7. Modification of Techniques to Handle Axisymmetric Simulation of Piercing Target Failure

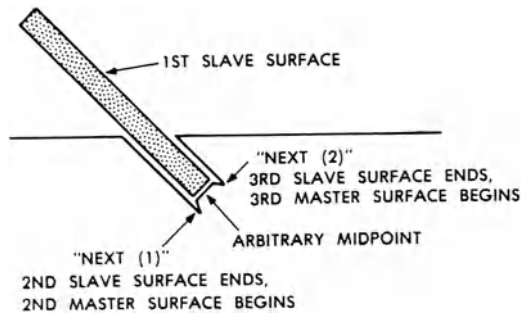


Figure 8. Modification of Techniques to Handle Plane Strain Simulations

with the hydrostatic tension limited to 100% of the ultimate strength; the "blowup" of the distal target elements disappeared. (See Figure 9.)

Extrapolation of Techniques to Other Impact Situations

A. Axisymmetric, Piercing Failure Simulations:

For axisymmetric simulations of piercing failure, the techniques discussed can be utilized with regard to the generation of the "split" and "next" nodes. However, symmetry is about the z axis and the nodes along the z axis are restrained radially. If the "next" node is restrained at the z axis (Figure 7) then it simply becomes the first node on the master sliding surface and the "split" node is not split: instead it is released from its restraint at the z axis. Until an unrestrained node becomes the "next" node, there is no generation of new master and slave surfaces.

B. Plane Strain Simulations:

The techniques discussed can also be utilized in plane strain simulations, the primary difference being the need to generate a third, as well as a second, sliding surface to handle plugging failure. The development of the third sliding surface would proceed exactly as the second. The subsequent inefficient and unnecessary overlap of second master surface with the third slave and master surfaces could be eliminated by choosing a convenient midpoint at which to arbitrarily end the second master surface and begin the third slave surface. (See Figure 8.)

C. Multi-Target Situations:

Once target nodes and elements other than those comprising a plug are no longer affected by the projectile, modifications can be instituted to eliminate these target nodes with sufficiently low velocity and their associated elements. In the calculation presented, the plug nodes had velocities which were an order of magnitude greater than the remaining target nodes. The second (and third, if for a plane strain simulation) sliding surface can then be eliminated and a second target surface generated. The various, possibly complex, sliding surface interactions which would be necessary would depend on the particular new target situation and whether the projectile and plug stayed together while impacting the second target.

Conclusions

Techniques have been described which dynamically relocate sliding surfaces and add new ones when necessary in order to enable EPIC-2 to handle deep penetration/perforation of targets in ballistic impact simulations. An axisymmetric ballistic impact test case where plugging due to high strains was the primary failure mode was presented. Future work includes testing the techniques developed for plugging due to adiabatic shear, impacts involving piercing target failure, and plane strain simulations. It should now be feasible to consider utilizing this modified Lagrangian code to address multiple target situations as well.

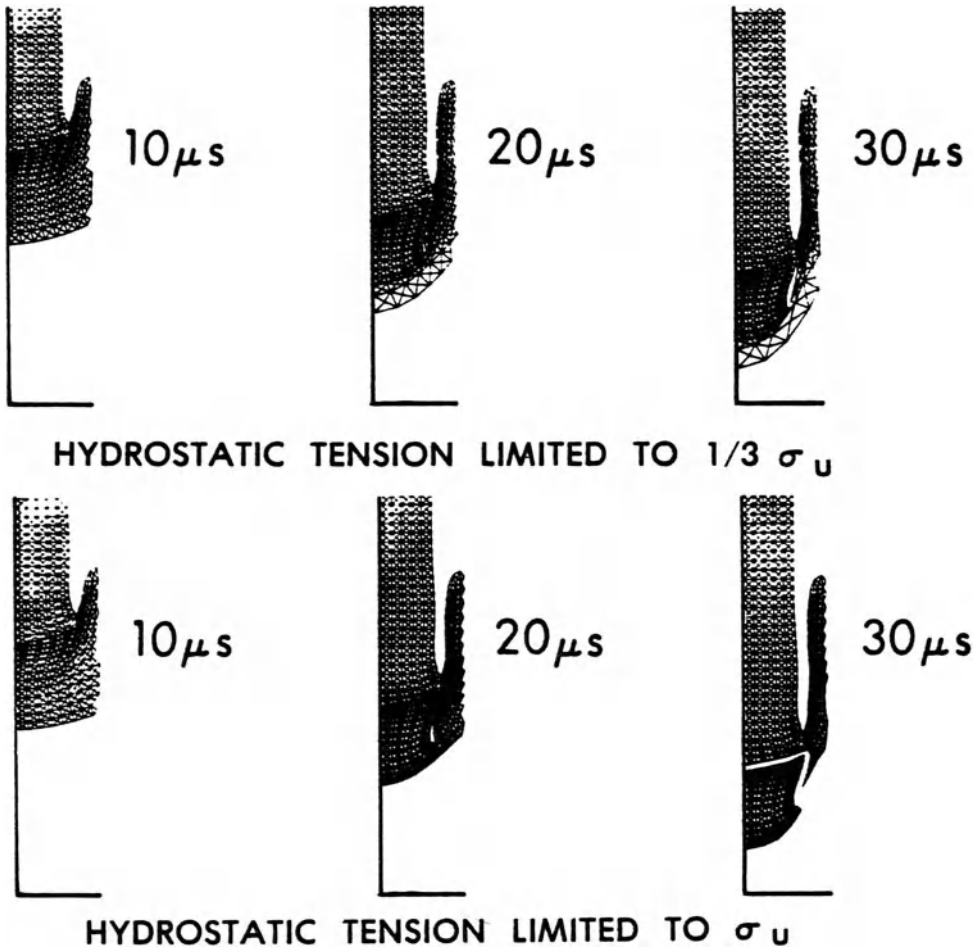


Figure 9. Comparison of Results With Different Hydrostatic Tension Limitations

VIII References

1. Johnson, G. R., "EPIC-2, A Computer Program For Elastic-Plastic Impact Computations in 2 Dimensions Plus Spin," US Army BRL Contract Report ARBRL-CR-00373, June 1978.
2. Moss, G. L., "Shear Strains, Strain Rates and Temperature Changes in Adiabatic Shear Bands," US Army BRL Report ARBRL-TR-02242, May 1980.
3. Zener C., Hollomon, J. H., "Effect of Strain Rate Upon Plastic Flow of Steel," J. Appl. Phys., V. 103, No. 1, March 1981.
4. Johnson, W., "Impact Strength of Materials," Edward Arnold Ltd., 1972.
5. Johnson, G. R., "Triangular Element Arrangement for EPIC-2," Internal Memorandum, July 1979.
6. Johnson, G. R., "Dynamic Analysis of Explosive-Metal Interaction in Three Dimensions," J. Appl. Mech., V. 103, No 1., March 1981.
7. Lambert, J. P., Private Communication.
8. Woodward, R. L., "The Penetration of Metal Targets Which Fail By Adiabatic Shear Plugging," Int. J. Mech. Sci., V. 20, 1978, 599-607.
9. Ringers, B. E., "New Sliding Surface Techniques Enable the Modeling of Target Plugging Failure," Ballistic Research Laboratory Report, to be published.
10. Woodward, R. L., Private Communication.

MATERIALS ISSUES IN COMPUTER SIMULATIONS OF PENETRATION MECHANICS

JOHN MESCALL

Army Materials and Mechanics Research Center
Watertown, Massachusetts

Summary

The importance of the role played by materials properties under shock loading conditions is outlined by a discussion of experimental results. Several inferences are then drawn from computer simulations of penetration events with applications to both kinematic and materials issues. A discussion is presented of suggested tests for characterizing material response in this regime.

Introduction

Computer simulations have proven to be extremely useful in assisting the interpretation of experimental results in both ballistic penetration and fragmentation munitions. Specifically, they can provide quantitative and

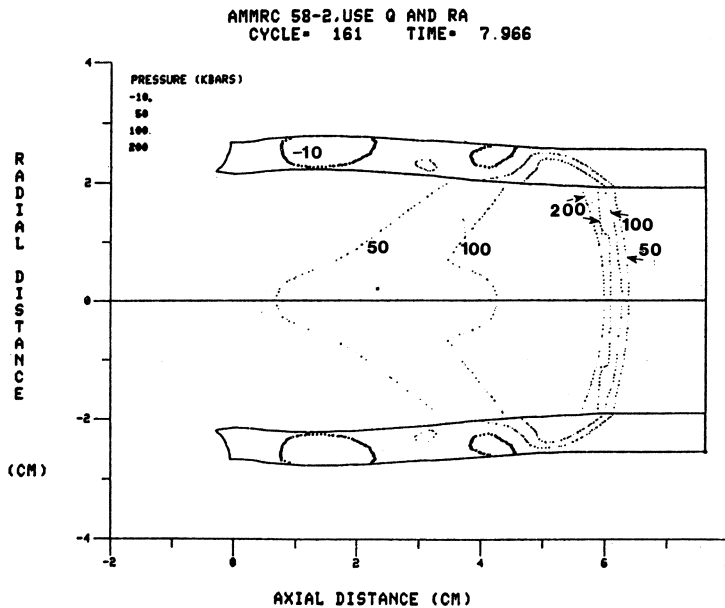


Fig. 1. Simulation of detonation wave moving through high-explosive within steel cylinder. Pressure isobars are in kilobars. Time is eight microseconds after detonation.

reliable details of stress, strain and deformation fields prevailing in these ordnance applications. However, our ability to compute such detail has far outstripped our level of understanding of the failure mechanisms involved in such applications. The conclusion to be drawn from this is clear and simple: if full use of computer simulations of penetration events is to be achieved, we need to focus a great deal more effort into understanding the role of material properties in such events as distinct from the kinematic issues (i.e. those pertinent to displacements or velocities). Most popular computer programs used in this context are able to estimate kinematic details very well indeed. For example, in the problem of a hollow steel cylinder filled with high-explosive which has been detonated, predicted details of the amplitude of the detonation wave in the explosive and the resultant velocity produced in the steel casing as well as the timing of such events agree with experimental observations to within a few percent. The number of fragments produced, however, depends strongly upon the specific material properties of the metal casing and are at present not predictable in a satisfactory manner.

It is the thesis of this report that an improvement in this arena is needed far more than improvements in, say, numerical algorithms over those presently available. Our objective is to illustrate by examples several problem classes of current interest which yield to numerical treatment and to point out deficiencies in the present understanding of how results depend on material response. Of particular concern is the question of how we presently characterize materials to be employed in ballistic environments involving stress fields with intensities ranging from tens to hundreds of kilobars and with durations of tens of microseconds. Finally, we observe that while the notion of material response certainly must include dynamic work-hardening, etc., nevertheless the more challenging and useful aspect of material behavior in this context is the proper description of those conditions leading to fracture. This includes both tensile fracture (spall) and shear (adiabatic or otherwise). A characteristic of the majority of penetration/fragmentation applications is that the shear modes of failure are far more common than the tensile mode.

Analytic Procedures

To describe the formulation behind the computer codes generally used in these applications as succinctly as possible, one might say that one begins with the conservation laws (mass, momentum and energy) expressed in one, two or three spatial dimensions, couples to these an equation of state (constitutive law) which is realistic for the high pressures and short times involved, casts the entire assembly into a finite difference formulation and integrates step by step

in time, explicitly. For details of the HEMP code formulation see Wilkins [1]. Constitutive relations employed consist typically of two elements, one governing the hydrostatic component of stress, one the deviatoric components. The former is developed for a given material in a series of light-gas gun uniaxial strain experiments under shock loading conditions, and is termed the Hugoniot curve for that material. An example is shown in figure (2). The stress path actually

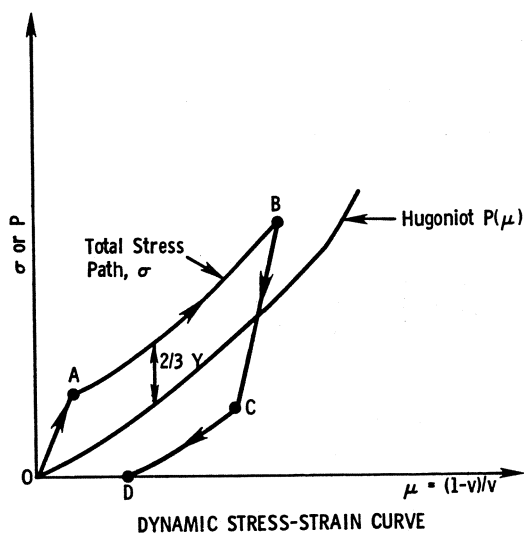


Fig. 2. Schematic constitutive law employed in computer simulations of shock-loading conditions.

followed by a material point subjected to shock loading is offset from the Hugoniot by an amount regulated by the dynamic strength of the material. If the material exhibits work-hardening under these conditions the offset Y is variable, increasing with increasing strain; if thermal softening effects are introduced, Y would decrease in a prescribed manner as plastic work is converted into a temperature rise.

In principle the curve describing the total stress path could be obtained from the light-gas gun experiments. In practice they are not, both for reasons of economy and because such experiments induce a rather special set of stress-strain states which are not representative of those obtained in penetration or fragmentation experiments. Instead, it is common practise in making a computer simulation to begin with a catalogued Hugoniot curve for a material and to

superimpose a flow stress, Y , obtained from static (usually uniaxial TENSION) tests. Most frequently a constant flow stress (no work-hardening) is employed.

Some Experimental Observations

There is abundant ballistic evidence to indicate that experimental results are strongly influenced by the mechanical properties of the materials employed. A particularly instructive example of this is shown in figure (3) taken from [2].

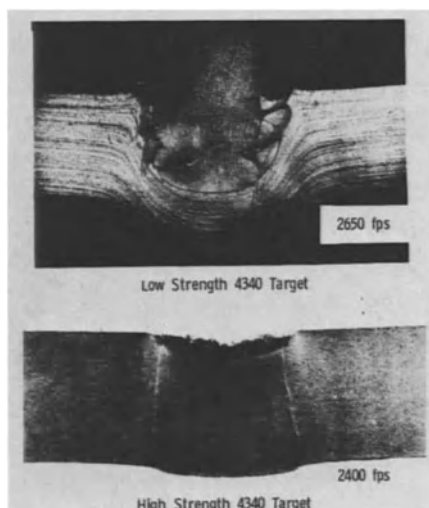


Fig. 3. Cross-sections of steel targets showing differences in failure modes for high and low strength targets.

Two targets made from the same steel alloy (4340), processed in the same way (VAR), but heat treated to two extremes of strength level (soft RCH20 and hard RCH52) were impacted with similar projectiles at a range of velocities. Recovered targets were cross-sectioned and etched. A comparison of the results shown in figure (3) shows that the softer target exhibits massive plastic flow and a large crater forms prior to failure in a plugging mode. The harder target resists indentation for a much larger range of velocities. However, above a critical velocity an adiabatic shear band, visible in the cross section, begins to form in the hard target and leads to premature failure of the target at velocities only slightly higher than the value of 2400 ft/sec shown in figure (3). Premature in this context refers to the observation that at an impact of

1900 ft/sec the hard target showed very little indentation, and a cross-section showed no evidence of adiabatic shear banding. One might conclude from a comparison of the damage observed in the soft and hard targets at 1900 ft/sec impact velocities that the ballistic limit of the hard target should be substantially higher than that of the soft target. It turns out however, that the hard target failed at an impact velocity of 2450 ft/sec while the softer one failed at a velocity of 2700 ft/sec. This diminished performance is directly attributable to the onset of a new mode of failure (adiabatic shear) in the harder target and illustrates one of the subtler nuances of the role of material properties in this context.

Adiabatic shear banding is a term sometimes used to describe the tendency of certain materials to change from a relatively homogeneous deformation pattern to one which includes an extremely localized band of deformation. These bands form after a certain amount of deformation has been induced and appear to be the vehicle by which such materials accommodate the externally imposed loading; i.e. after they appear most of the further deformation occurs within the band. They are often precursors to a shear mode of fracture, with cracks frequently observed within the shear bands. Later in this paper we shall discuss some of the factors thought to contribute to the development of adiabatic shear bands as well as to some initial attempt to model their occurrence.

In the ballistic experiments just referenced the occurrence of shear bands in the targets was not observed until the target hardness was in excess of RCH45, a medium to high strength level for 4340 steel. On the other hand such shear bands have been observed in much softer steels under different loading conditions such as the explosive loadings shown in figure (1).

Inferences From Some Computer Simulations

Figure (4) is extracted from a HEMP simulation of a long-rod uranium penetrator impacting a thick steel target at 5000 ft/sec. The simulation shows conditions prevailing at 22 microseconds after impact. A deep crater is being formed whose diameter is roughly twice the projectile diameter; both projectile and target material are flowing back toward the impact face. These kinematic details are in substantial agreement with experimental observations.

The specific advantage provided by computer simulations such as the one shown is that they provide quantitative information on interior stress and strain states which are not obtainable from any other source. See for example figure (4b).

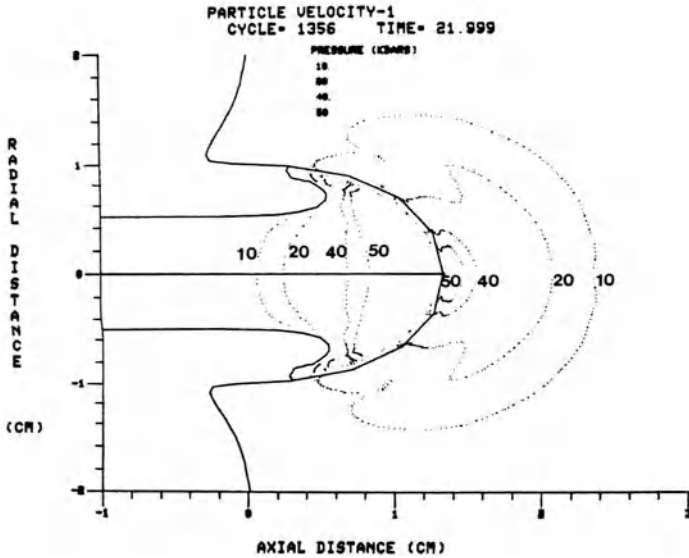
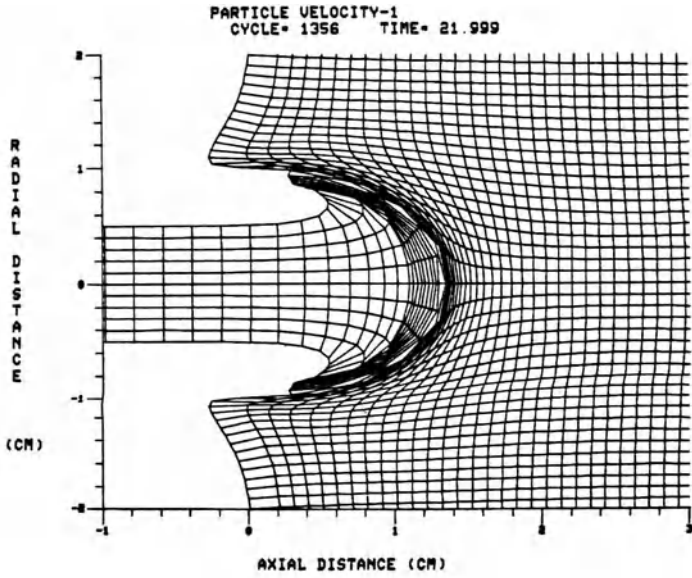


Fig. 4 (a,b). Computer simulation of penetration of steel target by DU long rod. Impact velocity was 5000 ft/sec. Pressure contours shown in figure 4b are in kilobars. They outline the active process zone of the problem.

A detailed examination of the simulation results of which figure (4) is representative would be too lengthy to provide here. However, the following summary involving both kinematic and materials issues can be substantiated in quantitative detail. Note that we are restricting attention for the moment to penetration of a target by an erosion mechanism. This places restrictions on geometric and velocity parameters. The target thickness for example must be comparable or greater than the projectile diameter. The impact velocity must be high enough and the projectile length great enough to excite and sustain the erosion process. With these reservations, which are frequently met in practice we can say that (a) the time of the penetration process may be broken down into stages with distinctive characteristics and (b) during the second of these stages there develops a relatively small spatial region within which most of the events of physical interest occur. This zone, termed by us the process zone, moves in time but does not diffuse spatially.

The stress history within both target and projectile following impact can be divided into three phases. There is an initial shock-propagation phase during which local pressures are extremely high near the impact zone. In the present example of figure (4), peak stresses close to 400 kbars are achieved. This phase is extremely brief in duration compared to the time required for perforation of even a moderately thick target; in the present instance it lasted only 3 microseconds. There is a second phase which persists for a relatively long time (say 100 microseconds or more depending on projectile length and target thickness). The key characteristic of this dominant phase of the erosion process is a quasi steady-state condition of stress in the immediate vicinity of the moving target-projectile interface. The amplitude of this stress state is an order of magnitude lower than that associated with the shock phase. In the example at hand it is roughly 50 - 60 kbars. There is finally a third stage which is characterized by a lower amplitude stress level and one which is more oscillatory in nature. This third stage corresponds to the first stages of the structural response phase of target response.

During the second stage of penetration there exists a highly localized spatial region (the "process zone") within which nearly all the events of physical interest occur. In our present example this zone is about one projectile diameter in extent, is centered at the projectile - target interface and moves with this interface. The outline of this zone can be discerned in figure (4b) from the pressure isobars. Once the second stage (quasi steady-state) of erosion is entered, only elastic waves move away from the process zone. One consequence of this is that deceleration of projectile and acceleration of target material occurs within the process zone, for the most part. It does NOT occur (by way of

contrast) uniformly along the projectile length by propagation of plane waves down the cylinder axis. There is clear experimental evidence to confirm this prediction of the HEMP simulation. Sequential flash x-rays taken as a long-rod penetrates a thick target show that the projectile tail is still moving with very nearly its launch velocity even though nearly fifty percent of the projectile's front end has been eroded away in the penetration process.

The concept of a local process zone helps to explain several anomalous ballistic observations dealing with kinematic features of the problem. For example, if a projectile does perforate a target at a velocity V_0 , then for impact velocities only slightly above V_0 there is a very sharp increase (from zero) in the observed residual velocity of projectile material which passes through the target. In terms of the process-zone model the explanation of this observed behavior is that for the given target thickness and given projectile length, and for velocities below V_0 the penetrator length is completely consumed by the erosion mechanism and no projectile matter is observed behind the target. If the projectile length, target thickness and impact velocity are such that the moving process zone reaches the target rear surface and perforation is achieved before the rear of the projectile enters the process zone, then the projectile stub will have retained a high percentage of its original velocity, as it emerges behind the target.

As another example of the utility of the concept of a process zone, we note another kinematic ballistic anomaly. It is sometimes useful to measure the depth of penetration as a function of impact velocity for a long rod attacking a target with sufficient thickness to prevent perforation [3]. If the velocity is increased to the point that perforation does occur, an abrupt change in the slope of the curve of penetration depth vs. impact velocity is observed - i.e. penetration becomes "easier". An explanation of this behavior would note that for those cases where perforation was not achieved, the process zone did not closely approach the target rear surface. On the other hand, if the zone "sees" the target free surface, the result of their interaction would be an enhanced acceleration of the target material remaining in front of the projectile, rendering the final stage of penetration easier than the earlier phase. This, we believe, is the physical explanation of the observed anomaly.

Before leaving the realm of kinematics to address some of the materials implications of the processing zone concept, we observe that there are approximate theories which provide some assistance in these areas. See for example Tate [4]. These approximate theories are sometimes grouped under the

label of hydrodynamic models of penetration. This label is appropriate NOT because there is any melting of the projectile or target but because the central idea of these models is to apply Beroulli's law to the stagnation point at the projectile - target interface. When the equation which results from the pressure balance there is "integrated in time" (read projectile length) the result is the estimate that: the ratio of the depth of penetration to projectile length is equal to the square root of the ratio of the projectile density to target density. Original versions of this model [5] were successfully applied to shaped charge penetrations of steel targets. Tate [4] adapted the model to the much lower velocity regime associated with kinetic energy penetrators and added correction terms for strength of projectile and target. However, such correction factors have yet to be clearly identified with well - established material parameters measurable in the laboratory.

The utility of these approximate models is that they do provide in simple formulae a correct assessment of the general trend of experimental ballistic results, provided the impact velocity is sufficiently high to justify application of underlying assumptions.

The concept of a process zone has even more interesting implications with regard to material properties. During the steady state phase of the erosion mode (i.e. the bulk of the penetration process in many cases) material within the process zone is subjected to a prevailing compressive stress field of moderate intensity (in the example cited previously, 50 kbars) but accompanied by very large strain fields. Fifty to one hundred percent strains are common. With this in mind it is clear that we need to characterize materials for these applications in terms of a laboratory test which approximates in some sense the compressive stress/strain states actually encountered. It is not surprising to find that correlations of ballistic performance with static TENSILE properties are frequently inadequate and confusing.

It is true that as a penetrator material flows out of the process zone, pressure is relieved and the material may fail in shear (or even tension). This is somewhat beside the point, however, since such material has left the arena of interest and now has little effect on subsequent penetration.

Laboratory Tests For Material Characterization

The applications we have in mind involve compressive tri-axial stress fields of moderate to high intensity, large plastic strains and high loading rates. Ideally, the laboratory tests employed to rank candidate materials for use in

these applications should reflect all of these features. At present no single test is available which incorporates all of them and is at the same time sufficiently well understood to permit us to extract simple parameters that may be used to estimate ballistic performance. Consequently we shall briefly discuss several tests which address part of the problem, alluding to the difficulties encountered with each.

Possibly the simplest test that may be used to characterize compressive behavior is the upset test, in which a cylindrical specimen is squeezed between two rigid plates. The initial response is one of uniaxial (compressive) stress and can be thought of as the analog to the uniaxial tension test, by far the most common mechanical test. Depending upon the frictional effects between specimen and plate, barreling of the specimen occurs and a non-uniform stress state sets in. If the compressive loading is continued to substantial reduction-in-height levels (say 50 percent and more) fracture will occur in one of two modes. Cracks may appear first on the exterior surface of the barreled specimen, or fracture may initiate within the interior of the specimen (possibly undetected). Both modes of fracture are due to very complex states of stress and associated strains which are not easily interpreted in terms of the simple parameters usually measured in the test, i.e., the applied load or specimen end displacement. On the other hand, it is clear that the upset test if properly understood could prove quite valuable for our stated purpose in that it involves fracture under nominally compressive loads and after substantial plastic deformation. Unfortunately no simple and reliable analysis of these complex states exists - there is no compressive analog for example of the Bridgman correction factor used to estimate the interior states of stress in the neck of a tension specimen.

Numerical simulations of the upset test have recently been conducted by the writer [6] and compared with experimental observations [7]. When proper attention is paid to details of the frictional boundary conditions and to special features observed experimentally (the roll-over effect) the agreement between the numerical results and experimental observations is excellent as is shown in figure (5). These simulations quantify the complex set of stress and strain states which is set up both within the specimen and on its surface. They reveal for example that the exterior surface fractures are associated with a biaxial tension field. It is intuitively clear that a tensile hoop stress develops at the specimen equator as barreling proceeds; what is not as obvious is that the axial stress at that location becomes less and less compressive and in fact is tensile when fracture occurs, despite a constantly increasing compressive axial load. Figure (6) shows the external fracture pattern observed in a high strength

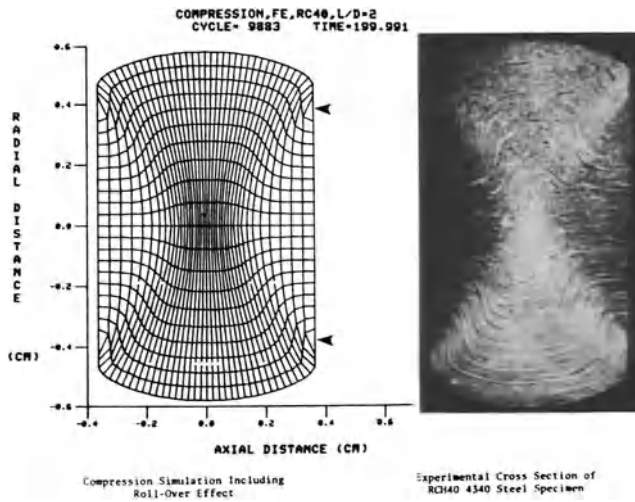


Fig. 5. Comparison of experimental cross-section of compressed steel specimen with computer simulation of same test. 4340 steel specimen (RCH 40) had been reduced-in-height by fifty percent. Arrows give location in deformed specimen of the material originally located on the specimen top surface. Material outside arrows was originally on curved cylindrical surface.

4340 steel specimen which had been reduced in height by 70 percent. Figure (7) illustrates the complex strain pattern set up in the specimen shown in figure (5). Of particular interest is the observation that regions of maximum strain occur in two places: one at the specimen center, one in the area adjacent to the loading platen near the specimen's outer edge. There is however, a packet of high hydrostatic pressure (compression) at the specimen center; this should permit the occurrence of very large strain fields without fracture. It is to be expected that if internal fractures occur they should originate near the second zone of intense strain and indeed just such fracture patterns have been found for certain materials among which are tungsten, depleted uranium and titanium alloys. These interior fractures preceded the exterior fractures (which may occur independently in the same specimen); they have been detected only by interrupting the test and sectioning the specimen.

The present status is that more work is needed (both numerical and experimental) to correlate the theoretical values of stress and strain with the experimental



Fig. 6. Cracked outer surface of upset steel cylinder after approximately 70 percent reduction-in-height.

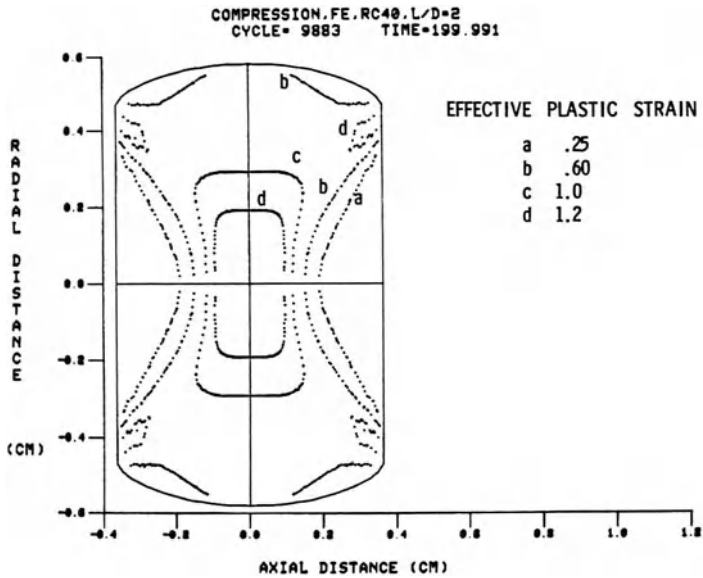


Fig. 7. Contours of effective plastic strain within upset cylinder shown in figure 5.

observations of the onset of fracture in these tests in order to establish a failure criterion useful for ordnance applications. One encouraging feature of note is that the calculated states of stress and deformation in the upset test are much closer in character to those calculated in penetration simulations than are the states produced in tensile tests. In particular figure (8) shows a cross section through the equatorial plane of the specimen of figure (6). The depth of the surface cracks has been limited by a central compression zone analogous to the process zone. Of considerable interest is the large number of adiabatic shear bands found in this test run under static conditions. We shall discuss these bands in more detail later.

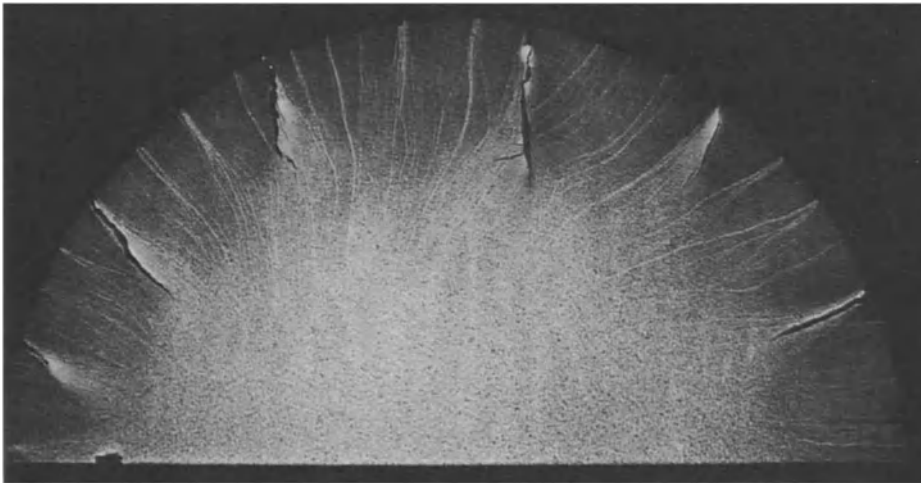


Fig. 8. Cross-section of equatorial plane of fractured specimen shown in figure 6.

While static upset tests offer promise, they clearly ignore the role of high strain rates associated with the ballistic penetration problem. One simple laboratory test which does include such effects is the Taylor Test, first proposed by G. I. Taylor as a vehicle for estimating the dynamic flow stress of materials. The test consists of impacting a cylindrical specimen into a rigid wall. Using a simple one-dimensional wave propagation analysis and a rigid-perfectly-plastic material model, Taylor was able to estimate material strength in terms of the initial and final projectile length, its density and impact velocity. Computer simulations of such a test provide a much more detailed picture of internal deformation states. In particular they reveal the necessity in general to incorporate work-hardening details into the constitutive model if suitable agreement between theory and experiment is to be obtained over

a sufficiently wide range of geometric and deformation conditions.

It is worth observing that the Taylor Test can be extended beyond Taylor's original intention; by increasing the impact velocity, conditions of incipient fracture under high compressive loading rates may be obtained and studied. Figure (9) shows a representative specimen. It has been noted by the writer

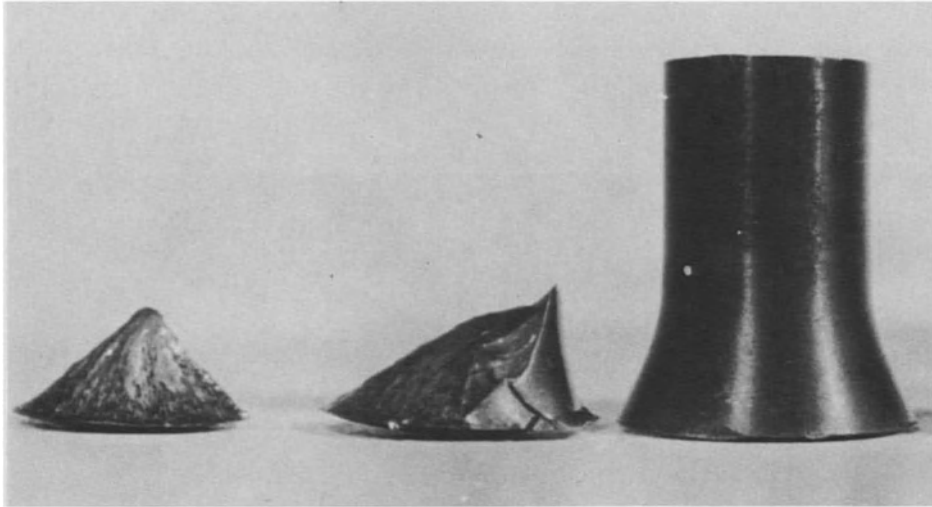


Fig. 9. Fracture mode induced in high-strength steel in Taylor Test. Impact velocity imposed increases for specimens on left.

and his associates [8] that quite different modes of fracture are obtained in Taylor tests for different hardness levels of the 4340 steel discussed earlier in connection with ballistic experiments.

Adiabatic Shear Bands

Because of the complexity of applied loadings encountered in ordnance applications it is not surprising that by far the most prevalent failure mode observed is shear. As noted earlier in the discussion associated with figure (3), shear failure may be gradual and follow after massive plastic deformation as in the softer target in figure (3) where a plug is eventually sheared out of the target plate. In other materials shear failure may follow the development of extremely local bands of intense deformation, termed adiabatic shear bands. These were discussed as early as 1944 by Holloman and Zener who interpreted their formation as the eventual overwhelming of work - strengthening effects by thermal softening; the latter is induced by conversion of plastic deformation and work

into a temperature rise under adiabatic conditions. Clearly this is a complex materials problem; it is at the frontier of much of the current research into the mechanical behavior of materials under dynamic loading condition.

In a recent study, Olson, Mescall and Azrin [9] showed how the onset of such localized deformation bands can be associated with an instability in the stress-strain curve of certain materials under dynamic shear loading. A HEMP simulation of the response of materials which exhibit such an instability in dynamic torsion tests was conducted. The problem posed was that of the deformation in pure shear under plane strain conditions of a material whose constitutive description included a plastic instability (a maximum in its true stress - true strain curve) as opposed to the deformation of a material without such an instability. Figure (10) shows the spontaneous development of a

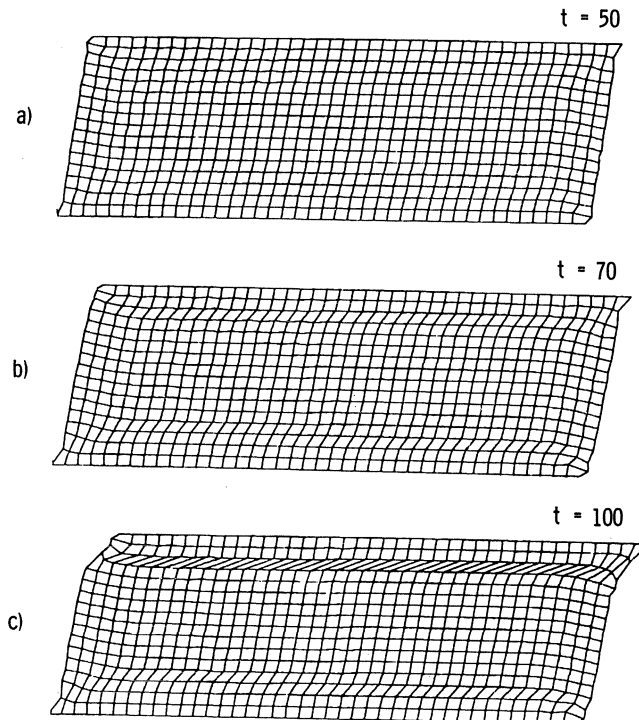


Fig. 10. Computer simulation of the development of localized shear band for a material with an instability in its stress-strain curve. Lower edge is moved relative to upper edge at 4000 cm/sec. Time in microseconds.

localized shear band after the instability strain had been exceeded for the former class of materials. The simulation under identical conditions for a material not exhibiting the instability in its constitutive law did not produce any localization of deformation.

Such results clearly show the problem of material failure under ballistic and explosive loading conditions to be extremely complex. They serve to re-emphasize the point made at the outset of this paper - that in the development of computer simulations of penetration events, more attention needs to be directed toward improvement in constitutive modeling than toward refinements in numerical algorithms associated with either finite difference grid distortions, artificial viscosities or slide-line routines.

REFERENCES

1. Wilkins, M. L., Calculation of Elastic-Plastic Flow, Lawrence Radiation Lab., Livermore, CA Rep. No. UCRL-7322, Rev. 1. (1969).
2. Mescall, J. and Papirno, R., Spallation in Cylinder-Plate Impact, *Experimental Mechanics*, Vol. 14, July 1974, pp 257-266.
3. Tate, A., Green, K. E. B., Chamberlain, P. G., and Baker, R. G., Model Scale Experiments on Long Rod Penetration, Proceedings of the Fourth International Symposium on Ballistics, Oct. 1978.
4. Tate, A., A Theory For the Deceleration of Long Rods After Impact, *J. Mech. Phys. Solids*, Vol. 15, 1967 pp 387-399.
5. Birkhoff, G., McDougall, D. P., Pugh, E. M., and Taylor, G. I., *J. Appl. Physics*, Vol. 19, 1948, p 563.
6. Mescall, J., Papirno, R. and McLaughlin, J., Stress and Deformation States Associated With Upset Tests In Metals, ASTM STP XXX (in print) 1983.
7. Papirno, R., Mescall, J., and Hansen, A., Fracture In Axial Compression Tests of Cylinders, ASTM STP XXX (in print) 1983.
8. Papirno, R., Mescall, J. and Hansen, A., Beyond the Taylor Test to Fracture, Proceedings of the Army Symposium of Solid Mechanics, 1980, AMMRC MS-80-4.
9. Olson, G. B., Mescall, J. F., and Azrin, M., Adiabatic Deformation and Strain Localization, in *Shock Waves and High Strain Rate Phenomena in Metals*, Ed. Meyers and Murr, Plenum Pub. Corp., (1981) NY, NY.

IMPACT ON LAMINATED COMPOSITE PLATES: A REVIEW OF RECENT COMPUTATIONAL DEVELOPMENTS

J. N. Reddy

Department of Engineering Science and Mechanics
Virginia Polytechnic Institute and State University
Blacksburg, Virginia 24061

Summary

A review of the literature on high velocity impact calculations is presented, with emphasis on laminated composite plates. A summary of results of the geometrically nonlinear transient analysis of layered anisotropic composite plates is presented.

Introduction

The impact by projectiles of various shapes, sizes, and materials into targets of various kinds has long been studied because of its application to space and defense technology. With the advent of new technology the need for better understanding of the response of materials and structures to intense impulsive loading has greatly increased. Current interest in the research related to impact in solids is motivated by many practically important problems such as, impact and explosive loading on military and space vehicles, impact by tornado-borne debris and collision of aircraft on nuclear reactor housings, meteoroid impact on space vehicles, transportation vehicles, etc. Most of the published literature deals with normal impact of spheres and bullets or short cylindrical rods on a flat surface. These studies employed single-material (i.e., metals), isotropic, models. A number of review articles that list extensive references on high and hyper-velocity impact have appeared to date (see [1-11]).

With the increased use of advanced fiber composite materials in aerospace and military vehicles, a more accurate prediction of the response of composite materials and structures to intense impulsive loading is needed. However, the amount of literature available on impact on composite structures is alarmingly small when compared to the vast literature on impact in metals. The present article is devoted to a review of the literature on impact in composite structures and the transient analysis of laminated composite plates.

Impact Phenomenon

Depending upon impact conditions such as the velocity of impact, impact angle, materials strengths, size and shape, etc., the projectile and target can undergo a variety of deformation processes (see [12,13]). It is informative to consider the

normal impact of a right circular cylinder on a semi-infinite target of possibly dissimilar material (see Fig. 1). Immediately after impact, plane shockwaves are produced on both sides of the projectile-target interface. These shock waves propagate away from the moving interface into the projectile and target materials. In theory, the pressure behind the shock waves is the largest pressure that exists throughout the entire deformation process. Since the projectile is of finite dimensions, rarefaction waves are also generated and transmitted toward the axis of symmetry, as shown in Fig. 1. Formation of rarefaction waves results in the ejection of target and projectile material particles at the interface. Moreover, the rarefaction waves weaken the shock waves, and change their plane shape to approximately spherical. The strength of the shock continues to decrease due to the spherical attenuation and generation of additional rarefaction waves. From this point in time onward, effects of the material strengths must be taken into account. If the target is not sufficiently thick, the stress waves produced by the impact will be reflected off the back surface as tensile waves and can produce spalling and fracture of the material.

The study of impact phenomena in solids, in general, is quite involved. Depending on the velocity of impact, the analysis can be simplified. For hyper-velocity impact regime, 2000-3000 m/s, the region near the interface experiences pressures that exceed by an order of magnitude the strength of the material, and the projectile and target can be treated as fluids in the initial stages of impact [14-17]. For impact velocities between 500 m/s and 1500 m/s, the response of the target in the impact region (typically, two or three projectile diameters) can be described by wave motion. For impact velocities less than 250 m/s, the phenomena can be analyzed using structural dynamics concepts [18]. Local penetration (i.e., entrance of the projectile into the target without completing its passage through the target) is intimately coupled with the overall deformation of the target. A complete and accurate treatment of the impact response of materials requires the consideration of impact velocity, geometry of projectile and targets, elastic-plastic shock wave propagation, nonlinear strain-displacement relations, strain rate effects, work hardening, thermal and frictional effects, local softening, initiation and propagation of fracture in the colliding materials [19].

Computational Aspects

The equations governing the impact of solids are, in general, nonlinear, and forbid classical (analytical) solution to the problem. Numerical analysis of the equations is necessary to determine the response. This is particularly true if a three-dimensional state of stress exists in the problem. There are two types of errors introduced into the numerical solution of any physical problem: errors introduced via simplifying assumptions made in deriving the governing equations and errors

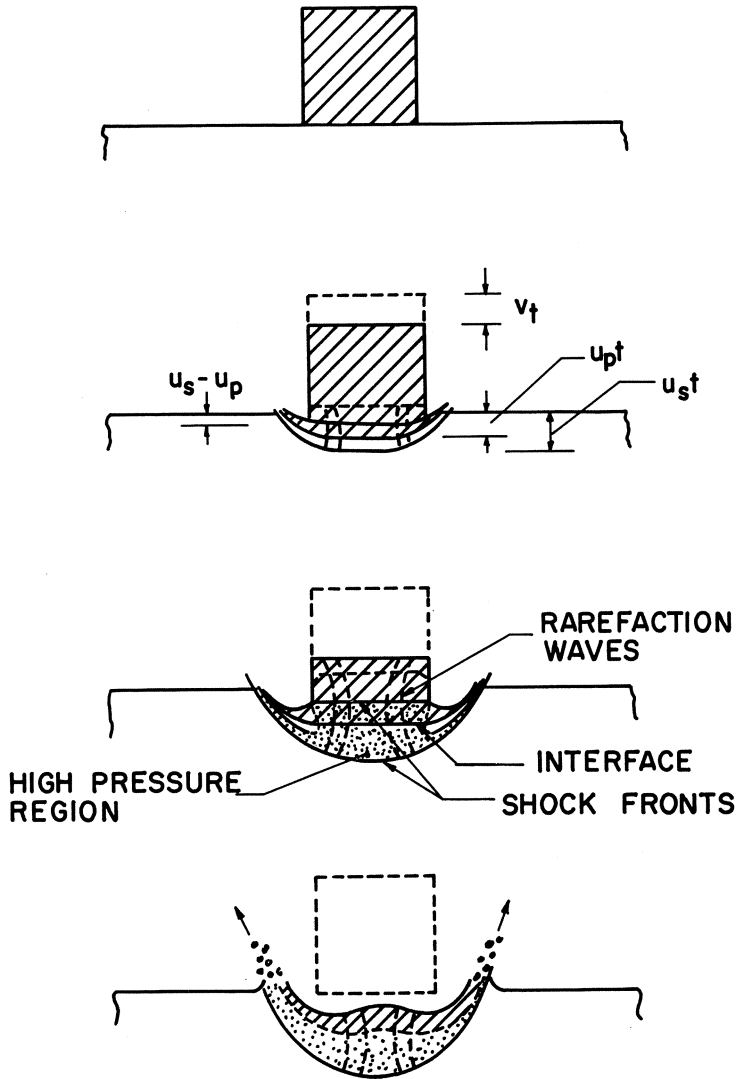


Figure 1 Schematic representation of the impact phenomenon in semi-infinite targets (from Reference 13)

introduced via numerical approximation of these equations. Thus, it is academic to solve an over-simplified equation very accurately. The accuracy and utility of any computer program depend on the exactness of the equations being solved and the numerical method employed. In the numerical analysis of structures subjected to intense impulsive loading, care should be taken to include proper constitutive equations and computational schemes.

All of the computer programs developed for impact to date are based on one of the two numerical methods: the finite difference method and the finite element method. In the finite difference method [20], differential equations are approximated directly by replacing the derivatives by difference quotients. In the finite element method [21], the governing differential equations are first cast in an integral (or variational) form and then the solution is sought in the form of a linear combination of algebraic polynomials defined over simple subregions (called elements) of the domain. A common feature of the two methods is the local (i.e., cell-wise or element-wise) separation of the spatial dependence from the time dependence of the dependent variables. While the spatial discretizations are performed differently in the two methods, the temporal approximations are the same in both methods. Most of the temporal approximations employ the central and forward difference schemes [22-25].

All of the finite difference and finite element computer programs consist of three main logical units: preprocessor, processor, and post-processor. The preprocessors and post-processors can be a few FORTRAN statements to read and write pertinent information, simple subroutines, or complex programs linked to other units via disk and tape files. The processor, where typically large amounts of computing time are spent, consists of several subroutines, each having a special purpose (e.g., a subroutine to calculate cell or element matrices, a subroutine for the equation of state, etc.). For impact calculations, the preprocessor unit is used to read in and/or generate the input data, such as the initial geometry, boundary conditions, initial conditions, parameters in the material and failure models, etc. The computational scheme is implemented in the processor unit. The scheme consists of the generation of discretized equations for the whole problem and the solution of these equations. The equations being discretized are: conservation of mass, conservation of momentum, conservation of energy, and entropy production inequality. These equations are appended with the equation of state, failure criterion, and post-failure criterion. The post-processor unit is used to generate stresses, pressure and temperature fields, velocities and accelerations, etc. from the primary dependent variables. This information is tabulated and/or plotted for ready interpretation of the output.

All of the computer programs developed for impact calculations utilize equations that are derived using one of the two kinematic descriptions [26]: Lagrangian and Eulerian. In the Lagrangian description of motion, attention is focussed on individual material particles or cells and the deformation of the cell is described in terms of a coordinate system fixed in the cell. As the cell deforms, the computational grid distorts. In the Eulerian description of motion, the coordinate system is fixed in space and the deformation of all particles passing through it is studied. These two descriptions can be compared, respectively, with a traffic policeman following an automobile, and one sitting at a traffic light and watching all automobiles passing through the light.

While each of the two descriptions have their advantages and disadvantages, one can exploit the individual advantages for impact calculations. Such mixed (or hybrid) descriptions use the Lagrangian description to model material interfaces and deformation outside of the impact region and the Eulerian description in the impact region, where gross flow and distortions are expected (see [27]).

Capabilities of Available Computer Programs

Computer programs for the analysis of impact in solids have been in existence since 1958, when Bjork [28] developed a hydrodynamic computer program for hypervelocity impact. Until recently, all of the computer programs available for impact calculations were based on two-dimensional description of the phenomenon. The advent of fourth generation computers, such as the CRAY1, have made it possible to perform calculations using three-dimensional models. However, generally speaking, such elaborate computational facilities are available only to scientists at national laboratories; researchers at academic institutions cannot compete with scientists at various laboratories in the way of computing.

All of the existing special purpose computer programs for impact were developed either at national laboratories or industrial firms (with the sponsorship of DOD organizations). A summary of many of the computer programs available to date is given in Table 1 (also see Zukas [4,5,19]). Note should be made of the fact that none of the programs include anisotropic composite material models.

Literature on Impact in Composite Plates

Compared to the vast literature available in the review articles [1-10] on impact in metals, the number of papers available on impact in composite materials is quite sparse. This can be attributed to two main reasons. First, the composite-material technology is relatively new; second, the material behavior, especially in the nonlinear range, is not well understood.

Table 1 Capabilities of some available computer programs for high velocity impact simulation

Program Name	Developers	General Characteristics and Capabilities
HEMP3D (HEMP for two dimensions)	M. L. Wilkins and associates at Lawrence Livermore Labs; for a documentation, see Report UCRL-51574, 1975.	Lagrangian description; second-order accurate finite difference approximation of the field equations; von Mises yield criteria for plastic flow; Mie-Gruneisen Type (see [5]) equation of state; Ductile and brittle fracture criteria are also available; sliding surface capability included; a semi-automatic zoning is available; an interactive program for verification of input data and interpretation of output is also included; the program is interactively capable of rotating, translating, and scaling the domain modeled; the program is fully vectorized on the CRAY computer.
EPIC-3 (EPIC-2 for two dimensions)	G. R. Johnson, Honeywell, Defense Systems Division, Hopkins, Minnesota; for a documentation, see Report AFATL-TR-78-81, July 1978, Air Force Armament Laboratory.	Lagrangian description; discretization of the equations by tetrahedral finite elements; von Mises yield criteria for plastic flow; strain rate and temperature effects are accounted for; has an anisotropic model for strength and pressure; the Mie-Gruneisen type equation of state for isotropic materials and another equation of state for orthotropic materials; element failure criteria based on a specified volumetric strain and/or true plastic strain is included; sliding with and without friction, void formation, collapse, tunneling and erosion of material (slaving) are permitted; has a preprocessor capability to generate rectangular and circular plates, hollow or solid uniform or tapered rods, hollow or solid spheres, and ogival and conical nose shapes; an extensive postprocessing capability (with geometry, perspective, and contour plots) is available; the program has been implemented on UNIVAC 1108, Honeywell 6080, CDC 7600, and CRAY computers.
DYNA3D (DYNA2D, NIKE2D, NIKE3D)	J. O. Hallquist, Lawrence Livermore Laboratories; for a documentation, see Report Nos. UCRL-52429, 1978; UCRL-17268, Rev 1, UCRL-52678, 1979.	Lagrangian description; employs both finite difference and finite element approximations; future versions of DYNA3D will use only the finite element option; elasto-plastic work-hardening materials undergoing finite strains and rotations are permitted; a crushable foam model that permits treatment of concrete and geological materials is included; contains a one-term equation of state relating pressure and compression; pressure cutoff for tensile fracture simulation and failure (continued on the next page)

Program Name	Developers	General Characteristics and Capabilities
HULL	D. A. Matuska and R. E. Durrett, Orlando Technology, Inc., Shalimar, Florida; for a documentation, see Report AFATL-TR-78-125, Air Force Armament Laboratory, 1978.	<p>based on volumetric strain are included; sliding surfaces with and without friction and void opening and closing are permitted; rigid barriers are also permitted; a mesh generator is being developed; a postprocessor to generate deformation plots is included; the program runs on CDC7600 and CRAY computers.</p> <p>Eulerian description; a second-order accurate finite difference scheme is employed; the von-Mises yield criterion is employed for plastic flow; has extensive library of equations of state-solids and liquids are modeled with the Mie-Gruneisen equation of state and the Gamma Law (see [5]) after vaporization, and an equation of state for concrete; failure criteria based on maximum principal stress or strain is included; a triaxial failure criterion for metals is also added; a rezoning capability that permits a continuous translation of the computational mesh at a continuous velocity in any one or all coordinate directions is included; preprocessor and postprocessor capabilities exist; multimaterial capability is included; the program is available on CDC 7600, CYBER 176, IBM 370, and CRAY; recently, HULL is linked to EPIC-3 (hybrid description).</p>
TRIOIL, TRIDORF, TRISOIL	W. E. Johnson, Computer Code Consultants, Inc., Los Alamos, New Mexico; a documentation of TRIOIL can be found in the report GAMD 7310 (1967), General Atomic, and that of TRIDORF in CCC-976 (1976) Computer Code Consultants.	<p>Eulerian description; finite difference approximation is used; TRIOIL solves the hydrodynamic equations in three dimensions; TRIDORF is a two-material version of TRIOIL and includes rigid plastic strength formulation; TRISOIL is a four material version of TRIOIL and incorporates operator splitting techniques and elastic-plastic strength model; the Tillotson and Mie-Gruneisen equations of state are used in all three codes; the failure criteria is based on cell density; a rezoning feature that permits motion and expansion of the grid to maintain fine zoning in regions of maximum gradients is included; preprocessing capability allows the generation of data for various shapes, including cones, simple parallelepipeds, cylinders, etc.; the postprocessing capability uses graphics packages that are proprietary to Los Alamos Scientific Labs and Lawrence Livermore Labs; the programs have been run on CDC7600, UNIVAC 1108, the VAX minicomputer, and CRAY.</p> <p>(the table is continued on the next page)</p>

Program Name	Developer	General Characteristics and Capabilities
METRIC (HELP)	<p>L. J. Hageman and E. P. Lee, System, Science, and Software, Inc., La Jolla, California; a documentation can be found in Report, BRL-CR-305, Ballistic Research Laboratory, 1976.</p>	<p>Eulerian description; a first-order finite difference approximation is used; the strength model uses a linear elastic constitutive relation; the von Mises yield criterion is used for plastic flow; the Tillotson equation of state is used for condensed material and a modified form for transition between condensed and expanded states; the material failure criteria is based on the maximum allowable value of $(\sigma/\rho)^{1/3}$, ρ being the reference density; no rezoning capability exists; preprocessing capability to generate various geometric shapes exists; postprocessing consists of printer maps and CALCOMP plots.</p>
CELFE	<p>C. J. Lee and associates, Lockheed Missiles and Space Company, Huntsville, Alabama; a documentation can be found in NASA-CR-159395, NASA-CR-159396, 1978.</p>	<p>The discretization is divided into three parts: Eulerian description with the finite element method used to simulate the dynamic behavior in the impact zone (hydrodynamic approximation), Lagrangian description with the finite element method used to simulate the dynamic behavior outside the impact regions and interface description to match the two parts; the program can be coupled with a structural analysis program such as NASTRAN; the von Mises yield criterion and the Prandtl-Reuss flow rate are used for plastic flow; orthotropic materials can also be analyzed; the Tillotson and Los Alamos equations of state (see [13]) are used; sliding with and without friction is permitted; no rezoning; preprocessing and postprocessing capabilities are known to exist; the program accommodates rigid boundaries, free surfaces, symmetry planes, and interforces.</p>
<p><u>NOTE:</u> For additional details and description of other computer programs for impact simulation, see Zukas [5].</p>		

Composite materials exhibit higher stiffness-to-weight ratios and increased corrosion resistance compared to metals. The anisotropic material properties of layered composites can be varied by varying the fiber orientation and stacking sequence. While this feature gives the designer an added degree of flexibility, the stiffness mismatch of the orthotropic layers bonded together with different fiber orientations leads to interlaminar stresses in the vicinity of free edges. For certain stacking sequences, loading, and boundary conditions, interlaminar stresses can be so large that they alone dictate the design of the structure.

Previous analyses of layered composite plates can be divided into two groups: (i) analyses based on a lamination theory, and (ii) analyses based on a fully three-dimensional theory. The lamination theory is either an extension of classical plate theory (CPT) or the Reissner-Mindlin shear-deformable plate theory (SDT) to layered composite plates. The first lamination theory is apparently due to Reissner and Stavsky [29]. Yang, Norris, and Stavsky [30] presented a generalization of the Reissner-Mindlin thick-plate theory for homogeneous, isotropic plates to arbitrarily laminated anisotropic plates. Whitney and Pagano [31] (also see Reddy and Chao [32]) presented closed-form solutions to the theory when applied to certain cross-ply and angle-ply rectangular plates. Reddy [33] presented a finite-element analysis of the lamination theory. A higher-order lamination theory that accounts for a cubic variation (as opposed to linear in [30-32]) of the inplane displacements and quadratic variation of the transverse displacement through the thickness is presented by Lo, Christensen, and Wu [34].

In the lamination theory it is assumed that the laminate is in a state of plane stress (an assumption carried from classical plate theory) and integrals through the thickness of a laminate are equal to the sum of integrals through the thickness of individual laminae. These assumptions lead to inaccurate prediction of interlaminar stresses at the free edges. Away from free edges the lamination theory solutions are very accurate. Thus, lamination theory is not accurate in a boundary layer region which extends inward from the edge to a distance approximately equal to the laminate thickness.

With the increased application of advanced fiber composite materials to jet engine fan or compressor blades and in high performance aircraft, studies involving transient response of plates made of such materials are needed to assess the capability of these materials to withstand the forces of impact due to foreign objects (e.g., the ingestion of stones, nuts and bolts, hailstones, or birds in jet engines). However, without a basic understanding of material behavior in the nonlinear range [35,36], it is not realistic to assess the capability of composite materials to intense impulsive loading. The following review of the literature on

impact in composites should provide some idea of the state-of-the art.

A review of the literature on stress waves in composite materials can be found in [37] for a period up to December 1972. The paper also presents a review of the behavior of composites under impact loading. Literature relevant to the resistance to perforation of a multi-plate shield under attack from a high speed projectile is reviewed by Zaid, et al. [38]. A review of the recent literature on the analysis of impact in composite plates is presented here.

The local damage and impulse characteristics delivered to simulated blades from 0.50-caliber projectile impacts were investigated by Rosenblatt et al. [39] using a combined approach involving numerical calculations and experiments. The study concludes that the normal impact calculations compare very well with the experimental results; it also points out that the major uncertainty in axisymmetric problems is in determining realistic dynamic material properties for composite materials. Blade material ductility, compressive and tensile strengths are the most important properties involved in fan blade damage and momentum transfer.

A number of investigators used the lamination theory of layered composite plates to investigate transient responses. An analysis for the transient deflections, bending strains, and interlaminar shear stresses in a simply supported laminated composite plate subjected to low velocity impact is presented by Dobyms and Porter [40]. The effect of plate geometry and impact location on damage mode is investigated. The analysis is based on a series solution to the plate governing equation. Using the Hertz impact theory and Reissner-Mindlin thick plate theory, Moon [41-43] modeled the response of a laminated blade to short duration impact forces. The analyses make use of the fast Fourier transform. The study concludes that the $+15^\circ$ or -15° laminated plates experience lower flexural stresses than 0° , $+30^\circ$, -30° , $+45^\circ$, or -45° plates. Sun and Chatopadhyay [44] investigated the central impact of a mass on a simply-supported laminated composite plate under initial stress. The contact force and the dynamic response of the plate are obtained by solving a nonlinear integral equation. It is found that higher initial stress results in less energy transfer from the striking mass to the plate. A computerized, analytical methodology is developed by Humphreys [45] to study damage accumulation during low velocity lateral impact of layered composite plates. The impact event is modeled as perfectly plastic with complete momentum transfer to the plate structure. The finite element method is used to analyze the problem and to predict damage that includes fiber failure, matrix ply failure, and interlaminar delamination.

Additional references to research on impact in composite materials can be found in the proceedings of various conferences (see [46-48]).

Recently, the present author investigated geometrically linear [49,50] and nonlinear [51] transient response of layered anisotropic composite rectangular plates and presented extensive numerical results for center deflection and stresses. The analysis is based on the laminated plate theory of composite plates. The details of this investigation are discussed in the next section.

Transient Response of Laminated Composite Plates

The geometrically nonlinear theory of laminated anisotropic plates to be reviewed is based on a combination of the Timoshenko-type theory and the von Karman plate theory. This theory is known to be able to predict accurately the global behavior; however, it is not accurate enough to predict edge stresses and hence delamination. The theory assumes that the stresses normal to the midplane of the plate are negligible when compared to the inplane stresses, and normals to the plate midsurface before deformation remain straight but not necessarily normal to the midsurface after deformation.

The plate under consideration is composed of a finite number of orthotropic layers of uniform thickness, with principal axes of elasticity oriented arbitrarily with respect to the plate axes. The x and y coordinates of the plate are taken in the midplane (Ω) of the plate. The displacement field is assumed to be of the form

$$\begin{aligned} u_1(x,y,z,t) &= u(x,y,t) + z\psi_x(x,y,t), \\ u_2(x,y,z,t) &= v(x,y,t) + z\psi_y(x,y,t), \\ u_3(x,y,z,t) &= w(x,y,t). \end{aligned} \quad (1)$$

Here t is time: u_1, u_2, u_3 are the displacements in the x, y, z directions, respectively: u, v, w are the associated midplane displacements: and ψ_x and ψ_y are the slopes in the xz and yz planes due to bending only. The strains in the von Karman plate theory (which accounts for moderately large deflections and small strains) can be expressed in the form

$$\begin{aligned} \epsilon_1 &= \frac{\partial u}{\partial x} + \frac{1}{2} \left(\frac{\partial w}{\partial x} \right)^2 + z \frac{\partial \psi_x}{\partial x} \equiv \epsilon_1^0 + z\kappa_1 \\ \epsilon_2 &= \frac{\partial v}{\partial y} + \frac{1}{2} \left(\frac{\partial w}{\partial y} \right)^2 + z \frac{\partial \psi_y}{\partial y} \equiv \epsilon_2^0 + z\kappa_2 \\ \epsilon_6 &= \frac{\partial u}{\partial y} + \frac{\partial v}{\partial x} + \frac{\partial w}{\partial x} \frac{\partial w}{\partial y} + z \left(\frac{\partial \psi_x}{\partial y} + \frac{\partial \psi_y}{\partial x} \right) \equiv \epsilon_6^0 + z\kappa_6 \end{aligned} \quad (2)$$

$$\epsilon_5 = \psi_x + \frac{\partial w}{\partial x}, \quad \epsilon_4 = \psi_y + \frac{\partial w}{\partial y}$$

wherein the squares of the first spatial derivatives of u and v are neglected. The strain ϵ_3 does not enter the equations because the constitutive relations, to be given shortly, are based on the plane-stress assumption. Note that the transverse shear strains, ϵ_4 and ϵ_5 , are constant through the thickness. If a linear distribution of the transverse shear strains through the thickness is desired, one must add higher order terms in z to the displacements u_1 and u_2 , and/or u_3 . With each additional term, an additional dependent variable is introduced into the problem.

Neglecting the body moments and surface shearing forces, we write the equations of motion in the presence of applied transverse forces, q , as

$$\begin{aligned} \frac{\partial N_1}{\partial x} + \frac{\partial N_6}{\partial y} &= P \frac{\partial^2 u}{\partial t^2} + R \frac{\partial^2 \psi_x}{\partial t^2} \\ \frac{\partial N_6}{\partial x} + \frac{\partial N_2}{\partial y} &= P \frac{\partial^2 v}{\partial t^2} + R \frac{\partial^2 \psi_y}{\partial t^2} \\ \frac{\partial Q_1}{\partial x} + \frac{\partial Q_2}{\partial y} &= P \frac{\partial^2 w}{\partial t^2} + q(x,y,t) - N(w, N_i) \\ \frac{\partial M_1}{\partial x} + \frac{\partial M_6}{\partial y} - Q_1 &= I \frac{\partial^2 \psi_x}{\partial t^2} + R \frac{\partial^2 u}{\partial t^2} \\ \frac{\partial M_6}{\partial x} + \frac{\partial M_2}{\partial y} - Q_2 &= I \frac{\partial^2 \psi_y}{\partial t^2} + R \frac{\partial^2 v}{\partial t^2} \end{aligned} \quad (3)$$

where $N(w, N_i)$ is the contribution due to the nonlinear terms

$$N(w, N_i) = \frac{\partial w}{\partial x} \left(\frac{\partial N_1}{\partial x} + \frac{\partial N_6}{\partial y} \right) + \frac{\partial w}{\partial y} \left(\frac{\partial N_6}{\partial x} + \frac{\partial N_2}{\partial y} \right). \quad (4)$$

The stress resultants (N_i and Q_i) and moment resultants (M_i) are related to the displacement gradients by

$$\begin{Bmatrix} N_1 \\ N_2 \\ N_6 \\ M_1 \\ M_2 \\ M_6 \end{Bmatrix} = \begin{bmatrix} A_{11} & A_{12} & A_{16} & B_{11} & B_{12} & B_{16} \\ & A_{22} & A_{26} & B_{12} & B_{22} & B_{26} \\ & & A_{26} & B_{16} & B_{26} & B_{66} \\ \text{symm.} & & & D_{11} & D_{12} & D_{16} \\ & & & & D_{22} & D_{26} \\ & & & & & D_{66} \end{bmatrix} \begin{Bmatrix} \epsilon_1^0 \\ \epsilon_2^0 \\ \epsilon_6^0 \\ \kappa_1 \\ \kappa_2 \\ \kappa_6 \end{Bmatrix} \quad (5)$$

$$Q_2 = \bar{A}_{44} \left(\frac{\partial w}{\partial x} + \psi_x \right) + \bar{A}_{45} \left(\frac{\partial w}{\partial y} + \psi_y \right) \quad (6)$$

$$Q_1 = \bar{A}_{45} \left(\frac{\partial w}{\partial x} + \psi_x \right) + \bar{A}_{55} \left(\frac{\partial w}{\partial y} + \psi_y \right).$$

The A_{ij} , B_{ij} , D_{ij} ($i, j = 1, 2, 6$), and \bar{A}_{ij} ($i, j = 4, 5$) are the inplane, bending-inplane coupling, bending or twisting, and thickness-shear stiffness, respectively:

$$(A_{ij}, B_{ij}, D_{ij}) = \sum_m \int_{z_m}^{z_{m+1}} Q_{ij}^{(m)}(1, z, z^2) dz, \quad \bar{A}_{ij} = \sum_m \int_{z_m}^{z_{m+1}} k_i k_j Q_{ij}^{(m)} dz \quad (7)$$

Here z_m denotes the distance from the mid-plane to the lower surface of the m -th layer, and k_i are the shear correction coefficients.

The finite-element model of (3) is given by (see [51])

$$[\hat{K}]\{\Delta\}_{n+1} = \{\hat{F}\}_{n, n+1} \quad (8)$$

where

$$\begin{aligned} [\hat{K}] &= [K] + a_0[M], \quad \{\hat{F}\} = \{F\}_{n+1} + [M](a_0\{\Delta\}_n + a_1\{\dot{\Delta}\}_n + a_2\{\ddot{\Delta}\}_n), \\ a_0 &= 1/(\beta\Delta t^2), \quad a_1 = a_0\Delta t, \quad a_2 = \frac{1}{2\beta} - 1. \end{aligned} \quad (9)$$

and $[K]$, $[M]$, etc. are given in Appendix A of reference 51. Once the solution $\{\Delta\}$ is known at $t_{n+1} = (n+1)\Delta t$, the first and second derivatives (velocity and accelerations) of $\{\Delta\}$ at t_{n+1} can be computed from

$$\begin{aligned} \{\ddot{\Delta}\}_{n+1} &= a_0(\{\Delta\}_{n+1} - \{\Delta\}_n) - a_1\{\dot{\Delta}\}_n - a_2\{\ddot{\Delta}\}_n \\ \{\dot{\Delta}\}_{n+1} &= \{\dot{\Delta}\}_n + a_3\{\ddot{\Delta}\}_n + a_4\{\ddot{\Delta}\}_{n+1} \end{aligned} \quad (10)$$

where $a_3 = (1 - \alpha)\Delta t$, and $a_4 = \alpha\Delta t$.

The stiffness matrix $[\hat{K}]$ is of the form

$$[\hat{K}] = [K^L + \hat{K}^N(\{\Delta\}_{n+1})] \quad (11)$$

where $[K^L]$ denotes the linear stiffness matrix and $[K^N]$ denotes the nonlinear (geometric) stiffness matrix. Because $[K^N]$ depends on the unknown solution $\{\Delta\}_{n+1}$, the assembled equation must be solved iteratively until a convergence criterion is satisfied at time, $t = t_{n+1}$. In the present study the Picard type successive iteration scheme is employed. In this scheme, the nonlinear equations (8) are approximated by the following equation

$$[\hat{K}(\{\Delta^r\}_{n+1})]\{\Delta^{r+1}\}_{n+1} = \{\hat{F}\}_{n,n+1} \quad (12)$$

where r is the iteration number. In other words, the nonlinear stiffness matrix for the $(r + 1)$ -th iteration is computed using the solution vector from the r -th iteration. Such successive iterations are continued until the error

$$E \equiv \left[\sum_{i=1}^N |\Delta_i^r - \Delta_i^{r+1}|^2 / \sum_{i=1}^N |\Delta_i^r|^2 \right] \quad (13)$$

for any fixed time $t = t_{n+1}$, is less than or equal to some preassigned value (say, one percent). The iteration at time $t = t_{n+1}$ is started by using the converged solution at $t = t_n$ (at $t = t_0 = 0$, the initial conditions are assumed to be known).

The results discussed in the following paragraphs were obtained using quarter plate models. The boundary conditions are given by

$$\text{BC1: } \begin{aligned} v = w = \psi_y = 0 \text{ at } x = 0 \text{ and } a \\ u = w = \psi_x \text{ at } y = 0 \text{ and } b \end{aligned} \quad (14)$$

$$\text{BC2: } \begin{aligned} u = w = \psi_y = 0 \text{ at } x = 0 \text{ and } a \\ v = w = \psi_x \text{ at } y = 0 \text{ and } b \end{aligned} \quad (15)$$

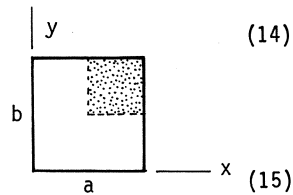


Figure 2 contains the plot of the center deflection versus time for a simply supported (BC1) two-layer cross-ply ($[0^\circ/90^\circ]$) plate. The plate dimensions and material properties are given by

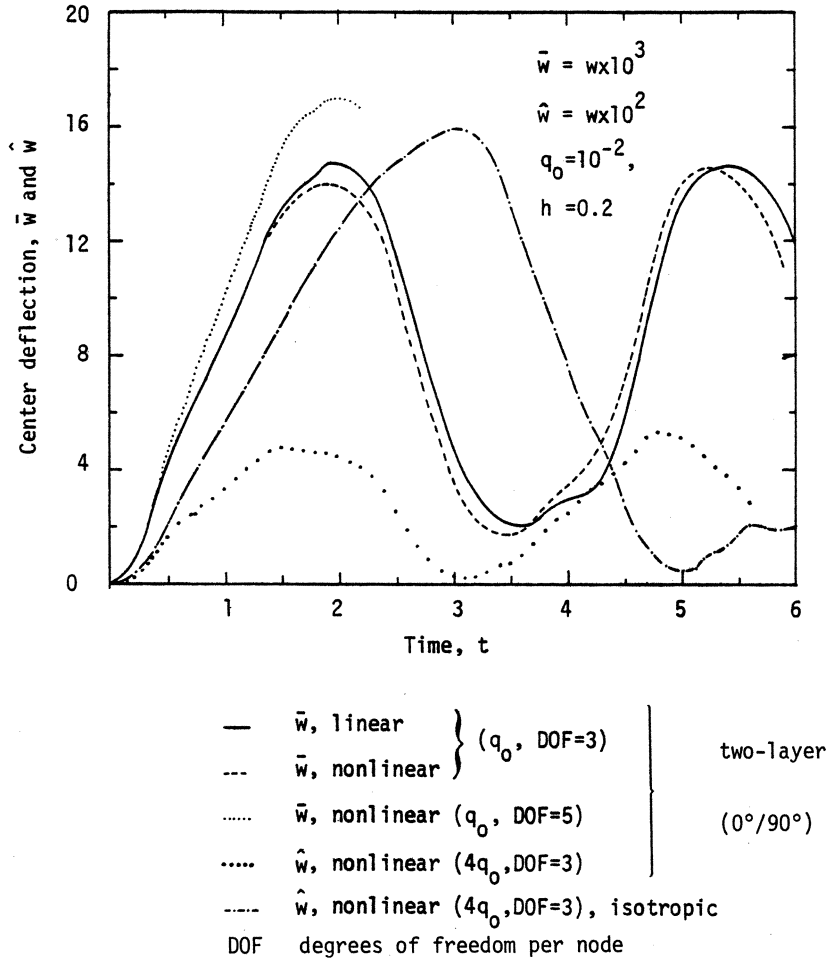


Figure 2. Transient response of two-layer cross-ply ($0^\circ/90^\circ$) rectangular plates under suddenly applied patch loading

$a = \sqrt{2}$, $b = 1$, $h = 0.1$ and 0.2 , $\Delta t = 0.1$, $q = q_0 H(t)$ (step load)

$$q_0 = \begin{cases} 10^{-2}, & a-0.2 < x < a+0.2, b-0.2 < y < b+0.2 \\ 0, & \text{otherwise} \end{cases} \quad (16)$$

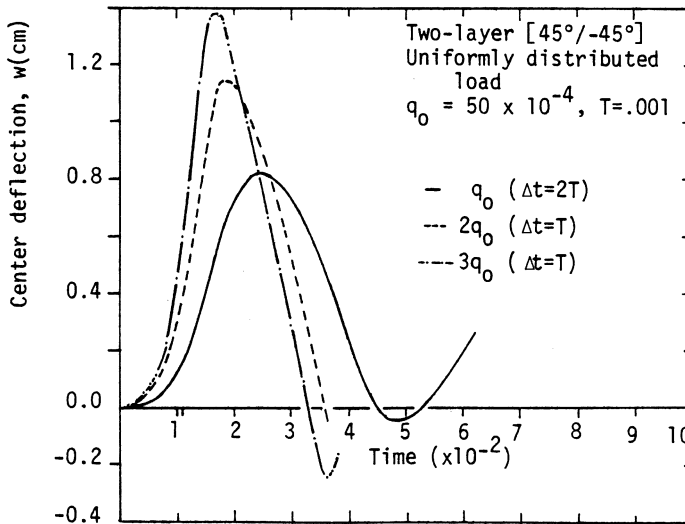
$$E_1/E_2 = 25, G_{12} = G_{13} = 0.5E_2, G_{23} = 0.2E_2, \nu_{12} = 0.25$$

The effect of coupling between the inplane displacements and bending deflections is to increase the amplitude of the center deflection.

The plot of the center deflection versus time for a two-layer, angle-ply, $[45^\circ/-45^\circ]$, plate under suddenly applied uniform loading is presented in Fig. 3. The plate dimensions (material properties used are the same as those in (16)) are given by

$$a=b=243.8 \text{ cm}, h=0.635 \text{ cm}, \Delta t=0.005 \text{ sec.}, q_0=4.882 \times 10^{-4} \text{ N/cm}^2,$$

$$\rho = 2.547 \times 10^{-6} \text{ N sec}^2/\text{cm}^4. \quad (17)$$



Angle-ply $[45^\circ/-45^\circ]$ plates

Figure 3. Nonlinear transient response of laminated square plates under suddenly applied uniform loading

The effect of the nonlinearity on the amplitude and period of the center deflection is apparent from the plots. For additional results and discussion the reader can consult references 49-51.

Summary and Recommendations

A review of the literature on computational aspects of penetration mechanics is presented, with particular emphasis on the analysis of layered composite plates. A review of the literature indicates that extensive work has been done in the last two decades in the development of two- and three-dimensional computer programs for the analysis of high velocity impact. Much of the current computational research is focussed on a realistic modeling of impact phenomena, especially material modeling and failure.

In view of the increasing application of fiber-reinforced composites in aerospace and military vehicles, it is obvious that a better understanding of the material behavior and failure due to intense impulsive loading in composites is needed, and implementation of composite-material behavior into the existing computer programs is warranted.

Acknowledgements

The support of this work by the Air Force Office of Scientific Research is gratefully acknowledged. It is also a pleasure to acknowledge the skillful typing of this manuscript by Mrs. Vanessa McCoy.

References

1. Johnson, W.; Travis, F. W.; Loh, S. Y.: High speed cratering in wax and plasticine. Int. J. Mech. Sci., 10 (1968) 593-605.
2. Carrel, J.; Johnson, W.; Travis, F. W.: High-speed impact of plasticine projectiles with laminated plasticine targets. Int. J. Mech. Sci., 10 (1968) 677-680.
3. Backman, M. E.; Goldsmith, W.: The mechanics of penetration of projectiles into targets. Int. J. Engng. Sci. 16 (1978) 1-99.
4. Zukas, J. A.: Impact Dynamics, Emerging Technologies in Aerospace Structures, Design, Structural Dynamics and Materials. Vinson, J. R. (ed.), ASME, New York (1980) 161-198.
5. Zukas, J. A.: Three-dimensional impact simulations: resources and results, Computer Analysis of Large-Scale Structures. Park, K. C.; Jones, R. F., Jr. (eds.), AMD-Vol. 49, ASME, New York (1981) 35-68.
6. Reid, S. R.; Edmonds, A. J.; Johnson, W.: Bending of long steel and aluminum rods during end impact with a rigid target. J. Mech. Engng. Sci., 23 (1981) 85-92.

7. Johnson, W.; Sengupta, A. K.; Ghosh, S. K.; Reid, S. R.: Mechanics of high speed impact at normal incidence between plasticine long rods and plates. J. Mech. Phys. Solids, 29 (1981) 413-445.
8. Johnson, W.; Sengupta, A. K.; Gosh, S. K.: High velocity oblique impact and Ricochet mainly of long rod projectiles: an overview. Int. J. Mech. Sci. 24 (1983) 425-436.
9. Goudreau, G. L.; Hallquist, J. O.: Recent developments in large scale finite element Lagrangian hydrocode technology. Second Int. Conf. Finite Elements in Nonlinear Mechanics, Stuttgart, W. Germany, 1981; Comp. Meth. Appl. Mech. Engng., to appear.
10. Johnson, W.; Sengupta, A. K.; Ghosh, S. K.: High velocity oblique impact and ricochet mainly of long rod projectiles: An overview. Int. J. Mech. Sci. 24 (1982) 425-436.
11. Williams, J. G.; Anderson, M. S.; Rhodes, M. D.; Starnes, J. H., Jr.; Stroud, W. J.: Recent developments in the design, testing and impact-damage tolerance of stiffened composite panels. NASA Technical Memorandum 80077, April 1979, Langley Research Center, Hampton, VA 23665.
12. Kinlow, R.: High-velocity impact phenomena. Academic Press, New York, 1970.
13. Reddy, J. N.: Finite element analysis of the initial stages of hypervelocity impact. Comp. Meth. Appl. Mech. Engng., 9 (1976) 47-63.
14. Fyfe, I. M.: Application of "hydrodynamic" theory to the low stress range of hypervelocity impact problems. Proc. Fifth Symp. on Hypervelocity Impact, Vol. 1, Pt. 1, Colorado School of Mines, Boulder, Colorado (1961) 299-305.
15. Olshaker, A. E.; Bjork, R. L.: Hydrodynamics applied to hypervelocity impact. Proc. Fifth Symp. on Hypervelocity Impact, Vol. 1 Pt. 1, Colorado School of Mines, Boulder, Colorado (1961) 225-234.
16. Walsh, J. M.; Tillotson, J. H.: Hydrodynamics of hypervelocity impact. Proc. Sixth Symp. on Hypervelocity Impact, Vol. 2, Pt. 1, Firestone Tire and Rubber Co., Akron, Ohio (1963) 59-104.
17. Walsh, J. M.; Johnson, W. E.: On the theory of hypervelocity impact. Proc. Seventh Hypervelocity Impact Symposium, Vol. 2, Martin Company, Orlando, Florida (1965) 1-75.
18. Herrmann, W.; Bertholf, L. D.; Thompson, S. L.: Computational methods for stress wave propagation in nonlinear solid mechanics. Computational Methods in Nonlinear Mechanics, Oden, J. T. (ed.), Springer-Verlag, New York, (1975).
19. Jonas, G. H.; Zukas, J. A.: Mechanics of penetration: analysis and experiment. Int. J. Engng. Sci., 16 (1978) 879-903.
20. Walsh, R. T.: Finite-difference methods. Dynamic Response of Materials to Intense Impulsive Loading, Chou, P. C.; Hopkins, A. K. (eds.), US Government Printing Office (1982).
21. Zienkiewicz, O. C.: The Finite Element Method in Engineering Science. Third Edition, McGraw-Hill, London (1973).
22. Belytschko, T.: Computer methods in shock and wave propagation analysis. Computing in Applied Mechanics, Hartung, R. F. (ed.), AMD-Vol. 18, ASME, New York (1977) 139-161.

23. Argyris, J. H.; Doltsinis, J. St.; Knudson, W. C.; Vaz, L. E.; William, K. J.: Numerical solution of transient nonlinear problems. Comp. Methods in Appl. Mech. Engr. 17 (1979) 341-409.
24. Herrmann, W.: Current problems in the finite difference solution of stress waves. Proc. Workshop on Nonlinear Waves in Solids, Ting, T. C. T.; Clifton, R. J.; Belytschko, T. (eds.), National Science Foundation (1977).
25. Bazant, Z. P.: Spurious reflection of elastic waves in nonuniform finite element grids. Comp. Meth. Appl. Mech. Engng. 16 (1978) 91-100.
26. Malvern, L. E.: Introduction to the Mechanics of a Continuous Medium. Prentice-Hall, Englewood Cliffs (1968).
27. Herrmann, W.: Nonlinear transient response of solids. Shock and Vibration Computer Programs, Reviews and Summaries, B. Pilkey (ed.) Shock and Vibration Information Center, Naval Research Laboratory, Washington, D.C. (1975).
28. Bjork, R. L.: Effects of meteoroid impact on steel and aluminum in space. Rand Corporation, P. 1662 (1958).
29. Reissner, E.; Stavsky, Y.: Bending and stretching of certain types of heterogeneous aeolotropic elastic plates. J. Appl. Mech., 28 (1961) 402-408.
30. Yang, P. C.; Norris, C. H.; Stavsky, Y.: Elastic wave propagation in heterogeneous plates. Int. J. Sol. Struct., 2 (1966) 665-684.
31. Whitney, J. M.; Pagano, N. J.: Shear deformation in heterogeneous anisotropic plates. J. Appl. Mech., 37 (1970) 1031-1036.
32. Reddy, J. N.; Chao, W. C.: A comparison of closed-form and finite element solutions of thick laminated anisotropic rectangular plates. Nuclear Engineering and Design, 64 (1981) 153-167.
33. Reddy, J. N.: A penalty plate-bending element for the analysis of laminated anisotropic composite plates. Int. J. Num. Meth. Engng., 15 (1980) 1187-1206.
34. Lo, K. H.; Christensen, R. M.; Wu, E. M.: A higher-order theory of plate deformation: part 1, homogeneous plates; part 2, laminated plates. J. Appl. Mech., 44 (1977) 663-668 and 669-676.
35. Hashin, A.; Bagchi, D.; Rosen, W. B.: Non-linear behavior of fiber composite laminates. NASA CR-2313, Material Sciences Corporation, Blue Bell, PA (1974).
36. Sandhu, R. S.: Nonlinear behavior of unidirectional and angle ply laminates. J. Aircraft, 13 (2) (1976) 104-111.
37. Moon, F. C.: A critical survey of wave propagation and impact in composite materials. Dept. of Aerospace and Mechanical Sciences, Princeton University, NASA-CR-121226 AMS-1103 (1973).
38. Zaid, A. I. O.; Travis, F. W.: A comparison of single and multi-plate shields subjected to impact by a high speed projectile. Proc. Mechanical Properties at High Rates of Strain, Oxford University, England (1974).
39. Rosenblatt, M.; Isabelle, T. R.; Fry, P. F.; Barber, J. P.; Taylor, H. R.: Investigation of local damage and impulse delivered to turbine blades by normal and oblique projectile impacts. Report No. AD-A041780 AFML-TR-76-208, California Research and Technology, Woodland Hills (1977).

40. Dobyns, A. L.; Porter, T. R.: A study of the structural integrity of graphite composite structure subjected to low velocity impact. Preprint A80-32058 12-24, Society of the Plastics Industry, New York (1980).
41. Moon, F. C.: Theoretical analysis of impact in composite plates. Report No. NASA-CR-12110 AMS-1099, Dept. of Aerospace and Mechanical Sciences, Princeton University (1973).
42. Moon, F. C.; Kim, B. S.; Fang-Landau, S. R.: Impact of composite plates: analysis of stresses and forces. Report No. NASA-CR-134999 AMS-1298, Dept. of Aerospace and Mechanical Sciences, Princeton University (1976).
43. Sung, Kim, B.; Moon, F.: Transient wave propagation in composite plates due to impact. Report No. AIAA 77-387, 18th Structures, Structural Dynamics and Materials Conference, San Diego, California (1977).
44. Sun, C. T.; Chatopadhyay, S.: Dynamic response of anisotropic laminated plates under initial stress to impact of a mass. Report No. Ad-A025906 AFML-TR-74-258, School of Aeronautics, Purdue University, Lafayette (1976).
45. Hunphreys, E. A.: Development of an engineering analysis of progressive damage in composites during low velocity impact. Report No. NASA-CR-165778 MSC-TFR-1205/0208, Materials Sciences Corporation, Spring House, Pa (1981).
46. Proc. Foreign Object Damage to Composites. ASTM Publication No. 568, American Society of Testing Materials, Philadelphia, PA (1973).
47. Chiao, T. T.; Schuster, D. M. : Proc. of the Symp. Failure Modes in Composites III. Las Vegas, Nev., 1976; American Institute of Mining, New York/
48. Vinson, J. R.: Emerging Technologies in Aerospace Structures, Design, Structural Dynamics and Materials. Aerospace Conference, San Francisco, 1980; ASME, New York.
49. Reddy, J. N.: On the solutions to forced motions of rectangular composite plates. J. Appl. Mech. 49 (1982) 403-408.
50. Reddy, J. N.: Dynamic (Transient) analysis of layered anisotropic composite-material plates. Int. J. Num. Meth. Engng. (1982) to appear.
51. Reddy, J. N.: Geometrically nonlinear transient analysis of laminated composite plates. AIAA J. (1983) to appear.

PART II

Physical Modeling and Constitutive Laws

A SURVEY OF PENETRATION MECHANICS FOR LONG RODS

T. W. WRIGHT

Ballistic Research Laboratory
Aberdeen Proving Ground, MD 21005

Summary

Some of the simpler methods in current use for analyzing ballistic impacts by long rod penetrators are reviewed and critiqued. In spite of several obvious shortcomings the eroding rod model has been used as a starting point and guide for an experimental investigation of penetration phenomena. Some of the principal results of that program are reviewed, and several areas for future work are identified. Carefully developed, time resolved data of the types described in this report should serve as a standard of comparison for large scale computations of penetration phenomena. These data are already being used to guide development of improved engineering models for long rod penetration.

Introduction

Long rod penetrators are modern equivalents of the cannonball, intended to pierce a target by depositing large amounts of kinetic energy in a concentrated region. Typical striking velocities lie in the range of approximately 1-3 km/s. Although a modern penetrator is a machined metal part of some complexity, since it must be fitted with various appurtenances to achieve efficient launch and flight, it may be idealized as a right circular cylinder with a ratio of original length to diameter, L_0/D , greater than some arbitrary number, say ten. The penetrator is intended to fly and to strike its target end on. When the target thickness is greater than a few penetrator diameters, the mechanism of penetration is a complex process in which a cavity is made in the target and the end of the penetrator erodes away. Some of the principal features of impact are shown in Figure 1.

Material response properties under impact conditions are also complex. It has been estimated in a recent report of the National Materials Advisory Board [1] that typical maximum pressures and maximum strain rates during penetration may lie in the ranges 5-50 GPa and 10^4 - 10^6 s⁻¹, respectively. The higher values are associated with the earliest times after impact and with shock waves, but pressures and strain rates, aided by the presence of nearby free surfaces, quickly decay toward the lower values for the bulk of the process. Since strong armor or penetrator materials may have ultimate stresses of 1-2 GPa, it is apparent that maximum pressures are not orders of magnitude higher than material strengths except perhaps locally for very short periods of time. In fact, because of wave reflections, tensile stresses occur as well. In short, although stresses are high, they are not so high that material properties can

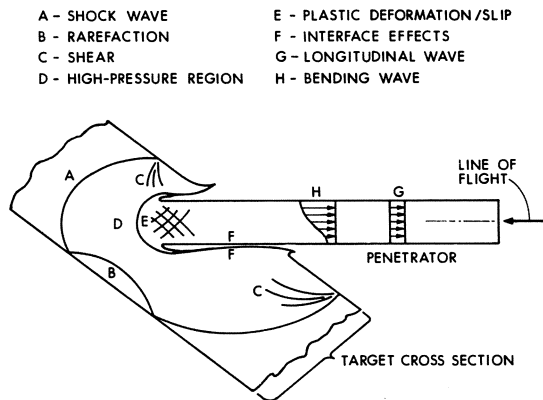


Fig. 1. Principal features of long rod penetration

be safely ignored. Furthermore, phase changes may occur in some materials, notably Fe and U, high pressures are well known to have a strong influence on flow and fracture characteristics, and strain rates are high enough to affect the response of many materials.

On the other hand, it is by no means clear how many details of physical and material processes are really required in order to achieve accurate and useful ballistic predictions.

There are three levels of analysis currently used in an effort to come to grips with the difficulties outlined above. In order of increasing complexity in the representation of physical and material response phenomena these are: (1) empirical data correlation, (2) engineering analysis, and (3) large scale computer codes. Each approach is useful, each has its own limitations, and to be effective each must be supported by its own brand of high quality experimentation. In this survey some comments will be made on all three approaches, but emphasis will be placed on one particular engineering model and related experimental results.

Data Correlation and Dimensional Analysis

At the simplest engineering level the ballistician would like to be able to predict the outcome of an encounter between a penetrator and target. That is, with given information about geometries and material identifications of both penetrator and target and on line of attack and striking velocity, one would like as a minimum to predict whether or not the target will be perforated. If it is not perforated, one would like to calculate depth of penetration, and if it is perforated, to calculate residual velocity and residual mass. Consequently, ballistic testing today

concentrates on careful control of line of flight and target attitude, and on accurate measurement of striking and residual velocities. When flash X-rays are used for velocity measurements (see Grabarek [2]), information is also gained on projectile yaw at impact and line of flight after impact. Often an estimate of residual mass can be made as well.

There have been many attempts to make empirical correlations of ballistic data, e.g., see Backman and Goldsmith [3] for a survey. Typical cases are listed below in Table I.

Table I: Typical Correlation Functions for Ballistic Data

$$\text{de Marre [4]} : MV_L^2 = CD^\beta T^\alpha$$

$$\text{Grabarek [5]} : MV_L^2/D^3 = C \left(\frac{T \sec\theta}{D} \right)^\alpha$$

$$\text{Thor [6]} : V_S - V_R = C T^\alpha M^\beta V_S^\gamma$$

M = projectile mass

V_S = striking velocity

D = projectile diameter

V_R = residual velocity

T = target thickness

V_L = limit velocity

θ = obliquity, measured from plate normal

α, β, γ, C = empirical, best fit parameters

These correlations and others like them can be extremely useful for predicting other cases that lie within the same general data set, that is, for data interpolations or even for small extrapolations. It will be noted, however, that none of the three cases cited contains information on material properties. Therefore, every change in material requires a new set of coefficients. In fact, none of the formulae in Table I is even given in non-dimensional form, so that the range of applicability in each case is unduly restrictive.

On the other hand, there are many dependent variables of possible interest, and even more independent variables that may influence the outcome of a given encounter. Some of the possibilities are shown in Table II. The rows of dots signify all other possible variables, and each entry in the list of material variables can be given for both penetrator and target. Even with the reduction to non-dimensional variables, the analyst is still faced with a bewildering array of possible influences, and because of limitations in both time and money available for testing, it invariably turns out that the test data are incomplete with respect to some variables.

Recently an attempt has been made by Bruchey [7] to include more variables than has been customary in the past. The non-dimensional form chosen by him for data correlation is given in eqn. (1).

Table II: Variables for Dimensional Analysis

Dependent Variables:

P = depth of penetration	M _R = residual mass
V _L = limit velocity	θ _R = angle of residual trajectory
V _R = residual velocity	v _h = hole volume
L _R = residual length

Independent Variables:

Physical Characteristics

L ₀ = initial length	M ₀ = initial mass
D = diameter	T = target thickness
.....	

Kinematic Characteristics

V _S = striking velocity	θ _S = angle of striking trajectory
α = angle of yaw

Material Characteristics

Σ _Y = yield stress	ρ = density
Σ _U = ultimate stress	K _{IC} = fracture toughness
h = hardness	
ε _U = elongation at Σ _U

$$\frac{\rho_p V_L^2}{E_p} \frac{L_0}{D} = C \left(\frac{T \sec \theta}{D} \right)^\alpha \left(\frac{E_p}{E_t} \right)^\beta \left(\frac{\rho_p}{\rho_t} \right)^\gamma \quad (1)$$

E_p and E_t both have the form

$$E = \frac{1}{2} (\Sigma_Y + \Sigma_U) \epsilon_U, \quad (2)$$

and represent measures of the energy per unit volume that can be absorbed in the penetrator and target materials before rupture occurs. T sec θ is the line of sight thickness of the target, and all other quantities are as listed in Table II. The coefficient C and the powers α, β, and γ are determined by a multilinear regression analysis. The total data set includes only 25 separate cases, but within that set there is substantial variation of the non-dimensional ratios. The ratio L₀/D varies by a factor of 2, T sec θ/D varies by 4, ρ_p/ρ_t varies by 1 1/4, E_p/E_t varies by 5, and ε_U varies by 4.

Other groupings of the variables could have been made. For example, instead of the left hand side of eqn. (1) as given, the grouping

$$\frac{\rho_p V_L^2 L}{E_t T \sec \theta}$$

could have been used. This form may be interpreted as the kinetic energy available per unit area normal to the line of flight compared with the ability of the target to absorb energy per unit area. When this form is used, the powers on the right hand side are all small numbers less than one, indicating only weak dependence, but the overall agreement after the regression analysis is no better than the original result.

For eqn. (1) the calculated vs. the observed limit velocities are shown in Fig. 2.

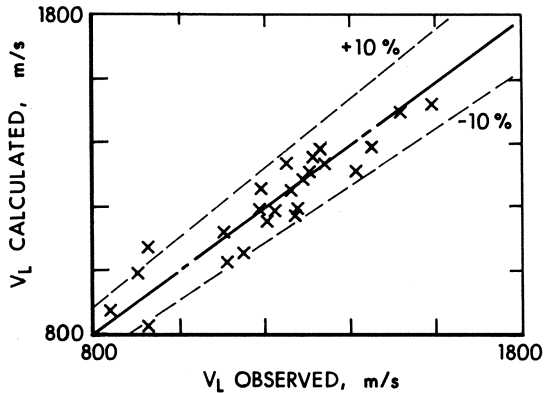


Fig. 2. Limit velocity as calculated from eqn. (1) compared with observed values

For velocity, varying by a factor of 2, agreement is generally within about 10%. For more restricted data sets, that is for data sets with less variation in material and geometric properties, much better agreement can be achieved, but only with a corresponding loss in generality of the correlations.

In that it attempts to incorporate some effect of material properties, eqn. (1) is an improvement over Table I, but it still uses only a few of the non-dimensional numbers possible from Table II. Furthermore, the assumed power law relationship among variables is an extremely limited choice of possible functional dependences.

As illustrated in Fig. 3 extrapolation with the weak power law dependence may, and in fact often does, cause substantial error. On the other hand, experimentation to determine general dependence of the form

$$\frac{\rho_p V L^2 L_0}{E_t T \sec \theta} = f \left(\frac{T \sec \theta}{D}, \frac{E_p}{E_t}, \frac{\rho_p}{\rho_t}, \frac{L_0}{D}, \dots \right), \quad (3)$$

for example, would be an enormous task. A better strategy would be to look for trends within subsets of the available data, where only one variable at a time is allowed to vary, and then to try to fit the data with simple functions that have limited degrees of freedom.

But no matter how the correlations are made, it will be difficult, if not impossible, to gain more than qualitative insight into the nature of the physical processes at work. For a quantitative view of these processes, it is necessary to construct physical models.

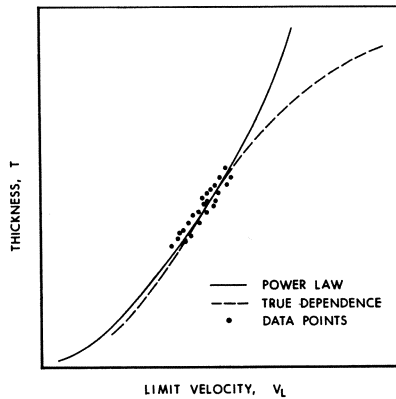


Fig. 3. Failure of extrapolation with a power law

Engineering Analysis

There have been many attempts to construct simple models of penetration. Many of these are described in a recent survey [3], but only one, the eroding rod model, will be summarized here, because it has proved useful as a starting point for an experimental program and for further theoretical refinements. The goal for any engineering model is to construct a system of equations with enough detail to be physically realistic but at the same time simple enough for rapid computation.

The eroding rod model in its simplest form was given independently by Alekseevskii [8] and Tate [9]. With the instantaneous length of the penetrator L , speed U , and depth of penetration P , the equations may be written as follows

$$\text{Mass:} \quad \dot{L} = \dot{P} - U \quad (4)$$

$$\text{Momentum:} \quad \rho_p L \dot{U} = -\Sigma_p \quad (5)$$

$$\text{Modified Bernoulli: } \Sigma_p + \frac{1}{2} \rho_p (U - \dot{p})^2 = \Sigma_t + \frac{1}{2} \rho_t \dot{p}^2 \quad (6)$$

In these equations the only material properties included are flow stress Σ and density ρ where subscripts p and t denote penetrator and target, respectively.

The interpretation of equations (4) and (5) as balance of mass and balance of linear momentum is straight forward. Equation (6) should be interpreted as showing equality of axial stresses at the interface between penetrator and target on the stagnation line. For the case of steady flow with perfect fluids the expression $p + \frac{1}{2} \rho v^2$ is constant along a streamline. At the stagnation point the velocity relative to that point vanishes so the constant is the interface pressure. If both the rod and target are assumed to behave like perfect fluids in steady flow for some short distance away from the interface where the solid character of each material reasserts itself, then the left side of (6) holds for the rod and the right side for the target with the equality holding because stresses must match at the interface.

Inherent in the model is the assumption that both penetrator and target may be approximated as rigid/plastic materials. That is, either material flows at its characteristic stress Σ or it locks up and doesn't deform at all. For example, if $\Sigma_t > \Sigma_p$, both penetrator and target material flow only if $U > \sqrt{2(\Sigma_t - \Sigma_p)/\rho_p}$. At this critical speed \dot{p} becomes zero and the target ceases to deform, but the penetrator continues to erode until U drops to zero. On the other hand, if $\Sigma_p > \Sigma_t$, both materials flow only if $\dot{p} > \sqrt{2(\Sigma_p - \Sigma_t)/\rho_t}$. When the rate of penetration drops below that speed, erosion of the penetrator stops, $U = \dot{p}$, and the right side of (5) must be replaced by $-(\Sigma_t + \frac{1}{2} \rho_t \dot{p}^2)$. The penetrator then continues to penetrate as a rigid body until U drops to zero.

Equations (4) - (6) are simple enough to be solved on a programmable hand calculator. Typical predictions are shown in Fig. 4 where non-dimensional penetration is plotted as a function of non-dimensional striking velocity. The qualitative features of the model are striking and useful in themselves. The curve moves to the right for increasing target strength and to the left for increasing penetrator strength, which is in accord with common sense, of course, but the model gives a quantitative estimate of the amount of change as well. All curves have a characteristic S-shape and show a saturation value for high impact speeds. This is in sharp contrast to the shape of the power law curves customarily used for data correlation. The eroding rod model also brings out important natural scaling effects, the most important one being that penetration is proportional to penetrator length if all other properties are held fixed. Thus, to maximize penetration for a penetrator of fixed mass, the ratio L_0/D should be as high as possible, consistent with structural stability and other engineering constraints.

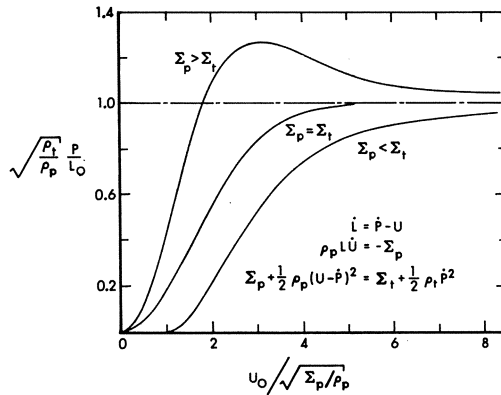


Fig. 4. Typical predictions of the eroding rod model

A less obvious consequence of the model is that for a fixed amount of kinetic energy and fixed L_0/D there is an optimum striking velocity that will maximize penetration. That same velocity also minimizes the energy required to achieve a fixed depth of penetration. These facts follow simply from the saturation effect. Penetration may be represented as $P = L_0 S(U_0)$ where $S(U_0)$ is the S-shaped saturation curve. Then, since kinetic energy K is proportional to $L_0^3 U_0^2$ for fixed L_0/D , the results follow from a minimization problem with side constraint. The optimum velocity is the solution of

$$\frac{dS}{dU_0} = \frac{2}{3} \frac{S}{U_0}, \quad (7)$$

and may easily be found graphically. There will be no solution to (7) if the curve $S(U_0)$ does not bend over far enough so the tendency toward saturation is essential for this result to hold. Results of this kind have previously been given by Frank [10].

Figure 5 shows experimental data reported by Stilp and Hohler [11]. Similar data were given by Tate, et al. [12]. The striking similarity of the experimental curve and the theoretical curve for $\Sigma_p < \Sigma_t$ is clearly evident.

Equations (4) - (6), therefore, have considerable intuitive appeal, combining as they do simplicity with qualitative accuracy, but they are difficult to use quantitatively because values for the characteristic flow stresses are not readily available *a priori*. The usual procedure has been to choose the stresses so as to fit an experimental S-curve, and then to consider them as material constants. Due to approximations inherent in the model, this procedure is unlikely to be satisfactory in all cases. There are several difficulties, nearly all of which are associated with the modified Bernoulli equation itself. These have been described in some detail previously by Wright [13].

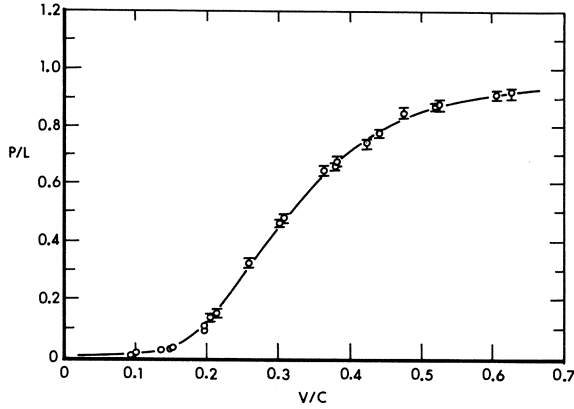


Fig. 5. Experimental curve of penetration vs. striking velocity (after Stilp and Hohler [11])

The first problem is in the origin of equation (6). Strictly speaking, the equation only applies for steady flow in perfect fluids. The stresses in the equation would be those that occur at interfaces where the penetrator or target material undergoes a transformation from rigid solid to perfect fluid. Furthermore, the fluid layers must be imagined to have constant thickness so that the fluid/solid interfaces both have the speed \dot{p} . Melting can occur in ballistic impact if the speed is high enough, but in any case there will be a region of plastic flow on either side of the penetrator/target interface. For normal impact with the z -axis along the centerline of the rod, the z -component of the momentum equation may be written

$$t_{zz,z} + t_{zy,y} + t_{zx,x} = \rho(u_{z,t} + u_x u_{z,x} + u_y u_{z,y} + u_z u_{z,z}) \quad (8)$$

where the commas denote partial differentiation. On the centerline the transverse components of velocity, u_x and u_y , are zero by symmetry and, for steady, flow $u_{z,t}$ is also zero. Shear stresses also vanish on the centerline, but not their derivatives, so integration of (8) between points a and b , assuming incompressibility, yields

$$t_{zz}(b) - t_{zz}(a) + \int_a^b (t_{zy,y} + t_{zx,x}) dz = \frac{1}{2} \rho [u_z^2(b) - u_z^2(a)] . \quad (9)$$

If point b is the stagnation point at the penetrator/target interface, and if point a lies at the rigid/plastic boundary in either penetrator or target, then with $t_{zz}(a) = -\Sigma$ for compressive stresses eqn. (6) must be replaced by

$$\Sigma_p + I_p + \frac{1}{2} \rho_p (U - \dot{p})^2 = \Sigma_t + I_t + \frac{1}{2} \rho_t \dot{p}^2 \quad (10)$$

where I is the integral in eqn. (9). If Σ and I are lumped together, then eqn. (10) has the same form as (6), but the integrals are undetermined.

A second problem concerns the validity of the assumptions of steady flow and rigid/plastic materials. Taken overall, kinetic energy penetration is clearly an unsteady process, especially in the initiation and final stopping or breakout phases, but there may be parts of the process, localized in both space and time that are nearly steady. For example, during the intermediate stages of penetration a local interaction region may form near the penetrator/target interface, within which eqn. (10) holds approximately. If the target is thick enough and the penetrator long enough, this intermediate stage will be the dominant phase of penetration.

Even in such a case, however, there is no clear way to make an accurate estimate of the characteristic stresses from knowledge of measured mechanical properties. The stress/strain curve of most real high strength materials cannot be well approximated by the rigid/plastic assumption because of work hardening. Furthermore, failure processes in a high rate interaction zone must be regarded as largely unknown so that it is impossible to specify either a maximum strain or a maximum stress at failure with any degree of confidence. Thus, there is at present no well defined way to choose the characteristic flow stresses. Even a criterion based on energy equivalence does not seem particularly feasible.

In addition to the uncertainty concerning flow stresses and the integrals in eqn. (10), there is further uncertainty concerning the spherical component of stress in both penetrator and target. The axial stress in eqn. (9) or (10) may be decomposed into the sum of a spherical and a deviatoric part. The flow stress is associated only with the latter, but the spherical or hydrostatic part is totally undetermined. In the penetrator nearby free lateral surfaces will tend to minimize the spherical stress, but in the target there are no lateral surfaces, and the hydrostatic component will be the major part of the axial stress.

Still another consequence of real non-rigid material behavior is that there will be considerable plastic deformation at some distance from the quasi-steady interaction zone. In the rod this has the effect of slowing material down before it reaches that zone so that the speed U to be used in eqn. (10) is less than that of the rear end. In the target, plastic deformation (including bulging of the rear surface) has the effect of increasing the spatial rate of penetration. Target deformation and bulging has been explicitly included in the model for perforation by rigid projectiles given by Ravid and Bodner [14].

Finally, inertia will tend to increase the crater size even after the active driving forces have ceased. The effect of crater inertia is particularly pronounced for low

ratios of L_0/D or ultra high velocities and has the effect of increasing penetration above the curves calculated in Fig. 4. This effect has been considered by Frank [15] and more recently by Tate [16].

The third and final problem is that the stress tending to decelerate the rod in eqn. (5) is an average stress over the cross section, whereas the stress that enters into the modified Bernoulli equation is the local stress on the centerline. These may be somewhat different from each other especially if the integral in eqn. (9) is lumped together with the axial stress to give an effective value for Σ .

For all of the above reasons - the origin and meaning of the modified Bernoulli equation, the questionable validity of steady flow and rigid/plastic assumptions, and the inequality of average and centerline stresses - the eroding rod model is difficult to use quantitatively and gives only limited insight into the details of the actual penetrator/target interaction. Nevertheless, in spite of its shortcomings the model appears to contain the germ of a sound theory of penetration for long rods, as shown by the qualitative success of its predictions.

An Experimental Program

Penetration is controlled by flow and failure processes that occur at or near the penetrator/target interface. These processes depend only on the material properties of the particular materials involved, and therefore, in large measure they will depend only on the local stress and strain fields, and possibly the gradients or time rates of change of those fields. These ideas are at least compatible with the formation of a region of quasi-steady flow at the interface. Since it is a local phenomenon, it seems reasonable to suppose that the steady conditions established will depend only on the local geometry and the mass flux through the region.

With the ideas of the preceding paragraph as a working hypothesis several experiments have been devised to begin probing the details of the interaction process. Obviously measurements cannot be made directly in the interaction region, but they can be made in both penetrator and target in material immediately adjacent to it. In fact, in terms of the modified Bernoulli equation, it has been possible to make independent measurement of Σ_p , Σ_t , U , and \dot{P} .

1. Experiments with Instrumented Rods

In the first of these experiments, done by Hauver [17, 18] and Hauver and Melani [19], strain gages are placed on the long rod penetrators and strain-time histories are recorded at several stations on the rod. Then from the one-dimensional theory of wave propagation it is possible to reconstruct the stress and particle velocity histories throughout the rod. This is done as follows. The simplest equations for 1-D wave propagation may be written

$$\Sigma_{,Z} = \rho \dot{W}_{,t}, \quad \dot{W}_{,Z} = \epsilon_{,t} \quad (11)$$

where Σ is the average axial stress in the rod (referred to the initial cross section), ρ is the initial density, \dot{W} is the particle velocity, and ϵ is engineering strain. The spatial location, z , is a function of the material particle, Z , and time, t , so that

$$z = z(Z,t), \quad \dot{W} = Z_{,t} \quad \epsilon = z_{,Z}^{-1} \quad (12)$$

With ϵ - t data for several stations at hand, curves of constant strain may be plotted in z - t space. Along such a curve the slope, c_p , called the plastic wave speed, may be measured.

$$d\epsilon = \epsilon_{,t} dt + \epsilon_{,Z} dZ = 0 \quad (13)$$

$$\frac{dZ}{dt} = c_p = - \frac{\epsilon_{,t}}{\epsilon_{,Z}} \quad (14)$$

These curves need not be straight lines, but if they are, as all experiments to date indicate, the analysis is greatly simplified because c_p then depends only on ϵ . Typical data is shown in Fig. 6, taken from Hauver [18]. The actual experiments were performed in a 4" light gas gun with the penetrator stationary for ease of instrumentation and the target plate launched from the 4" gun. The experiment is shown schematically in Figure 6. For details see [17], [18], and [19].

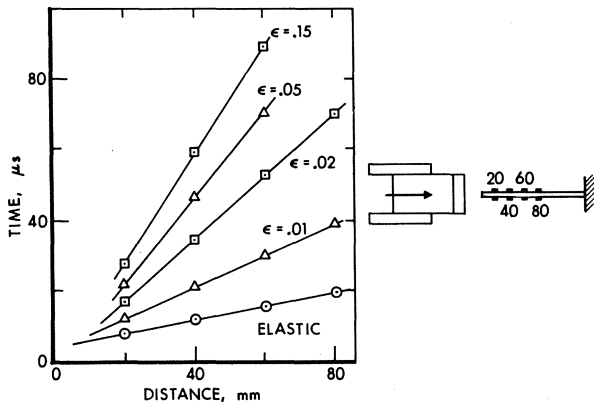


Fig. 6. Curves of constant strain in rod coordinates for a high strength steel rod and an armor steel target. Impact speed was 1000 m/s.

Equations (11) may be integrated with respect to Z along lines $t = \text{constant}$ as has been described by Kolisky [20] and others. If the rod has speed \dot{W}_0 and zero stress

and strain at any station before a wave arrives, we have

$$\dot{W}(Z,t) = \dot{W}_0 - \int_0^{\epsilon(Z,t)} c_p(\epsilon) d\epsilon, \quad (15)$$

$$\Sigma(Z,t) = \int_0^{\epsilon(Z,t)} \rho c_p^2(\epsilon) d\epsilon. \quad (16)$$

Note that the stress can be obtained from eqn. (16) without recourse to any constitutive assumption. Typical results obtained by Hauver [17, 18] and Hauver and Melani [19] are shown in Fig. 7.

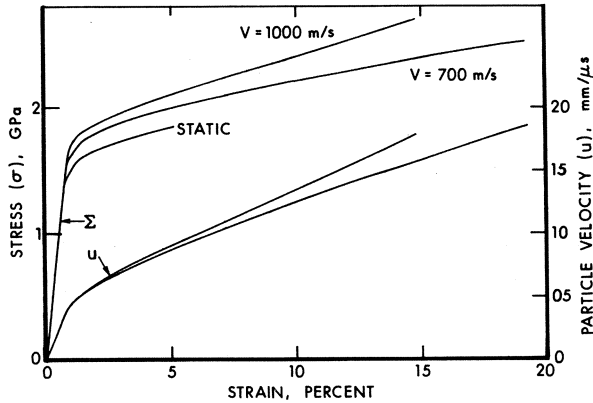


Fig. 7. Calculated stress and particle velocity for rod in Fig. 6 at two impact speeds. Also shown is the measured quasi-static stress/strain curve for the rod.

The most striking and immediately obvious feature of these results is that the stress, as computed from experiment, does not agree with the measured static stress and in fact the computed stress depends on the striking velocity, V . On the other hand, the particle velocity, as computed from the experiment, agrees well with other experiments also conducted by Hauver and Melani [19], in which particle motion was determined directly by observing fiducial lines on the penetrator with a streak camera. It is not possible to measure stresses directly, but within the limitations of eqns. (11), there is no reason to believe that computed stresses are less accurate than computed particle velocities.

Two reasons have traditionally been given for discrepancies between static and dynamic determinations of stress/strain relations. The first, viscoplastic or rate effects, has been ruled out as a major contributor for the penetrator material in this case. Standard Hopkinson bar tests, as reported by Chou [21], have not shown significant rate effects. The second possibility, the effect of finite radius, must therefore be explored.

Motivated by the results described above, Wright [22] has examined a higher order rod theory where radial strain, u , is treated as an internal variable, and given equal status with the axial displacement, W , as a dependent variable. Either by use of a variational principle to arrive at a one-dimensional formulation directly, or by integration of the three-dimensional equations through a cross section, one can arrive at a coupled pair of one-dimensional equations.

$$\frac{\partial S}{\partial Z} = \rho \frac{\partial^2 W}{\partial t^2}, \quad (17)$$

$$\frac{\partial Q}{\partial Z} - P = \frac{1}{2} \rho a^2 \frac{\partial^2 u}{\partial t^2}. \quad (18)$$

Here S is the average axial stress, P is the average lateral pressure on the rod, Q is the average polar moment of radial shear stress, a is the initial radius of the rod, and ρ , u , and W are as previously defined. In the constitutive equations for S , P , and Q the basic kinematic variables are the axial strain, $\frac{\partial W}{\partial Z}$, the radial strain, u , and the gradient of radial strain, $\frac{\partial u}{\partial Z}$. Analysis of these equations yields quantitative and qualitative information about the structure of wave-like solutions, either for the nonlinear elastic case as in [22] or for the elastic/plastic case, which is currently being studied.

Note that eqn. (17) is the same as eqn. (11)₁. Furthermore, eqn. (11)₂ applies as a compatibility condition in the present context as well as previously. Therefore, in the treatment of experimental data eqns. (15) and (16) are still valid for the computation of particle velocity and stress in the wave. Now, however, there should be no surprise that the stress, as computed for the dynamic case, does not agree with the static curve since the radial strain is still completely undetermined. Analytically it can only be determined through the coupling with eqn. (16), which describes the radial motion of the rod.

Since stress is also constant along the lines of constant strain in Fig. 6, it would be possible to determine the load history on the end of the eroding penetrator provided that extent of erosion is known as a function of time and that the erosion trajectory cuts across the straight lines. No experiment has yet been devised to measure extent of erosion directly, but an indirect approach seems possible by determining target penetration as a function of time and matching that curve with the projected arrival trajectories of various rod stations.

2. Experiments to Measure Penetration

Using the same penetrator and target materials and the same impact conditions as were

used by Hauver, Netherwood [23] attempted in a second series of experiments to measure rate of penetration by means of insulated switch wires which were inserted in small holes drilled into the side of the target block. The situation is sketched in Fig. 8. The penetrator is launched by a 4" gas gun, and the switch wires short out in order upon arrival of the penetrator at their target stations. Typical data are shown in Fig. 8 with the upper and lower curves representing bounds on the data over several repetitions of the test with switch pins located at different stations for different tests. Distance is measured with respect to the undeformed target and, therefore, is a material coordinate. The curves show a rapid entry zone, followed by a nearly steady zone of slow penetration. The last part of the curves should not be interpreted as a rapid exit zone, but rather as an erratic failure zone where a small plug forms near the rear target surface and shears off the switch pins before actual arrival of the penetrator. The erratic behavior is believed to be caused by the somewhat random nature of material failure.

The detailed shape of the curves in Fig. 8 cannot be taken too literally because plastic flow of target material may well cause the switch pins to trigger before penetrator arrival. Clearly, however, the real curve must lie on or below the apparent curve so that the data give an upper bound for depth of penetration at any time. The straight, middle portion of the apparent curve might be supposed to lie parallel to the real curve where quasi-steady flow occurs, but doubt has been cast on that interpretation, as well, by Hauver's recent work [18]. It seems fair to say that truly definitive measurements of penetration vs. time have yet to be made, although Netherwood's experiments represent a major step in that direction.

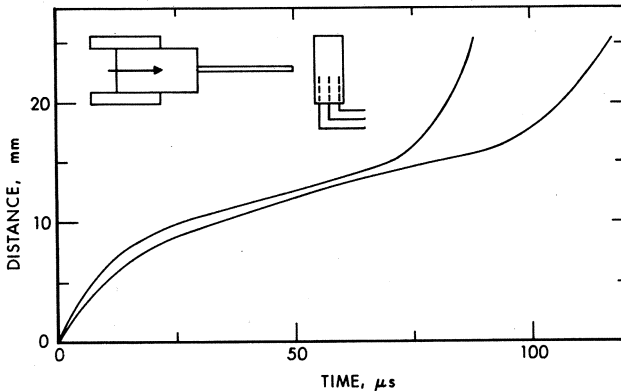


Fig. 8. Measured penetration vs. time for same rod and target as in Fig. 6.

To compare the penetration curve with the projected arrival trajectories of various rod stations it is necessary to use a common coordinate system. The rod data were taken in the material coordinates of the rod, and the target data were taken in the

material coordinates of the target, but both sets of data, as well as the curves of constant strain, may be transformed into a common spatial or laboratory coordinate system.

In material coordinates for the penetrator, the trajectories of constant strain may be written as $Z = Z(t)$ so from use of eqn. (12), the trajectories in spatial coordinates may be represented as $z = z(Z(t), t)$. These have slope

$$\frac{dz}{dt} = \frac{\partial z}{\partial t} + \frac{\partial z}{\partial Z} \frac{dZ}{dt} \quad (19)$$

The first term on the right hand side is given by eqn. (15), and the second term is the product of $(1 + \epsilon)$ and c_p by eqns. (12)₃ and (14). Therefore, in spatial coordinates the trajectories of constant strain have speed $\frac{dz}{dt}$ as follows.

$$\frac{dz}{dt} = \dot{w}_0 - \int_0^\epsilon c_p d\epsilon + (1 + \epsilon) c_p . \quad (20)$$

Eqn. (20) shows that if c_p depends only on ϵ , these trajectories are straight lines in spatial coordinates as well as material coordinates. Several lines of constant strain are shown in Fig. 9. Note that as penetration occurs, the higher strain levels are actually carried into the target cavity.

The spatial trajectory of any rod station may be computed by integrating eqn. (15) with respect to time, Z being held fixed. All that is needed is the strain history at a fixed rod station, and those histories are available either directly from the strain gage records or by interpolation from Fig. 6. Some trajectories of this kind are also shown in Fig. 9. Note that the retardation due to axial compression is clearly visible. The trajectory labeled 96 mm corresponds to the initial length of the recovered penetrator as determined by weighing in one particular test.

Finally the spatial trajectory of penetration is also shown in Fig. 9. This has been drawn simply by translating the points of the material trajectory by the amount of the free surface motion at corresponding times, ignoring any compression of target material between the penetrator and the free surface. Surface motion was measured by Netherwood, using a streak camera, and in some of his tests a small plug approximately 5 mm in thickness was also recovered [24].

The trajectories of the 96 mm station, the free surface, and penetration, together with the known plug thickness, form a remarkably coherent picture, and show with graphic clarity the need to account for deformation in a sound physical theory of penetration. That need is evident in spite of the uncertainty in locating the penetration curve.

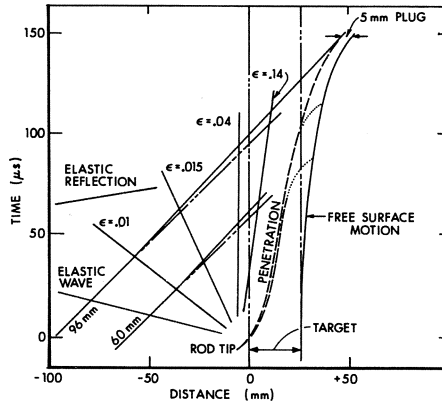


Fig. 9. Composite penetration diagram in laboratory coordinates.

The highest strains measured all propagate with nearly the same speed. In Fig. 9 that speed appears to be slightly less than the rate of penetration so that it is not clear from the experiments where the erosion trajectory should be shown in Fig. 8. A good approximation is probably a straight line drawn slightly to the left of the highest strain shown, but with a slightly greater slope.

3. Experiments to Measure Target Stress

In a third series of experiments Pritchard [25, 26, 27] has measured the stress in the target normal to the path of penetration and directly on the path. A sketch of the experiment is shown in Fig. 10. A manganin foil stress gage was placed in the center of a split rod, the rod was inserted into a hole drilled in the target, and the alignment was adjusted so that the gage lay directly on the line of penetration. This experiment was also performed in a 4" light gas gun. Since the manganin gage is subjected to a diverging strain field, it is necessary to compensate by measuring strain independently and correcting the pressure determination. This is done with a constantin gage, which is actually interleaved with the manganin gage. Details have been given by Pritchard [25, 26].

Typical data are shown in Fig. 10 for a tungsten alloy rod and a steel target [27]. Stress histories begin with shock arrival and increase until gage failure some time before actual arrival of the penetrator. Notice that there is no sharp jump in stress at shock arrival, at least for these cases in which the penetrator had a hemispherical nose, and that the rate of increase is more rapid for the shallower gage location. For the two records shown gages failed at less than half the time to penetrator arrival so that extrapolation to penetrator arrival is hazardous at best. Nevertheless, it is at least interesting to note that reasonable extrapolations give a peak stress that is roughly in the range of 50-55 kb for both curves. Data have also been reported for

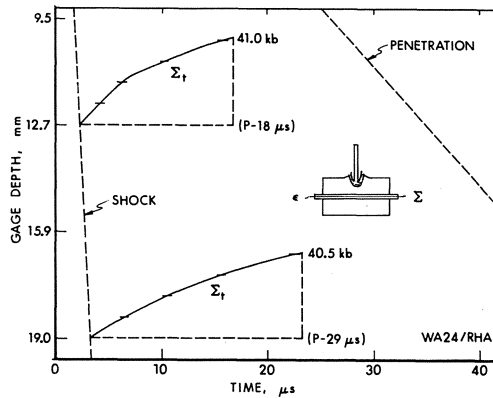


Fig. 10. Measured target stress vs. time at depths of 12.7 mm and 19.0 mm below the impact surface. The rod is a tungsten alloy and the target is armor steel.

the same combination of materials shown in Fig. 6. The general trend of the data is the same as Fig. 10, but the quality of the data is not as high. (See Pritchard [25, 26]).

Other Considerations

The experiments described above go a long way towards indicating the phenomena that should be included in a reasonable theory of long rod penetration, but there are other important considerations as well. These may be grouped into three sets of phenomena: hole growth in the target, the failure and discard of eroded penetrator material, and the effects of bending.

Neither the eroding rod model nor any of the experiments described above gives any consideration to the dynamics of hole growth, although some attention has been devoted to this problem in the literature, e.g., Hanagud and Ross [28] or Ravid and Bodner [14]. As the penetrator moves through the target, target material must flow to the sides around the penetrator. At the lower rates of penetration, the extent of lateral motion must be at least great enough to admit passage of any eroded and discarded penetrator material. At higher rates, inertia may drive both target and eroded penetrator material somewhat away from the sides of the remaining intact penetrator, or in the case of a non-eroding penetrator, inertia may cause separation of the flow between target and penetrator.

Ductility and fracture characteristics also have a significant effect on penetration. For example, a very ductile material may simply pile up on the target surface at low impact velocities or actually turn inside out to form a tube as it penetrates at higher velocities (Frank [29]). In any case, excessive penetrator ductility tends to

increase the contact area between penetrator and target, thus providing a larger retarding force to the penetrator. In attempting to simulate numerically some of Hauver's data on instrumented rods, Misesy [30] found that it was essential to include at least a crude fracture criterion in his two-dimensional code. Without a fracture criterion the computed strains in the penetrator increased much more rapidly than the experimental data indicated. This would seem to indicate that a fracture criterion would also be useful in an engineering model of penetration.

Finally, in any complete engineering theory of penetration some consideration must be given to the effects of bending as induced by oblique impact or penetrator yaw at impact, and should include lateral stability or bending enhancement due to axial loading. A start was made by Abrahamson and Goodier [31], who considered lateral stability of an elastic/linear work hardening rod in normal impact on a rigid target. However, they did not consider the effect of moments or transverse forces at the impact end as might be induced by yaw and obliquity, and even more important from the point of view of penetration mechanics, they did not include the effect of penetrator erosion, which in effect provides a moving boundary for the application of forces and moments. No thorough experimental study on bending effects seems to have been undertaken, although limited data exists, Hauver [17].

Computer Codes

The third approach to penetration mechanics uses large scale numerical simulation with the full equations of continuum physics. The characteristics of some typical codes and their limitations have been described by Zukas [32] and Jonas and Zukas [33] so that only a few comments are required here. The ordnance regime still remains today as extremely difficult for making accurate numerical predictions, especially for impact speeds near the limit velocity. This difficulty is commonly attributed to lack of adequate knowledge concerning both dynamic material properties and fracture descriptions in the codes (see [33] for example). The determination of deformation and fracture properties at high pressures and high rates of strain requires exceptional experimental skill and ingenuity, especially since the dynamic situation makes it all but impossible to determine constitutive properties without imposing *a priori* constitutive models or assumptions. There is always some circularity in the common procedure of "backing out" constitutive properties by choosing free parameters in a given model so as to obtain rough agreement between a calculation and experimental data. On the other hand, there often seems to be little other choice. All that can be asked is that critical judgment and restraint be used in interpreting and accepting results. Reference [1] gives a thorough review of current practice in constitutive modeling for codes and recommends avenues for future improvements.

As constitutive models become more comprehensive, ever greater burdens will be placed on computing capacity, which must be offset either by increases in machine size and

speed or by increases in the efficiency of computing algorithms. Computing power should be reserved for those parts of the problem that most need it, and not wasted on regimes where little is happening. Fortunately, rapid advances are being made in both hardware and software so that advances in constitutive modeling can be expected to be implemented in penetration calculations.

Conclusions

The three current approaches to penetration mechanics - data correlation, engineering models, and large scale computer codes - will all continue to evolve with increasing emphasis being placed on the role of material properties and the mechanics of material deformation and failure in each case. In many respects the approach using engineering models is the least developed of the three, but it holds the promise of encompassing virtually all of the relevant physics, yet at far less computational cost than the large scale codes. The benefit comes from one-dimensional rather than three-dimensional numerical simulation. Data correlations will still be indispensable for organizing large volumes of ballistic data, but engineering models can be expected to suggest improved functional forms for non-dimensional analysis. The engineering models themselves should play their biggest role in aiding designers and systems analysts. The large codes will remain as the indispensable tool for examining the details of interaction, and as constitutive models improve, may well permit actual material design for ballistic applications.

References

1. Materials response to ultra-high loading rates. National Materials Advisory Board publ. NMAB-356, Washington: National Academy of Sciences 1980.
2. Grabarek, C.; Herr L.: X-ray multi-flash system for measurement of projectile performance at the target. Ballistic Research Laboratory BRL-TN-1634 (1966) AD 807619.
3. Backman, M. E.; Goldsmith, W.: The mechanics of penetration of projectiles into targets. Int. J. Eng. Sci. 16 (1978) 1-99.
4. deMarre, J.; Perforation of iron and steel sheets with normal firing (trans.), Memorial de l'Artillerie de Marine 14 (1886). Empirical formulas of this type for limit energy are often called deMarre relations, at least in the U. S. In his original paper deMarre gave the formula with $\alpha = 1.4$ and $\beta = 1.5$.
5. Grabarek, C.: Penetration of armor by steel and high density penetrators. Ballistic Research Laboratory BRL-MR-2134 (1971) AD 518394L.
6. Project Thor Tech. Rept. No. 47. The resistance of various metallic materials to perforation by steel fragments; empirical relationships for fragment residual velocity and residual weight. Ballistic Analysis Laboratory, The Johns Hopkins University (1961).
7. Bruchey, W.: Private communication. In preparation as a report, Ballistic Research Laboratory.
8. Alekseevskii, V. P.: Penetration of a rod into a target at high velocity. Comb., Expl., and Shock Waves 2 (1966) 63-66, trans. from Russian.

9. Tate, A.: A theory for the deceleration of long rods after impact. *J. Mech. Phys. Sol.* 15 (1967) 387-399, and Further results in the theory of long rod penetration. *J. Mech. Phys. Sol.* 17 (1969) 141-150.
10. Frank, K.: A qualitative determination of the velocity, mass, and fineness ratio required to defeat single plate targets. Spring Technical Conf. (1978) Ballistic Research Laboratory.
11. Hohler, V.; Stilp, A. J.: Penetration of steel and high density rods in semi-infinite steel targets. Third Int. Symp. Ballistics, Karlsruhe, Germany 1977.
12. Tate, A.; Green, K. E. B.; Chamberlain, P. G.; Baker, R. G.: Model scale experiments on long rod penetrators. Fourth Int. Symp. Ballistics, Monterey, Cal. 1978.
13. Wright, T. W.: Penetration with long rods: a theoretical framework and comparison with instrumented impacts. Ballistic Research Laboratory ARBRL-TR-02323 (1981).
14. Ravid, M.; Bodner, S. R.: Dynamic perforation of viscoplastic plates by rigid projectiles. Report of the Material Mechanics Laboratory, Technion, Haifa, Israel (1982).
15. Frank, K.: Unpublished work. His essential idea was to combine the results of the eroding rod model with hypervelocity cratering results of Christman and Gerhring, *J. Appl. Phys.* 37 (1966) 1579-1587.
16. Tate, A.: Extensions to the modified hydrodynamic theory of penetration. Preprint, to be published.
17. Hauver, G. E.: Penetration with instrumented rods. *Int. J. Eng. Sci.* 16 (1978) 871-877.
18. Hauver, G. E.: Experiments with instrumented long-rod penetrators. Fifth Int. Symp. Ballistics, Toulouse, France 1980.
19. Hauver, G. E.; Melani, A.: Strain-gage techniques for studies of projectiles during penetration. Ballistic Research Laboratory ARBRL-MR-03082 (1981).
20. Kolsky, H.: *Stress waves in solids*. New York: Dover Publ. (1963).
21. Chou, P.-C.: Letter report to Ballistic Research Laboratory from Army Mechanics and Materials Research Center 1980.
22. Wright, T. W.: Nonlinear waves in rods. Proc. IUTAM Symp. on Finite Elasticity, Carlson, D. E.; Shield, R. T. (eds.). The Hague, Boston, London: Nijhoff Publishers 1980.
23. Netherwood, P. H.: Rate of penetration measurements. Ballistic Research Laboratory ARBRL-MR-02978 (1979).
24. Netherwood, P. H.: Private communication (1979).
25. Pritchard, D. S.: Measurements of dynamic stress and strain components in targets struck by penetrators. Ballistic Research Laboratory ARBRL-MR-03095 (1981).
26. Pritchard, D. S.: Piezoresistive gauge measurements in deforming environments during penetration. Proc. First Symp. on Gauges and Piezoresistive Materials, Arcachon, France 1981.
27. Pritchard, D. S.; Hauver, G. E.: Private communication of unpublished data (1982). The raw data were taken by Pritchard and reduced and analyzed by Hauver.

28. Hanagud, S.; Ross, B.: Large deformation, deep penetration theory for a compressible strain-hardening target material. AIAA journal 9 (1971) 905-911.
29. Frank, K.: Private communication on test results.
30. Misesy, J. J.; Gupta, A. D.; Wortman, J. D.: Comparison of penetration codes for strain measurements in kinetic energy penetrators. Ballistic Research Laboratory ARBRL-TR-02231 (1980).
31. Abrahamson, G. R.; Goodier, J. N.: Dynamic flexural buckling of rods within an axial compression wave. J. Appl. Mech. 33 (1966) 241-247.
32. Zukas, J. A.: Numerical simulation of impact phenomena (Chap. 10), Three-dimensional computer codes for high velocity impact simulation (Chap. 11). In Impact Dynamics, J. A. Zukas, T. Nicholas, H. F. Swift, L. B. Greszcek, D. R. Curran. New York: Wiley-Interscience 1982.
33. Jonas, G. H.; Zukas, J. A.: Mechanics of penetration: analysis and experiment. Int. J. Eng. Sci. 16 (1978) 879-903.

SOME EXAMPLES OF THE USE OF CONTINUUM MECHANICAL COMPUTATIONAL MODELS IN THE DEVELOPMENT OF ENGINEERING MODELS

MARVIN E. BACKMAN

Detonation Physics Division
Research Department
Naval Weapons Center
China Lake, CA 93555

Abstract

Engineering models of impact events can use continuum mechanical computation schemes either as the modeling device or for guidance and validation. Examples include dynamic finite element codes that determine structural response of a penetrator to impact against extended targets in order to predict survivability, the use of an Eulerian hydrocode to perform computer simulations of inhomogeneous plastic deformations, and the role of sophisticated computational models in the development of highly simplified models that predict penetration through aircraft or light vehicle assemblies.

Introduction

Several efforts at modeling impact events depend on continuum mechanical models either as the modeling device or for guidance and validation. Examples include the application of dynamic finite element codes to determine structural response of a penetrator to impact against extended targets in order to predict its survivability, the use of an Eulerian hydrocode to perform computer simulations of inhomogeneous plastic deformations and the simulation of the penetration resistance of a protective case when backed by various materials. In each of these examples computational models represent continuum mechanical theory in an interface with an experimental program.

The paper also discusses a continuing need to develop highly simplified models for methodologies that predict penetration through aircraft or light vehicle assemblies and the role of more sophisticated computational models in this development. Although the required models must have highly simplified forms they must provide comprehensive predictions, e.g., they must cover a wide range

of obliquities, target materials, projectile shapes and masses. In addition these models must either describe or properly account for changes of penetrator and target failure modes; thus, although the methodologies have the superficial appearance of simplicity, they must incorporate a high degree of phenomenological complexity. Above all, this model requirement emphasizes the need for an improved capacity to model material failure processes in a comprehensive penetration methodology.

Penetrator Survivability

Finite element analyses provide one means for determining the stresses and deformations within a warhead during penetration. The analyses at the Naval Weapons Center have had two parts. In the first part, terminal ballistic theory and data determine a loading history (force-time curve) to represent the resistance of the target material to penetration. In the second part, a finite element analysis of the warhead uses this loading history to determine stresses and deformation in the warhead.

The separate determination of the loading history and response by the warhead significantly simplifies the finite element solution; however, this approach ignores the coupling between the target material and the warhead and could lead to some inaccuracy in the results. One warhead design was analyzed in this way and also tested on the Supersonic Naval Ordnance Test Track (SNORT) at the Naval Weapons Center. The target was a combination of granite boulders, reinforced concrete slabs and sand and was considerably more complex than the homogeneous half space assumed in the analysis. The test warhead was uninstrumented so that the data for comparison with the analytical results was the permanently deformed shape of the warhead after the test. Despite gross simplifications of the target the final shape predicted by the analysis resembled that of the test.

The warhead consisted of a cylindrical 4340 steel case 50 inches long and 8 inches in diameter and filled with PBX explosive. The overall weight of the warhead was 511 pounds, of which 56 pounds is explosive.

The force-time curves that represent the resistance of the target material to penetration come from a cavitation theory of penetration due to Bernard and Creighton [1] and experimental data to determine certain parameters.

The cavitation theory treats penetration into an infinite medium as the expansion of a cavity from zero radius to a radius, a . For conical-nosed projectiles traveling at high velocities, the radial stress σ and maximum shear stress τ become

$$\sigma = (1 + \sin \eta) \frac{4}{3} c (1 + \ln I) + v \sqrt{\rho \sigma_s} \quad (1)$$

$$\tau = (1 + \sin \eta) c \exp \left(-\rho v^2 / \sigma_s \right) \quad (2)$$

where η is the cone half-angle, c the cohesion, ρ is the density of the target material, v is the projectile velocity, σ and I the index of rigidity, which is defined as the inverse of the maximum deviatoric strain at failure. The drag force becomes

$$F = \pi a^2 \left(\sigma + \frac{\pi}{2} \tau \right). \quad (3)$$

Conservation of momentum for the projectile requires that

$$F = m \dot{v} \quad (4)$$

where m is the mass of the projectile.

These equations can be easily integrated numerically on a computer to determine the projectile velocity and the force applied to it. In addition, another integration will yield the penetration depth of the projectile as a function of time.

The cavity expansion theory applies to conical-nosed projectiles, while the warhead being analyzed is blunt-ended. Experiments with small cylindrical, blunt-ended steel projectiles fired into both plaster of Paris and simulated concrete targets have shown that conical caps form on the front of blunt projectiles shortly after initial impact and are carried along by the projectiles so that

blunt-ended projectiles effectively become conical-nosed during penetration and are subject to the above theory. In analyzing this warhead, the cone half-angle was taken as 45 degrees. The cavity expansion theory was used to generate loading histories for penetration into two types of concrete and a rock called diorite. The concretes had strengths of approximately 5,000 and 10,000 psi. The 5,000-psi concrete corresponds to a good structural grade. The 10,000-psi concrete is not practically realizable, but represents a stronger material, possibly similar to a reinforced concrete. Diorite is a primary constituent of the granite boulders in the test target.

Program HONDO was used for the finite element analysis [2]. This program performs large deformation dynamic analysis of impulsively loaded solids of revolution. Because no stiffness matrices are calculated or stored, rather large problems are easily treated. Eight material subroutines model elastic, viscoelastic, elastic-plastic, crushable foam and soil behavior.

The finite element model of the warhead consisted of 1,141 nodal points and 1,027 quadrilateral elements. The axial drag force as a function of time derived from penetration theory was applied to the warhead in the form of a normal pressure distributed over the front end and proportional to the cosine of the angle between the normal to the surface and the axis of the warhead.

For 5,000 psi concrete a stress wave created by the sudden application of pressure over the front end propagates down the length of the warhead (Fig. 1). At 10 microseconds the front of the wave is nearly planar except near the lateral surface of the case where the applied pressure drops off. At 50 microseconds the wave has split into two parts around the front of the explosive cavity. At 200 microseconds the wave has nearly reached the rear of the warhead. After about 250 microseconds an unloading wave is reflected off the rear surface of the warhead and begins to travel back towards the front, reducing the stress levels in the case walls as it does so. At 500 microseconds this unloading wave reaches the front end of warhead. Due to the reduction in cross-sectional area of the case around the explosive cavity, the highest compressive stresses in

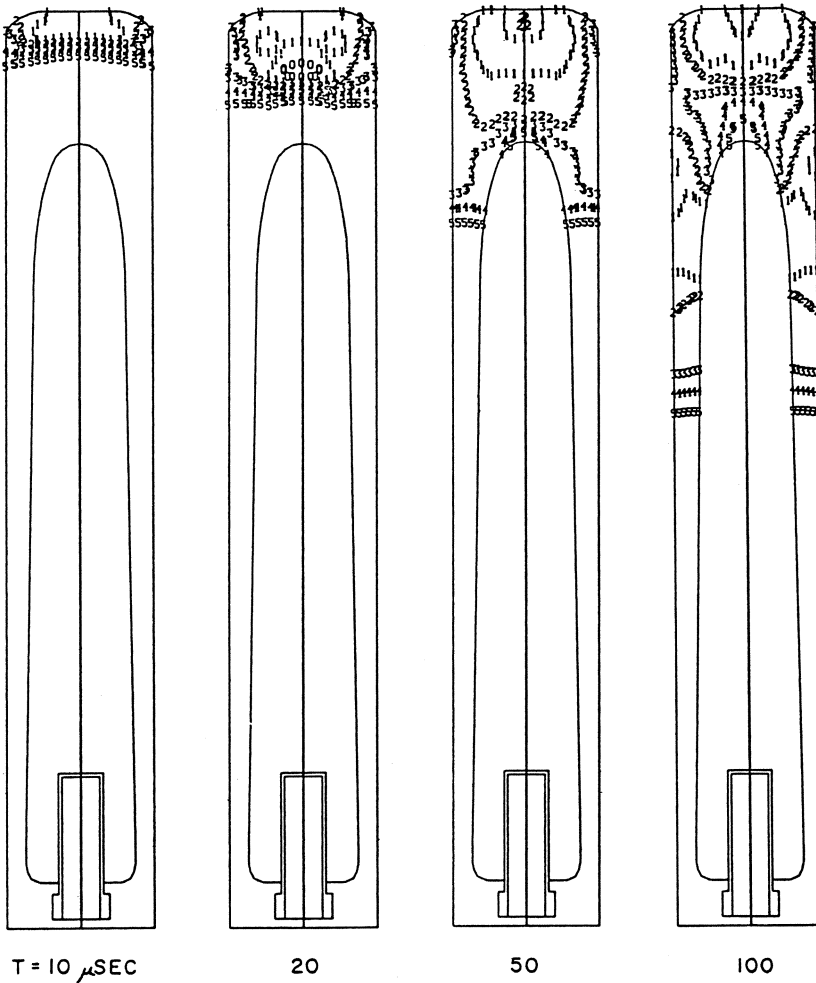


Fig. 1. Axial stress contours at selected times during penetration into 5,000-psi concrete.

the structure (in excess of -145,000 psi) occur in the tapered side walls of the case (plot at 300 microseconds).

Stresses in the explosive are much lower than in the case, due to their lesser moduli. At 40 microseconds stresses have just started to appear at the front of the explosive. Propagation of these stresses down the length of the cavity does not occur at the wave propagation speed for the explosive; rather the stresses are dragged along at a higher rate by the stresses in the surrounding case.

A maximum compressive stress of -28,000 psi occurs in Element 154 at the front of the explosive cavity.

For 10,000 psi concrete, the highest stresses now occur near the front end, and the stresses in the tapered walls surrounding the explosive cavity are considerably less (though still high enough to cause yielding).

The results for penetration into 10,000 psi concrete show that the loading in this case is considerably more severe than for 5,000 psi concrete. Stresses are above the elastic limit over a larger portion of the case and considerable plastic flow occurs. Nevertheless, it would appear that deformations in the case itself are not so large as to produce structural failure of the case. However, stresses in the explosive are sufficiently high that deflagration of the explosive is possible.

Computer Simulations of Plastic Instabilities

In impact a mode of failure called adiabatic shears constitute an essential element of the dynamics of localized plastic deformations. The explanations of adiabatic shears have usually invoked stability criteria for localized plastic shears on the basis of the generation of thermally-softened material within a narrow band. The details of internal deformation shown in micrographs of crater, projectile or fragment cross-sections suggest that transitions from plastic to elastic deformation and rigid body motion play a key role in the formation of localized plastic deformation. This has been demonstrated for impact by projectiles fired against plates of different materials and heat treatment in which shear bands form in fragments and craters. Material on opposite sides of the shear bands exhibited different degrees of deformation beyond the immediate region of intense shear. The shear bands had configurations that approximated slip-surfaces for the loading conditions. The patterns tend to be consistent in configuration, but not completely reproduceable. There is clear evidence that a group of shear bands begins on the contact surface between projectile and plate and extends into the plate. Sometime ago, we proposed that this is a fracture-like process in which the

instability requirements are met in a zone at the "tip" [3]. At present, there has been no quantitative treatments in propagation rates in terms of shear zones and associated fractures suggested a primary role for the shear bands and that the fractures follow the bands in a secondary role.

An examination of several impact craters and recovered projectiles for steel projectile and normal obliquities, and simulation by the HELP code leads to the following view of the role of rigid body motions in the penetration of a plate by a deforming sphere. The interaction between the sphere and the plate begins with extensive mutual deformations consisting of penetrations into the plate and the flattening and expansion of the sphere. The HELP code also shows regions of predominantly rigid body motion and states of stress close to hydrostatic develop about the center of the contact surface. In both the deforming sphere and the plate slip surfaces enclose a part of the body on the axis of symmetry and proceed inward from a locus of points on the contact surface toward the axis of symmetry. The slip surfaces of the target are concave with respect to the axis of symmetry while those of the sphere are convex. The result is an axisymmetrical region of common motion that has an arrowhead shaped cross-section (Fig. 2).

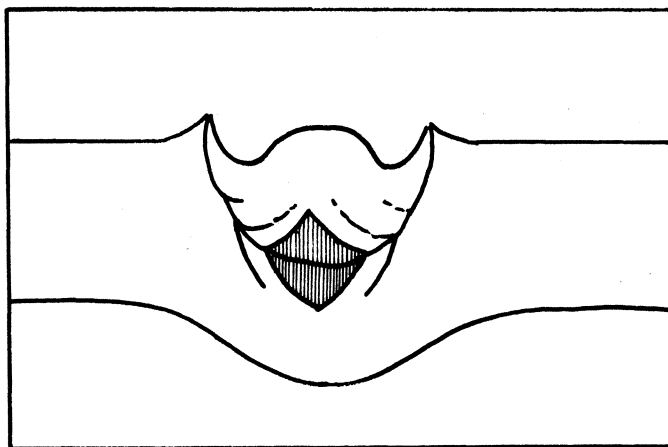


Fig. 2. Idealized representation of slip surfaces in sphere striking a plate.

At velocities near the ballistic limit, the minimum velocity for perforation, and for plates that have thicknesses less than the diameter of the sphere, there tends to be only one slip surface system; its curvature is small, and it originates away from the axis of symmetry. As the velocity of impact increases, the number of slip systems increases. Our hypothesis is that as the impact stresses increase it is feasible for these arrowhead shaped regions to develop earlier in time and closer to the axis of symmetry.

As the penetration proceeds additional layers of rigid body motion are added to the arrowhead. Eventually, fractures will occur along the boundaries of these incremental enlargements probably due to the stress conditions that develop in the later phases of the penetration process.

The parts of the arrowhead that belong to the sphere and the plate have the same rigid body velocity since these are in contact; however, the slip systems for the sphere do not, in general, have the same origin on the contact surface. In many craters the plate material has imposed its flow requirements on the sphere, although occasionally the reverse is true. In this view of the impact process, the rigid arrowhead is embedded in a plastic region in which plastic material flows around the arrowhead toward the surface of contact. As the projectile "mushrooms" through its flow, it accelerates more of the target material while the target simultaneously decelerates this expanding part of the projectile. Thus, these flows around the existing arrowhead zones, the process starts at the contact surface and follows slip directions. The process of arrowhead formation is not always completed, apparently because the stress conditions that favor regions of rigid body motion do not exist throughout the sphere and plate.

The Ballistic Limit of a Backed Plate

The critical value of impact speed commonly called the ballistic limit is the minimum speed of a specified projectile that will perforate a given protective covering or armor. Usually, some finite distance separates the armor and other components of interest so that perforation of the armor and interaction with a second

component constitutes completely separable events and independent processes. If, on the other hand, the protective covering contacts the second component then perforation of the protective covering and interaction of the secondary components become overlapping events and interdependent processes. The concept of a ballistic limit for the first element remains unchanged but obviously may depend on the characteristics of the second component. This investigation concerns the influence of the secondary layers of a composite target on the ballistic limit of the primary element.

An experimental investigation determined the ballistic limit of mild steel spheres impacting composite targets made up of plates. The choice of spheres and plates simplified the test procedures and increased reproducibility of results, since impact at ordnance velocities tend to develop a common target-projectile interface so that minor differences of shape have little effect. In most of the tests of the investigation, the ratio of plate thicknesses to projectile diameter was nominally one.

Firings against materials with markedly dissimilar material characteristics showed the range of effects that the second element can produce. The impacts were at normal incidence. The targets consisted of 6.4 mm thick mild steel plates followed by approximately 10 cm of the secondary element. The plates were not bonded or clamped to the secondary elements. The plasticine (modeling clay) which flows readily and has reasonable density, produced no discernable change in the ballistic limit of the plate. The plaster of Paris, which is low strength and moderate density, and the explosive simulant, a rubber-like material, increased the ballistic limit of the plate by about 10% (the plaster of Paris from 1.25 Km/s to 1.37 Km/s and the simulant to 1.39 Km/s). The Plexiglas backed plate resisted perforation up to 2.51 Km/s.

These preliminary findings demonstrate the potential for a considerable effect of a secondary element on the behavior of the first element and in addition identify Plexiglas as a material for further study. The remainder of the present report will attempt to identify more precisely the behavior of this material as a

secondary element. This task involves several methods of measuring the responses of the target. First, the phenomena observed by the most direct methods will be summarized, then a number of techniques for further observation will be presented.

We have chosen measurements of crater dimensions as a function of impact speed as a means for making a detailed comparison of the responses of unbacked and Plexiglas backed systems. Figure 3 compares the development of penetration in the two systems. It turns out that all transitions in the deformation and failure have been influenced by the backing material. Changes in the system such as the completion of internal failures, the formation of a plug and plug expulsion are all retarded by the presence of the secondary element. Some success has been attained in correlating these transition points to critical points on stress curves defined from crater dimensions and impact velocity.

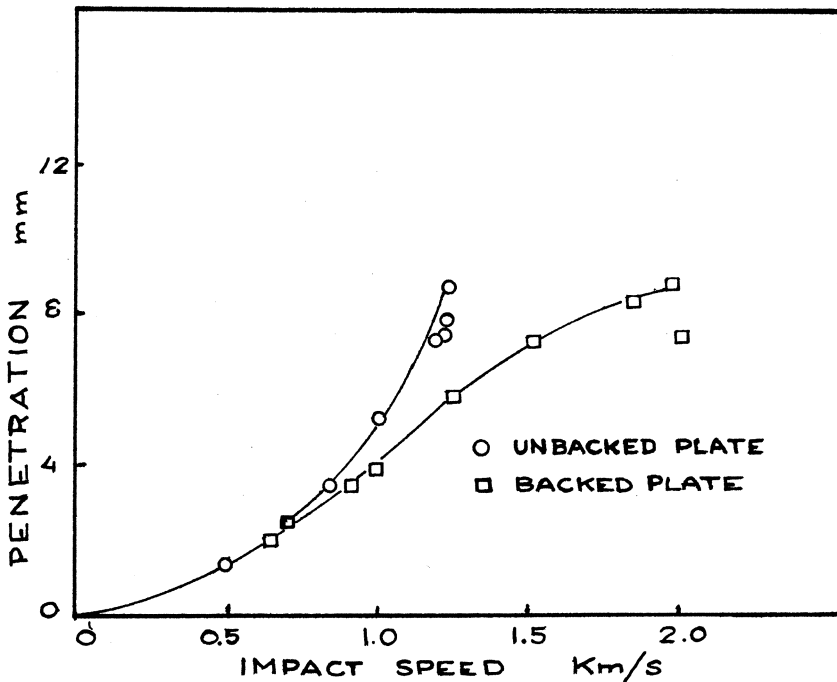


Fig. 3. The development of penetration in an unbacked 6.35 mm plate and one backed by Plexiglas.

We used two methods to determine the ballistic limit. A method developed by Recht [4] was used to determine the ballistic limit of the unbacked plates. This method required the use of a ballistic pendulum to obtain momentum measurements and presumes perforation and therefore cannot be used for the backed plates. The standard method for determining V_{bl} was used in this case, and in determining special transition points not related to perforation.

The significant increase in ballistic limit observed for Plexiglas backing raises the question as to how the Plexiglas compares, in its influence on penetration, to additional steel. A series of firings against 35 mm mild steel plates were made for comparison. The 35 mm mild steel plates showed significantly less penetration than the 6.3 mm mild steel plates backed with Plexiglas (approximately 30% lower at 1.5 Km/s).

The Eulerian Code (HELP) that predicts the dynamic behavior of the system on the basis of continuum mechanical equations has been used as a theoretical tool.

The computational effort involved systematic variation of parameters of the HELP code in an attempt to match experimentally observed penetration and cratering. Figures 4 and 5 show examples of these computations for backed and unbacked plates of the same thickness. The comparison of deformations and penetration depths reveals some of the effects that come from a backing with Plexiglas. One very obvious difference is the absence of bending in the unbacked case.

Terminal Ballistic Models for Vulnerability Analyses

Aircraft and missiles possess minimal armor but have complex internal structures that a kinetic-energy penetrator must defeat to reach vulnerable components. Many vulnerability analyses depend on detailed calculations of the penetration of such structures. The analyses use a descriptive-geometric-representation of the target given by a computer program. In the analysis a set of parallel shot-lines passes through the target to

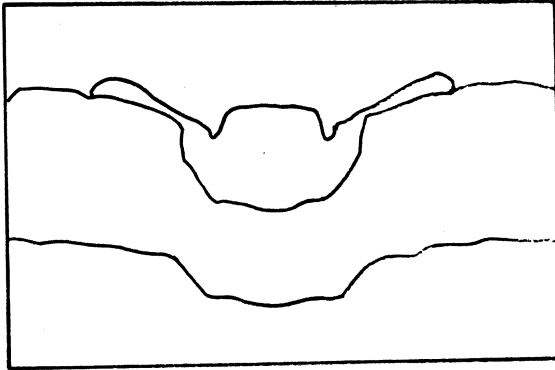


Fig. 4. HELP calculation of target and projectile configuration (plate not backed).

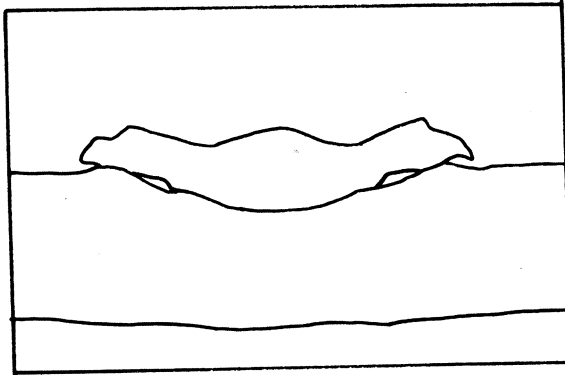


Fig. 5. HELP calculation of target and projectile configuration (plate backed by Plexiglas).

represent a given attack condition and the analysis determines the penetration through the target elements found along each shot-line. Thus, the vulnerability assessment procedure requires a penetration methodology that predicts the changes in the state of motion and the configuration of the projectile in progress through each target element of the array. The penetration methodology appropriate for this purpose needs to have minimal computational complexity but must include all relevant phenomena and apply to a broad range of materials.

There are changes in the outcome of an impact that takes place abruptly as the initial state of motion is changed. For example,

the ballistic limit velocity determines the critical state of motion for a change from a non-perforating impact to a perforating impact. Other changes of interest are the change from an intact projectile to one for which the jacket has been stripped, and the change from an intact core to a broken core. In one way or another, these changes are all due to failure of either the material of the component or the projectile. For any impactor and target component the final results of impact can be grouped into a discrete number of sets according to these changes. Each of these sets can be given a simple description such as projectile perforates intact, projectile perforates with jacket stripped, etc. The decision-making equations and some specified logical interrelation among them define these sets.

The separation of all the initial states of motion into discrete sets can be geometrically represented by a "phase diagram" in which the initial conditions are the dimensions of a space [5,6]. The variables, velocity V and obliquity θ are analogous to the temperature T and pressure P on a thermodynamic phase diagram. Decision-making equations define the boundaries of the phases. The phases can be represented by two-dimensional phase diagrams with coordinates V and θ .

The ballistic limit equation, for example, divides the phase space into two parts. For a given obliquity, velocities above the ballistic limit correspond to perforations; those below correspond to ricochets. For consistent yaw, the phase space can be represented by V and θ alone as in Figure 6, and the ballistic limit curve is as shown where the shape of the curve is that of the secant function. The points above the ballistic limit represent initial states of motion for which the impactor deforms the component such that ruptures or fractures develop in the component that allow the impactor to pass through.

The equations for the ballistic limit curve are empirical forms that represent the dependence of the ballistic limit speed upon the thickness of the component, the presented area of the projectile nose shape, and the projectile weight. Empirical observation

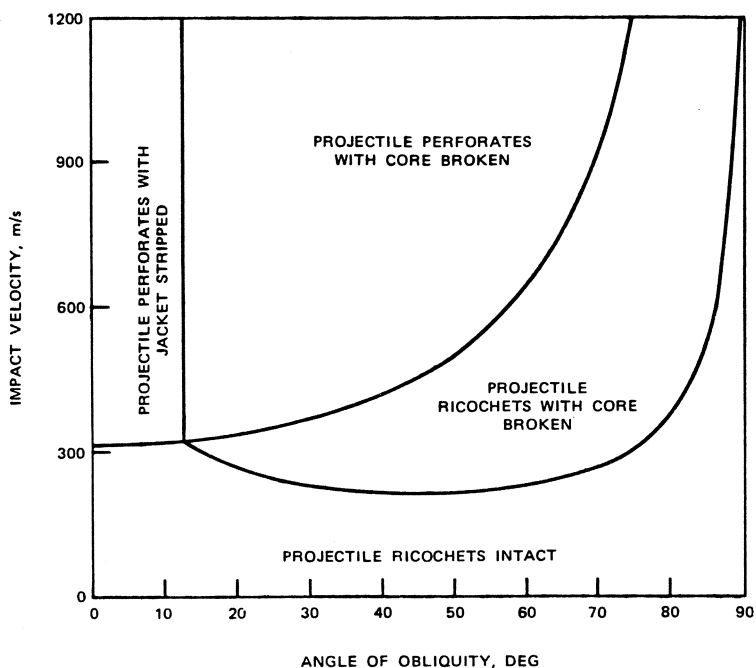


Fig. 6. An example of a phase diagram for a projectile (0.30 cal) and a plate (0.058 inch 2024 aluminum).

show that the ballistic limit tends to vary with obliquity as the secant function of the obliquity angle.

The equations for the normal ballistic limits for projectiles are expressed in the form

$$V_{bl} = c \left(\frac{\rho_c T A_p}{W} \right)^b + k \quad (5)$$

which has a dimensionless argument. This empirical form has been compared with theoretical equations and data. The corresponding equations for fragments are taken from other studies which used the form

$$V_{bl} = 10^c (TA_p)^\alpha (W)^{-\beta} \quad (6)$$

where α , β , c are THOR exponents. This equation has been rewritten as

$$V_{bl} = c \left(\frac{\rho_C T A_P}{W} \right)^\beta \left(\frac{\rho_C T A_P}{W_o} \right)^{(\alpha - \beta)} \quad (7)$$

to preserve the original prediction, but to also allow the use of dimensionless arguments and more direct comparison to the projectile equations. The last factor on the right can be interpreted as a scaling factor which will determine the changes in the prediction of the ballistic limit for a uniform increase in the size of every dimension of the impactor and target element. It should be noted that the scaling effect implied by the equation is not large. However, the original empirical equation and its constants were derived to describe a large body of data but there was no intention of establishing scaling relations.

Two modes of failure allow the impactor to pass through the component. A pointed impactor produces intense deformation and rupture of the component at the tip of the impactor. This piercing failure traverses the component as the projectile moves into it. A blunt impactor produces failures at the periphery of contact that form a plug ahead of the impactor. These two forms of perforation correspond to significant differences in ballistic limit. In addition plugging results in the removal of a significant mass from the target. This causes a significant change in the state of motion.

The projectile core fails primarily by brittle failure processes, i.e., the projectile core breaks because of the abrupt development of cracks under an essentially elastic state of stress. The number of cracks that occur and their location and direction cannot be precisely determined for an individual projectile, and they vary significantly from impact to impact. But there is a statistical consistency that can be correlated to the dynamic state of the projectile during impact. Thus, it is observed that breakup does not occur until critical impact conditions are achieved. When breakup does occur at first impact, the largest fragment of the core tends to be one-half the mass of the unbroken core.

Unyawed AP cores which impact aircraft components at normal incidence rarely shatter. However, yaw and obliquity induce bending stresses which do cause projectiles to breakup. Equations that predict breakup, estimate the ratio of the applied bending moment to the bending moment required to break the core.

Figure 6 is the phase diagram for a 0.30-caliber projectile and a 0.058-inch-thick, 2024-T4 aluminum-alloy target. The limit curve for projectile breakup during perforation is given by the critical angle defined by Equation 8 and which, for this system, is nearly 72 degrees.

$$\lambda_r = \frac{16^* V_{bl}^2 \sin \beta}{\pi C_2 g \sigma_c d_c^3 \cos \theta} \quad (8)$$

For all conditions above the ballistic limit and to the left of this line, the projectile perforates intact. For conditions above the ballistic limit and to the right of this line, the projectile perforates but is broken. Below the ballistic limit a crescent-shaped region represent conditions for which the projectile recochets and is broken. Everywhere else below the ballistic limit the projectile ricochets intact.

References

1. Bernard, R. S. and D. C. Creighton, "Projectile Penetration in Earth Material: Theory and Computer Analysis." Defense Nuclear Agency, Washington, D.C., Nov 1976. (Contract Report S-76-13).
2. Schulz, J. C., "Finite Element Analysis of a Kinetic Energy Warhead Penetrating Concrete," in Proceedings of the 4th International Symposium on Ballistics, Monterey, California, October 1978. Washington, D.C., American Defense Preparedness Association, 1978.
3. Backman, M. and S. Finnegan, "The Propagation of Adiabatic Shear," in Metallurgical Effects at High Strain Rates, edited by Rohde, et al, Plenum Press, NY, 1974.
4. Ipson, T. and R. F. Recht, "Ballistic-Penetration Resistance and Its Measurement," Experimental Mechanics, Vol. 15, No. 7, July 1975.
5. Backman, M. and W. Goldsmith, "The Mechanics of Penetration of Projectiles into Targets," Int J. Engng Sci, Vol. 16, pp. 1-99, 1978.
6. Naval Air Systems Command. "Penetration Equations Handbook for Kinetic Energy Penetrators," by the Joint Technical Coordinating Group for Munitions Effectiveness, Aerial Target Vulnerability Subgroup, Marvin E. Backman, Chairman. Washington, D.C., Report No. 61 JTCG/ME-77-16, November 1977.

RHEOLOGY VIA NONEQUILIBRIUM MOLECULAR DYNAMICS [1]

WILLIAM G. HOOVER

Department of Applied Science
University of California at Davis/Livermore
and Lawrence Livermore National Laboratory
Post Office Box 808, Livermore, California 94550

Abstract

The equilibrium molecular dynamics formulated by Newton, Lagrange, and Hamilton has been modified in order to simulate rheological molecular flows with fast computers. This modified "Nonequilibrium Molecular Dynamics" (NEMD) has been applied to fluid and solid deformations, under both homogeneous and shock conditions, as well as to the transport of heat. The irreversible heating associated with dissipation could be controlled by carrying out isothermal NEMD calculations. The new isothermal NEMD equations of motion are consistent with Gauss' 1829 "Least-Constraint" principle as well as certain microscopic equilibrium and nonequilibrium statistical formulations due to Gibbs and Boltzmann. Application of isothermal NEMD revealed high-frequency and high-strain-rate behavior for simple fluids which resembled the behavior of polymer solutions and melts at lower frequencies and strain rates. For solids NEMD produces plastic flows consistent with experimental observations at much lower strain rates. The new nonequilibrium methods also suggest novel formulations of thermodynamics in nonequilibrium systems and shed light on the failure of the "Principle of Material Frame Indifference."

Introduction

Newton's and Fourier's linear formulations of viscous flow and heat flow have long served as useful descriptions of monatomic simple-fluid behavior. At least for gases, the basic physics of these linear theories was well understood by the close of the 19th century. At that time, Boltzmann's transport equation, soon to be solved by Chapman and Enskog [2], gave a quantitative explanation of Newtonian gas viscosity and Fourier's heat conductivity.

For more complicated molecular or polymeric fluids, particularly lubricants, deviations from Newtonian viscous flow have been abundantly documented in the 20th century, since Boltzmann's day. Very recently, advances in computer technology have made it possible to simulate these deviations via nonequilibrium molecular dynamics (NEMD), reproducing nonlinear non-Newtonian effects observed experimentally. NEMD has even been able to show that non-Newtonian effects occur for the very simplest materials at high rates of strain.

Nonlinear problems, and their simulation using computers, are attracting attention in many places--Australia, Belgium, England, France, Holland, Italy, Japan, Russia, and the United States [3]. The main goal of this modern research is to make a quantitative connection between the microscopic interatomic and intermolecular force laws and observed macroscopic rheological laws.

Of course the many-body correlations present in dense fluids and solids are contained in the fundamental dynamical equations of Newton, Lagrange, and Hamilton. So why has it taken so long to apply these equations to rheological problems? Straightforward application is limited by computer hardware to relatively short (nanoseconds) and small (millimicrons) problems. These calculations are further complicated by small-system boundary effects and by the relatively large size of statistical fluctuations. It has taken time to develop methods circumventing these problems.

In the last decade, nonequilibrium molecular dynamics has begun to simulate steady homogeneous flows in the absence of physical boundaries. The NEMD methods, which are based on modifications of the equations of motion to include dynamical constraints, are beginning to be applied to polyatomic molecules of rheological interest. Here we describe results obtained so far for relatively simple central-force models. We forecast the possibilities for calculations in the next few years.

Because computational advances have outstripped theoretical ones, the theoretical side of nonlinear transport in dense fluids and solids is wide open. The effects found in relatively straightforward computer simulations deviate substantially from theoretical predictions. It is not clear why this is so or how the theory will come to terms with the new results [4]. In rheology it is taken for granted that material behavior can be nonanalytic. This assumption is less common in microscopic physics, but certainly is strongly suggested by some theoretical approaches and the new computer experiments.

Equilibrium Molecular Dynamics

Equilibrium molecular dynamics was developed by Alder, Rahman, Verlet, Vineyard, and their co-workers [5-8]. The main goals of molecular dynamics are (1) characterizing the approach to equilibrium, (2) characterizing equilibrium, and (3) characterizing reproducible nonequilibrium phenomena. In every case a correspondence must be established between the microscopic view of matter, based on Newton's, Lagrange's, or Hamilton's equations, and the phenomenological kinetic and constitutive equations of continuum mechanics. The microscopic laws are typified by Newton's "Equation of Motion":

$$m\ddot{q} = F . \quad (1)$$

The macroscopic analog, for a material with a pressure tensor P , a density ρ , and a stream velocity u , is the continuum "Equation of Motion"

$$\rho\dot{u} = -\nabla \cdot P . \quad (2)$$

Newton's microscopic equations are incomplete in the sense that the boundary conditions need to be specified in detail before nonequilibrium problems can be attacked. The macroscopic equations are likewise incomplete. The "Constitutive Relations" relating the pressure tensor, temperature, and heat flux to the strain-rate tensor and the temperature gradient, must be given to specify a well-posed problem. The constitutive relations are usually imagined to come from clever experiments. The ambition of a molecular-level theorist is to circumvent the laboratory and find the constitutive properties using microscopic equations of motion instead.

To link the microscopic and macroscopic points of view it is first necessary to formulate microscopic analogs of the continuum macroscopic variables: temperature, energy, the pressure tensor, and so on. The formulation of Irving and Kirkwood [9] is the usual basis for these definitions. Temperature, for instance, is related to the mean-squared velocity relative to the local stream velocity:

$$(3/2)kT = (1/2)m\langle(v-u)^2\rangle . \quad (3)$$

Trajectories governed by the equilibrium equations of motion (1) are easily generated. The early calculations [5-8] solved these coupled equations for up to several hundred particles, and successfully characterized the approach to equilibrium and the equilibrium equation of state. The linear transport coefficients were also obtained from the Green-Kubo linear response theory [10]. The equilibrium results--pressure and temperature as functions of energy and volume--agreed well with the Los Alamos Monte-Carlo estimates--pressure and energy as functions of volume and temperature--based on Gibbs' statistical mechanics [11-12].

The early thermodynamic results showed that deviations from the large-system thermodynamic limit can be as small as $1/N$ or $(\ln N)/N$, provided that periodic boundary conditions are used to eliminate surface effects [13]. Thus a reasonable equilibrium equation of state can be obtained with only 100 particles.

About ten years later in 1969, perturbation theories were developed [14] which made it possible to calculate, by using known hard-sphere functions, the equations of state for "simple fluids" with pairwise-additive forces. It became possible to generate complete phase diagrams for these simple fluids by perturbation theory, without further simulations. The equilibrium properties of simple fluids became a "mature" field.

The linear nonequilibrium properties are a remaining challenge. The straightforward nonequilibrium perturbation theory doesn't seem to converge [15], and the Green-Kubo calculations are both time-consuming and imprecise.

Evolution of Nonequilibrium Molecular Dynamics

To verify linear viscosities and conductivities, and to explore nonlinear transport, the equilibrium work had to be generalized. It was necessary to formulate boundary conditions, or altogether new equations of motion, to measure nonlinear effects: How does the viscosity vary with strain rate? How does thermal conductivity vary with temperature gradient? How are the momentum and heat currents coupled together? Dealing with the nonlinear problems was a two stage process. The first stage was to use special boundaries [16-17] or external fields [18] to maintain local temperatures or velocities. This work showed that experimental viscosities and conductivities could be reproduced, with uncertainties on the order of several percent, by several independent methods. The next stage was the development of more efficient calculational methods, to reduce the uncertainties, for application to nonlinear problems. The two major obstacles were (1) the relatively large influence of physical boundaries and (2) the nonsteady increases in temperature and pressure caused by irreversible heating. Both difficulties have been eliminated by using clever nonequilibrium schemes.

At first, moving physical boundaries were used to drive viscous shear and dilatational flows. These were later eliminated by using time-dependent periodic boundaries in conjunction with equations of motion which reproduced the desired macroscopic flow fields [19]. The simplest case is plane Couette flow, with the x component of stream velocity proportional to y. A "Doll's Tensor" Hamiltonian, formed by adding the microscopic velocity (p_x/m) to the stream velocity $\dot{\epsilon}y$, reproduces the macroscopic flow field and also generates new momentum-dependent Coriolis' forces:

$$H = H_0 + \dot{\epsilon} \sum y p_x ; H_0 = \Phi + \sum (p^2/2m) ; \quad (4)$$

$$\dot{x} = (p_x/m) + \dot{\epsilon}y ; \dot{y} = (p_y/m) ; \quad (5)$$

$$\dot{p}_x = F_x ; \dot{p}_y = F_y - \dot{\epsilon} p_x . \quad (6)$$

The set of Doll's-tensor equations of motion derived from (4) can be shown to reproduce identically the first law of thermodynamics for Couette flow:

$$\dot{E} \equiv - \dot{\epsilon} V P_{xy} , \quad (7)$$

where the energy E and the pressure-tensor component P_{xy} are the instantaneous values of fluctuating microscopic variables. The moving boundaries used in conjunction with these nonequilibrium equations of motion are identical to those of Lees and Edwards [16]. A variant of these boundaries, in which periodic images move toward the central periodic cell, can be used to simulate shockwaves [20].

Heat conduction could not be handled in such a straightforward way. To generate a heat current in a homogeneous periodic system an external force linear in the energy (pushing energy-rich particles to the right and energy-poor particles to the left) had to be developed [21]. Once this was done, both deformation and heat current could be simulated in small periodic systems.

What about the irreversible heating? This was a potentially serious problem, because large gradients are required in order to measure a statistically well-defined response. The heating leads to thermodynamic changes of state. In Ashurst's original calculations reservoir regions were maintained at constant temperatures by rescaling the velocity distribution, relative to its mean, to maintain a constant second moment. This same end can be achieved, more elegantly, by imposing a "nonholonomic" (i.e., involving velocities, not just coordinates) constraint on the motion:

$$(d/dt) \sum (p^2/2m) = 0 . \quad (8)$$

If the constraint is arbitrarily imposed by adding to each particle an acceleration proportional to its momentum:

$$\Delta \dot{\mathbf{p}} = -\zeta \mathbf{p} , \quad (9)$$

then the (time-dependent) friction coefficient ζ can be given as an explicit function of the interparticle forces and the momenta:

$$\zeta = \sum \mathbf{F} \cdot \mathbf{p} / \sum \mathbf{p} \cdot \mathbf{p} . \quad (10)$$

With both the artificial boundaries and the irreversible heating removed, it became possible to study steady nonlinear flows, with large gradients, for the long times necessary to obtain good statistics. The main unresolved question then was: would the computer calculations correspond to laboratory experiments?

Is NEMD Legitimate Physics?

Do the NEMD simulations correspond to physical reality? One way to approach this question is empirical. Calculations can be carried out with different constraints. For instance, constant temperature or constant energy or constant pressure constraints could be imposed on a system undergoing shear deformation. To the extent that the resulting shear stress is independent of the constraint type, it is at least plausible that the measured stress-strain rate relation is physically correct. Evans carried out such an investigation, comparing shear stresses under conditions of constant temperature and constant energy. The two simulations agreed within the relatively small shear stress fluctuations [22].

It is also possible to analyze some of the NEMD methods theoretically. The isothermal dynamics used by Ashurst, for instance, can be simply related to Gauss' variational principle of least constraint [23]. Gauss believed that the trajectory observed, in a constrained system, would be that which minimized the mean-squared change in the particle accelerations due to the constraints:

$$\sum m (\delta \ddot{\mathbf{q}})^2 = \text{minimum} . \quad (11)$$

If this minimization is carried out under the constraint of fixed kinetic energy then exactly Ashurst's velocity-rescaling scheme results. The same isothermal NEMD calculations can also be related to Gibbs' equilibrium ensemble studies [24]. Gibbs proved that the most likely distribution for a fixed-temperature fixed-volume system is one in which the state probability varies as $\exp(-E/kT)$. It is interesting that isochoric NEMD equations of motion which fix T , but allow E to vary, identically reproduce Gibbs' canonical distribution if that distribution is chosen initially.

It is also possible to connect NEMD with low-density nonequilibrium theory [25]. Boltzmann showed how to treat the collisional evolution of nonequilibrium systems by computing the single particle distribution function $f(q,p)$. In the case that the only nonvanishing component of the strain-rate tensor is $\dot{\epsilon} = du_x/dy$, Chapman and Cowling's results show [26] that the shear and normal stresses, for Maxwell molecules, are

$$\begin{aligned} P_{xy}V/NkT &= -\dot{\epsilon}\tau + O(\dot{\epsilon}\tau)^3 ; \\ P_{xx}V/NkT - 1 &= +(4/3)(\dot{\epsilon}\tau)^2 + O(\dot{\epsilon}\tau)^4 ; \\ P_{yy}V/NkT - 1 &= -(2/3)(\dot{\epsilon}\tau)^2 + O(\dot{\epsilon}\tau)^4 ; \\ P_{zz}V/NkT - 1 &= -(2/3)(\dot{\epsilon}\tau)^2 + O(\dot{\epsilon}\tau)^4 , \end{aligned} \quad (12)$$

where the "collision time" τ is of the order of the time between collisions. The system gradually heats up: $d\ln T/dt = (2/3)\dot{\epsilon}^2\tau$.

How must these results be modified if the isothermal NEMD restriction is imposed, so that temperature is fixed? This situation can be analyzed from the viewpoint of the relaxation-time model of the Boltzmann equation [10]:

$$(\partial f/\partial t) = -d(\dot{q}f)/dq - d(\dot{p}f)/dp + (f_0 - f)/\tau , \quad (13)$$

where f_0 is the local equilibrium distribution:

$$f_0 = (N/V)\exp(-p^2/2mkT)/(2\pi mkT)^{3/2} . \quad (14)$$

If f is expanded as a power series in the collision time, $f = f_0 + \tau f_1 + \tau^2 f_2 + \dots$ then the equations of motion,

$$\begin{aligned}
 \dot{x} &= (p_x/m) + \dot{\epsilon}y ; \\
 \dot{y} &= (p_y/m) ; \\
 \dot{z} &= (p_z/m) ; \\
 \dot{p}_x &= F_x - \dot{\epsilon}p_y - (\dot{\epsilon}^2 \tau/3)p_x ; \\
 \dot{p}_y &= F_y - (\dot{\epsilon}^2 \tau/3)p_y ; \\
 \dot{p}_z &= F_z - (\dot{\epsilon}^2 \tau/3)p_z ;
 \end{aligned} \tag{15}$$

are consistent with (13) if

$$\begin{aligned}
 f_1/f_0 &= -\dot{\epsilon}[p_x p_y / mkT] , \\
 f_2/f_0 &= \dot{\epsilon}^2 [(p_x p_y / mkT)^2 - (p_x^2 + 4p_y^2 + p_z^2) / 3mkT] + 1 .
 \end{aligned} \tag{16}$$

It is easily verified that this steady-state isothermal NEMD distribution function (16) reproduces the known exact pressure tensor (12).

Results so far Obtained from NEMD

The first NEMD results [16-18] established that computed linear viscosities and heat conductivities agreed with experiment. Work on the non-linear frequency and amplitude dependence of the transport coefficients can not so easily be compared with experiment because very high rates are involved. It is necessary that neighboring particles move at a non-negligible velocity, relative to the sound speed, in order for the small-system shear stress to exceed background fluctuations. It was therefore extremely interesting to find [27] that the solid-phase power-law dependence of stress on strain rate established in NEMD simulations at very high rates could be extrapolated, over four orders of magnitude in strain rate, to give satisfactory agreement with experimentally-measured plastic flows. The extrapolation and the experimental data are both somewhat uncertain, but the good agreement suggests an underlying simplicity in the flow mechanism over a wide range of rates.

Similar agreement will probably result for liquids. It has long been known that Maxwell's relaxation-time model of viscoelasticity is an oversimplification for large molecules. Lamb[28] has presented a corresponding states plot of the real and imaginary parts of the shear impedance as functions of frequency for a variety of large molecules. The frequency-dependent viscosity derived from these curves deviates substantially from the Maxwellian model, but resembles much more closely [4] corresponding calculations carried out by Evans [29] for a simple central-force model at much higher frequencies.

Hanley and Evans have considered the nonequilibrium thermodynamics of systems undergoing shear [30]. Analogs of the thermodynamic Maxwell relations, but involving the strain rate as an independent variable, were developed and checked numerically. This thermodynamic work made it possible to evaluate the shift in equilibrium phase diagrams induced by shear. With the development of this theory there is motivation to characterize phase-diagram shifts experimentally.

Finally the Principle of Material Frame Indifference, notoriously hard to test in laboratory experiments due to the high angular velocities involved, can readily be tested in computer experiments. These computer experiments established that high rotational speeds cause an angular heat flow in response to a radial temperature gradient, a violation of Fourier's law which is easily understood from the point of view of the Boltzmann equation [31].

What Lies Ahead?

Work in progress suggests that new results will emerge at an accelerating pace over the next few years. Groups working on larger molecules, butane [32] and decane [33], as well as platelike and rodlike molecules capable of undergoing smectic and nematic liquid-crystal phase transitions [34] should begin to assess the importance of molecular shape to rheological nonlinearities. Work is also in progress on the simulation of granular materials, a promising potential application of NEMD where a variety of interesting experimental data already exists [35]. The possibility of transverse displacement of periodic images, with a superimposed constant normal force, suggests that solid-phase coefficient of friction measurements could also be carried out.

The generalization of the results obtained so far to the more complicated molecular models should proceed smoothly. This should make possible a detailed comparison of microscopic simulations with the mesoscopic models developed by Bird and his Wisconsin coworkers [36] to describe polymeric systems. These latter models are already firmly linked to experiment, so that the end product of the developing NEMD techniques will be a detailed physical understanding of rheological flows.

References

1. This work was supported, at Davis, by the Army Research Office and Electric Power Research Institute and carried out, at LLNL, under the auspices of the Department of Energy, under contract W-7405-ENG-48 with the University of California. Conversations and correspondence with Denis Evans, Jim Dufty, Jim Haile, Tony Ladd, Tom Leete, Bill Moran, and Solveig Shearer were pertinent, stimulating, and helpful.
2. Brush, S. G., Kinetic Theory, Vols. I (1948), II (1966), III Pergamon Press (1972).
3. *Physica*, Proceedings of the NBS Conference on Nonlinear Fluid Phenomena, Boulder, Colorado, June 1982 (1983, to appear).
4. Zwanzig, R., *Kinam*, Recent developments in non equilibrium statistical mechanics, *Kinam* 3, pp. 5-13 (1981).
5. Alder, B. J.; Wainwright, T., Molecular Dynamics by Electronic Computers, Proceedings of the [Brussels, 1956] International Symposium on Transport Processes in Statistical Mechanics, pp. 97-131, Prigogine, I. (ed.), Interscience (1958).
6. Rahman, A., Correlations in the Motion of Atoms in Liquid Argon, *Phys. Rev.* 136, pp. A405-411 (1964).
7. Levesque, D.; Verlet, L.; Kurkijarvi, J., Computer "Experiments" on Classical Fluids, IV. Transport Properties and Time-Correlation Functions of the Lennard-Jones Liquid near Its Triple Point, *Phys. Rev. A* 7, pp. 1690-1700 (1973).
8. Erginsoy, C.; Vineyard, G. H.; Englert, A., Dynamics of Radiation Damage in a Body-Centered Cubic Lattice, *Phys. Rev.* 133, pp. A595-606 (1964).
9. Irving, J. H.; Kirkwood, J. G., The Statistical Mechanical Theory of Transport Processes. IV. The Equations of Hydrodynamics, *J. Chem. Phys.* 18, pp. 817-829 (1950).
10. McQuarrie, D. A., Statistical Mechanics, pp. 507- 509, Harper & Row (1976).
11. Metropolis, N.; Rosenbluth, A. W.; Rosenbluth, M. N.; Teller, A. H.; Teller, E., Equation of State Calculations by Fast Computing Machines, *J. Chem. Phys.* 21, pp. 1087-1092 (1953).
12. Wood, W. W., Monte Carlo Studies of Simple Liquid Models, Physics of Simple Liquids, pp. 114-230, Temperley, H. N. V.; Rowlinson, J. S.; Rushbrooke, G. S., (eds.), North-Holland (1968).
13. Hoover, W. G.; Alder, B. J., Studies in Molecular Dynamics. IV. The Pressure, Collision Rate, and Their Number Dependence for Hard Disks, *J. Chem. Phys.* 46, pp. 686-691 (1967).
14. Mansoori, G. A.; Canfield, F. B., Variational Approach to the Equilibrium Thermodynamic Properties of Simple Fluids I., *J. Chem. Phys.* 51, pp. 4958-4972 (1969).

15. Snook, I. K.; Watts, R. O. W., Perturbation theories in non-equilibrium statistical mechanics. I. Methods based on the time-displacement operator, II. Methods based on memory function formalism, *Mol. Phys.* 33, pp. 431-452 (1977).
16. Lees, A. W.; Edwards, S. F., The computer study of transport processes under extreme conditions, *J. Phys. C*, 5, pp. 1921-1929 (1972).
17. Ashurst, W. T., Dense Fluid Shear Viscosity and Thermal Conductivity Via Non-Equilibrium Molecular Dynamics, dissertation, 174 pages, UC Davis-Livermore, (1974); Hoover, W. G.; Ashurst, W. T., "Nonequilibrium Molecular Dynamics" Advances in Theoretical Chemistry, I, pp. 1-51 (1975)
18. Gosling, E. M.; McDonald, I. R.; Singer, K., On the calculation by molecular dynamics of the shear viscosity of a simple fluid, *Mol. Phys.* 26, pp. 1475-1484 (1973).
19. Hoover, W. G., Evans, D. J.; Hickman, R. B.; Ladd, A. J. C.; Ashurst, W. T.; Moran, B., Lennard-Jones triple-point bulk and shear viscosities, Green-Kubo theory, Hamiltonian mechanics, and nonequilibrium molecular dynamics, *Phys. Rev. A*, 22, pp. 1690-1697 (1980).
20. Holian, B. L.; Hoover, W. G.; Moran, B.; Straub, G. K., Shock-wave structure via nonequilibrium molecular dynamics and Navier-Stokes continuum mechanics, *Phys. Rev. A*, 22, pp. 2298-2808 (1980).
21. Evans, D. J., Homogeneous NEMD Algorithm for Thermal Conductivity: Application of Non-Canonical Linear Response Theory, *Phys. Lets. A* (to appear).
22. Evans, D. J., Computer Experiment for non-linear thermodynamics of Couette Flow, *J. Chem. Phys.* (to appear).
23. Gauss, K. F., Über ein neues allgemeines Grundgesetz der Mechanik, *Journal für die reine und angewandte Mathematik* ("Crelle's Journal"), Berlin, pp. 232-235 (1829).
24. Tolman, R. C., The Principles of Statistical Mechanics, Oxford University Press (1938).
25. I particularly thank Jim Dufty for educational conversations and correspondence illustrating the solution of the Boltzmann equation for various Couette-flow problems.
26. Chapman, S.; Cowling, T. G., The Mathematical Theory of Non-Uniform Gases, 3rd Ed., Cambridge University Press (1970).
27. Hoover, W. G.; Ladd, A. J. C.; Moran, B., High-Strain-Rate Plastic Flow via Nonequilibrium Molecular Dynamics, *Phys. Rev. Lets.* 48, pp. 1818-1820 (1982).
28. Lamb, J., Viscoelasticity and Lubrication: A Review of Liquid Properties, *J. Rheology*, 22, pp. 317-347 (1978).
29. Evans, D. J., Enhanced $t^{-3/2}$ Long-Time Tail for the Stress-Stress Time Correlation Function, *J. Stat. Phys.* 22, pp. 81-90 (1980); Nonlinear Viscous Flow in the Lennard-Jones Fluid, *Phys. Lets.* 74A, pp. 229-232 (1979).

30. Hanley, H. J. M.; Evans, D. J., A thermodynamics for a system under shear, *J. Chem. Phys.* 76, pp. 3225-3232 (1982).
31. Hoover, W. G.; Moran, B.; More, R. M.; Ladd, A. J. C., Heat conduction in a rotating disk via nonequilibrium molecular dynamics, *Phys. Rev. A*, 24, pp. 2109- 2115 (1981).
32. Bellemans, A.; Ryckaert, J. P. (Belgium).
33. Berendsen, H. J. C. (Holland).
34. Frenkel, D.; Eppenga, R., Monte Carlo Study of the Isotropic-Nematic Transition in a Fluid of Thin Hard Disks, *Phys. Rev. Lett.*, 49, pp. 1089-1092 (1982).
35. Jenkins, J. T.; Savage, S. B., The Mean Stress Resulting from Interparticle Collisions in a Rapid Granular Shear Flow, submitted to the Proceedings of the Fourth International Conference on Continuum Models of Discrete Systems (Stockholm 29 June-4 July 1981).
36. Bird, R. Byron, Kinetic Theory and Constitutive Equations for Polymeric Liquids, *J. Rheology*, 26, pp. 277-299 (1982),; *Polymer Kinetic Theories and Elongational Flows*, *Chem. Eng. Commun.*, 16, pp. 175-187 (1982).

Notes on Softening and Local Instability

Gilbert Strang

Department of Mathematics

M.I.T.

Cambridge, MA 02139

M. Abdel-Naby

Department of Mathematics

Ain Shams University

Cairo, Egypt

Summary

We discuss some of the consequences of a loss of monotonicity in the constitutive law. In penetration problems this occurs for adiabatic heating, and shear bands appear; they have been analyzed by Clifton, Needleman, Hutchinson, Bodner, and many others, and we mention a forthcoming paper of Merzer. In a different context we consider the model equation $u_t = (\sigma(u_x))_x$, and describe Höllig's construction of a family of solutions. Where $\sigma' < 0$ this is a backward heat equation, but the numerical calculations remain stable (convergence is not so clear); u_x jumps into neighboring regions where $\sigma' > 0$. We reproduce in a simple form the Brézis-Ekeland variational principle for the heat equation, and we follow Nohel in speculating on its convexification for a law that has a "softening range" $\sigma' < 0$.

1. Introduction.

For a linear equation $\text{div}(\sigma(\text{grad } u)) = f$, any failure of ellipticity will be disastrous. There is in general no solution to boundary value problems, and if we include a dynamic term u_{tt} , the initial value problem explodes instantly at $t = 0$. For nonlinear equations the situation can be entirely different. We may have a stress σ which is not monotonic over some range of strains $\text{grad } u$, and still a solution can exist. It is not so smooth as before, but both physically and mathematically it can be fascinating.

This loss of ellipticity was identified by Knowles and Sternberg [1] in the properties of the stored energy function for known hyperelastic materials; it led to elastostatic

shocks. It can be created in other ways--possibly by the growth of voids, or by phase transformations (see Slemrod on the van der Waals problem), or by corners in the plastic yield surface. In the applications to penetration mechanics, it appears as a region of rapid straining and is signalled by shear bands. There the thermal effects are decisive; it is adiabatic shear that produces the phenomenon, and Merzer [2] has been able to model it with sufficient accuracy to reproduce computationally what is observed experimentally: The width of the shear band is independent of the scale of the imperfection which touches off the process. There is dependence on thermal and strain-rate properties, and the region narrows with ongoing deformation--but the scale is controlled by diffusion of the heat produced locally (and suddenly).

Mathematically, these problems of local instability with global stability are not well understood. The analysis of shear banding is comparatively advanced, and was a part of the workshop presentations by Clifton and Needleman. We mention only one additional paper, by Gurtin and Temam [3], who speculate on the possible connection with the convexification process that we describe below. In one dimension, the simplest model comes from a scalar stress-strain law $\sigma = \sigma(u_x)$ which is not everywhere monotonic. In that case $\varphi(u_x)_x = f$ is partially elliptic, $u_{tt} = \varphi(u_x)_x$ is partially hyperbolic, and $u_t = \varphi(u_x)_x$ is a forward-backward heat equation. In one form, it is simply $u_t = u_{xx}$ for $|u_x| \geq 1$, $u_t = -u_{xx}$ for $|u_x| \leq 1$. The solution must exit instantaneously from the second alternative $u_t = -u_{xx}$ and enter the first.

It is the parabolic equation, less strongly motivated by the applications and therefore less familiar, that we discuss in this note. It appeared in an oceanographic problem of Wilander, circulated but apparently never published (and no longer current). The major part of the analysis has been done by and encouraged by John Nohel

at Wisconsin. Bona and Wahlbin contributed to a priori estimates which establish stability when the solution exists--for example they prove $|u_x| \leq \text{constant}$ --and recently Höllig constructed an infinite family of solutions [4]. Here we describe and simplify his construction, using a lemma on piecewise linear approximation with variable nodes, and we comment on numerical experiments at M.I.T. for Wilander's steady state problem (as distinct from Nohel's Cauchy problem). Finally we introduce the Brézis-Ekeland variational principles [5] for the heat equation, and mention its convexification and the appearance of the Maxwell line.

2. Höllig's solutions to the Cauchy problem.

The nonlinear heat equation $u_t = \varphi(u_x)_x$, with a smooth and strictly increasing φ and with Neumann condition $u_x = 0$ imposed at the boundaries $x = 0$ and $x = 1$, has a unique (and smooth) solution. Any discontinuities in the initial data f disappear for $t > 0$. This smoothing property seems to be lost already in the marginal case when φ is constant over some interval. And if there is "strain softening," so that $\varphi' < 0$ for a range of values of u_x , the regularity of the solution fails completely. It is only recently that a solution was shown to exist, and its slope can oscillate with arbitrarily high frequency between one stable region (where $\varphi'(u_x) > 0$) and another.

We describe the construction for a continuous piecewise linear φ , with $\varphi(s) = s$ for $s \leq 3/2$, $\varphi' = -1$ in the unstable region $3/2 < s < 5/2$, and $\varphi(s) = s + 2$ for $s \geq 5/2$. Höllig's inspiration was to split u into a sum $v + w$, with v reasonable and w_x oscillating between 0 and 2. The key step is to notice that

$$\varphi(v_x + w_x) = v_x \quad \text{if} \quad \left\{ \begin{array}{l} w_x = 0 \quad \text{for} \quad v_x \leq \frac{1}{2} \\ w_x = 0 \quad \text{or} \quad 2 \quad \text{for} \quad \frac{1}{2} \leq v_x \leq \frac{3}{2} \\ w_x = 2 \quad \text{for} \quad v_x \geq \frac{3}{2} \end{array} \right.$$

The stable regions of increasing φ are separated by the fixed distance 2, and w_x produces jumps back and forth. Therefore the equation $u_t = \varphi(u_x)_x$ becomes $v_t + w_t = v_{xx}$, a linear heat equation for v with inhomogeneous term $-w_t$. The initial condition $u(x,0) = f(x)$ is satisfied with $v = f$ and $w = 0$ at $x = 0$, and

$$v_x = f_x, w_x = 0 \quad \text{when} \quad f_x \leq 1 - \epsilon$$

$$v_x = 1, w_x = f_x - 1 \quad \text{when} \quad 1 - \epsilon \leq f_x \leq 1 + \epsilon$$

$$v_x = f_x - 2, w_x = 2 \quad \text{when} \quad f_x \geq 1 + \epsilon$$

Therefore the initial values of w_x are in the interval $[0,2]$, and the problem is to find for $t > 0$ a function $w(x,t)$ with the required properties: w_x is everywhere 0 or 2, w approaches $w(x,0)$ as $t \rightarrow 0$, and $|w_t| \leq \text{constant}$. This last condition assures that the inhomogeneous term $-w_t$ is acceptable in the equation for v .

There is a certain circularity in the definitions: v is determined by w , but in the conditions given above for $\varphi(v_x + w_x) = v_x$, w is constrained by v . For small times the two are not contradictory.

Our construction of w , with derivative alternating between 0 and 2, comes from the following lemma. We hope to determine whether it has an extension to x in \mathbb{R}^n , and to what degree it is new.

LEMMA. Given $h(0) = 0$ and $0 \leq h'(x) \leq 2$. There exists a continuous $w = w_\Delta(x)$ such that $w(0) = 0$, $w' = 0$ or 2 on each interval $k\Delta < x < (k+1)\Delta$, and $|h-w|_\infty \leq \Delta$.

The difference $h-w$ is monotonically increasing or monotonically decreasing in each interval, so if $|h(k\Delta) - w(k\Delta)| \leq \Delta$ at every endpoint $x = k\Delta$ the result is proved. This holds for $k = 0$; using induction, we assume it holds at $x = k\Delta$. Over the next interval, choose

$$|w_t| = \frac{|w(M)-w(B)|}{\Delta} \leq \frac{|w(M)-h((k+1)\Delta)|}{\Delta} + \frac{|w(B)-h((k+1)\Delta)|}{\Delta} \leq 3.$$

The third triangle has the vertices B, D, and E = ((k+2)\Delta, \Delta), with DE vertical, and the first argument applies again.

Since $|h-w_\Delta| \leq \Delta$, $w(x,t) \rightarrow h(x) = w(x,0)$ as $t \rightarrow 0$. This completes the construction. We emphasize that w is far from unique; rescaling t to αt , for example, gives a different solution for every $\alpha > 0$. The outstanding problem is to determine whether one particular solution is distinguished above the others. It is comparable to the family of weak solutions to a nonlinear hyperbolic conservation law, where entropy determines the unique choice which is physically correct. In that case finite difference approximations are a guide to the distinguished solution, and we anticipate a similar possibility for $u_t = \varphi(u_x)_x$.

3. The steady-state problem.

The original oceanographic application, described to the authors by Lou Howard, involved inhomogeneous boundary conditions and a solution that did not decay. Instead it converges (in numerical experiments) to a steady state. The unusual property in our partly unstable case is that this final state varies with the initial condition $u(x,0)$.

For the ordinary heat equation $u_t = u_{xx}$, with $u = 0$ at $x = 0$ and $u = s$ at $x = 1$, the only steady state is the linear function $u(x,\infty) = sx$. It comes directly from the time-independent equation $u_{xx} = 0$. A similar result holds for a monotonic φ : there is a unique solution $u = sx$ to

$$\varphi(u_x)_x = 0 \quad \text{with} \quad u(0) = 0, \quad u(1) = s.$$

It is the limit of $u(x,t)$ as $t \rightarrow \infty$, regardless of $u(x,0)$. For a φ which is not monotonically increasing, and for a choice of s at which $\varphi'(s) < 0$, the situation is completely changed. A first integral of the equation is still $\varphi(u_x) = \text{constant}$, but in a typical case there are three slopes $s < s_\circ < s$, which share the same value of φ :

$$w' = \begin{cases} 0 & \text{if } h((k+1)\Delta) \leq w(k\Delta) + \Delta \\ 2 & \text{if } h((k+1)\Delta) > w(k\Delta) + \Delta. \end{cases}$$

In the first case $w((k+1)\Delta) = w(k\Delta)$ satisfies, since $h' \geq 0$,

$$\Delta \geq h((k+1)\Delta) - w((k+1)\Delta) \geq h(k\Delta) - w(k\Delta) \geq -\Delta.$$

In the second case, $w((k+1)\Delta) = w(k\Delta) + 2\Delta$ satisfies, since $h' \leq 2$,

$$\begin{aligned} \Delta &\geq (h(k\Delta)+2\Delta) - (w(k\Delta)+2\Delta) \geq h((k+1)\Delta) - w((k+1)\Delta) \\ &> (w(k\Delta)+\Delta) - (w(k\Delta)+2\Delta) = -\Delta. \end{aligned}$$

Thus $|h-w| \leq \Delta$ at $x = (k+1)\Delta$ and the induction is complete.

CONSTRUCTION OF $w(x,t)$.

The function w will be piecewise linear on triangles that have vertices at $x = k\Delta$, $t = \Delta$; we use the sequence of times $\Delta = 2^{-n}$. At each time level the lemma produces (choosing h to be the initial value $w(x,0)$) a piecewise linear function of x . This function has $w_x = 0$ or $w_x = 2$ on an interval which is the horizontal edge of a triangle in the x - t plane. Therefore $w = a + bt$ or $w = a + 2x + bt$ inside this triangle, and we shall show that $|w_t| = |b| \leq 3$.

There are triangles of three types, fitting into a typical rectangle bounded by $t = \Delta$, $t = 2\Delta$, $x = k\Delta$, and $x = (k+2)\Delta$, k even. One triangle has vertices at $A = (k\Delta, \Delta)$, $B = ((k+1)\Delta, \Delta)$, and $C = (k\Delta, 2\Delta)$. In this case the edge AB is horizontal and AC is vertical; the time derivative is the quotient

$$|w_t| = \frac{|w(C)-w(A)|}{\Delta} \leq \frac{|w_{2\Delta}(k\Delta)-h(k\Delta)|}{\Delta} + \frac{|w_{\Delta}(k\Delta)-h(k\Delta)|}{\Delta} \leq 3.$$

The bound is 2 at $t = 2\Delta$, and 1 at $t = \Delta$. The second triangle has the same vertices B and C , together with $D = ((k+2)\Delta, 2\Delta)$. Now the edge CD is horizontal, centered at the point $M = ((k+1)\Delta, 2\Delta)$ above B . Therefore w_t is the vertical difference quotient

$$\varphi(s_-) = \varphi(s_0) = \varphi(s_+) \quad \text{with} \quad \varphi'(s_-) > 0, \varphi'(s_0) < 0, \varphi'(s_+) > 0.$$

(We imagine that φ has only one interval in which $\varphi' < 0$, so that a horizontal line intersects the graph of φ in at most three points.) Therefore the possible steady states include all piecewise linear functions which satisfy the boundary conditions and possess slopes that alternate among these three candidates. We emphasize that the points of alternation are unknown, as is the common (constant) value of φ . The only direct constraints, insufficient to determine $u(x, \infty)$, are the boundary conditions.

There is one additional constraint. We do not expect the steady state to possess, over any finite interval, a slope like s_0 which lies in the unstable range $\varphi'(s_0) < 0$. For the most natural finite difference analogue, the explicit equation

$$\frac{u_i^{n+1} - u_i^n}{\Delta t} = \frac{1}{h} \left[\varphi\left(\frac{u_{i+1}^n - u_i^n}{h}\right) - \varphi\left(\frac{u_i^n - u_{i-1}^n}{h}\right) \right],$$

the corresponding property can be expressed in the language of linear algebra. With boundary conditions $u_0^n = 0$ and $u_{N+1}^n = s$, where $(N+1)h = 1$, this equation represents an iteration toward the solution of the N simultaneous nonlinear equations

$$\varphi\left(\frac{u_{i+1}^\infty - u_i^\infty}{h}\right) - \varphi\left(\frac{u_i^\infty - u_{i-1}^\infty}{h}\right) = 0, \quad u_0^\infty = 0, \quad u_{N+1}^\infty = s.$$

This system describes the discrete steady state. As in the continuous case its solution is not unique. It is no surprise that the limit u^∞ depends on the initial value u^0 ; for any discrete system in which some solutions are "points of attraction," each initial condition sufficiently close to one of these points will be pulled in as $n \rightarrow \infty$.

Again we emphasize the large number of solutions: The slopes $s_i = (u_{i+1}^\infty - u_i^\infty)/h$ may alternate as before between three values of s_i , with $\sum s_i = (N+1)s$ as the only direct constraint. In this case we set $\alpha_i = \varphi'(s_i)$, and confirm the additional constraint noted earlier; no unstable value

$\alpha_i < 0$ can appear in the computed steady state. In other words, the only points of attraction are those which combine slopes at which $\alpha_i > 0$. The test is to examine the Jacobian matrix of the function

$$F(u) = u + \frac{\Delta t}{h^2} \left[\varphi\left(\frac{u_{i+1}-u_i}{h}\right) - \varphi\left(\frac{u_i-u_{i-1}}{h}\right) \right]$$

whose iteration $u^{n+1} = F(u^n)$ is the difference equation. The Jacobian of F is tridiagonal:

$$J = I + \frac{\Delta t}{h^2} \begin{bmatrix} & & & & & \\ & & & & & \\ & & \alpha_i & & & \\ & & & -\alpha_i - \alpha_{i+1} & & \\ & & & & & \\ & & & & & \alpha_{i+1} \end{bmatrix}$$

If the eigenvalues of J satisfy $|\lambda_j| < 1$ at a fixed point of F , it is a point of attraction; if some $|\lambda_j| > 1$, the point is inadmissible as a steady state. (The fixed point equation $F(u) = u$ coincides with the steady state equation.)

If all $\alpha_i > 0$, the matrix displayed above is negative definite--it is diagonally dominant with negative diagonal--so the eigenvalues of J are below 1. With the stability condition $2\Delta t \alpha_{\max}/h^2 < 1$, Gerschgorin's theorem shows that the displayed matrix has eigenvalues greater than -2 . Then J has $\lambda_j > -1$, so that all $|\lambda_j| < 1$ and the fixed point is attractive.

In the case of Höllig's φ , piecewise linear with stable slopes $\alpha = +1$ and unstable slopes $\alpha = -1$, the argument is easy to reverse: If any α_i in J equals -1 , the displayed matrix has at least one diagonal entry $-\alpha_i - \alpha_{i+1} \geq 0$, and cannot be negative definite (or even semidefinite, since the off-diagonal entries are nonzero). Therefore J has some eigenvalue $\lambda_j > 1$, and the fixed point is repulsive.

The fact of convergence to some steady state, under the usual stability bound on $\Delta t/h^2$, is the one significant result of our numerical experiments. The alternatives do not seem to occur. However the computations have not been sufficiently accurate to decide the behavior as $h \rightarrow 0$. The same difficulty has been met

in the Wisconsin experiments on the Cauchy problem; for fixed $h = \Delta x$, and for sufficiently small Δt , the difference equations are stable. But convergence to a solution of the continuous problem (or in our case to a steady state) is not yet established, either theoretically or experimentally.

4. A variational principle for the heat equation, and convexification.

A true minimum principle leading to the heat equation was an open question for many years. It is not well known that an answer has been found [5]. The statement is very direct, minimizing a quadratic over all functions $v(x,t)$ which satisfy the initial conditions. We begin by deriving the corresponding principle for an ordinary differential equation $u_t + Au = 0$, where A is a positive definite symmetric matrix and $A^{1/2}$ is its positive definite symmetric square root. For any $v(t)$, the Schwarz inequality applied to the inner product $(v, -v_t) = (A^{1/2}v, -A^{-1/2}v_t)$ yields

$$\begin{aligned} \int_0^T (v, -v_t) dt &\leq \int_0^T |A^{1/2}v| |A^{-1/2}v_t| dt \\ &\leq \int_0^T \left(\frac{|A^{1/2}v|^2}{2} + \frac{|A^{-1/2}v_t|^2}{2} \right) dt. \end{aligned}$$

The integral on the left is $\frac{1}{2}|v(0)|^2 - \frac{1}{2}|v(T)|^2$. The squares on the right are the inner products (v, Av) and $(v_t, A^{-1}v_t)$. Therefore every vector function $v(t)$ satisfies the inequality

$$|v(0)|^2 \leq |v(T)|^2 + \int_0^T [(v, Av) + (v_t, A^{-1}v_t)] dt = J(v).$$

This suggests a minimum principle for $u_t + Au = 0$: The true solution $u(t)$ is the function which minimizes $J(v)$ over all candidates with the correct initial condition $v(0) = u_0$. The left side has the fixed value $|u_0|^2$, and we have only to show that equality holds-- $J(v)$ attains its minimum value $|u_0|^2$ --at the solution $v = u$. But for this choice (u, Au) equals $(u, -u_t)$, and so does $(u_t, A^{-1}u_t)$; substituting $-2(u, u_t)$ into the integral, the inequality becomes an equation.

In other words, equality holds in the Schwartz and arithmetic-geometric mean inequalities only when $A^{1/2}v = -A^{-1/2}v_t$. This is the same as $v_t + Av = 0$, so v must solve the given equation.

For the heat equation $u_t = u_{xx}$, A is the positive definite operator $-\partial^2/\partial x^2$ and the same argument applies. Formally, $A^{1/2}$ is $i\partial/\partial x$ and $A^{-1/2}$ is its inverse--an integration with respect to x , in which the constant of integration is chosen to satisfy the boundary conditions. With boundary conditions $v(0,t) = v(1,t) = 0$ and initial condition $v = u_0(x)$, the inequality becomes

$$\int_0^1 u_0^2 dx \leq \int_0^1 v(x,T)^2 dx + \int_0^T \int_0^1 [v_x(x,t)^2 + (\int_0^x -v_t dx + c)^2] dx dt = J(v).$$

Again equality holds and J attains its minimum at the true solution u . We note the exceptional features of J : the terminal values $v(T)$ appear, as well as the indefinite integral of v_t .

The principle extends beyond linear equations; A can be the subdifferential ∂C of a convex function $C(u)$. This wider framework includes our nonlinear problem $u_t = \varphi(u_x)_x$ provided φ is monotonic. In that case

$$C(u) = \int_0^1 \mathfrak{F}(u_x) dx \quad \text{with} \quad \mathfrak{F}(s) = \int_0^s \varphi(y) dy,$$

which reduces in the linear case back to

$$C(u) = \int_0^1 \frac{1}{2} u_x^2 dx \quad \text{with} \quad \mathfrak{F}(s) = \int_0^s y dy = \frac{s^2}{2}.$$

The integrand in J is $C(v) + C^*(-v_t)$, no longer quadratic when A is no longer linear. C^* is the conjugate function to C ; it is the smallest function to satisfy the Young-Fenchel inequality

$$(v, -v_t) \leq C(v) + C^*(-v_t).$$

With this as replacement for the Schwartz inequality, the minimum principle follows as before.

Finally we come to the case in which φ is not monotonic;

softening and local instabilities may be present. We can construct its integral Φ as before; it will be nonconvex, $\Phi'' < 0$, in each interval where $\varphi' < 0$. If convexification were justified, Φ would be replaced by the largest convex function Φ_c not exceeding Φ . Where the two agree, their derivative is φ . Where they disagree, Φ_c is linear and its derivative φ_c is constant. In order that $\Phi = \Phi_c$ at the ends of this interval of disagreement, the graph of φ must have equal areas above and below the horizontal line $\varphi_c = \text{constant}$. This is the "Maxwell line."

Unfortunately, this convexification of the problem remains a mystery. It may seem improbable that it can ever be reasonable to replace a nonconvex energy J by a different (and convex) J_c , and then minimize J by minimizing J_c . Nevertheless it succeeds in the elliptic case. If our functional J were simply $C(v)$, without the integration over $0 \leq t \leq T$ and the additional term $\frac{1}{2}|v(T)|^2$, then minimizing sequences for J are also minimizing for J_c --and in the latter problem the minimum is actually attained. This possibility is illustrated in [5] and [6], and it is the foundation of our work with Robert Kohn on optimal design. Roughly speaking, the minimizing v have derivatives v_x which stay in the range where $\Phi = \Phi_c$; v_x jumps back and forth so as to avoid the unstable interval.

It is this rapid oscillation which may in the elliptic case have a connection with shear bands. And although Höllig observes that it cannot in the parabolic case produce a genuine solution, the suspicion (or even conviction) remains that it may still be a key to the resolution of local instabilities.

Acknowledgement

The research of the first author was supported by NSF contract MCS 81-02371 and ARO contract DAAG 29-80-K0033.

References

1. Knowles, J. K., and Sternberg, E.: On the failure of ellipticity of the equations for finite elastostatic plane strain. Arch. Rat. Mech. Anal. 63 (1977) 321-336.
2. Merzer, A. M.: Modelling of adiabatic shear band development from small imperfections. J. Mech. Phys. Solids, to appear.
3. Gurtin, M. E., and Temam, R.: On the anti-plane shear problem in finite elasticity. J. Elasticity 11 (1981) 197-206.
4. Höllig, K.: Existence of infinitely many solutions for a forward backward heat equation. Trans. Amer. Math. Soc., to appear.
5. Brézis, H., and Ekeland, I.: Un principe variationnel associé à certaines équations paraboliques. Comptes Rendus Acad. Sc. Paris 282 (1976) 971-974.
6. Ekeland, I., and Temam, R.: Convex Analysis and Variational Problems. Amsterdam: North-Holland 1976.

COMMENTS ON SOME PROBLEMS IN COMPUTATIONAL PENETRATION MECHANICS

J. T. ODEN

Texas Institute for Computational Mechanics
ASE/EM Department
University of Texas at Austin

Summary

Three problem areas in the computer simulation of large-scale penetration mechanics problems are discussed briefly in this note: numerical instabilities due to incomplete integration of the momentum or continuity equations, constitutive modelling, and friction affects.

Introductory Comments

Among the many difficulties encountered in the computer simulation of highly-non-linear thermomechanical phenomena characteristic of projectile penetration problems, we comment on three here which have a significant influence on computed results. First, we consider the problem of numerical instabilities encountered in finite-element approximations of the momentum and/or continuity equations of continuum mechanics. While low-order element models have proved to be reasonably adequate for modelling many gross kinematical features of the response in impact and penetration problems, they are frequently too crude to capture many important details. This has led to the use of higher-order elements. However, a significant increase in computing time is needed when such higher-order elements are used. To off set this loss in computing efficiency, it is now common practice to under-integrate various terms in the equations of motion. In the present paper, we comment on this practice and, by confining our attention to only linear static cases, show that it can lead to serious numerical instabilities.

Second, and perhaps the most difficult area in penetration mechanics, is the problem of developing appropriate constitutive equations for nonlinear materials. Our comments here on this issue are brief and somewhat superficial, but indicate some directions in which fruitful research might be taken. The point of these comments is that in constitutive theories in which Helmholtz energy potentials and internal variables are used to describe thermo-elasto-plasticity and possibly strain-rate effects, the usual assumptions of convexity and differentiability of these potentials are not generally valid.

Finally, we comment on friction laws used in many penetration simulators. Classical friction models are generally inadequate and can have a significant influence on computed results. Some more general, non-classical models of dry friction are described.

Model Problems in Elastostatics

While many of the numerical instabilities mentioned earlier are experienced in highly nonlinear applications, it suffices to consider only problems in linear elastostatics in order to identify some major deficiencies in the finite-element modelling procedures. Consider, then, a linearly elastic body Ω subjected to body forces \underline{f} and surface tractions \underline{t} on a portion Γ_F of its boundary. The principle of virtual work asserts that the body is in equilibrium whenever the actual displacement field \underline{u} satisfies

$$\int_{\Omega} E^{ijkl} u_{k,\ell} v_{i,j} dx = f(\underline{v})$$

*for all admissible virtual
displacements \underline{v} in V*

(1)

where standard index notations are used, E^{ijkl} are the elastic constants of the material, and f is the virtual work done by the external forces:

$$f(\underline{v}) = \int_{\Omega} \underline{f} \cdot \underline{v} dx + \int_{\Gamma_F} \underline{t} \cdot \underline{v} ds$$
(2)

($dx = dx_1 dx_2 dx_3 =$ volume element; $ds =$ surface area element). In (1), V is the space of admissible displacements, defined by

$$V = \{ \underline{v} = (v_1, v_2, v_3) = \text{kinematically admissible displacement}; \\ \|\underline{v}\|_V < \infty, \underline{v} = \underline{0} \text{ on } \Gamma_D \}$$
(3)

where $\|\cdot\|_V$ is, for instance, the energy norm,

$$\|\underline{v}\|_V^2 = \int_{\Omega} v_{i,j} v_{i,j} dx$$
(4)

and Γ_D is the portion of the boundary on which displacements are prescribed. If the stress and strain are, as usual, given by

$$\sigma_{ij}(\underline{u}) = E^{ijkl} u_{k,\ell}, \quad \epsilon_{ij}(\underline{v}) = \frac{1}{2}(v_{i,j} + v_{j,i})$$
(5)

then the internal virtual work is defined by the symmetric bilinear form

$$a(\underline{u}, \underline{v}) = \int_{\Omega} \sigma_{ij}(\underline{u}) \epsilon_{ij}(\underline{v}) dx$$
(6)

Then the equilibrium problem (1) can be put in the form,

Find \underline{u} in V such that

$$a(\underline{u}, \underline{v}) = f(\underline{v}) \quad \text{for all } \underline{v} \text{ in } V$$
(7)

If, instead of (7), we deal with a constrained equilibrium problem such as is encountered in the study of incompressible elastic materials, then, for example, (7) is replaced by

Find \underline{u} in K such that

$$a(\underline{u}, \underline{v}) = f(\underline{v}) \quad \text{for all } \underline{v} \text{ in } K \quad (8)$$

where K is the constraint set

$$K = \{ \underline{v} = \text{admissible displacement} \mid \text{div } \underline{v} = 0 \text{ in } \Omega \} . \quad (9)$$

Then it is customary to introduce the hydrostatic pressure p as a Lagrange multiplier and to solve the saddle point problem,

Find a displacement field \underline{u} in V and a hydrostatic pressure p in a space Q of admissible pressures such that

$$\begin{aligned} a(\underline{u}, \underline{v}) - (p, \text{div } \underline{v}) &= f(\underline{v}) , \\ (q, \text{div } \underline{u}) &= 0 \end{aligned} \quad (10)$$

for all \underline{v} in V and all q in Q ,

where (\cdot, \cdot) is the $L^2(\Omega)$ -inner product,

$$(q, \text{div } \underline{u}) = \int_{\Omega} q \text{ div } \underline{u} \, dx . \quad (11)$$

There are three key operators associated with problem (10); A , B , and B^* :

$$\left. \begin{aligned} \langle A\underline{u}, \underline{v} \rangle &\equiv a(\underline{u}, \underline{v}); \quad A : V \rightarrow V' \\ [q, B\underline{u}] &\equiv (q, \text{div } \underline{u}) = \langle B^*q, \underline{u} \rangle = - \int_{\Omega} \nabla q \cdot \underline{u} \, dx \end{aligned} \right\} \quad (12)$$

Here V' is the dual of V and $\langle \cdot, \cdot \rangle$ and $[\cdot, \cdot]$ denote duality pairing on $V' \times V$ and $Q' \times Q$, respectively. Formally, A is the "elasticity operator"

$$A\underline{u} = - \frac{\partial}{\partial x_j} E^{ijkl} \frac{\partial u_k}{\partial x_l} \quad (+ \text{ boundary conditions}),$$

B is the constraint operator,

$$B\underline{u} = \text{divergence } \underline{u} + \text{boundary conditions}$$

and B^* is its transpose,

$$B^*q = -\text{gradient } q + \text{boundary conditions}.$$

The null spaces of these operators are:

$$\begin{aligned} \ker A &= \{ \tilde{v} \text{ in } V \mid \tilde{v} = \text{a rigid motion of the body} \} \\ \ker B &= \{ \tilde{v} \text{ in } Q \mid [q, \operatorname{div} \tilde{v}] = 0 \text{ for all } q \text{ in } Q' \} \\ \ker B^* &= \{ q \text{ in } Q' \mid \langle \tilde{B}^* q, \tilde{v} \rangle = 0 \text{ for all admissible displacements } \tilde{v} \text{ in } V \}. \end{aligned}$$

The norm on V , we recall, is given by (4) whereas the norm on Q is the usual least-squares norm $\|q\|_Q^2 = (q, q)_Q = \int_{\Omega} q^2 dx$. If we eliminate rigid motions in V and constant pressures in Q , then it is meaningful to work with spaces "modulo rigid motions" and "modulo constant pressures," in which case one uses the quotient space norms,

$$\|\tilde{v}\|_{V/\ker A} \text{ and } \|q\|_{Q/\ker B^*}. \quad (13)$$

Now it is well known (see, e.g. Oden and Reddy [1]), that a *unique solution to the constrained elasticity problem (10) exists* [unique in displacements up to within an arbitrary rigid motion and unique in pressures up to within an arbitrary constant pressure] *if the following conditions hold:*

1. The bilinear virtual work form $a(\cdot, \cdot)$ is continuous on the space V of admissible displacements
2. The bilinear virtual work form $a(\cdot, \cdot)$ is elliptic on $\ker A$; i.e. there exists a constant $\alpha > 0$ such that

$$a(\tilde{v}, \tilde{v}) \geq \alpha \|\tilde{v}\|_{V/\ker A}^2 \text{ for all } \tilde{v} \text{ in } V \quad (14)$$

3. The LBB condition (see Oden and Kikuchi [2]) is satisfied; i.e., there exists a constant $\beta > 0$ such that

$$\beta \|q\|_{Q/\ker B^*} \leq \sup_{\tilde{v} \text{ in } V} \frac{(q, \operatorname{div} \tilde{v})}{\|\tilde{v}\|_V} \quad (15)$$

for all admissible hydrostatic pressures q in Q .

Generalizations of such results to nonlinear problems in mechanics have been developed by Oden [3] and Le Tallec and Oden [4].

Finite Element Approximations

In a very formal way, finite element approximations of problems such as (10) are developed by

1. partitioning Ω into a finite element mesh Ω_h the coarseness of which is defined by the mesh parameter $h = \max_e h_e$, $h_e =$ diameter of element e . $1 \leq e \leq E$
2. constructing finite dimensional subspaces

$$V^h \subset V \text{ and } Q^h \subset Q$$

by developing piecewise polynomial approximations \underline{v}_h and q_h of the admissible fields \underline{v} and q on Ω_h .

3. Seeking a discrete admissible displacement field \underline{u}_h in V^h and a discrete hydrostatic pressure field p_h in Q^h such that

$$\begin{aligned} a(\underline{u}_h, \underline{v}_h) - (p_h, \operatorname{div} \underline{v}_h) &= f(\underline{v}_h), \\ (q_h, \operatorname{div} \underline{u}_h) &= 0, \end{aligned} \quad (16)$$

for all \underline{v}_h in V^h and all q_h in Q^h .

Further details and a complete analysis of convergence characteristics of the method (16) can be found in the text of Oden and Carey [5]; for an introductory account, see the book of Becker, Carey, and Oden [6].

Reduced Integration

Unfortunately, the system (16) is rarely used in practical finite element computations. The virtual work terms such as $a(\underline{u}_h, \underline{v}_h)$ and $(p_h, \operatorname{div} \underline{v}_h)$ are evaluated using numerical quadrature rules such as Gaussian quadrature, and instead of (16) we are led to the problem,

Find \underline{u}_h in V^h and p_h in Q^h such that

$$I(\underline{u}_h, \underline{v}_h) - J(p_h, \operatorname{div} \underline{v}_h) = f(\underline{v}_h), \quad (17)$$

$$J(q_h, \operatorname{div} \underline{u}_h) = 0,$$

for all \underline{v}_h in V^h and q_h in Q^h ,

where $I(\cdot)$ and $J(\cdot)$ are approximate integration rules of the type

$$I(f) = \sum_{e=1}^E \sum_{j=1}^G w_j^e f(\xi_j^e) \quad (18)$$

etc., wherein w_j^e = quadrature weights and ξ_j^e = quadrature points for element e in the finite element mesh. Remarkable as it may seem, devices such as this are used in virtually every large-scale nonlinear finite element code so as to reduce the number of operations and increase efficiency in the solution process. In fact, the use of "reduced integration" wherein a quadrature rule is selected of an order lower than that required to integrate the above forms exactly is employed routinely in finite element analysis with the result of substantial savings in computing time. In this case, we have, instead of (12) the approximate operators,

$$\left. \begin{aligned} \langle A_h u_h, v_h \rangle &\equiv I(u_h, v_h); \quad A_h : V^h \rightarrow V^h \\ [q_h, B_h v_h] &= \langle B_h^* q_h, v_h \rangle \equiv J(q_h \operatorname{div} v_h) \\ &\quad B_h : V^h \rightarrow Q^h \end{aligned} \right\} \quad (19)$$

with corresponding kernels, in analogy with those for the operators A , B , and B^* defined earlier, given by

$$\left. \begin{aligned} \ker A_h &= \{v_h \text{ in } V^h \mid I(u_h, v_h) = 0 \text{ for all } u_h\} \\ \ker B_h &= \{v_h \text{ in } V^h \mid J(q_h \operatorname{div} v_h) = 0 \text{ for all } q_h\} \\ \ker B_h^* &= \{q_h \text{ in } Q^h \mid J(q_h \operatorname{div} v_h) = 0 \text{ for all } v_h\} \end{aligned} \right\} \quad (20)$$

Returning to the conditions listed earlier for the existence of unique solutions to the continuous problem, we see that, to within arbitrary elements in $\ker A_h$ and $\ker B_h^*$, a unique solution u_h in V^h and p_h in Q^h , to the discrete equilibrium problem (17) exists whenever

1. There exists a constant $\alpha_h > 0$ (possibly depending on the mesh parameter h) such that

$$I(v_h, v_h) \geq \alpha_h \|v_h\|_{V/\ker A_h}^2 \quad (21)$$

for all v_h in V^h [recall (14)].

2. A discrete LBB condition is satisfied; i.e. there exists a constant $\beta_h > 0$ (possibly dependent on the mesh parameter h) such that

$$\beta_h \|q_h\|_{Q/\ker B_h^*} \leq \sup_{v_h \text{ in } V^h} \frac{J(q_h \operatorname{div} v_h)}{\|v_h\|_V} \quad (22)$$

for all q_h in Q^h [recall (15)].

Instabilities, Hourglassing, Checkerboards

The variational crime used in constructing the finite element approximation leads to significant numerical difficulties:

1. In general,

$$\ker A_h \not\subset \ker A \quad \text{and} \quad \ker B_h^* \not\subset \ker B^*$$

Indeed, $\ker A_h$ not only contains rigid motions but also spurious kinematic modes

known in the numerical analysis literature as "hourglassing," or "chickenwiring" also; $\ker B_h^*$ may not only include constant hydrostatic pressures but the spurious "checkerboard" patterns often seen in pressure calculations. The history of hourglassing effects and a discussion of various numerical devices used to combat them in hydrodynamic codes can be found in the recent paper of Flanagan and Belytschko [7]. These are illustrated in Fig. 1.

2. In general, the key stability parameters α_h and β_h introduced in (21) and (22) will depend upon the mesh size h . It is conjectured that the error in finite element approximations of the type (17) behaves like

$$\begin{aligned} \|\tilde{u} - u_h\|_V &\leq \frac{C}{\alpha_h \beta_h} E(h) \\ \|\tilde{p} - p_h\|_Q &\leq \frac{C}{\alpha_h \beta_h^2} E(h) \end{aligned} \quad (23)$$

where C is a generic constant and $E(h)$ is the so-called interpolation error. One then generally observes oscillations in the approximations \tilde{u}_h and p_h which increases in magnitude as the mesh is refined.

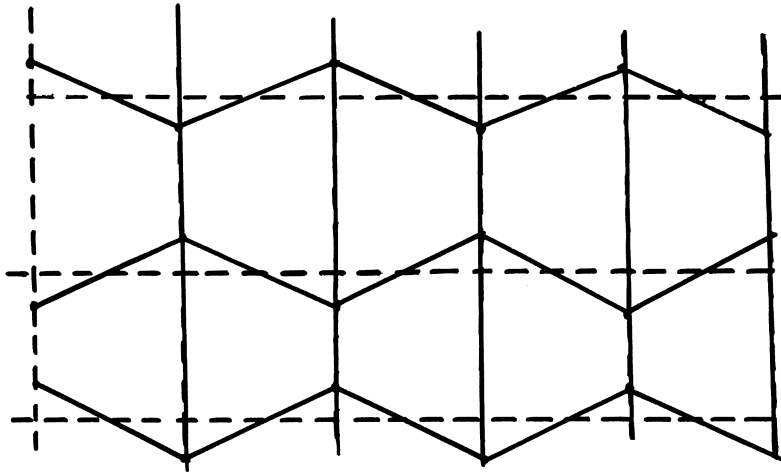
3. The natural norms on the approximate solutions are mesh-dependent (as is clear from (21) and (22)), a generally undesirable feature.

4. Ad hoc schemes to stabilize these methods, such as the use of "hourglassing viscosity" and "pressure filtering" may dampen out oscillations in solution but produce an inconsistent scheme which converges to the solutions of the "wrong" problem. In some cases, convergent but suboptimal convergence rates are obtained.

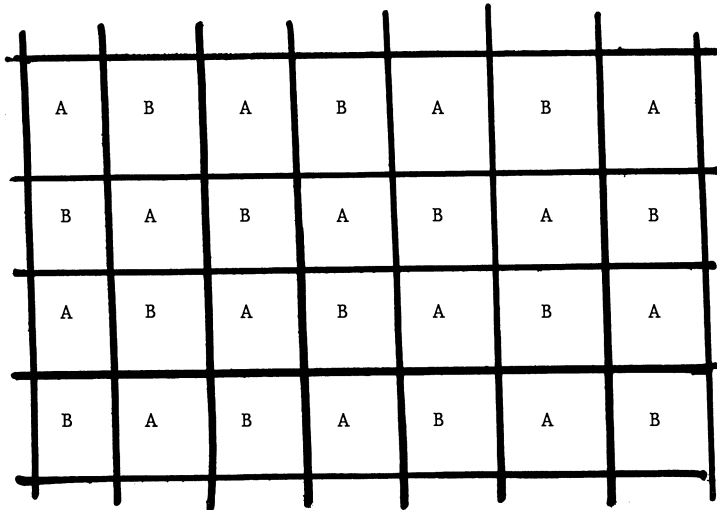
Only instabilities of the checkerboard type have been analyzed in some detail and this has been only very recently in the work of Oden and Kikuchi [1] and Oden and Jacquotte [8]. Examples of some of their results are listed in Table 1. It is emphasized that these results pertain only to the approximation of the constraint $\operatorname{div} \tilde{u} = 0$ and not to hourglassing instabilities of the type noted earlier. We observe that among the unstable elements are the very popular bilinear, trilinear, 8-node, and 20-node isoparametric elements. Pressure filtering will stabilize certain of these elements, but it is then not known if the resulting scheme is convergent or suboptimal in the sense that its rate-of-convergence is below the best possible for this choice of element.

Nonlinear Materials

We shall now provide some brief comments on some specific issues in constitutive modelling of nonlinear materials. We employ standard notations of continuum mechanics and a Lagrangian (material) description of motion, and denote by $\tilde{\gamma}$ the Green St-Venant strain, $\tilde{\alpha}$ an internal variable (see, e.g. Coleman and Gurtin [9], and θ the absolute temperature.



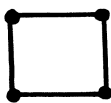
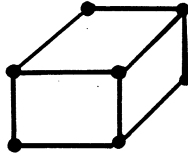
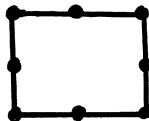
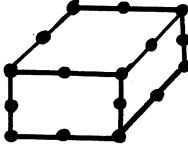
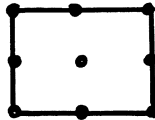
(A)



(B)

Figure 1. a) Hourglassing instability phenomena and b) checkerboarding in pressure calculations using finite elements with reduced integration.

TABLE Examples of Element Stability Calculations for $\text{div } \underline{u} = 0$

ELEMENT	INTEGRATION RULE	STABILITY PARAMETER β_h	COMMENT
1.  Bilinear	1-point	0(h)	Unstable
2.  Trilinear	1-point	0(h)	Unstable
3.  8-node Isoparametric	2x2-point 1-point	0(h) 0(h)	Unstable Suboptimal
4.  20-node Brick	2x2x2-point 1-point	0(h) 0(1)	Unstable Suboptimal
5.  Biquadratic	2x2-point 3-point 1-point	0(h) 0(1) 0(1)	Unstable Optimal Suboptimal

Let us assume that the material at particle X at time t is characterized by the five response functions:

$$\begin{aligned}\phi &= \Phi(\underline{\gamma}, \underline{\alpha}, \theta, \underline{g}) \\ \underline{S} &= \underline{S}(\underline{\gamma}, \underline{\alpha}, \theta, \underline{g}) \\ \eta &= N(\underline{\gamma}, \underline{\alpha}, \theta, \underline{g}) \\ \underline{q} &= \underline{Q}(\underline{\gamma}, \underline{\alpha}, \theta, \underline{g}) \\ \underline{\alpha} &= \underline{A}(\underline{\gamma}, \underline{\alpha}, \theta, \underline{g})\end{aligned}\tag{24}$$

where $\underline{g} = \text{grad } \theta$ and we have omitted expressing the possible explicit dependence of the response functions on X and t . These functions are assumed to satisfy the usual requirements of objectivity, etc.

Let us assume that $(\underline{\gamma}, \underline{\alpha}, \theta, \underline{g}) \rightarrow \Phi(\underline{\gamma}, \underline{\alpha}, \theta, \underline{g})$ is C^1 in each argument. Then it is well known (see, e.g. Coleman and Gurtin [9]) that

- i) Φ, \underline{S} , and N must be independent of \underline{g} (so we now write, $\phi = \Phi(\underline{\gamma}, \underline{\alpha}, \theta)$, etc.)
- ii) \underline{S} and N are determined by Φ :

$$\underline{S}(\underline{\gamma}, \underline{\alpha}, \theta) = \frac{\partial \Phi(\underline{\gamma}, \underline{\alpha}, \theta)}{\partial \underline{\gamma}} : N(\underline{\gamma}, \underline{\alpha}, \theta) = - \frac{\partial \Phi(\underline{\gamma}, \underline{\alpha}, \theta)}{\partial \theta}\tag{25}$$

- iii) \underline{A} and \underline{Q} must satisfy the inequality

$$\underline{A}(\underline{\gamma}, \underline{\alpha}, \theta) \cdot \underline{A}(\underline{\gamma}, \underline{\alpha}, \theta) - \frac{1}{\theta} \underline{Q}(\underline{\gamma}, \underline{\alpha}, \theta, \underline{g}) \cdot \text{grad } \theta \geq 0\tag{26}$$

for every $(\underline{\gamma}, \underline{\alpha}, \theta, \underline{g})$ ($\theta > 0$), where \underline{A} is the thermodynamic force dual to $\underline{\alpha}$:

One approach toward a rather general framework for finite plasticity theories has been proposed by several authors, and we mention in particular Rice [9] and Halphen and Nguyen [10] as examples. One approach is to construct a conjugate functional in terms of the Piola-Kirchhoff stress \underline{S} according to

$$\Phi^*(\underline{S}, \underline{\alpha}, \theta) = \sup_{\underline{\gamma}} \{ \underline{S} : \underline{\gamma} - \Phi(\underline{\gamma}, \underline{\alpha}, \theta) \}\tag{27}$$

If Φ^* is differentiable with respect to \underline{S} (which may not necessarily be the case), we have

$$\underline{\gamma} = \frac{\partial \Phi^*}{\partial \underline{S}} = \underline{\Gamma}(\underline{S}, \underline{\alpha}, \theta)\tag{28}$$

Then we can define the plastic strain as that strain $\underline{\gamma}^P$ arising from structural changes in the material as measured by $\underline{\alpha}$; e.g.

$$\dot{\tilde{\gamma}}^p = \frac{\partial \gamma}{\partial \tilde{\alpha}} : \dot{\tilde{\alpha}} = \frac{\partial \Gamma(\tilde{S}, \tilde{\alpha}, \theta)}{\partial \tilde{\alpha}} : A(\tilde{\gamma}, \tilde{\alpha}, \theta) \quad . \quad (29)$$

One direction that could be taken at this point is to establish conditions sufficient to guarantee the existence of a functional Ψ such that

$$\dot{\tilde{\gamma}}^p \in \partial \Psi(\tilde{S}, \tilde{\alpha}, \theta) \quad . \quad (30)$$

The derivation of yield criteria, normality conditions, kinematic hardening, etc. for problems of finite deformation can precipitate from (36) if Ψ is endowed with appropriate properties.

Microstructural Influences

There are several major shortcomings of the general theoretical approaches just outlined:

1. They are too general, in the sense that they provide only a very broad structure in which one can characterize materials. More specific forms of the constitutive equations are needed to model specific classes of materials. These more detailed models, while possibly fitting many aspects of the general theory, should reflect microstructural features which are known to play a dominant role in non-linear thermomechanical behavior of materials.
2. The specific assumptions of convexity and differentiability are generally invalid.

Space limitations prevent a more detailed discussion of these points, but these are to be the subject of a forthcoming paper. For the present work, we shall simply review a model of twinning which generalizes that of H. Achenbach et al [11] and which leads to a non-convex energy functional. More general models incorporating dislocation densities and grain-boundary sliding, are under study.

Consider two adjacent lattices of martensite crystals with different orientations M^- and M^+ meeting along a twin defect as shown in Fig. 2a. If a tensile test is performed on a specimen of this material, as indicated, a shearing of the crystals will occur. Suppose that an M^- crystal is in a state of stable equilibrium prior to the application of this load. Then we may assert that it possesses a free energy ϕ which, for this crystal configuration, is a relative minimum. Attempts to distort this lattice orientation by small shear deformations Δ will produce an increase in energy and, thus, an elastic response of the crystal. This deformation may continue until a peak critical energy level is reached, at which point the crystal assumes a stable M^+ orientation. This is then a permanent deformation.

Let us now interpret this situation in the language of internal variables. As one

possible choice, let α denote the fraction of M^+ crystals in a martensite specimen and suppose that prior to deformation all crystals are in the M^- orientation. Then $\alpha = 0$. If the deformation Δ is applied in the direction of the orientation, then an elastic response will result for indefinitely large Δ . However, if an opposite Δ is given, then a critical level is reached at which some fraction of the crystals move to an M^+ orientation. If all crystals assume the M^+ orientation, then $\alpha = 1$ (an unlikely situation); whereas if $\alpha = \alpha_0$, $0 < \alpha_0 < 1$, a portion $1 - \alpha_0$ crystals will be in the M^- static and α_0 will be in the M^+ state. Thus, the situation is like that illustrated in Fig. 2b: the result of and fraction $\alpha > 0$ is a non-convex energy functional and a "permanent" deformation.

Two related observations are important:

1. The actual response of such a lattice will not generally follow any of the family of curves $\alpha = \text{constant}$ indicated in the figure since additional twin defects will be produced during the deformation. Thus, the actual variation in energy observed may be given by the solid line shown.
2. This model also easily accomodates growth twins which are produced during annealing (such as those produced in recrystallization of fcc crystals). Indeed, one would then initiate the deformation process from a curve with α given, $0 < \alpha < 1$.
3. It is clear that the free energy here is dependent upon the concentration α . Thus, a more accurate depiction of the behavior could be illustrated in a three-dimensional setting such as that sketched in Fig. 3c.

Similar models for dislocations can be developed and a report on this subject by the author is forthcoming.

What is the actual path on the ϕ -surface along which the given crystal system will traverse? In a more general situation, we may take α to be a vector-valued variable with components representing one or more of the mechanisms for microstructural changes mentioned earlier. Then consider the two constitutive equations

$$\begin{aligned}\phi &= \Phi(\underline{\gamma}, \underline{\alpha}, \theta) \\ \dot{\underline{\alpha}} &= \underline{A}(\underline{\gamma}, \underline{\alpha}, \theta, \underline{g})\end{aligned}\tag{31}$$

For a process taking place over a time interval $[0, t]$, let $F(\cdot)$ denote the first integral of the evolution equation for $\underline{\alpha}$ over this interval (symbollically,

$$\begin{aligned}F(\underline{\gamma}, \underline{\alpha}, \theta) &= \int_0^t \underline{A}(\underline{\gamma}(s), \underline{\alpha}(s), \theta(s), \underline{g}(s)) ds \\ &\quad - \underline{\alpha}(t) + \underline{\alpha}(0)\end{aligned}\tag{32}$$

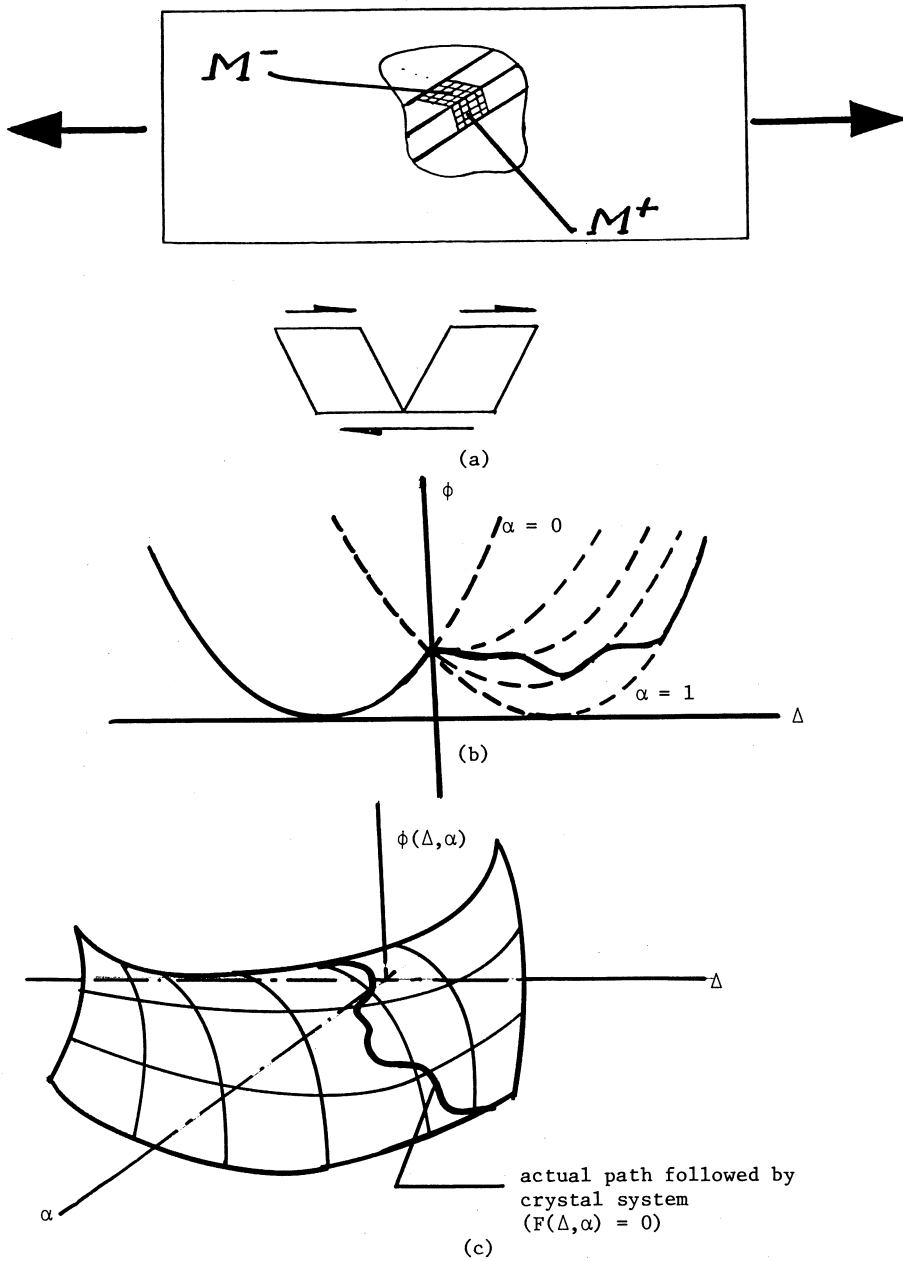


Figure 2. a) Orientation of crystals at a twin defect, b) free energy as a function shear Δ for various values of the internal variables α and c) free energy as a function of α and Δ .

Suppose that θ is held constant; then any real thermodynamic process on such a material must trace out a trajectory on the intersection of the surfaces

$$\begin{aligned}\phi - \Phi(\gamma, \alpha, \theta) &= 0 \\ F(\gamma, \alpha, \theta) &= 0.\end{aligned}\tag{33}$$

This situation for the simple twin model is illustrated in Fig. 2c.

Friction Effects

Finally, we comment on models of friction between metallic bodies. Numerical experiments using finite element models of metal-on-metal contact with large elasto-plastic deformation have shown that large differences in stress distributions can result from small changes in the friction forces. These instabilities inherent in most classical (Mohr-Coulomb-type) friction models have led to the consideration of non-classical friction laws which attempt to model non-local effects and the elasto-plastic behavior of junctions and asperities on the contact surface (see Oden and Pires [13, 14, 15]).

One such friction law asserts that the tangential stress σ_T on the contact surface Γ_C is related to the normal stress $\sigma_n(u)$ and the tangential component \dot{u}_T of the velocity Du/Dt on Γ_C according to

$$\sigma_T = \nu S_p(\sigma_n(u)) \phi_\epsilon(|\dot{u}_T|) \frac{n \cdot \dot{u}_T}{|\dot{u}_T|}\tag{33}$$

where ν is the coefficient of friction, S_p is a smoothing operator mollifying σ_n over a deformed asperity of radius p , ϕ_ϵ is a nonlinear function modelling elasto-plastic functions with an initial stiffness (elastic modulus) of ϵ^{-1} , and $\frac{n \cdot \dot{u}_T}{|\dot{u}_T|}$ is a unit vector opposite in direction to \dot{u}_T . Typically, S_p is of the form,

$$S_p(\sigma_n)(x) = \int_{\Gamma_C} w_p(|x-y|) \sigma_n(y) dy\tag{34}$$

where w_p is a smooth kernel which vanishes outside a disk of radius p , and ϕ_ϵ is of the general form indicated in Fig. 3.

Friction laws of the form (31) have been proposed by Oden and Pires [13-15] and their properties have been studied in some detail. Some of their features of interest are: 1) in the limit as ϵ tends to zero, a nonlocal friction law is obtained, 2) as p tends to zero, a nonlinear friction law with inherent hysteresis effects for cases of load reversal can be obtained, 3) existence and uniqueness theorems for quasi-static elasticity problems in which the general friction law holds have

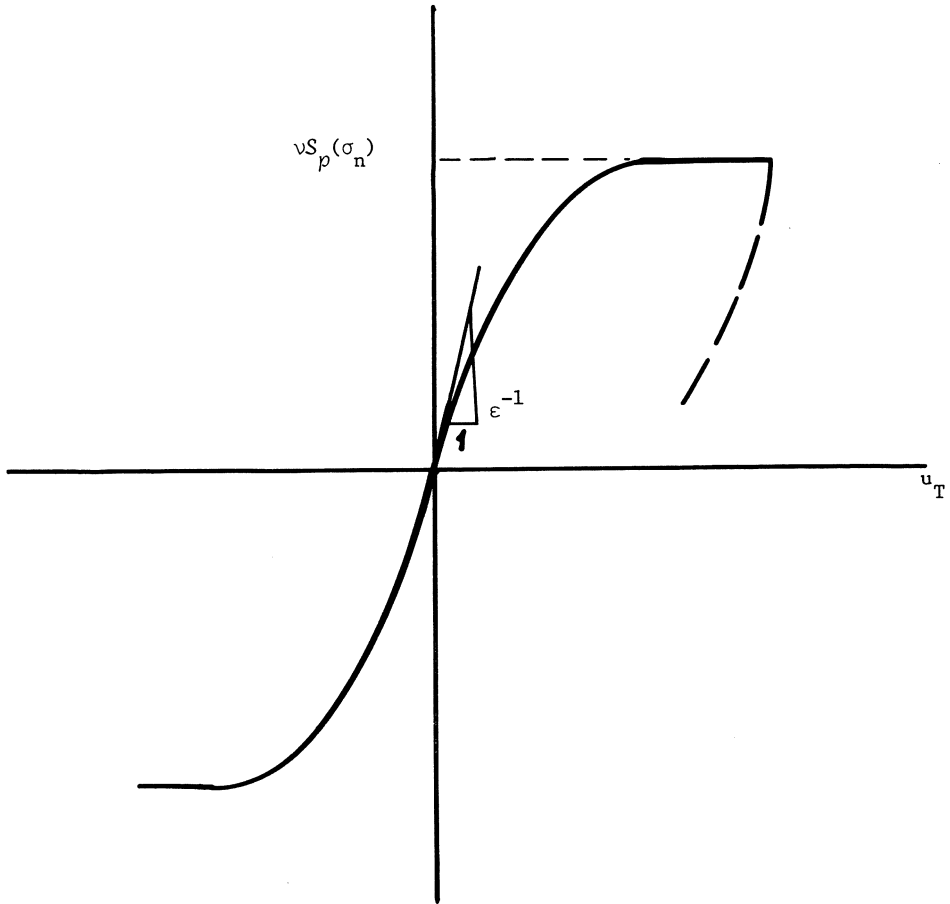


Figure 3. Typical form of a function ϕ_ϵ in nonlinear friction law.

been developed [14], 4) error estimates and convergence proofs have been derived for finite element approximations of contact problems in which this type of friction law is assumed to hold [13, 14], 5) algorithms for implementing such non-classical laws exist and have produced encouraging numerical results [15]. Space limitations prevent a more detailed account of these results, but additional information can be found in [13-15].

Acknowledgement

Support of the work on finite-element instabilities by NASA under Grant NG-3-329 and of the work on friction by AFOSR under contract F-49620-78-C-0083 is gratefully acknowledged.

References

1. Oden, J.T. and Reddy, J.N., Introduction to the Mathematical Theory of Finite Elements, Wiley-Interscience, N.Y., 1976.
2. Oden, J.T. and Kikuchi, N., "Finite Element Methods for Constrained Problems In Elasticity," Int'l J. Num. Meth'ds Engr'g., Vol. 18, pp. 701-725, 1982.
3. Oden, J.T., "Penalty Methods for Constrained Problems in Nonlinear Elasticity," Finite Elasticity, Edited by D.E. Carlson and R.T. Shields, Martinus Nijhoff, The Hague, 1982, pp. 281-300.
4. LeTallec, P. and Oden, J.T., "Existence and Characterization of Hydrostatic Pressures in Finite Deformations of Incompressible Elastic Rods," J. of Elasticity, Vol. 11, No. 4, 1981, pp. 341-357.
5. Oden, J.T. and Carey, G.F., Finite Elements: Mathematical Aspects, Prentice-Hall, Englewood Cliffs, N.J., 1982.
6. Becker, E.B., Carey, G.F., and Oden, J.T., Finite Elements: An Introduction, Englewood Cliffs, N.J., 1981.
7. Flanagan, D.P. and Belytschko, T., "A Uniform Strain Hexahedron and Quadrilateral With Orthogonal Hourglass Control," International J. Num. Mth'ds Engr'g., Vol. 17, pp. 679-706, 1981.
8. Oden, J.T. and Jacquotte, O., "Stable RIP/PL Schemes for Incompressible Viscous Flow," Finite Elements in Fluids, Vol. V, John Wiley and Sons, Ltd., London (to appear).
9. Coleman, B.D. and Gurtin, M., "Thermodynamics with Internal Variables," J. Chemistry and Physics, Vol. 67, pp. 597-613, 1967.
10. Rice, J.R., "Inelastic Constitutive Relations for Solids: An Internal-Variable Theory and Its Application to Metal Plasticity," J. Mech. Phys. Solids, Vol. 19, pp. 433-455, 1971.
11. Halphen, B. and Nguyen, Q.S., "Sur les Matériaux Standards Généralisés," J. de Mécanique, Vol. 14, No. 1, 1975, pp. 39-63.
12. Achenbach, H., Muller, I., and Wilmski, K., "A Model for Creep and Strain Hardening in Martensitic Transformation," J. Thermal Stresses, Vol. 4, 1981, pp. 523-534.

13. Oden, J.T. and Pires, E.B., "Contact Problems with Nonlocal Friction," Finite Elements: Special Problems in Solid Mechanics, by J.T. Oden and G.F. Carey, Prentice-Hall, Englewood Cliffs, (to appear).
14. Oden, J.T. and Pires, E.B., "Nonlocal and Nonlinear Friction Laws for Contact Problems in Elastostatics," J. of Appl'd. Mech., (to appear).
15. Oden, J.T. and Pires, E.B., "Numerical Analysis of Certain Contact Problems In Elasticity with Non-classical Friction Laws," Computers and Structures, (to appear).
16. Oden, J.T. and Pires, E.B., "Algorithms and Numerical Results for Finite Element Approximations of Contact Problems with Non-classical Friction Laws," Computers and Structures, (to appear).

AUGMENTED LAGRANGIANS IN FINITE ELASTICITY AND IN PLASTICITY

P. LE TALLEC

Laboratoire Central des Ponts et Chaussées
58 bld Lefebvre
75732 PARIS Cedex 15 - France

Two kinds of nonlinearity are involved in penetration mechanics : yielding and large deformations. Each of them separately can be numerically treated by the augmented Lagrangian techniques described in [1]. As a first step towards their eventual use in case where both nonlinearities are present, this paper describes augmented lagrangian methods in a rather abstract form, which covers a large spectrum of applications.

Consequently, Paragraph 1 presents the general frame in which augmented lagrangians are applied to nonlinear solid mechanics. Paragraph 2 illustrates these techniques on the numerical solution of equilibrium problems in incompressible finite elasticity. A second example is given in Paragraph 3, concerning limit load computation in plasticity.

1. THE ABSTRACT PROBLEM

1.1. Initial Formulation. We consider herein the numerical solution of nonlinear problems of the type

$$(1.1) \quad \text{Minimize } J(\underline{u}, f(\nabla \underline{u})) \text{ on } K,$$

where K denotes some set of vector fields \underline{u} , defined on a bounded domain of \mathbb{R}^N , $f(\nabla \underline{u})$ a function of the gradient of \underline{u} with values in a set M , J a given functional from $K \times M$ into \mathbb{R} . An alternative formulation of the problem, not necessarily equivalent, is

$$(1.2) \quad \left\{ \begin{array}{l} \text{Find } \underline{u} \in K \text{ such that for any } \underline{y} \text{ in } dK(\underline{u}) \text{ we have :} \\ \partial_{\underline{u}} J(\underline{u}, f(\nabla \underline{u})) \cdot \underline{y} + \partial_{\underline{F}} J(\underline{u}, f(\nabla \underline{u})) \cdot \left[\frac{\partial f}{\partial \nabla \underline{u}} \cdot \nabla \underline{y} \right] = 0, \end{array} \right.$$

where $dK(\underline{u})$ is formally the tangent space to K at \underline{u} , and $\partial_{\underline{y}} J$ denotes the Gateaux derivative of J with respect to the variable \underline{y} .

In usual cases, these formulations are well-posed for K a subspace of a Sobolev space. A direct finite element discretisation of K with C^0 finite elements is then possible which, combined with an adequate numerical method for the inversion of the nonlinear discrete operator, say Newton Raphson, normally gives satisfactory numerical results.

But, in some cases, like plastic limit loads computation or equilibrium problems in finite elasticity, the situation is more complicated, either because of the structure

of the set K which can involve highly nonlinear constraints (finite elasticity) or because of the functional J itself (plasticity). A mixed formulation of augmented lagrangian type, which will split the difficulty, might then be very useful.

1.2. Augmented Lagrangian Formulation. The basic idea of the method is to consider \underline{u} and its gradient as two independent variables, related by an external linear constraint. This constraint is together dualized, which ensures that it is exactly satisfied at the solution, and penalized to improve the local convexity of J , if any. This leads to the introduction of the following lagrangian:

$$(1.3) \quad \mathcal{L}(\underline{u}, \underline{F}, \underline{\lambda}) = J[\underline{u}, f_1(\nabla \underline{u}) + f_2(\underline{F})] + \underbrace{\frac{R}{2} \|\nabla \underline{u} - \underline{F}\|_{0,2,\Omega}^2}_{\text{penalty}} + \underbrace{\langle \underline{\lambda}, \nabla \underline{u} - \underline{F} \rangle}_{\text{duality}}$$

where f has been decomposed into the sum $f_1 + f_2$. The new formulation of our problem is then :

$$(1.4) \quad \left\{ \begin{array}{l} \text{Find } \underline{u} \in X, \underline{F} \in Y, \underline{\lambda} \in Z \text{ such that} \\ \text{(i) } \partial_{\underline{u}} \mathcal{L}(\underline{u}, \underline{F}, \underline{\lambda}) \cdot \underline{v} = 0, \quad \forall \underline{v} \in dX(\underline{u}), \\ \text{(ii) } \partial_{\underline{F}} \mathcal{L}(\underline{u}, \underline{F}, \underline{\lambda}) \cdot \underline{G} = 0, \quad \forall \underline{G} \in dY(\underline{F}), \\ \text{(iii) } \partial_{\underline{\lambda}} \mathcal{L}(\underline{u}, \underline{F}, \underline{\lambda}) \cdot \underline{\mu} = \langle \underline{\mu}, \nabla \underline{u} - \underline{F} \rangle = 0, \quad \forall \underline{\mu} \in Z. \end{array} \right.$$

Any solution of the above lagrangian formulation satisfies $\underline{F} = \nabla \underline{u}$ in the dual Z' of Z . Therefore, it is a solution of the initial problem when the sets X and Y , and the space Z are correctly chosen. These choices, as well as the splitting of f into $f_1 + f_2$, are rather arbitrary. What is needed is first to have

$$K = \left\{ \{ \underline{u}, \underline{F} \} \in X \times Y, \underline{F} - \nabla \underline{u} = 0 \text{ in } Z' \right\},$$

and second to give the right topologies to X , Y and Z to ensure the equivalence with the initial problem when the latter is well-posed.

A natural way to proceed is to simplify the problem in \underline{u} as far as possible and to concentrate the major difficulties on the problem in \underline{F} , where no derivatives are involved and where a local treatment is often possible.

1.3. Discretization. The above lagrangian formulation allows a separate discretization of X , Y and Z . Once finite approximations X_h , Y_h , Z_h of X , Y and Z are defined, and a discrete gradient operator ∇_h from X_h into Z_h' is introduced, the discrete form of (1.4) is simply,

$$(1.5) \quad \left\{ \begin{array}{l} \text{Find } \underline{u}_h \in X_h, \underline{F}_h \in Y_h, \underline{\lambda}_h \in Z_h \text{ such that} \\ \partial_{\nabla_h} \mathcal{L}(\underline{u}_h, \underline{F}_h, \underline{\lambda}_h) \cdot \underline{v}_h = 0, \quad \forall \underline{v}_h \in dX_h(\underline{u}_h), \\ \partial_{\underline{F}_h} \mathcal{L}(\underline{u}_h, \underline{F}_h, \underline{\lambda}_h) \cdot \underline{G}_h = 0, \quad \forall \underline{G}_h \in dY_h(\underline{F}_h), \\ \partial_{\underline{\lambda}_h} \mathcal{L}(\underline{u}_h, \underline{F}_h, \underline{\lambda}_h) \cdot \underline{\mu}_h = 0, \quad \forall \underline{\mu}_h \in Z_h, \end{array} \right.$$

with

$$\begin{aligned} \mathcal{L}_h(u_h, \mathbb{F}_h, \lambda_h) = & J[u_h, f_1(\nabla u_h) + f_2(\mathbb{F}_h)] + \frac{R}{2} \|\nabla_h u_h - \mathbb{F}_h\|_{0,2,\Omega} \\ & + \langle \lambda_h, \nabla_h u_h - \mathbb{F}_h \rangle \end{aligned}$$

The construction of X_h , Y_h , Z_h and ∇_h is a very important step of the numerical treatment of the initial problem. First, the topologies of X, Y, Z which are used in the existence theory of the initial problem must be respected. Second, as for every mixed formulation, a compatibility condition of Ladyzenskaya-Babuska-Brezzi type must relate X_h , Y_h and ∇_h in order to ensure existence and convergence of discrete solutions ([2]).

A separate analysis has to be done in each particular case. It is not possible to be more specific in the general approach taken here, but we will detail this point in the forthcoming examples.

1.4. Algorithm. For the numerical solution of the discrete formulation (1.5), an Uzawa algorithm combined with a block relaxation for the resolution of the primal problem can be used. It separates the numerical treatment of the problem in each variable, therefore taking a real advantage of the lagrangian decomposition made in (1.4). It can be written :

$$\lambda^0, u^{-1} \text{ given in } Z_h, X_h ;$$

then, for $n \geq 0$, assuming λ^n and u^{n-1} are known, $\{u^n, \mathbb{F}^n\}$ is computed in $X_h \times Y_h$ by block relaxation, i.e. by

$$\text{setting } u_0^n = u^{n-1}$$

and computing sequentially \mathbb{F}_{k+1}^n and u_{k+1}^n by solving

- $\partial_{\mathbb{F}_h} \mathcal{L}_h(u_h^n, \mathbb{F}_{k+1}^n, \lambda_h^n) \cdot \mathbb{G} = 0, \forall \mathbb{G} \in dY_h(\mathbb{F}_{k+1}^n),$ (problem in \mathbb{F})
- $\partial_{u_h} \mathcal{L}_h(u_{k+1}^n, \mathbb{F}_{k+1}^n, \lambda_h^n) \cdot v = 0, \forall v \in dX_h(u_{k+1}^n) ;$ (problem in u)

when u^n and \mathbb{F}^n are known, the multiplier λ^n is updated by

$$\lambda^{n+1} = \lambda^n + R(\nabla_h u^n - \mathbb{F}^n).$$

This algorithm was initially derived for lagrangians which were convex functions of the pair $\{u, \mathbb{F}\}$. In that case, convergence results can be proved [3]. But in fact, this algorithm can be successfully used when only local convexity properties are satisfied, mainly that u^n locally minimizes $\mathcal{L}_h(\cdot, \mathbb{F}^n, \lambda_h^n)$ over X_h and that \mathbb{F}^n locally minimizes $\mathcal{L}_h(u_h^n, \cdot, \lambda_h^n)$ over Y_h .

To check these local convexity requirements, the penalty coefficient R , initially arbitrary, plays a key role. In many cases, for R sufficiently large, and although J might not satisfy these requirements, the regularized lagrangian \mathcal{L}_h will ([4]). A very good numerical value of R , which leads to an efficient algorithm, is then the minimal value which ensures this local convexity.

1.5. Characteristics of the Method. The described method achieves three different goals :

- it takes into account the different topologies which must be used for \underline{u} and for its gradient ;
- it reduces the nonlinearity to local problems where no derivatives are involved, which can be independently and efficiently solved through an adequate algebraic analysis ;
- in case of multiple solutions, it almost automatically converges towards the most stable solution (Recall that it is a fixed step method which does not involve tangent stiffness).

2. EQUILIBRIUM PROBLEMS IN FINITE ELASTICITY

2.1. The Physical Problem. We consider the problem of finding equilibrium positions of an hyperelastic body submitted to a certain distribution of external loads and imposed displacements. Any particle \underline{x} of the body is labeled by its position in a stress-free reference configuration, related to a fixed Cartesian rectangular coordinate system. With these conventions, the interior of the body can be identified to be an open set Ω of \mathbb{R}^N ($N = 2$ or 3).

The body is subjected to body forces of intensity \underline{f} per unit mass in the reference configuration and to surface tractions \underline{t} , measured per unit area in the reference configuration, prescribed on a portion $\partial\Omega_2$ of the boundary of Ω . The motion \underline{u} takes on prescribed values \underline{u}_0 on $\partial\Omega_1 = \partial\Omega - \partial\Omega_2$. Using the equilibrium equations in Lagrangian coordinates (conservation of linear momentum), and the hyperelasticity law, we can formally characterize the equilibrium positions of the body as the solutions of the following system :

$$\text{equilibrium equations} \quad (2.1) \quad \left\{ \begin{array}{l} - \operatorname{div} \underline{\tau} = \underline{f} \quad \text{on } \Omega, \\ \underline{\tau} \cdot \underline{n} = \underline{t} \quad \text{on } \partial\Omega_2, \end{array} \right.$$

$$\text{hyperelasticity} \quad (2.2) \text{ (a)} \quad \underline{\tau} = \frac{\partial \sigma}{\partial \nabla \underline{u}}(\underline{x}, \underline{u}, \operatorname{adj} \nabla \underline{u}, \det \nabla \underline{u}) ;$$

(compressible)

$$\text{hyperelasticity} \quad (2.2) \text{ (b)} \quad \underline{\tau} = \frac{\partial \sigma}{\partial \nabla \underline{u}}(\underline{x}, \nabla \underline{u}, \operatorname{adj} \nabla \underline{u}) + p(\operatorname{adj} \nabla \underline{u})^T ;$$

(incompressible)

$$\text{orientation conservation} \quad (2.3) \text{ (a)} \quad \det \nabla \underline{u} > 0 ;$$

(compressible)

$$\text{incompressibility condition} \quad (2.3) \text{ (b)} \quad \det \nabla \underline{u} = 1.$$

Above, $\underline{\tau}$ denotes the first Piola Kirchhoff stress-tensor, $\operatorname{adj} \nabla \underline{u}$ the adjugate (transpose of matrix of cofactors) of the gradient of \underline{u} . The equations (a) correspond to the compressible case, equations (b) to the incompressible case. We now restrict ourselves to incompressible bodies, which generally lead to more delicate numerical problems. The compressible case could be similarly treated as well.

2.2. Variational and mixed formulation. The variational form of equilibrium equations (2.1)-(2.3) taken here is

$$(2.4) \quad \left\{ \begin{array}{l} \text{Find } \underline{u} \in \underline{W}^{1,s}(\Omega), \underline{\mathcal{A}} \in (\underline{L}^s(\Omega))' \text{ such that} \\ \bullet \quad \underline{u} = \underline{u}_0 \text{ on } \partial\Omega_1, \det \nabla \underline{u} = 1 \text{ a.e. in } \Omega, \\ \bullet \quad \int_{\Omega} \left\{ \frac{\partial \sigma}{\partial \nabla \underline{u}} + \underline{\mathcal{A}} \right\} \cdot \nabla \underline{v} = \int_{\Omega} \rho_0 \underline{f} \cdot \underline{v} + \int_{\partial\Omega_2} \underline{t} \cdot \underline{v}, \\ \quad \nabla \underline{v} \in U^{1,s} = \{ \underline{w} \in \underline{W}^{1,s}(\Omega), \underline{w} = 0 \text{ on } \partial\Omega_1 \} \\ \bullet \quad \int_{\Omega} \underline{\mathcal{A}} \cdot \underline{\mathcal{T}} = 0, \forall \underline{\mathcal{T}} \in \underline{L}^s(\Omega), (\text{adj } \nabla \underline{u})^T \cdot \underline{\mathcal{T}} = 0 \text{ a.e. in } \Omega. \end{array} \right.$$

Formally, from the last equation, $\underline{\mathcal{A}}$ corresponds to the term $p(\text{adj } \nabla \underline{u})^T$. There is a slight discrepancy between the above formulation and the minimization formulation proposed by BALL [5] and for which existence results have been derived. Unfortunately, BALL's minimization formulation does not lead to equivalence results with either some kind of equilibrium formulation or with an augmented lagrangian one. Thus, we have chosen a slightly different form of the equations, equivalent with the minimization formulation only for regular solutions ([6]) or for the discrete version ([7]).

An equivalent augmented lagrangian formulation can then be introduced as in (1.4) by defining ([8]) :

$$\begin{aligned} X &= \{ \underline{u} \in \underline{W}^{1,s}(\Omega), \underline{u} = \underline{u}_0 \text{ on } \partial\Omega_1 \}, \\ Y &= \{ \underline{F} \in \underline{L}^s(\Omega), \underline{G} \cdot \underline{F} = N \text{ a.e. on } \Omega, \underline{G} = (\text{adj } \underline{F})^T \}, \\ dY(\underline{F}) &= \{ \underline{T} \in \underline{L}^s(\Omega), \underline{G} \cdot \underline{T} = 0 \text{ a.e. on } \Omega \}, \\ Z &= (\underline{L}^s(\Omega))', \\ \mathcal{L}(\underline{u}, \underline{F}, \underline{\lambda}) &= \int_{\Omega} \{ \sigma(\underline{x}, \nabla \underline{u}, \text{adj } \underline{F}) + \frac{R}{2} |\nabla \underline{u} - \underline{F}|^2 + \underline{\lambda} \cdot (\nabla \underline{u} - \underline{F}) \} \\ &\quad - \int_{\Omega} \rho_0 \underline{f} \cdot \underline{u} - \int_{\partial\Omega_2} \underline{t} \cdot \underline{u}. \end{aligned}$$

2.3. Discretization. As seen in Paragraph 1, the discretization of the lagrangian version of (2.4) requires the introduction of finite dimensional approximations of X, Y, Z. To do so, let us introduce the three following finite element spaces :

$$\begin{aligned} X_h &\subset \underline{W}^{1,\infty}(\Omega) \cap [U^{1,s} + \underline{u}_0], \dim X_h < +\infty ; \\ P_h &\subset L^\infty(\Omega), \dim P_h < +\infty, \\ H_h &\subset L^\infty(\Omega), \dim H_h < +\infty, \underline{H}_h = (H_h)^{N \times N}. \end{aligned}$$

The space X_h approximates the motion space, P_h the pressure space (the multiplier of the incompressibility constraint), H_h is used for approaching the gradient space.

Then, Y_h and Z_h are defined by :

$$\begin{aligned} Y_h &= \left\{ \underline{G}_h \in \underline{H}_h, \int_{\Omega} \{ (\text{adj } \underline{G}_h)^T \cdot \underline{G}_h - N \} \cdot \underline{q}_h = 0, \forall \underline{q}_h \in P_h \right\}, \\ Z_h &= \underline{H}_h, \end{aligned}$$

where $\text{adj}_h \underline{\mathbb{G}}$ denotes the L^2 projection of $\text{adj} \underline{\mathbb{G}}$ on Z_h . Three approximations are made in constructing $Y_h : \underline{\mathbb{L}}^s(\Omega)$ is replaced by $\underline{\mathbb{H}}_h$, the adjugate of $\underline{\mathbb{G}}$ is replaced by its projection onto Z_h , the incompressibility condition is only satisfied in the dual space of P_h . The projection of the adjugate preserves the symmetrical role played by $\underline{\mathbb{F}}$ and $\underline{\mathbb{G}}$ in the existence theory and will be very useful numerically. Weakening the incompressibility condition is crucial to avoid too big a restriction of Y_h . Once ∇_h is defined, the discrete augmented lagrangian version of equilibrium equations (2.4) is simply (2.5) written with the above definitions.

The topologies of X, Y, Z have been respected in the above discretization. What remains to be checked is the compatibility condition between X_h, Y_h, ∇_h , which can be written here ([2], [4], [9]) :

$$\left\{ \begin{array}{l} \text{For } \underline{u}_h \text{ in } X_h, \text{ with } \nabla_h \underline{u}_h \text{ in } Y_h, \text{ we have} \\ \text{Inf}_{q_h \in P_h} \quad \text{Sup}_{\underline{v}_h \in X_h - \underline{u}_0} \quad \frac{\int_{\Omega} q_h \frac{\partial}{\partial \underline{\mathbb{F}}} [(\text{adj}_h \nabla_h \underline{u}_h)^T \cdot \nabla_h \underline{u}_h] \cdot \nabla \underline{v}_h}{\|q_h\| \|\underline{v}_h\|} > 0. \end{array} \right.$$

This condition ensures the existence of a solution of the discrete problem ([7]). A slightly generalized version is needed to prove the convergence of the discrete solutions towards the continuous ones [2]. Moreover, it can be interpreted in many cases as the classical linear inf-sup condition (LADYZENSKAYA, BABUSKA, BREZZI), but written in the configuration after deformation. The philosophy is then to choose finite element spaces X_h and P_h which keep the same nature after deformation and which work reasonably well in linear incompressible elasticity.

In the numerical examples presented, two discretizations, among other possible ones, have been used. The first one, simple but, dangerous because the compatibility condition might not be correctly satisfied, takes :

$$\begin{aligned} X_h &= \{ \underline{v} \in \underline{\mathcal{C}}^0(\bar{\Omega}), \underline{v}|_{\Omega_k} \in Q_1(\Omega_k) \}, \\ P_h = H_h &= \{ q, q|_{\Omega_k} = \text{constant} \}, \\ \nabla_h \underline{v}|_{\Omega_k} &= \frac{1}{\text{mes}(\Omega_k)} \int_{\Omega} \nabla \underline{v}, \end{aligned}$$

where the Ω_k are regular hexaedrons which build a finite element triangulation of Ω . The second discretization introduced by RUAS [9], corresponds to a triangulation of Ω into a finite set of asymmetric tetraedrons. On each tetraedron, pressures and gradients are constant, and the displacements are interpolated in five points, the four vertices and the center of one face.

2.4. Algorithm and Numerical Examples. The algorithm used is of course the Uzawa algorithm described in Paragraph 1.4. In this case, the problem in displacements is a standard convex minimization problem over a linear space, but the problem in $\underline{\mathbb{F}}$ con-

sists of a series of independent algebraic systems of nine equations of order 3. Its numerical solution requires a further decomposition which is described in [4].

Two numerical examples illustrating the above methods applied to the resolution of equilibrium problems in incompressible finite elasticity are presented, both in ill conditioned situations with high compression rates. The first one represents the compression of half a rubber cylinder at a 40% rate (first discretization). The second one represents the compression at the same rate of 1/8 of a cube, computed with the second type of finite elements.

3. LIMIT LOAD COMPUTATION IN PLASTICITY

3.1. Limit Load Analysis. The limit load analysis of a structure does not consider the prediction of the global behavior of the structure but only the problem of determining whether a given load can be supported or not. It only requires a partial knowledge of the local behavior of the structure, i.e. what stresses can be locally supported, and gives an information of great practical importance for structures design. It can be the only information available in situations like in soil mechanics where a precise knowledge of the material behavior is practically out of reach.

In that context, let us consider a structure occupying a domain Ω of \mathbb{R}^N , and suppose that the set of locally admissible stresses is characterized at each point \underline{x} of Ω by a closed convex set $C(\underline{x})$ of $\mathbb{R}_s^{N \times N}$. This structure is submitted to an external load distribution of body forces \underline{f} and surface tractions \underline{t} .

DEFINITIONS 3.1. A load $\{\underline{f}, \underline{t}\}$ is potentially admissible if and only if there exists a stress distribution \underline{g} almost everywhere admissible ($\underline{g}(\underline{x}) \in C(\underline{x})$) equilibrating this load.

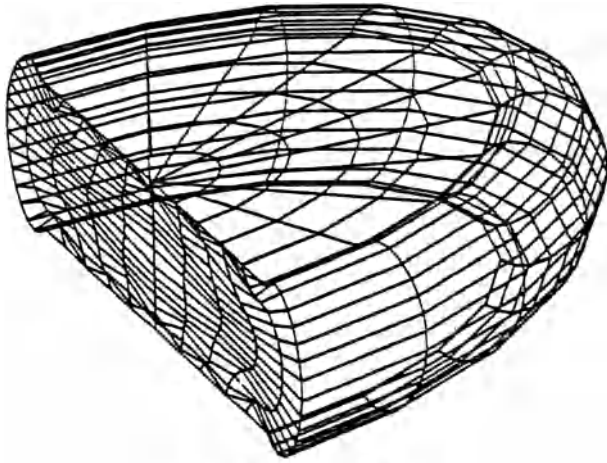
In no case, non potentially admissible loads can be supported. The converse is true for small strains perfect plasticity. Our problem is now to characterize formally and numerically potentially admissible loads in small strains.

3.2. Kinematic Characterization. General assumptions on the convex sets $C(\underline{x})$ of locally admissible stresses allow the replacement of the above static characterization of potentially admissible loads by an equivalent kinematic approach ([10], [11]) :

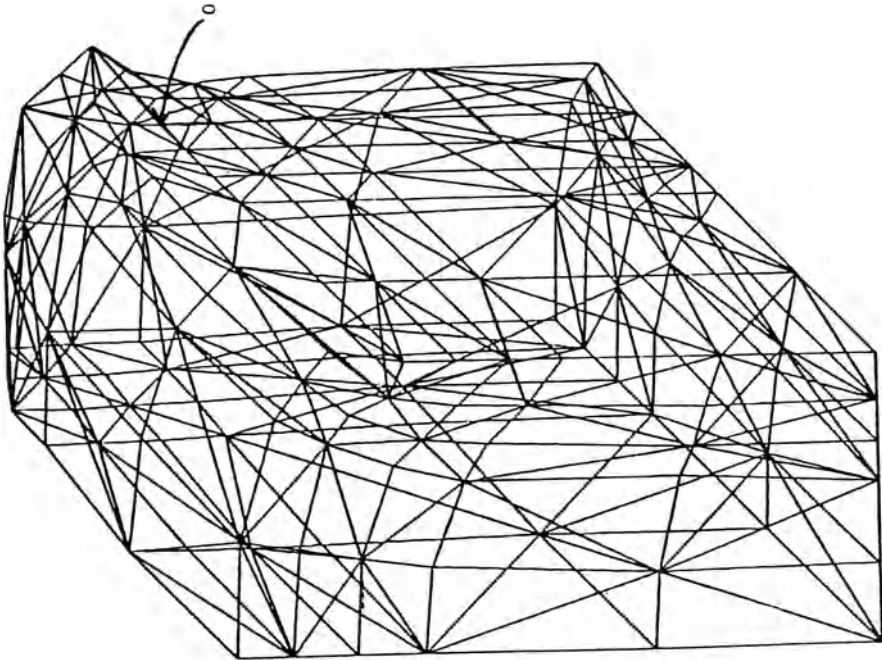
THEOREM 3.1. Assume $C(\underline{x})$ (respectively its projection on the zero trace tensor space if $C(\underline{x})$ is invariant by translation along scalar tensors) to be closed, convex, uniformly bounded. Then, a load $\{\underline{f}, \underline{t}\}$ is potentially admissible if and only if

$$(3.1) \quad \inf_{\underline{v} \in V} \left\{ \int_{\Omega} \psi_c(\underline{g}(\underline{v})) - \int_{\Omega} \underline{f} \cdot \underline{v} - \int_{\partial\Omega_1} \underline{t} \cdot \underline{v} \right\} = 0,$$

where $\psi_c(\underline{g}) = \sup_{\underline{g} \in C(\underline{x})} \underline{g} \cdot \underline{g}$.



40% Compression



Compression of rubber parts

Above $\underline{\varepsilon}(\underline{v})$ denotes the deformation rate tensor associated to the velocity field \underline{v} and V represents the set of kinematically admissible velocity fields which can be taken as

$$V = \{ \underline{v} \in H^1(\Omega), \underline{v} = 0 \text{ on } \partial\Omega - \partial\Omega_1 \}.$$

This theorem means that, for a potentially admissible load, the plastic dissipation energy must be greater than the external potential energy for every kinematically admissible velocity field.

3.3. Regularization. Problem (3.1) cannot be directly treated by the methods of Paragraph 1, because its solution exists only in the space $BD(\Omega)$ ([11], [12]) whose approximation by finite element spaces is not yet satisfactory. The same difficulty arises for the somewhat equivalent Hencky's formulation of equilibrium problems in plasticity studied in [13].

Therefore, we first introduce as in [14], a regularized variational form of (3.1), using Norton-Hoff's type materials, whose asymptotic behavior leads to (3.1) when the viscosity tends to zero. The convergence of the minima can be proved, but not the convergence of the solutions. However, this convergence is sufficient for characterizing admissible loads. We have [14] :

THEOREM 3.2. *Under the assumptions of Theorem 3.1, a load $\{\underline{f}, \underline{t}\}$ is potentially admissible if and only if*

$$(3.2) \quad \lim_{p \rightarrow 1} G_p(\underline{f}, \underline{t}) = 0,$$

$$(3.3) \quad G_p(\underline{f}, \underline{t}) = \left\{ - \frac{p}{(p-1)\text{mes}(\Omega)} \inf_{\underline{v} \in V_p} J_p(\underline{v}) \right\}^{1-1/p},$$

$$(3.4) \quad V_p = \{ \underline{v} \in \widetilde{W}^{1,p}(\Omega), \underline{v} = 0 \text{ on } \partial\Omega - \partial\Omega_1 \},$$

$$(3.5) \quad J_p(\underline{v}) = \frac{1}{p} \int_{\Omega} |\psi_c(\underline{\varepsilon}(\underline{v}))|^p - \int_{\Omega} \underline{f} \cdot \underline{v} - \int_{\partial\Omega_1} \underline{t} \cdot \underline{v}.$$

Moreover, G_p is a function convex and positively homogeneous of order 1 in $\{\underline{f}, \underline{t}\}$ monotone in p .

The numerical way of characterizing admissible loads is then straightforward :

Let $\{\underline{f}, \underline{t}\}$ be a given load ;

Build, for fixed p a minimizing sequence \underline{v}_{np} of J_p ;

Compute

$$\lambda = \sup_p \sup_{\underline{v}_{np}} \left\{ - \frac{p}{(p-1)\text{mes}(\Omega)} J_p(\underline{v}_{np}) \right\}^{1-1/p} ;$$

Conclude :

{ if $\lambda > 1$, the load is not potentially admissible ;
if $\lambda < 1$, the load is potentially admissible.

This method leads to the following comments :

a/ no differentiability assumption has been made on ψ_c . Thus the method is quite general. It can be applied in the three-dimensional case ;

b/ as soon as for one \underline{v}_{np} , the quantity $[p/(p-1)\text{mes}(\Omega)]J_p$ is greater than one, the load is not potentially admissible ;

c/ Norton-Hoff viscoplastic regularization was used long ago in [15] and [16], but these authors were using the convergence of the solutions, which is wrong. Here is only used the convergence of the minima ;

d/ it is easier numerically to compare λ to 1 than comparing energies to zero as in [17].

3.4. Augmented Lagrangian Formulation. To characterize the potentially admissible loads, we just need now to build a minimizing sequence of J_p on V_p . For simplicity, we will assume that J_p is Lipschitz continuous on V_p , which holds under the assumptions of Theorem 3.1 only when $C(\underline{x})$ is bounded. Otherwise, the constraint $\text{div } \underline{v} = 0$ has to be imposed on the kinematically admissible velocity fields in order to recover this continuity, which changes the discretization technique but not the numerical method.

To introduce a discrete augmented lagrangian formulation for the minimization of J_p , consider :

$$V_h = \{ \underline{v} \in C^0(\bar{\Omega}), \underline{v}|_{\Omega_k} \in P_1(\Omega_k) \},$$

$$L_h = \{ q, q|_{\Omega_k} = \text{constant} \},$$

where the Ω_k are a family of regular N -simplices which form a triangulation of Ω .

Now define

$$X_h = V_h \cap V_p,$$

$$Y_h = Z_h = L_h,$$

$$\mathcal{L}(\underline{v}, \underline{F}, \underline{\lambda}) = \int_{\Omega} \left\{ \frac{1}{p} |\psi_c[(\underline{F} + \underline{F}^T)/2]|^p + \frac{R}{2} |\nabla \underline{u} - \underline{F}|^2 + \underline{\lambda} \cdot (\nabla \underline{u} - \underline{F}) \right\} - \int_{\Omega} \underline{f} \cdot \underline{v} - \int_{\partial\Omega_1} \underline{t} \cdot \underline{v},$$

and consider the problem :

$$\text{Find } \{ \{ \underline{u}, \underline{F} \}, \underline{\lambda} \} \text{ saddle-point of } \mathcal{L} \text{ on } (X_h \times Y_h) \times Z_h.$$

This problem is similar to (1.5). The same Uzawa algorithm can be used, which is

$$\underline{\lambda}^0 \text{ given in } Z_h.$$

For $\underline{\lambda}^n$ known, $\{ \underline{u}^n, \underline{F}^n \}$ is computed in $X_h \times Y_h$ by

$$\text{Minimizing } \mathcal{L}(\cdot, \cdot, \underline{\lambda}^n) \text{ over } X_h \times Y_h.$$

Then, $\underline{\lambda}^n$ is updated by

$$\underline{\lambda}^{n+1} = \underline{\lambda}^n + R(\nabla \underline{u}^n - \underline{F}^n).$$

Note that we are not interested in the solution \underline{u}^n , which might not converge very

quickly, but in G_p whose convergence is ensured by ([18]) :

THEOREM 3.3. For the above sequence $\{\underline{u}^n, \underline{\mathbb{E}}^n\}$,

$$g_p(\underline{u}^n, \underline{\mathbb{E}}^n) = \left[-\frac{p}{(p-1)\text{mes}(\Omega)} \left\{ \int_{\Omega} \left[|\psi_c((\underline{\mathbb{E}}^n + \underline{\mathbb{E}}^{nT})/2)|^p - \underline{\mathbb{E}} \cdot \underline{\mathbb{V}} \right] - \int_{\partial\Omega_1} \underline{\mathbb{E}} \cdot \underline{\mathbb{V}} \right\} \right]^{1-1/p}$$

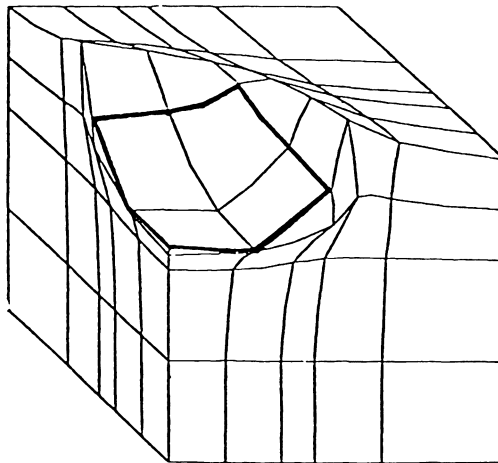
converges towards $G_p(\underline{\mathbb{E}}, \underline{\mathbb{E}})$ when $1/n$ and h tend to zero. The asymptotic rate of convergence is bounded independently of p and h by $\alpha / \sqrt{n \text{Log} n}$, α given in \mathbb{R}^+ , provided we satisfy for the considered values of p

$$G_p(\underline{\mathbb{E}}, \underline{\mathbb{E}}) \geq \alpha^{(p-1)/(3-2p)}.$$

With this result, the numerical characterization of potentially admissible load distributions is complete. It reduces to the computation of the dissipated energy for a sequence of quasi-static Norton-Hoff flow problems. This last problem is solved by augmented lagrangian techniques which give a converging estimation of this energy.

3.5. Numerical Example. The problem is to find the bearing capacity of a square foundation placed over a plane soil surface. The soil yielding criterium was Von Mises. The constraint $\text{div} \underline{\mathbb{V}} = 0$ was treated by an adequate discretisation of X_h and Y_h [18]. The minimization of $\ell(\cdot, \cdot, \underline{\lambda}^n)$ was solved by block relaxation.

The computed limit load corresponds to a pressure distribution 7 times greater than the limit load in a pure shearstress situation. The aspect of the soil after two seconds of the regularized viscoplastic-flow at $p = 1.02$ is represented on the next figure.



REFERENCES

- [1] FORTIN, M. ; GLOWINSKI, R.- Résolution Numérique de Problèmes aux Limites par des Méthodes de Lagrangien Augmenté. Collection Méthodes Mathématiques de l'Informatique. Dunod Bordas, Paris 1982.
- [2] LE TALLEC, P.- Existence and Approximation Results for Nonlinear Mixed Problems : Application to Incompressible Finite Elasticity. Numer. Math. 38, 365-382 (1982).
- [3] GLOWINSKI, R. ; LIONS, J.L. ; TREMCLIERES, R.- Numerical Analysis of Variational Inequalities, North Holland, Amsterdam 1981.
- [4] LE TALLEC, P.- Problème d'Equilibre d'un Corps Hyperélastique en Grandes Déformations. Thèse d'Etat, Université Pierre et Marie Curie, Paris 1981.
- [5] BALL, J.M.- Convexity Conditions and Existence Theorems in Non-Linear Elasticity. Arch. Rat. Mech. Anal. Vol. 63, 4, pp. 337-403 (1977).
- [6] LE TALLEC, P. ; ODEN, J.T.- Existence and characterization of hydrostatic pressure in finite deformations of incompressible elastic bodies. Journal of Elasticity, Vol. 11, n°4 (1981).
- [7] LE TALLEC, P.- Compatibility Condition and Existence Results in Discrete Finite Elasticity. Comp. Meth. in Appl. Mech. and Eng. 27, pp. 239-259 (1981).
- [8] GLOWINSKI, R. ; LE TALLEC, P.- A numerical Method in nonlinear incompressible elasticity using augmented Lagrangian techniques. SIAM Journal of Applied Math. Vol. 42, n°2, pp. 400-429 (1982).
- [9] RUAS, V.- A class of asymmetric simplicial finite element method for solving finite incompressible elasticity problems. Comp. Meth. in Appl. Mech. and Eng. Vol. 27, 3, pp. 319-343 (1981).
- [10] FREMOND, M. ; FRIAA, A.- Analyse limite. Comparaison des méthodes statique et cinématique. C.R.A.S. Paris, t. 286, Série A, pp. 107-109 (1978).
- [11] TEMAM, R. ; STRANG, G.- Duality and relaxation in the variational problems of plasticity, Jl. Mécanique, vol. 19, n°3, pp. 493-527 (1980).
- [12] SUQUET, P.- Sur les équations de la plasticité : existence et régularité des solutions. Jl. de Mécanique, vol. 20, pp. 1-39 (1981).
- [13] TEMAM, R.- Some asymptotic problems in mechanics. Conference on analytical and numerical approaches to asymptotic problems in analysis. Frank L.S. ed., Nijmegen, North-Holland, Amsterdam (1980).
- [14] FRIAA, A.- La loi de NORTON-HOFF généralisée en plasticité et viscoplasticité, Thèse d'Etat, Univ. P. et M. Curie (1979).
- [15] DELBECQ, J.M. ; FREMOND, M. ; PECKER, J. ; SALENCON, J.- Eléments Finis en plasticité et viscoplasticité. Jl. Méca. Appli., vol. 1, n°3, pp. 267-304 (1977).
- [16] CASCIARO, R. ; DI CARLO, A.- Mixed finite elements models in limit analysis. In Computational Methods in Nonlinear Mechanics, T.I.C.O.M., Austin (1974).
- [17] MERCIER, B.- Sur la théorie et l'analyse limite de problèmes de plasticité. Thèse d'Etat, Univ. P. et M. Curie (1977).
- [18] GUENNOUNI, T. ; LE TALLEC, P.- Calcul à la Rupture : Régularisation de Norton-Hoff et Lagrangien Augmenté. Journal de Mécanique (to appear).

PART III

Modern Numerical Methods

APPLICATION OF FRONT TRACKING TO TWO-DIMENSIONAL GAS DYNAMICS
CALCULATIONS*

B. Plohr, J. Glimm, O. McBryan

Courant Institute
New York University
New York, N.Y. 10012

Abstract

We present the results from some validation tests for a two-dimensional front tracking code for gas dynamics. We study initial value problems with circularly symmetric initial data and compare the results to those obtained by a one-dimensional calculation exploiting the circular symmetry. We also study the Kelvin-Helmholtz instability in the compressible, small amplitude regime and compare the results with a linear perturbation analysis. Results from a large amplitude calculation are included, showing vortex formation and roll-up.

1. Introduction

In this paper we present initial validation tests for a front tracking code with gas dynamics capabilities. The structure and design of the code allows the tracking of shock and contact discontinuities and their interactions. Here we present two series of test calculations which test the two-dimensional propagation of non-interacting shock and contact waves. The problems are chosen to allow verification by means of independent solution obtained by elementary means.

The modes of wave propagation in two-dimensional gas dynamics are shock waves (nonlinear sound waves) contact discontinuities (temperature fronts) and slip lines (transverse velocity discontinuities). Our

To test the propagation of slip lines, we study the classical Kelvin-Helmholtz instability of vortex sheets. The comparison solution is obtained by perturbation calculations in the compressible, small amplitude regime. We also include results from large amplitude calculations.

For the propagation of shock waves the standard method is to use finite differences. These methods, however, provide less resolution of the shock than does front tracking, and they fail to resolve the contact at all unless special modifications are made [1]. For the propagation of slip lines the method of finite differences is unsuitable, and specialized methods, such as vortex methods, are used. Vortex methods are based on integration of Laplace's equation, and so only apply to incompressible flows. Thus vortex methods do not apply to our test calculations.

We view our code as having two major advantages: flexibility as a general purpose fluid dynamics code, combined with the high resolution of special purpose codes.

2. Description of the Method

Our two-dimensional front tracking code is an extension to inviscid, compressible gas dynamics of a similar code [2] for the simulation of oil reservoirs. The data structure of our method contains a collection of time dependent curves (i.e. a front) in addition to a regular, time independent, two-dimensional spatial grid. The front divides the plane into connected components and the calculation is organized into the two steps of propagation of the curves and propagation of the solution in each connected components. In order to allow solutions which are discontinuous across these curves, additional state variables are introduced near the front, beyond those associated with regular grid positions.

The front and the solution values adjacent to it are propagated by solving Riemann problems. Two-dimensional effects, such as curvature of the wave front, act as an effective source term and can give rise to waves missing from the one-dimensional theory. In the present version we handle these effects in a somewhat ad hoc fashion by including operator splitting for the source term as a correction to a one-dimensional Riemann problem. This method will not be adequate in general and must be extended to a higher order Riemann solver, utilizing

higher order data (solution gradients as well as solution values) on each side of the front.

In each of the components, free of tracked discontinuities, the equations of motion are solved by a finite difference method, specifically the Lax-Wendroff method with spatial operator splitting. This extends the method described in [2], which used the random choice method in the interior. This extension was found to be useful for our gas dynamics calculations.

3. Propagation of Shocks and Contacts

We study initial value problems with circularly symmetric initial data. An initial pressure discontinuity across a circle gives rise to two discontinuous waves, a shock and a contact. It was found necessary to track the contact wave as well as the shock, since otherwise the Lax-Wendroff method was too unstable on reasonable grids. For these problems the comparison solution is obtained by an elementary one-dimensional calculation exploiting the radial symmetry. This calculation uses the random choice method, together with a time-splitting step to take account of the source term introduced by the change in coordinates [3].

In Figs. 1a - d are shown the results of a calculation with the pressure inside the initial circle 100 times higher than outside. Fig. 1a shows the positions of the contact (the inside circle) and the shock (the outside circle) together with the velocity distribution at a time midway in the run. The corresponding fixed-time density and pressure profiles as a function of radius are shown in Figs. 1b,c. In these profiles the solid curve is the result from the exact calculation, while the vertical error bars extend from the minimum to the maximum values in the two-dimensional solution at fixed radii, indicating the angular dependence of the solution. In Fig. 1d the contact and shock positions versus time, with the solid curve showing the exact answer, and the horizontal error bars showing the deviation of the two-dimensional front from being circular.

Similarly, Figs. 2a-d show the results for a calculation with the pressure on the inside 100 times smaller than the outside. Since for this run there is an outward-moving rarefaction it was necessary, in order to preserve the circular symmetry of the problem, to introduce

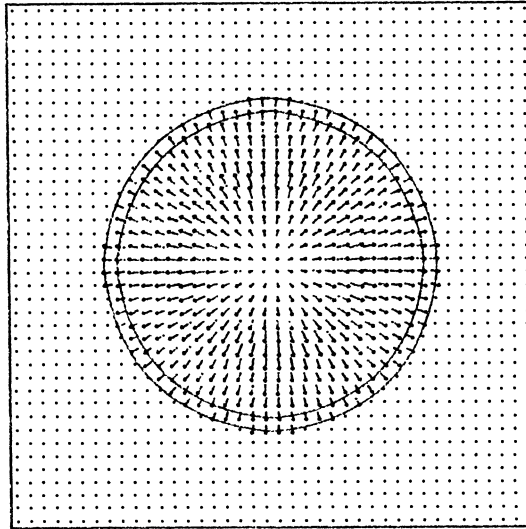


Fig. 1a. The velocity arrows and the tracked shock and contact discontinuities are pictured for a 40 x 40 run after 28 time steps. The initial data consisted of an initial discontinuity at radius .2 with pressure ratio $p_{in}/p_{out} = 100$, uniform density, and zero velocity.

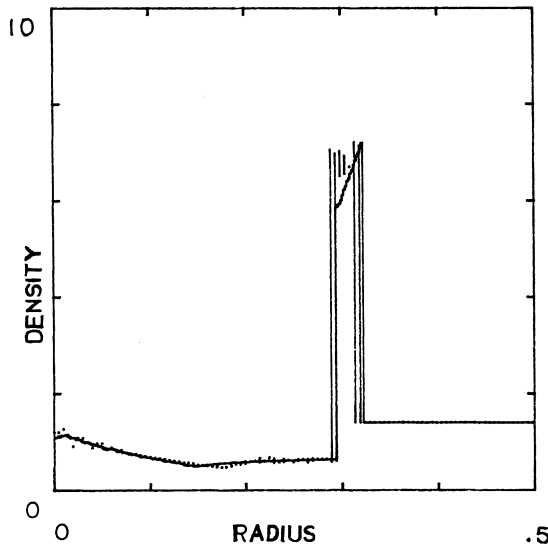


Fig. 1b. A plot of density vs. radius corresponding to Fig 1a. is shown. The solid line shows the results obtained by the one-dimensional calculation using the random choice method. The vertical lines represent the range of density values in the two-dimensional calculation at a fixed radius as the angle varies. Thus the vertical lines represent the error bars for the angular dependence.

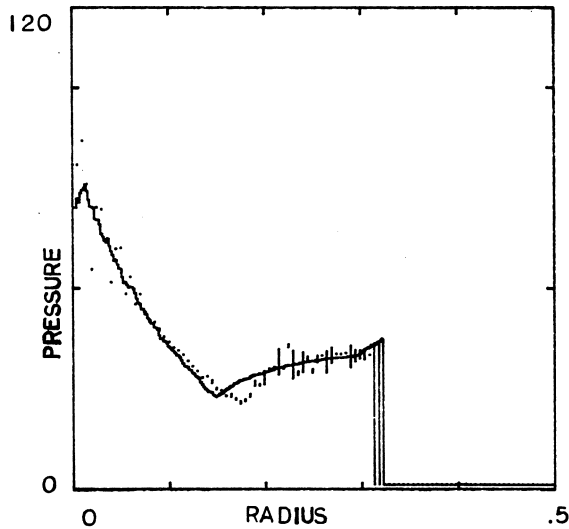


Fig. 1c. A plot of pressure vs. radius corresponding to Fig. 1a. is shown. The solid and vertical lines represent the one - and two-dimensional results, as explained in the caption to Fig. 1b.

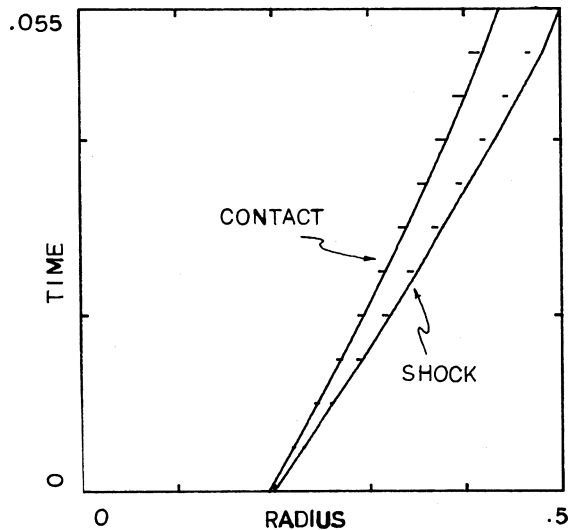


Fig. 1d. A plot of the radius of the contact and the radius of the shock as a function of time. The solid lines are obtained by passive tracking in the one-dimensional random choice solution. The horizontal lines represent the range of radius values as the angle varies, and so represents the deviation of the discontinuity from a circle.

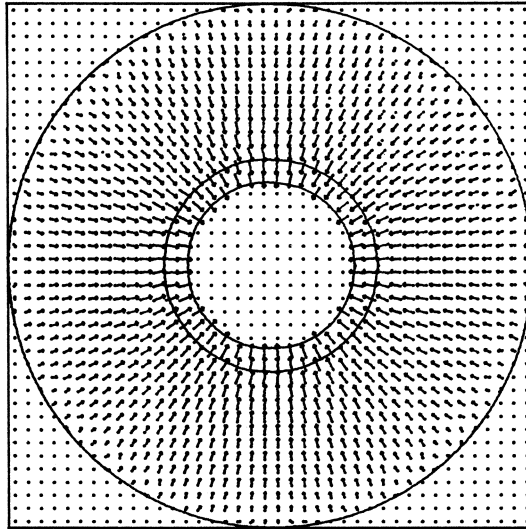


Fig. 2a. The velocity arrows and the tracked shock and contact discontinuities are pictured for a 40×40 run after 42 time steps. The initial data consisted of an initial discontinuity at radius .35 with pressure ratio $p_{in}/p_{out} = .01$, uniform density, and zero velocity. The outermost circle is a reflecting wall, introduced to maintain circular symmetry.

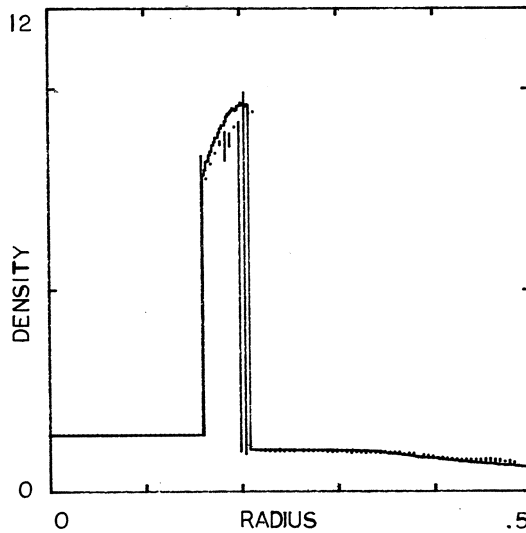


Fig. 2b. A plot of density vs. radius corresponding to Fig. 2a. is shown. The solid and vertical lines represent the one - and two-dimensional results, as explained in the caption to Fig. 1b.

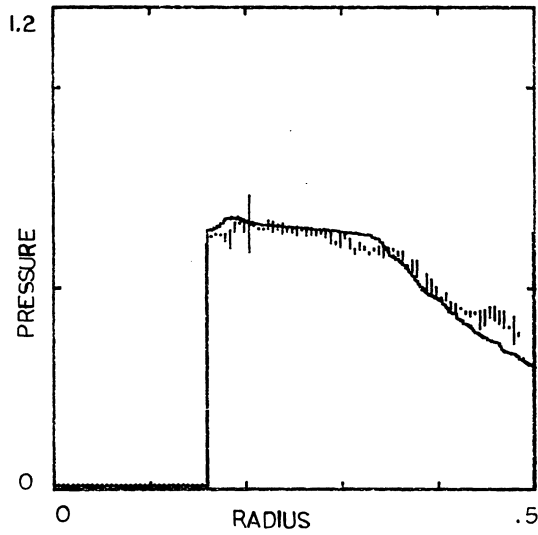


Fig. 2c. A plot of pressure vs. radius corresponding to Fig. 2a. is shown. The solid and vertical lines represent the one - and two-dimensional results.

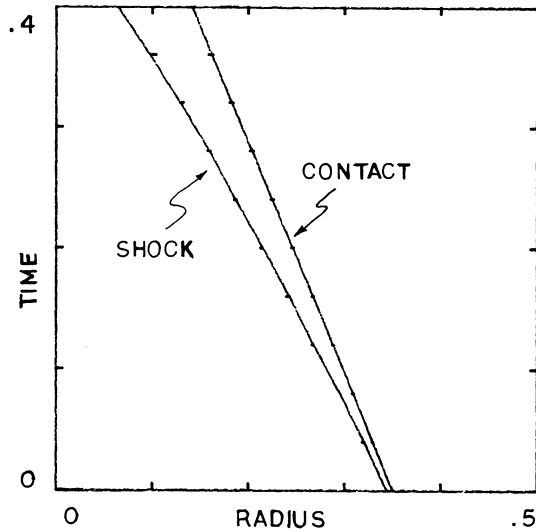


Fig. 2d. A plot of the radius of the shock and the radius of the contact as a function of time. The solid and horizontal lines represent the one - and two-dimensional solutions, as described in the caption to Fig. 1d.

a circular reflecting wall (the outer-most circle in Fig. 2a.).

4. Propagation of a Slip

The classical Kelvin-Helmholtz instability concerns two fluids separated by an interface across which there is a discontinuity in the tangential velocity. Such a flow configuration is unstable against a sinusoidal perturbation of the interface.

In the regime where the amplitude is small relative to the wave length, a first order correction to the linearized equations provides a comparison solution. Consider the situation illustrated in Fig. 3a. We look for a periodic solution of the equations of gas dynamics that reduces, in the limit where the amplitude of the slip line is small, to a flow with constant density ρ_0 and pressure p_0 throughout, and with particle velocity v_0 above and $-v_0$ below. Because the solution will have constant entropy throughout, and because the flow will be irrotational away from the slip line, the equations to be solved are (1) the conservation of mass equation and (2) Crocco's equation (which is the exact version of Bernoulli's equation for compressible flows):

$$\rho^{a,b} \frac{\partial}{\partial t} + \nabla_{\sim} \cdot (\rho^{a,b} \nabla_{\sim} \phi^{a,b}) = 0 \quad (1)$$

$$\phi^{a,b} \frac{\partial}{\partial t} + H(\rho^{a,b}) + \frac{1}{2} |\nabla_{\sim} \phi^{a,b}|^2 = H(\rho_0) + \frac{1}{2} v_0^2, \quad (2)$$

where we have written the velocities above and below as $\nabla_{\sim}^{a,b} = \nabla_{\sim} \phi^{a,b}$, and H is the enthalpy function. The boundary conditions reflect the requirements that (a) particles at the slip line remain at the slip line, so $(\frac{\partial}{\partial t} + \nabla_{\sim} \cdot \nabla_{\sim})(y - \hat{y}) = 0$, (b) there is no flow through the upper and lower boundaries, and (c) the flow is periodic in the x -direction:

$$\left. \frac{\partial \phi^{a,b}}{\partial y} \right|_{y=\hat{y}} = \hat{\frac{\partial y}{\partial t}} + \left. \frac{\partial \phi^{a,b}}{\partial x} \right|_{y=\hat{y}} \hat{\frac{\partial y}{\partial x}} \quad (a)$$

$$\left. \frac{\partial \phi^{a,b}}{\partial y} \right|_{y=y^{a,b}} = 0 \quad (b)$$

$$\phi^{a,b} \Big|_{x=x_l} = \phi^{a,b} \Big|_{x=x_r} + \text{const.} \quad (c)$$

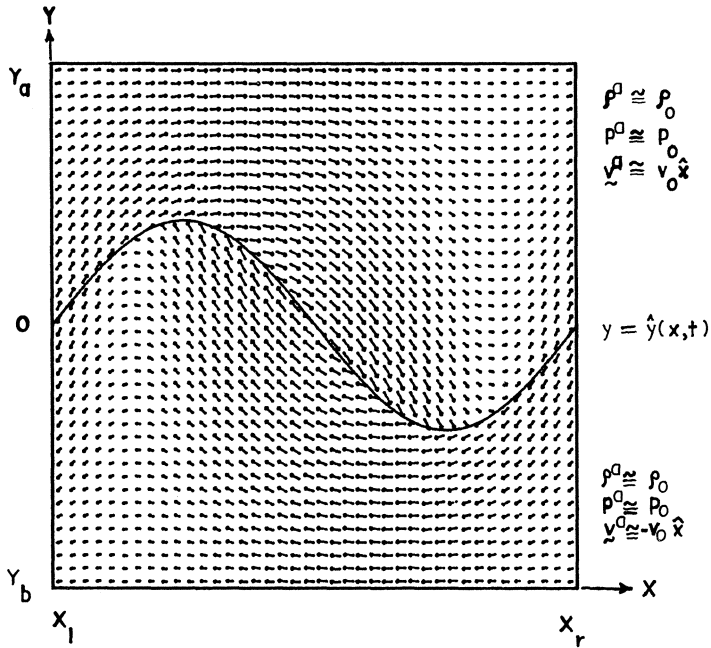


Fig. 3a. The flow configuration for the Kelvin-Helmholtz instability is pictured. There is a sinusoidal slip line separating the region above, with density ρ^a , pressure p^a , and velocity \underline{v}^a , from the region below, with density ρ^b , pressure p^b , and velocity \underline{v}^b . In the linear regime the density and pressure is almost constant throughout the flow, with values ρ_0 and p_0 , while the velocity above is approximately $v_0 \hat{x}$ and the velocity below is approximately $-v_0 \hat{x}$. The position of the slip line is given by $y = \hat{y}(x,t)$.

Substituting

$$\phi^{a,b}(x,y,t) = \pm v_0 x + \hat{\phi}^{a,b}(x,y,t)$$

$$\rho^{a,b}(x,y,t) = \rho_0 + \hat{\rho}^{a,b}(x,y,t)$$

and retaining only terms of first order in \hat{y} , $\hat{\rho}$, and $\hat{\phi}$ we obtain

$$\left(\frac{\partial}{\partial t} \pm v_0 \frac{\partial}{\partial x}\right) \hat{\rho}^{a,b} + \rho_0 \nabla^2 \hat{\phi}^{a,b} = 0 \quad (\hat{1})$$

$$\left(\frac{\partial}{\partial t} \pm v_0 \frac{\partial}{\partial x}\right) \hat{\phi}^{a,b} + H'(\rho_0) \hat{\rho}^{a,b} = 0 \quad (\hat{2})$$

$$\left.\frac{\partial \hat{\phi}^{a,b}}{\partial y}\right|_{y=0} = \left(\frac{\partial}{\partial t} \pm v_0 \frac{\partial}{\partial x}\right) \hat{y} \quad (\hat{a})$$

$$\left.\frac{\partial \hat{\phi}^{a,b}}{\partial y}\right|_{y=y_{a,b}} = 0 \quad (\hat{b})$$

$$\hat{\phi} \Big|_{x=x_\ell} = \hat{\phi} \Big|_{x=x_r} \quad (\hat{c})$$

Equations $(\hat{1})$ and $(\hat{2})$ combine to yield the wave equation

$$-\left(\frac{\partial}{\partial t} \pm v_0 \frac{\partial}{\partial x}\right)^2 \hat{\phi}^{a,b} + c_0^2 \nabla^2 \hat{\phi}^{a,b} = 0,$$

where $c_0^2 = \rho_0 H'(\rho_0)$ is the speed of sound. Assuming \hat{y} is of the form

$$\hat{y}(x,t) = \varepsilon e^{\sigma t} \sin\left(2\pi \frac{x}{x_r - x_\ell}\right)$$

these equations can be solved explicitly. The requirement that the pressure be constant across the slip line yields a nonlinear equation for the growth rate σ , which may be solved numerically by an iterative procedure.

We note that if compressibility effects are not taken into account, Crocco's equation is replaced by Bernoulli's equation and an analogous derivation yields Laplace's equation in place of the wave equation. The compressibility is thus seen to be governed by the Mach number v_0/c_0 .

The results from our numerical experiments are shown in Figs. 3b-c.

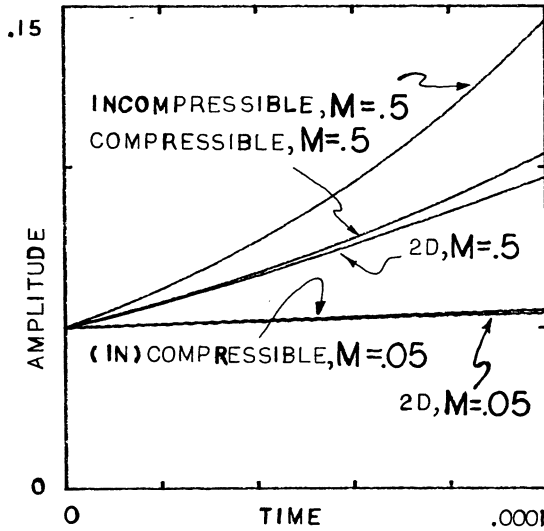


Fig. 3b. A plot of the amplitude of the slip line vs. time is shown for the Kelvin Helmholtz instability with Mach numbers $v_0/c_0 = .05$ and $.5$. The two-dimensional results were obtained on a 20×20 grid with 131 and 186 time steps, respectively; they were initialized with the results from the compressible linear analysis. Superimposed are the results from the compressible and incompressible perturbation analyses.

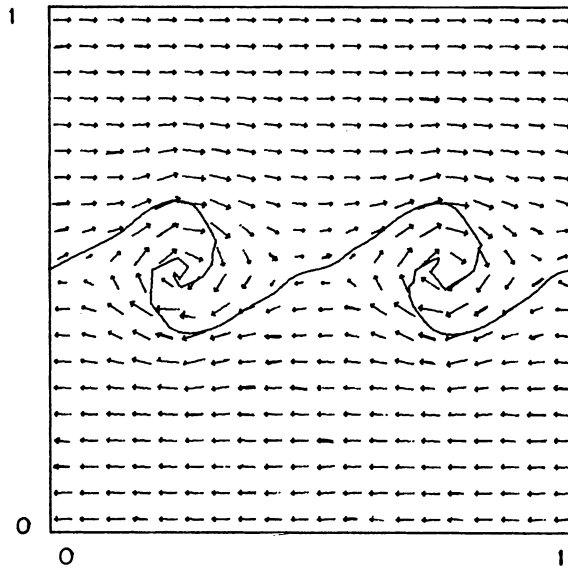


Fig. 3c. The vortex formation and rollup in the Kelvin Helmholtz instability are shown for a problem in the large-amplitude regime. The calculation was made on a 20×20 grid for 39 time steps. Initially the slip line was two periods of a sinusoid, and the Mach number was $.2$.

Fig. 3b is a plot of the amplitude of the sinusoidal slip line as a function of time for Mach numbers .5 and .05, with the initial amplitude small. The results from the linear analyses, both compressible, are superimposed. As this plot demonstrates, the assumption of incompressibility is invalid for flows with high Mach numbers. Fig. 3c shows the slip line and the velocities late in a run which was initialized as a sinusoid with a large amplitude. This example shows evidence of vortex formation and roll-up.

Conclusion

The figures summarizing our test results show that there is good agreement between the two-dimensional front tracking results and the comparison solutions. From the circular runs it is seen that the major discrepancy occurs in the regions away from the tracked discontinuity, where the solution is obtained by a finite difference method. The Kelvin-Helmholtz runs show that the two-dimensional solution follows the results of a compressible perturbation analysis even at high Mach numbers where compressibility is important. It also displays the correct qualitative behavior in the regime where perturbation theory is applicable, with the rollup of the slip line at the level of one mesh block.

These results indicate that to extend the code it is important to improve the finite difference calculation. One way is to incorporate local mesh refinement. In addition, the interaction of shocks with other shocks and contacts should be handled. Work in progress by I.-L. Chern on shock wave diffraction patterns using front tracking has been reported in [4]; see especially Fig. 3 there.

References

1. J. Harten, "The Method of Artificial Compression," AEC Research and Development Report C00-3077-50, New York University (1974).
2. J. Glimm, E. Isaacson, D. Marchesin and O. McBryan, "Front Tracking for Hyperbolic Systems," Adv. Appl. Math. Vol. 2, p. 91 (1981).
3. G. Sod, J. Fluid Mech. Vol. 83, p. 785 (1977).
4. J. Glimm, "Theoretical Problems and Numerical Results for Non-linear Conservation Laws", NYU preprint.

THE MOVING FINITE ELEMENT METHOD: STRONG SHOCK
AND PENETRATION APPLICATIONS

ROBERT J. GELINAS AND SAID K. DOSS

Science Applications, Inc.
1811 Santa Rita Road, Suite 104
Pleasanton, California 94566

Introduction

The present work on the moving finite element (MFE) method has been motivated by those challenging problems in non-equilibrium physics which involve the central topics of this workshop: (i) codes; (ii) physical basis and engineering model formulation; (iii) numerical ODE and PDE solution methods; and (iv) large-scale computing hardware and software. In this article, primary emphasis is directed toward problems in blast wave hydrodynamics and in penetration mechanics (although other applications could include radiation transport, plasmas, laser interactions, structural response, combustion, etc.) which have the following common features:

- such transient non-equilibrium systems can be sufficiently far from equilibrium that their macroscopic properties are strongly coupled to their microscale dissipation processes;
- one or more shocks/traveling waveforms may propagate and interact at disparate rates; and
- extremely high levels of resolution (which are frequently out of the reach of fixed node PDE methods) are required in numerous portions of the problem domain.

The Moving Finite Element (MFE) Method

The MFE method which is described in this work is a new computational method for solving some of the most difficult partial differential equation (PDE) systems under study in many disciplines of applied science and technology. This MFE method moves nodes (grid mesh points) systematically to those locations which can yield the most accurate and stable solutions of the PDE's which are under consideration. This is accomplished by a generalized minimization procedure, which extends beyond conventional fixed node finite element methods, as well as beyond the logical basis of finite difference methods.

It has been observed in several areas of technical applications that the MFE method (i) saves nodes; (ii) gives unprecedented resolution of

physical transport processes in shocks and steep fronts in both reactive and non-reactive hydrodynamics; (iii) has simultaneous Lagrangian and Eulerian properties; (iv) effectively eliminates dilemmas of numerical diffusion, artificial viscosities, Gibbs overshooting and undershooting, node-tangling, and remap aliasing. The MFE method additionally admits to semi-automatic "user-dialing", compilation, and numerical solution of very large classes of PDE's - with greatly reduced amounts of dedicated programming (analogous to the highly effective ODE solvers of recent years).

The MFE method was discovered in 1973-74 by Prof. Keith Miller^(1,2) and has been reduced to practice in 1-D as a semi-automatic PDE solver for such applied problems as shocks, plasmas, continuum mechanics, and other physical systems by Gelinas and Doss,^(3,4) and by Djomehri.⁽⁵⁾

EXAMPLE PROBLEMS

Strong Shocks in Gases

Model fluid equations for non-reacting viscid, compressible gases are given in 1-D by the transport equations

$$\frac{\partial \rho}{\partial t} + \frac{\partial m}{\partial x} = 0 \quad , \quad (1)$$

$$\frac{\partial m}{\partial t} + \frac{\partial}{\partial x} \left[\frac{m^2}{\rho} + p \right] = \nu_1 \frac{\partial^2}{\partial x^2} \left(\frac{m}{\rho} \right) , \quad (2)$$

$$\frac{\partial E}{\partial t} + \frac{\partial}{\partial x} \left[\left(\frac{m}{\rho} \right) (E + p) \right] = \frac{\nu_2 \partial^2}{\partial x^2} \left[(E/\rho) - (m^2/2\rho^2) \right] , \quad (3)$$

where ρ , m , E are mass, momentum, and total energy densities; T is a temperature; ν_1 and ν_2 are viscosity and thermal conduction coefficients; and γ is the ratio of specific heats (assumed to be 1.4 in these examples). The pressure relationship for an ideal gas is given by:

$$p = (\gamma - 1) \left(E - \frac{1}{2} \cdot \frac{m^2}{\rho} \right) . \quad (4)$$

An example of two colliding strong shocks has been presented previously by Woodward and co-workers.^(6,7) This example uses reflection boundary conditions at $x = 0$. and 1. and the following initial conditions:

$$m = 0 \qquad 0 \leq x \leq 1 \qquad (5)$$

$$\rho = 1 \qquad 0 \leq x \leq 1 \qquad (6)$$

$$E = \begin{cases} 2500 & 0 \leq x \leq .1 \\ 0 & .11 \leq x \leq .89 \\ 250 & .9 \leq x \leq 1. \\ \text{linear} & \text{otherwise} . \end{cases} \qquad (7)$$

The values of $v_1 = v_2 = 4 \times 10^{-3}$ in equations (2) - (3) were selected in an effort to have the MFE solutions correspond in some loose sense to the grid spacing used in 1200 node solutions of the inviscid fluid equations in References 6 and 7. Of course, one-to-one comparisons of these respective PDE solutions of the viscid and inviscid equations cannot be made in any strict sense because of those fundamental distinctions which hold between the physically derived dissipation mechanisms which appear explicitly as mathematical operators in the viscid fluid equations (1) - (3), vis á vis the numerical dissipation mechanisms associated with the finite grid spacing which are used to solve the inviscid equations in References 6 and 7.* It is nevertheless instructive to examine the potential role of physical transport processes in the non-equilibrium generation, evolution, and subsequent interactions in this strong shock example.

Figures 1 and 2 show the initial formation of those impulses which arise in the gas due to the removal at $t = 0$ of the hypothetical membranes at $x = 0.1$ and 0.9 . The MFE solutions in this example used 91 moving nodes. Figure 3 presents the MFE results at $t = 0.026$. The physical evolution of this problem up to the time of 0.026 can be summarized as follows:

Strong shocks are generated initially at $x = 0.1$ and at $x = 0.9$. The formation of these strong shocks evolves from the instantaneous generation at $t = 0+$ of large impulse functions with initially very narrow widths. These initial impulse functions and their subsequent evolution into strong shocks depend significantly upon the transport properties of the viscid fluid. While the shocks are running from both sides into the cold gas in the central region ($0.1 \leq x \leq 0.9$), strong rarefactions are propagating out into the hot gas regions adjacent to the walls. The cold gas is thus compressed, and dense slabs of gas are

*The moving node properties have effectively suppressed any dissipation of numerical origin, relative to the governing physical dissipative processes in the viscid fluid equations, in these MFE results.

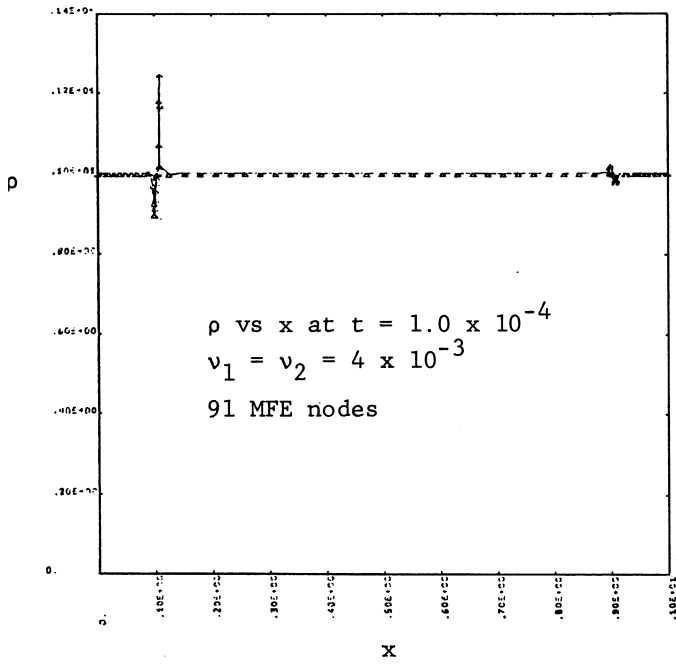


Figure 1. MFE Solution of Strong Shock Example

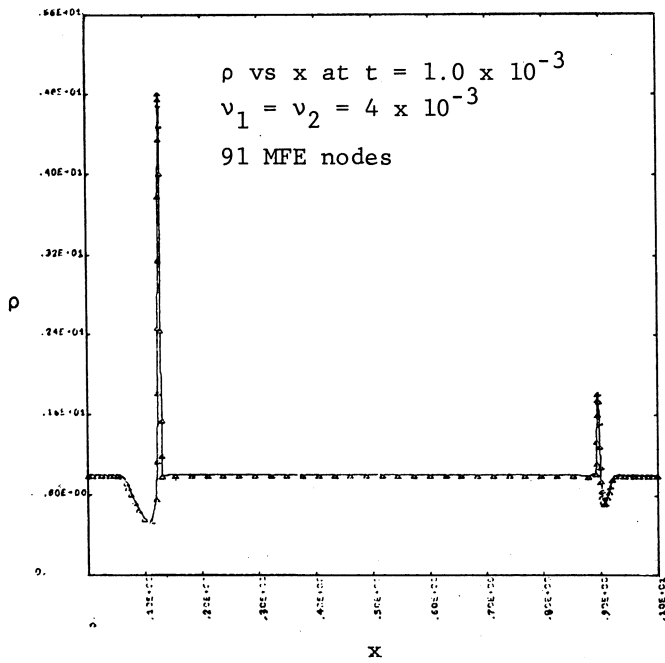


Figure 2. MFE Solution of Strong Shock Example

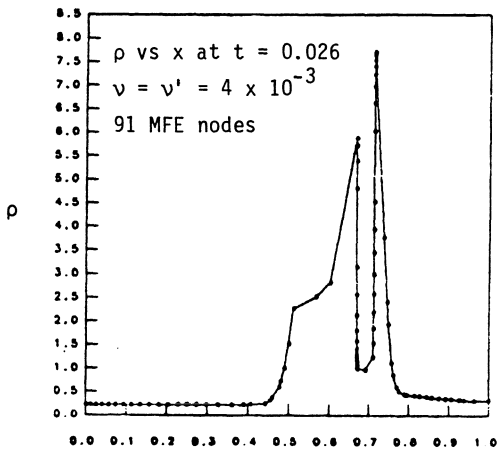


Figure 3. MFE Solution of the Viscid Fluid Equations. Strong Shock Example.

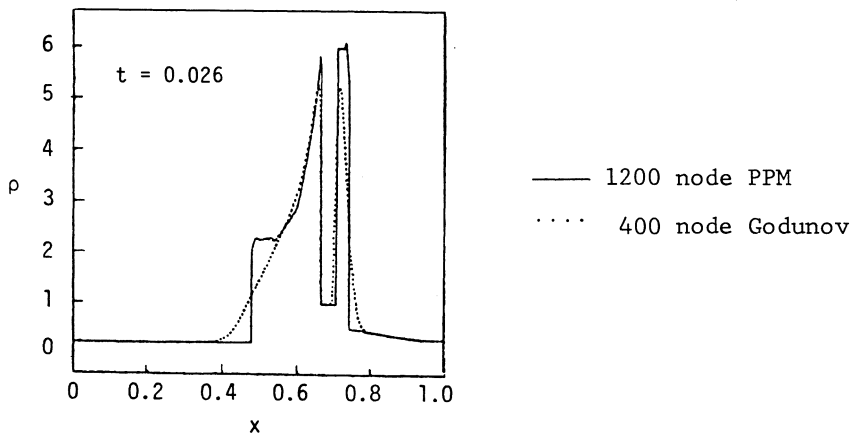


Figure 4. Godunov and PPM Solutions of the Inviscid Equations. Strong Shock Example.

formed which then move toward each other in the central region. At $t = 0.026$, the rarefactions have reflected from the walls and have caught up, from behind, and interacted with the contact surfaces which separate the hot and cold fluids at the rear edges of the slabs. During this time, the contact discontinuities have been broadened to an extent determined by the transport of energy across the contact

surface by thermal conduction. The strength of interactions between the reflected rarefactions, shocks, and contact discontinuities is determined by the magnitudes of the gradients of these fluid structures. Sensitivity tests in this work indicate that the fluid profiles in such strong shocks depend not only upon the magnitudes of transport coefficients v_1 and v_2 but also upon the effective functional forms of the dissipation operators in the fluid equations. For example, alternative functional forms were assumed and tested for constitutive model diffusion operators in equations (2) and (3);* and both quantitative and qualitative differences were noted in the resulting alternative MFE solutions. Corresponding solutions of the inviscid equations with a shock-tracking method (see Figure 4) show that the numerical dissipation effects in the inviscid PDE solutions do not correspond to the effects of the constitutive model operators in the viscid PDE solutions.

In these MFE solutions, neighboring nodes approached each other to within $\Delta x = 1 \times 10^{-6}$ during shock interactions. The 91 node MFE solutions required 300 sec. CPU time in order to run from $t = 0$ to $t=0.05$ on the CDC 7600 computer at the Lawrence Berkeley Laboratory. Vectorization and optimization of this purely research-oriented code can yield significant improvements in computational economy.

Colliding Steel Plates (Elastic-Plastic Deformation)

Figure 5 indicates schematically a classic plate-slap example.

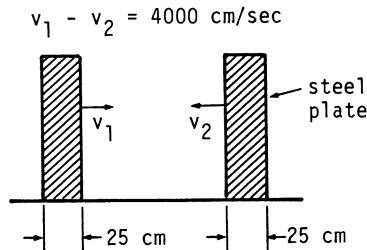


Figure 5. Schematic illustration of steel plate slap example.

*Whereas the functional forms of dissipation operators are well-defined in many gas dynamics applications, there exists at this time considerably greater uncertainty in visco-elastic and visco-plastic models in such other applications as continuum mechanics.

The hydrodynamic equations in 1-D slab geometry are written in the form

$$\frac{\partial \rho}{\partial t} = - \frac{\partial}{\partial x} m \quad (8)$$

$$\frac{\partial m}{\partial t} = - \frac{\partial}{\partial x} \left(\frac{m^2}{\rho} \right) + \frac{\partial}{\partial x} \Sigma \quad (9)$$

$$\frac{\partial E}{\partial t} = - \frac{\partial}{\partial x} \left(\frac{mE}{\rho} \right) + \frac{\partial}{\partial x} \left(\frac{m}{\rho} \Sigma \right) \quad , \quad (10)$$

where the stress tensor Σ can be written as

$$\Sigma = -p + s_1 \quad , \quad \text{with} \quad (11)$$

$$p = \frac{a_1}{\rho_0} (\rho - \rho_0) \equiv a_1 C \quad . \quad (12)$$

The PDE for the first stress deviator s_1 is

$$\frac{\partial}{\partial t} (\rho s_1) = - \frac{\partial}{\partial x} (m s_1) = \frac{4}{3} \rho \mu \frac{\partial}{\partial x} \left(\frac{m}{\rho} \right) \quad , \quad (13)$$

where μ is the shear modulus. Introducing $S_1 = \rho s_1$, these PDE's can be written and solved in the form:

$$C_t = -m_x / \rho_0 \quad (14)$$

$$m_t = [(m^2/\rho) + a_1 C - (S_1/\rho)]_x \quad (15)$$

$$E_t = -[(mE/\rho) + a_1(mC/\rho) - (mS_1/\rho^2)]_x \quad (16)$$

$$(S_1)_t = -[(mS_1/\rho) - (4\mu m/3)]_x - (4\mu \rho_0 m/3\rho) C_x \quad . \quad (17)$$

Two constitutive models were considered in this work. In the (first) classical Levy-Mises yield model, the solution of Equation (17) for S_1 is replaced by S_1 multiplied by $|2\rho Y_0/3S_1|$ whenever s_1^2 exceeds $(2Y_0/3)^2$. The material yield strength is denoted by Y_0 . Although this perfectly plastic formulation may have the appearance of a Newtonian viscid fluid formulation; it is, in fact, inviscid and is thus numerically ill-posed when truly infinite shock gradients are formed. (There is really no deformation rate dependence or viscosity implied by this classical Levy-Mises yield model due to the fact that, beyond the plastic limit, an increase in the rate of deformation components does not change the stress deviator component.)⁽⁸⁾ A Bingham model of visco-plasticity is therefore considered as a second constitutive model, as will be discussed further below.

In this example initial conditions on the interval $[0, 50]$ are: $\rho(x, 0) = \rho_0 = 7.85 \text{ g/cm}^3$ for $0. \leq x \leq 50.$; $m(x, 0) = 3.14 \times 10^4 \text{ g/cm}^2 \text{ - sec}$ for $0. \leq x \leq 24.95$ and for $25.05 \leq x \leq 50.0$; $m(x, 0) = \text{linear}$ for

$24.95 \leq x \leq 25.05$, and $m(x, 0) = 0$ for $x = 25.$; $E(x, 0) = (m^2/2\rho)$
and $S_1(x, 0) = 0.$ for $0. \leq x \leq 50.$

Sixty-one MFE nodes and the following parameter values are used in these calculations: $a_1 = 1.69 \times 10^{12}$ dynes/cm² (1.69 MB); $\mu = 8.22 \times 10^{11}$ dynes/cm² (0.822 MB); and $Y_0 = 3.0 \times 10^9$ dynes/cm³ (0.003MB). The MFE solutions were found to be perfectly symmetrical about the interface at $x = 25$ cm, and all of the results discussed below were reproducible with the use of 26 nodes on a domain $x = (0, 25)$ with reflection boundary conditions. The MFE solution in Figure 6 is nearly a weak solution for the stress tensor $\Sigma = (-p + S_1)$ which has approached the inviscid limit to within machine noise. This MFE solution was obtained by first attempting to solve the purely inviscid equations (14) - (17) (with the Levy-Mises yield model) above. In this case, when the PDE characteristics merge and attempt to form a truly infinite shock, the MFE nodes attempt repeatedly to move closer together than the allowed distances of closest approach--until those distances of closest approach are reduced essentially to a machine zero (much smaller than molecular scales). In this limiting case there is insufficient dissipation of kinetic energy, as evidenced by the momentum equation becoming extremely stiff and so ill-conditioned that numerical integration of the system halts prematurely. In the absence of essential physical dissipation processes, densities also assume non-physical, large values in these circumstances which are both physically and mathematically ill-posed. Faced with this condition of having too little numerical dissipation in the MFE method to maintain the nodes at physically reasonable distances of closest approach in the essentially inviscid equations (14)-(17), a tiny physical dissipation term of the form νm_{xx} was implemented in the material model for S_1 . This is essentially a Bingham model of viscoplasticity. With $\nu = 10^{-14}$ MB-sec, the MFE integration immediately became well-conditioned. The origin of the wave-like structure between $x = 10.$ and $x = 40$ in Figure 6 is uncertain. This structure does not have the familiar behavior of numerical oscillations, and it may be related in some way to a wave propagation effect in a nearly non-dissipative material. Additional sensitivity testing in this example suggested that these high levels of MFE resolution may be essential in calculations of those physical dissipation mechanisms which can govern fluid overpressure profiles under violent loading conditions. For example we observe that, for large values of dissipation (perhaps associated with a melting material), the stresses on

the back edges of the plates in Figure 6 were observed to go into tension, such as may occur in spalling. This testing also suggests that numerical PDE resolution may now have caught up with the detailed physics in dynamic loading models and that a new theoretical window has been opened for more quantitative visco-elastic and visco-plastic constitutive models to be hypothesized and tested in advanced physical simulations.

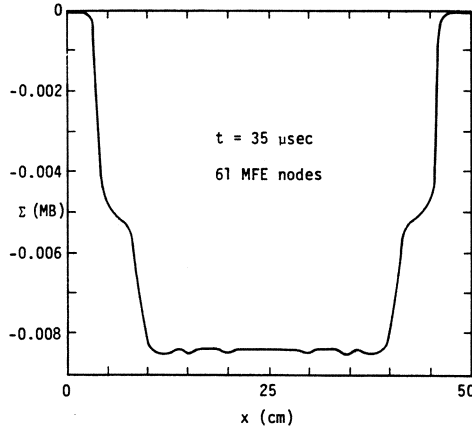


Figure 6. MFE solution of steel plate impact problem.

Testing of the MFE Method in 2-D

The extension of the MFE method from 1-D to 2-D is straightforward, as can be seen from the consideration of a general system of PDE's, $\dot{U} = L(U)$ (9,10)

$$\begin{aligned} \dot{u}_1 &= L_1(U) \\ \dot{u}_N &= L_N(U) \end{aligned} \quad (18)$$

Using piecewise linear approximants of $u_1 \dots u_N$, which are of the form $u = mx + ny + p$, on a hexagonally connected triangular mesh application of the chain rule to the differentiation of u_k gives

$$\dot{u}_k = \sum_j \dot{\alpha}^j \alpha^j k^j + \dot{x}_j \beta^j k^j + \dot{y}_j \gamma^j k^j, \quad \text{where} \quad (19)$$

$$\alpha^j k^j = \alpha^j = \frac{\partial u_k}{\partial \alpha^j}; \quad \beta^j k^j = \frac{\partial u_k}{\partial x_j}; \quad \gamma^j k^j = \frac{\partial u_k}{\partial y_j} \quad (20)$$

The basis functions α^j , β^j , and γ^j can be seen to be piecewise linear functions having their support in the hexagon of six triangles surrounding each j th node. The basic MFE method is formulated by requiring that the time derivatives $\{\dot{\alpha}_j, \dots, \dot{\alpha}_N, \dot{x}_j, \dot{y}_j\}$ be

found at each instant in such a way as to minimize the L^2 norm of the PDE residual, $||\dot{U} - L(U)||$. In order to handle the degeneracies which can sometimes occur in such a parametrization, regularization techniques are applied. That is, the more general function

$$\psi \equiv w_1^2 ||\dot{u}_1 - L_1(U)||^2 + \dots + w_N^2 ||\dot{u}_N - L_N(U)||^2 + \sum_{\substack{\text{triangle} \\ \text{altitudes}}} (\epsilon_j \dot{d}_j - S_j)^2,$$

is minimized with respect to the parameter derivatives $\{\dot{a}^1_j, \dots, \dot{a}^{N_j}_j, \dot{x}_j, \dot{y}_j\}$. The work in this article has applied the most elementary form of regularization functions in which the expressions for $\epsilon_j^2(d_j)$ and $\epsilon_j S_j = \epsilon_j(d_j)S_j(d_j)$ become extremely large (and thus restrict node motions) when any triangle altitude d_j approaches a user-specified minimum separation tolerance. More general, gradient-dependent penalty functions can be used, if desired, in later MFE work in 2-D. The variational equations for this minimization procedure are then the large set of ODE's which follows:

$$\begin{aligned} \sum_j \left[(\alpha^j, \alpha^i) \dot{a}k_j + (\beta k^j, \alpha^i) \dot{x}_j + (\gamma k^j, \alpha^i) \dot{y}_j \right] &= \\ (L_k(U), \alpha^i) \text{ for } k = 1, \dots, N, & \\ \sum_{k=1}^N \sum_j \left[(\alpha^j, \beta k^i) \dot{a}k_j + (\beta k^j, \beta k^i) \dot{x}_j + (\gamma k^j, \beta k^i) \dot{y}_j \right] &= \\ \sum_{k=1}^N (L_k(U), \beta k^i) + (\text{regularization terms}) & \quad (21) \\ \sum_{k=1}^N \sum_j \left[(\alpha^j, \gamma k^i) \dot{a}k_j + (\beta k^j, \gamma k^i) \dot{x}_j + (\gamma k^j, \gamma k^i) \dot{y}_j \right] &= \\ \sum_{k=1}^N (L_k(U), \gamma k^i) + (\text{regularization terms}) & . \end{aligned}$$

The sums on j in Equations (21) run over the seven neighboring nodes of i (including the i^{th} node itself) in the hexagonal grid. Equations (21) thus provide the basic working equations of the MFE method in 2-D.

cycles. The MFE nodes sense very quickly the correct characteristics of this solution, and the constant wave profile and speed of 1.0 are maintained to within 1 part in 10^3 at all coordinate positions and at all times--consistent with the local truncation error of 10^{-3} which is used in the Gear method of integration of the ODE's in the present code version. The node movements in the y-direction are also of interest. Because no forces are exerted on the nodes in the y direction by any operator in the PDE (23) the nodes are free to migrate within the specified error constraints, according to the regularization terms in the \dot{x} and \dot{y} equations (21b) and (21c). Results in this work indicate that wide latitude can be exercised in the selection of node controlling parameters in the functions ϵ_i^2 and $\epsilon_i S_i$. When relatively weak internodal forces are used, no nodal deviation in the y-direction is observed. As the internodal forces are increased, the nodes can be made to migrate toward the x-axis for the triangulation shown in Figure 7--meanwhile maintaining the accuracies indicated above. The direction of this migration can be reversed by using the opposite type of grid triangulation, and this node migration can also be altered by the use of different penalty functions. Node control is thus very flexible and desired accuracies are readily maintained. When PDE's contain non-trivial y-dependencies in their operators, the PDE's themselves resume their dominant role in governing the positioning of the nodes. The results in Figure 7 have been calculated with similar success with larger grids (e.g. 4 x 21) and with larger and smaller gradients across the front.

(ii) Burger-Like Equations.

A 2-D analog of Burger's 1-D model equation is given by the equations

$$\frac{\partial u}{\partial t} = - \frac{\partial(u^2)}{\partial x} - \frac{\partial}{\partial y} (uv) + v\nabla^2 u \quad (24)$$

$$\frac{\partial v}{\partial t} = - \frac{\partial}{\partial x} (uv) - \frac{\partial}{\partial y} (v^2) + v\nabla^2 v \quad (25)$$

where u and v can be viewed as x and y components of a fluid velocity, respectively. In order to maintain a close analogy to the 1-D Burger's model results which were discussed in Reference 3, initial and boundary conditions for this system of PDE's are first selected so as to

lead to the propagation of a uniform, step-like wave in a direction parallel to the x-axis; that is,

$$u(x,y,0) = 0. \quad 0. \leq x \leq 1.0; 0. \leq y \leq 1.0$$

$$v(x,y,0) = 1.0 \quad 0 \leq y \leq 0.100; 0 \leq x \leq 1.0$$

$$v(x,y,0) = 0. \quad 0.101 \leq y \leq 1.0; 0 \leq x \leq 1.0$$

$$v(x,y,0) = \text{linear} \quad \text{otherwise} \quad .$$

This problem is solved from $t = 0$ to $t = 0.5$ on a 4×19 grid with $\nu = 10^{-2}$.* The dependent variable v obeys zero-Neumann conditions along the y axis and along the (vertical) boundary at $x = 1.0$; and v obeys the Dirichlet conditions, $v = 1.0$ along the x axis and $v = 0.$ along the (horizontal) boundary at $y = 1.0$. The co-ordinates x and y obey the following Dirichlet conditions: $x = 0.$ along the y axis; $x = 1.0$ along the boundary $x = 1.0$, all y ; $y = 0.$ along the x axis; and $y = 1.0$ along the boundary $y = 1.0$, all x . The co-ordinate variables obey zero-Neumann conditions on y along the y axis and along the boundary at $y = 1.0$ for all x . (That is, the y co-ordinate is free to slide along the vertical boundaries, and the x co-ordinate is free to slide along the horizontal boundaries.) Figures 8-11 present the MFE solutions of this evolving wave front. The extensive migration of the MFE nodes from their initial positions to those positions which resolve the waveform at $t = 0.2$ is clearly evident in Figures 8 and 9. The speed of propagation and the shock-like wavefront solutions are resolved to accuracies of three significant figures, or better, consistent with the local truncation error constraint of the ODE solver. The magnitudes of the wave-front gradients are approximately 100 in this example, and MFE solutions of this problem can be obtained with similar facility and efficiency for much larger gradients (corresponding to smaller values of ν in equations (24) and (25)). Consistent with all other results obtained to date in 2-D, it is found that wide latitude can be exercised in the selection of node controlling parameters in the regularization terms of equations (21). When relatively weak internodal forces are used, no nodal deviation (or bias) in the x direction is observed. (There are no transverse forces in the PDE's,

*This problem can be solved with equal effectiveness on an MFE grid of 4×10 nodes. The 4×19 grid simply represents the initial attempt on this problem. The figures 8-11 below have rotated the co-ordinate axes in the x - y plane by 90° from the conventional orientation (\hat{x} horizontal and \hat{y} vertical) in order to improve the viewing angle for the plotted results in 3-D. The terms "horizontal" and "vertical" refer strictly throughout this discussion to the conventional orientation of the x - y plane.

per se, in this example.) As the internodal forces are increased to sufficiently large values, the nodes can be forced by the regularization terms to migrate toward the x-axis for the nodal triangulation shown in Figure 8--meanwhile maintaining the accuracies mentioned above. The direction of such forced nodal migration can be reversed by using the opposite type of grid triangulation, and this node migration can also be altered by the use of different penalty functions. Node control is thus very flexible and desired accuracies are readily maintained. When PDE's contain non-trivial x-dependencies in their

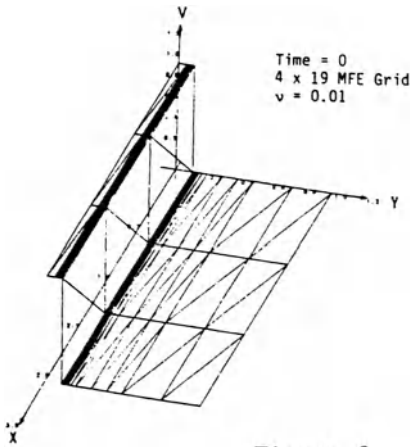


Figure 8

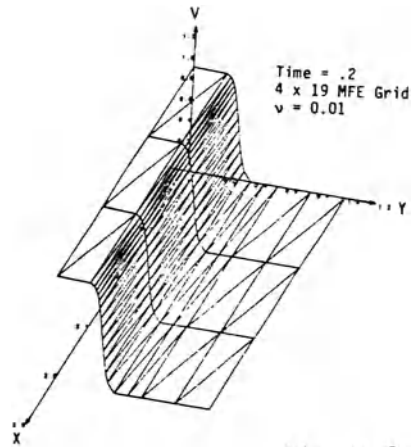


Figure 9

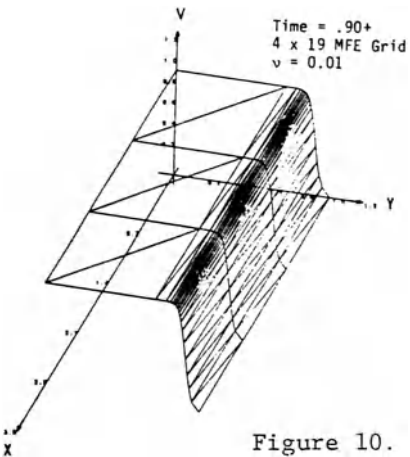


Figure 10.

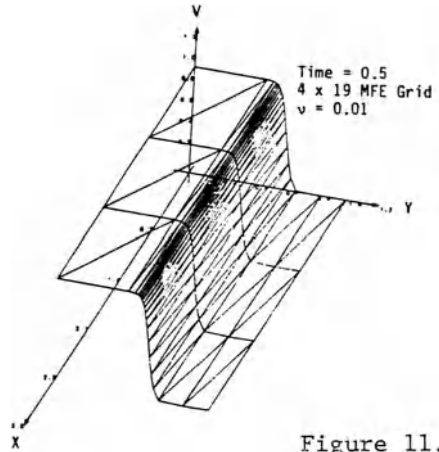


Figure 11.

MFE Solution of Burger-like Equation in 2-D.

operators, the PDE's themselves resume their dominant role in governing the positioning of the nodes, as will be seen in a skewed waveform example below. Figure 11 shows the formation of the boundary layer at the right hand boundary, as this MFE solution approaches its correct asymptotic solution.

This example can next be extended so as to generate a skewed, propagating wavefront (shock); the equations are given by

$$u_t = 0 \quad (26)$$

$$v_t = -1/2 (v^2)_y + v \nabla^2 v \quad , \quad (27)$$

on the unit square. An 8 x 8 grid of MFE nodes is used, and the initial conditions for u and v on uniformly spaced grid nodes are:

$$u(x,y,0) = 0. \quad \text{all } x,y$$

$$v(x,y,0) = 1+7\tau, 1+6\tau, 1+5\tau, \dots, 1 \quad \text{at nodes } 1, 2, 3, \dots, 8 \\ \text{along 1st row (x-axis)}$$

$$v(x,y,0) = -1, -(1+\tau), -(1+2\tau), \dots, -(1+7\tau) \\ \text{at nodes } 57, 58, 59, \dots, 64 \text{ along top row.}$$

The initial values of $v(x, y, 0)$ along a given vertical line are obtained by linear interpolation at interior nodes. The parameter τ is assigned a constant value of 0.01, and the value of v in equations (26)-(27) is assigned a value of 0.01 in the present run. As shown in Figure 12, these initial conditions on v simply map a plane in which v has the values +1.07 at the co-ordinates (0, 0); +1.0 at (1, 0); -1.0 at (0, 1); and -1.07 at (1, 1). Dirichlet boundary conditions are maintained on $v(x,y,t)$ and on x and y along the horizontal boundaries; zero-Neumann boundary conditions are applied to $v(x,y,t)$ and to y on the vertical boundaries; and Dirichlet boundary conditions are maintained on x along the vertical boundaries. This skewing of the initially counter-directed velocity components along the top and bottom boundaries leads to the evolution of non-uniform wavefront solutions which are seen in the results below. In the early stages of solution, prior to $t \cong 0.5$, a projection of the MFE solution on the x - y plane shows two counter-directed, quasi-horizontal fluid impulses which propagate from top to bottom and from bottom to top at speeds of approximately 0.5. (See Figures 13-15.) At $t = 0.5$, a shock is formed when the propagating impulses encounter each other near the horizontal centerline of the x - y domain. Subsequently, a skewed, shock-like waveform is generated and propagates in the

serpentine manner shown in Figures 16-17. The relatively large aspect ratios seen in Figure 17 for the MFE mesh at $t = 20$. were created deliberately by the use of Dirichlet boundary conditions on the x co-ordinates along the x axis and along the parallel boundary line at $y = 1$. The MFE node migration was fluid throughout and exhibited no grid-biasing effects. This problem was run from $t = 0$. to $t = 20$. in approximately 125 time-step cycles. The gradients of the fully developed shock are on the order of 100, consistent with the present value of $\nu = 0.01$. As above, MFE solutions of this problem on an 8×8 grid can be obtained for much larger gradients (smaller values of ν) with essentially the same levels of robustness and efficiency as are seen in the present example.

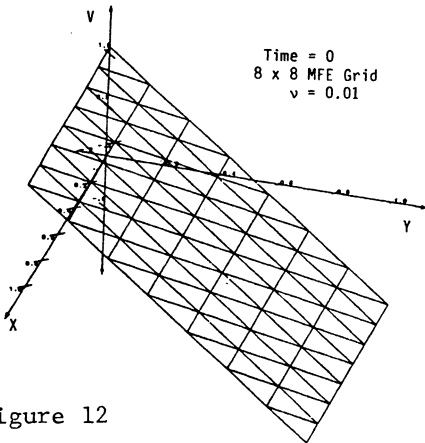


Figure 12

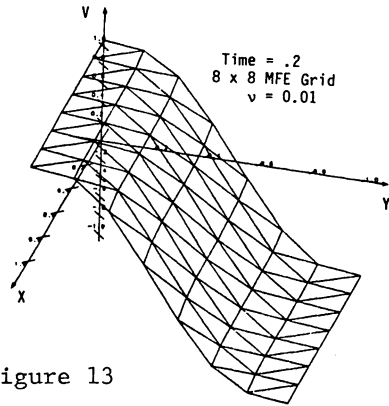


Figure 13

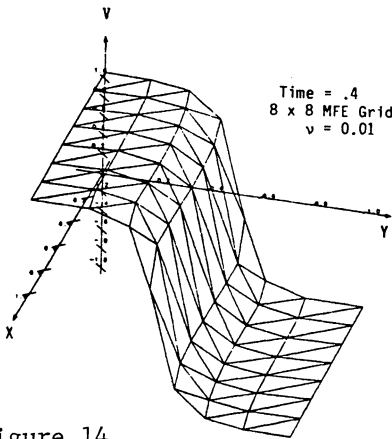


Figure 14

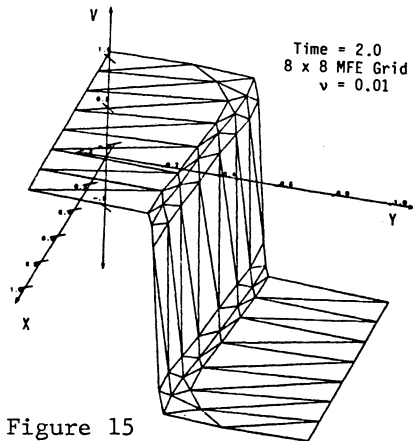


Figure 15

MFE Solution of Burger-like Equations for a Skewed Waveform in 2-D.

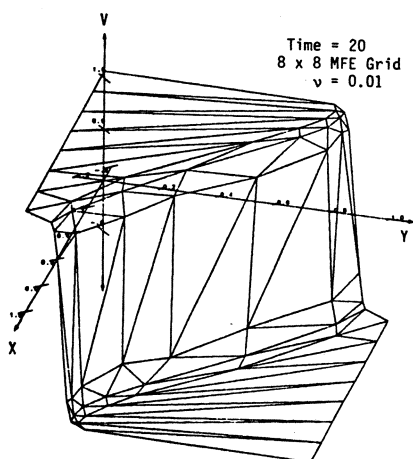


Figure 16. MFE Solutions to Burger-like Equations for a Skewed Waveform in 2-D.

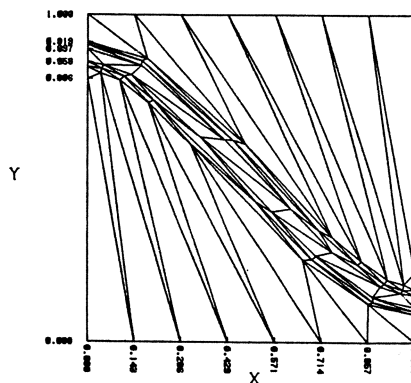


Figure 17. Projection on the x - y plane of the MFE solution of Burger-like equation for a skewed waveform in 2-D. Time = 20.; 8 x 8 MFE grid; $v = 0.01$.

ACKNOWLEDGEMENT

It is a pleasure to acknowledge the support provided by the Army Research Office for this MFE research under contract F499620-81-C-0073.

REFERENCES

1. Miller, K. and R. Miller, "Moving Finite Elements, Part I," SIAM J. of Num. Anal., 1019-32, Vol. 18, No. 6, December 1981.
2. Miller, K., "Moving Finite Elements, Part II," SIAM J. of Num. Anal., 1033-57, Vol. 18, No. 6, December 1981.
3. Gelinias, R.J., S.K. Doss and K. Miller, "The Moving Finite Element Method: Applications to General Partial Differential Equation with Multiple Large Gradients," J. Comp. Phys., 40, No. 1, pg. 202, March 1981.
4. Gelinias, R.J. and S.K. Doss, "The Moving Finite Element Method: A Semi-Automatic Solver for Diverse PDE Applications," Advances in Computer Methods for Partial Differential Equations - IV, pg. 230-239, edited by R. Vichnevetsky and R.S. Stepleman, Proceedings of the Fourth IMACS International Symposium on Computer Methods for Partial Differential Equations, Lehigh University, Bethlehem, PA, June 30-July 2, 1981.

5. Djomehri, M.J., "Moving Finite Element Solution of Systems of Partial Differential Equations in 1-Dimension," Ph.D. Thesis, University of California, Berkeley.
6. Woodward, P.R. and P. Colella, "High Resolution Difference Schemes for Compressible Gas Dynamics," Proc. Seventh Int. Conference on Numerical Methods in Fluid Dyn., Stanford, June 1980.
7. Woodward, P.R., "Trade-Offs in Designing Explicit Hydrodynamic Schemes for Vector Computers," Methods in Computational Physics, in press.
8. Malvern, L., Introduction to the Mechanics of a Continuous Medium, Prentice Hall, 1969.
9. Djomehri, J. and K. Miller, "A Moving Finite Element Code for General Systems of PDE's in 2-D," Technical Report PAM-57, Center for Pure and Applied Mathematics, University of California, Berkeley, Oct. 12, 1981.
10. Gelinas, R.J., S.K. Doss, J.P. Vajk, J. Djomehri and K. Miller, "Moving Finite Elements in 2-D," to be presented at the 10th IMACS World Congress on Systems Simulation and Scientific Computation, Montreal, Canada, August 8-13, 1982.

ON MESH STABILIZATION TECHNIQUES FOR UNDERINTEGRATED ELEMENTS

T. BELYTSCHKO AND W.K. LIU

Department of Civil Engineering
Northwestern University
Evanston, Illinois 60201

Summary

Mesh stabilization techniques for controlling the hourglass modes in underintegrated hexahedral and quadrilateral elements are examined. It is shown, using the Laplace equation as a model, that the "orthogonal" hourglass techniques previously developed can be obtained from simple requirements that ensure that the finite element patch test is also satisfied. By contrast, other hourglass control techniques fail to satisfy the patch test for elements that are not rectangular. These results also apply to certain finite difference methods. The extension of these techniques to solid mechanics problems is also discussed.

Introduction

As has been succinctly summarized by Zukas [1] in his survey of computer methods for impact and penetration, "computational techniques have advanced to the point where extremely difficult situations can be analyzed quickly...one dimensional problems in tens of minutes to a few hours, and three dimensional problems in a few hours to tens of hours." With the decreasing costs of computers, these figures, which apply to the larger main-frame computers, promise to diminish rapidly. Nevertheless, considering the cost and limited availability of computers suitable for two and three dimensional calculations, it is quite clear that we are still far from the stage where three dimensional, and even two dimensional calculations, can be used effectively in the design and decision-making process, since the parametric studies which are essential in such highly nonlinear simulations simply cannot be made within the normal framework of engineering time schedules because of their long running times.

However, substantial reductions in the cost of these computations can be achieved through improvements in the finite element formulations and the time integration procedure. For example, in the penetration code EPIC-3 [2] tetrahedral elements are used to permit the code to function under very large displacements where hexahedral elements often fail because of mesh instabilities. One of the chief causes of these mesh instabilities is a phenomenon known as hourglassing, which occurs when one-point quadrature is used. In the finite element literature, these modes are also called kinematic, or zero-energy modes; see for example Irons and Ahmad [3]. Yet

hexahedrons, when treated by one-point quadrature, require only one sixth of the constitutive equation evaluations required by tetrahedra, and in addition tend to converge better because they are not susceptible to the excessive stiffening that is found in tetrahedra. However, in the use of quadrilaterals or hexahedra, an effective "hourglass" control or mesh stabilization technique is essential.

Numerous techniques have been developed for the control of the hourglass mode in the four node quadrilateral and the corresponding two dimensional finite difference equations used in Lagrangian finite difference codes [4] which are in fact identical [5]. One of the earliest of these is the technique developed by Maenchen and Sack [6] who added artificial viscosity to inhibit opposing rotations of the sides of the quadrilateral zone. A finite element version of the Maenchen and Sack antihourglass viscosity has been developed by Belytschko and Kennedy [7]. Alternative methods have been developed in [4] and [8-11]. It has lately been recognized that the development of an effective hourglass control requires that the resistance be more general than a simple viscosity, and that care must be taken in developing the form of the hourglass generalized strains and stresses so that they are not activated in rigid body motion. The requirement that the generalized hourglass strains and stresses vanish under rigid body motions can be considered an orthogonality condition, for it implies that the hourglass operator is orthogonal to rigid body motion. A simple and unique form of this operator for both the 4-node quadrilateral and the 8-node hexahedron for 3D problems has been given in [11], where the hourglass operator was developed by subtracting the effect of the bilinear portion of the velocity field. More recent work suggests that the hourglass projection operator can be obtained more elegantly and simply by using the relationships derived in [11] and enforcing the certain conditions suggested by the rank deficiency of the discrete forms of the gradient operators.

An important byproduct which has emerged from this work is the recognition that any hourglass control which does not satisfy the orthogonality conditions does not meet the patch test [12-13]. Although the necessity and sufficiency of the patch test for convergence is not clearly established, it is widely accepted that elements that do not meet the patch test will have convergence difficulties. Thus, an hourglass control which fails to meet the patch test is not acceptable, and it is shown in this paper that the hourglass controls of [6] and [8] do not meet the patch test.

In this paper, for the sake of clarity, we will focus on the Laplace equation, which has the same characteristics as the two and three dimensional equations of solid mechanics, yet enables the salient features and characteristics of spurious modes and their control to be clearly demonstrated. In the next Section, we give the

basic finite element equations for the Laplace semidiscretization. The hourglass control procedure is then developed and the procedure is extended to the two dimensional solid mechanics problem. In the last section we examine the patch test for various hourglass control schemes.

Finite Element Form of Laplace Equation

Consider the Laplace equation

$$\nabla^2 u + s = 0 \quad (1)$$

As is well known, see for example [14], the finite element discretization of (1) can be written as

$$\underline{K} \underline{u} + \underline{r} = \underline{Q} \quad (2)$$

where \underline{K} is assembled from the element stiffnesses \underline{k}^e which are given by

$$K_{IJ}^e = \int_{V_e} N_{I,i} N_{J,i} dV \quad (3)$$

where V_e is the volume of the element and N_I are the shape functions which give the independent variable in the element by

$$u(\underline{x}) = N_I(\underline{x}) u_I \quad (4)$$

where \underline{x} are the spatial coordinates. Throughout this paper, standard indicial notation will be used, so repeated subscripts imply summation over the range of that subscript. Lower case subscripts refer to Cartesian coordinates and have a range equal to the dimension of the problem, while upper case subscripts correspond to the nodes of the element and have a range equal to the number of nodes in the element. Subscripts which follow a comma denote spatial derivatives.

If we use the standard bilinear, isoparametric shape functions for a quadrilateral in conjunction with one-point quadrature of the right hand side of Eq. (3) to evaluate \underline{k}^e , we obtain [15]

$$\underline{k}^e = \frac{1}{A} \underline{b}_i \underline{b}_i^T \quad (5a)$$

where A is the area of the element and

$$\underline{b}_i = A \underline{N}_{,i} \quad (5b)$$

with the right hand side evaluated at the centroid of the element so

$$\tilde{b}_1 = \frac{1}{2} [y_{24} \ y_{31} \ y_{42} \ y_{13}] \quad (6a)$$

$$\tilde{b}_2 = \frac{1}{2} [x_{42} \ x_{13} \ x_{24} \ x_{31}] \quad (6b)$$

$$A = \frac{1}{2} (x_{31}y_{42} + x_{24}y_{31}) \quad (6c)$$

$$x_{IJ} = x_I - x_J \quad (6d)$$

$$y_{IJ} = y_I - y_J \quad (6e)$$

with x_I, y_I the coordinates of the node I.

Note that the matrix \tilde{B} given by

$$\tilde{B} = \begin{Bmatrix} \tilde{b}_1^T \\ \tilde{b}_2^T \end{Bmatrix} \quad (7a)$$

is the discrete counterpart of the gradient operator, for the gradient of u in the finite element approximation is given by

$$\underline{g} = \begin{Bmatrix} u_{,x} \\ u_{,y} \end{Bmatrix} = \frac{1}{A} \tilde{B} \underline{u}^e \quad (7b)$$

We will also define the additional column vectors

$$\tilde{s}^T = [1, 1, 1, 1] \quad (8a)$$

$$\tilde{h}^T = [1, -1, 1, -1] \quad (8b)$$

$$\tilde{x}_1 = \tilde{x} = [x_1, x_2, x_3, x_4] \quad (8c)$$

$$\tilde{x}_2 = \tilde{y} = [y_1, y_2, y_3, y_4] \quad (8d)$$

It can be easily verified from Eqs. (7-8) that

$$\tilde{b}_i^T \tilde{x}_j = A \delta_{ij} \quad (9)$$

where δ_{ij} is the Kronecker delta and that

$$\underline{b}_i^T \underline{s} = 0 \quad (10a)$$

$$\underline{b}_i^T \underline{h} = 0 \quad (10b)$$

$$\underline{s}^T \underline{h} = 0 \quad (10c)$$

For any nondegenerate quadrilateral, \underline{b}_i , \underline{s} and \underline{h} are linearly independent and span the 4 dimensional space R^4 .

Hourglass Control for the Laplacian

The orthogonality properties, Eqs. (10), allow us to quickly examine the pathology of this element that results from one-point quadrature. If we let the nodal values of u for an element be given by \underline{s} , then

$$\underline{r}^e = \underline{K}^e \underline{u}^e = \underline{K}^e \underline{s} = \underline{0} \quad (11)$$

where the last step in the above follows from Eqs. (5) and (10a). This result is expected and in fact necessary since it indicates that for a constant field u , the nodal sources vanish. The one-dimensional space spanned by the vector \underline{s} will be called the proper null-space of \underline{K}^e .

If we let $\underline{u}^e = \underline{h}$, Eqs. (5) and (10b) again show that $\underline{r}^e = 0$. This result is quite unexpected since the field associated with these nodal values is obviously not constant. The contradictory nature of this result can be appreciated further by noting that for a square element, with all nodes at $+1$ and -1 , $\underline{u}^e = \underline{h}$ corresponds to $u(x,y) = xy$, yet Eqs. (7) and (10b) show that discrete gradient of this field vanishes. The one-dimensional space spanned by \underline{h} will be called the improper null-space of \underline{K}^e .

In the finite element literature of solid mechanics, modes such as \underline{h} are called spurious singular modes, or zero-energy modes. The latter term reflects the fact that these modes, while not rigid body modes, are not accompanied by any work on the element.

Mathematically the difficulty can be seen to result from the fact that the null-space, or kernel, of the discrete gradient operator \underline{B} does not coincide with the kernel of the continuous gradient. Since the nodal variables form a space R^4 , and since the kernel of the continuous gradient is limited to constant fields if the

discrete and continuous kernel are to coincide, \underline{B} (and \underline{K}^e) must be a matrices of rank 3.

This suggests that the pathology of this element may be eliminated by defining an additional gradient \tilde{g} by

$$\tilde{g} = \underline{\chi}^T \underline{u}^e \quad (12)$$

so that

$$\underline{B}^* = \left\{ \begin{array}{c} \underline{b}_1^T \\ \underline{b}_2^T \\ A \underline{\chi}^T \end{array} \right\} \quad (13)$$

The discrete gradient operator of Eq. (7) performs properly on linear fields, which can be seen by letting $\underline{u}^e = \underline{x}$ or $\underline{u}^e = \underline{\chi}$ and using Eqs. (9). Thus γ should not distort the behavior of \underline{B}^* or \underline{K}^e on linear fields.

Therefore $\underline{\chi}$ will be chosen so that

- i. for any nodal values associated with linear fields, $\tilde{g} = 0$
- ii. if \underline{u}^e is in the improper null-space, $\tilde{g} \neq 0$.

To obtain $\underline{\chi}$, we expand it in terms of the base vectors of R^4 as follows

$$\underline{\chi} = a_1 \underline{b}_1 + a_2 \underline{b}_2 + a_3 \underline{s} + a_4 \underline{h} \quad (14)$$

For an arbitrary linear temperature field

$$\underline{u}^e = c_1 \underline{x} + c_2 \underline{\chi} + c_3 \underline{s} \quad (15)$$

and using Eqs. (8-10), we obtain that condition (i) implies that

$$\underline{\chi} = \frac{1}{A} [A \underline{h} - (\underline{h}^T \underline{x}) \underline{b}_1 - (\underline{h}^T \underline{\chi}) \underline{b}_2] \quad (16)$$

Since $\underline{\chi}$ is linearly independent of \underline{b}_i , \underline{B}^* must span the complement of the proper null-space of R^4 and condition ii is met.

The resulting element matrix is given by

$$\underline{K}^e = \frac{1}{A} \underline{b}_i \underline{b}_i^T + \epsilon \underline{\chi} \underline{\chi}^T \quad (17)$$

The second term on the right hand side can be called a stabilization matrix [16], since it serves the purpose of eliminating the spurious singular mode which leads to mesh instabilities.

Hourglass Control for Continuum Element

In solid mechanics, the components of the displacement field are approximated in a finite element analogously to Eq. (4) by

$$u_i(\underline{x}) = N_I(\underline{x}) u_{iI} \quad (18)$$

The deformation of the material is characterized by strains

$$E_{ij} = \frac{1}{2} (u_{i,j} + u_{j,i}) \quad (19)$$

so the discrete operator \underline{B} for a quadrilateral with one-point quadrature is given by

$$\underline{B} = \begin{bmatrix} \underline{b}_1^T & 0 \\ 0 & \underline{b}_2^T \\ \underline{b}_2^T & \underline{b}_1^T \end{bmatrix} \quad (20)$$

where

$$\underline{E} = \frac{1}{A} \underline{B} \underline{d}^e \quad (21)$$

and

$$\underline{E}^T = [E_x, E_y, 2E_{xy}] \quad (22)$$

$$\underline{d}^e = \begin{Bmatrix} \underline{u}_x^e \\ \underline{u}_y^e \end{Bmatrix} \quad (23)$$

Using the orthogonality properties of Eq. (10), it follows immediately that the null space of \underline{B} consists of the following vectors

$$\underline{d}^e = \begin{bmatrix} \underline{s} & 0 & \underline{y} & \underline{h} & 0 \\ 0 & \underline{s} & -\underline{x} & 0 & \underline{h} \end{bmatrix} \quad (24)$$

where each column of the above constitutes a separate vector \underline{d}_1^e so that $\underline{B} \underline{d}_1^e$

vanishes.

The first two vectors are obviously rigid body translations and the third is rigid body rotation. The fourth and fifth are spurious singular modes associated with displacement fields for which the strains should not vanish. Hence we define the space spanned by the first three vectors of Eq. (24) to be the proper null space of \underline{B} ; the remaining two columns constitute the improper null space, which is of dimension 2.

As before, we can introduce 2 additional generalized strains, which when combined with \underline{B} , span the complement of the proper null space. The resulting matrix \underline{B}^* is given by

$$\underline{B}^* = \begin{bmatrix} \underline{b}_1^T & \underline{0} \\ \underline{0} & \underline{b}_2^T \\ \underline{b}_2^T & \underline{b}_1^T \\ A_\gamma^T & \underline{0} \\ \underline{0} & A_\gamma^T \end{bmatrix} \quad (25)$$

and using the same arguments as those in the previous section that led to Eqs. (14-16), it follows that γ for the solid mechanics problem is also given by Eq. (16). Although the character of the null-space (kernel) of the operator \underline{B} is now somewhat different, the requirement of condition (i) that the additional strains not affect linear fields automatically leads to a form of \underline{B}^* in which rigid body rotations are included in the kernel. It can be shown that the rows of \underline{B}^* are linearly independent for a nondegenerate geometry, so \underline{B}^* is of rank 5 and spans the complement of the proper null-space.

The implementation of this hourglass control procedure for both small and large displacement problems is described in [11]. Forms for both two and three dimensional problems are given. Although the method of derivation is different, it leads to the same results. In [11], no results are given for nonlinear material problems; the proper choice of constants corresponding to ϵ in Eq. (17) for nonlinear problems is still a topic of research.

Hourglass Control and Patch Test

The patch test will be examined for hourglass control methods for the Laplace equation. For this purpose we consider the mesh shown in Fig. 1. The function u is

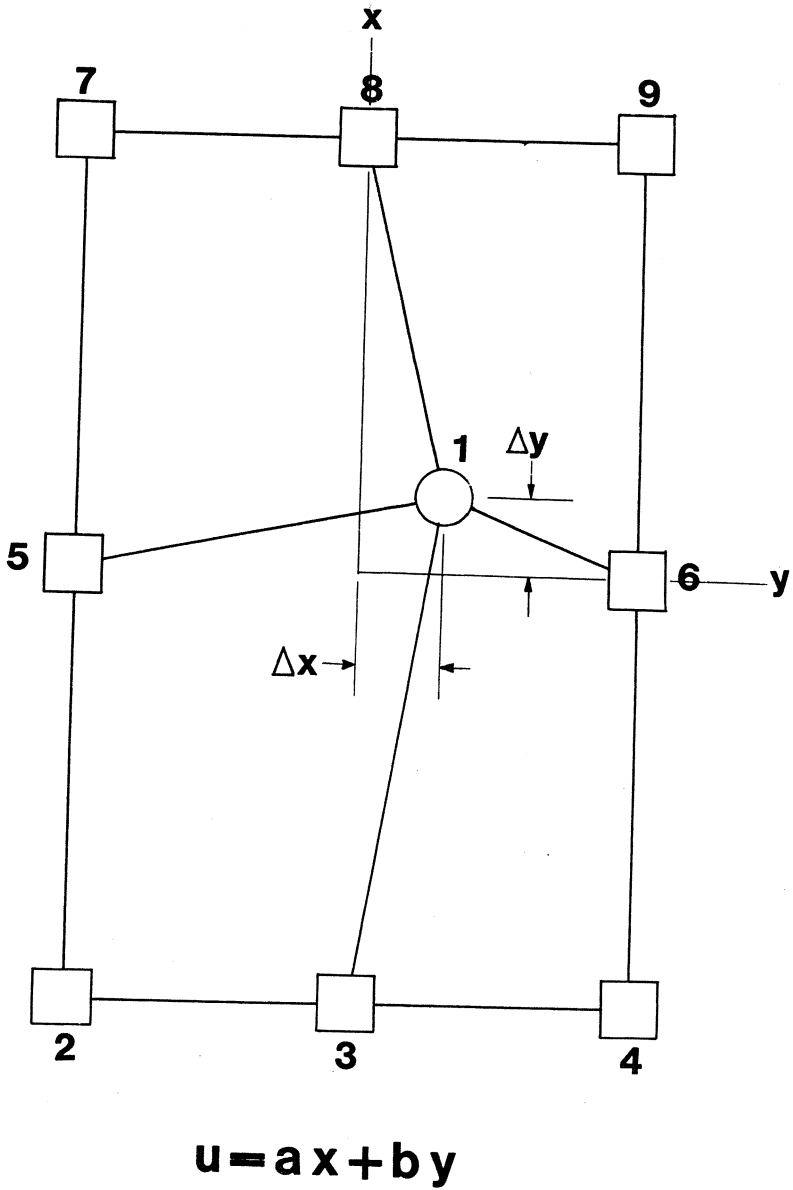


Fig. 1. Finite element mesh used for the analytic patch test with the Laplace equation.

prescribed by a linear function along all outside nodes, so in each element

$$\underline{u}^e = a \underline{x} + b \underline{y} \quad (26)$$

where a and b are arbitrary constants.

The homogeneous form of the Laplace equation is considered. According to the patch test, the assembled value of r_1 which represents the contributions of all elements to r_1 , must then vanish if the value of u at the center node is given by the same linear function. In the standard patch test, the value of u_1 is obtained by solving the governing equations and then compared to the exact solution for the patch. Setting the value of u_1 and then checking r_1 is obviously an equivalent procedure.

If we use the form of the hourglass operator given in Eq. (16), and hence the element stiffness given by Eq. (17), we find with the help of Eqs. (9-10) that r_1 is given by

$$\begin{aligned} r_1 &= a(y_{53} + y_{36} + y_{68} + y_{85}) + b(x_{35} + x_{63} + x_{86} + x_{58}) \\ &= 0 \end{aligned} \quad (27)$$

This result is independent of the hourglass control parameter ϵ since the generalized hourglass \tilde{g} is not activated by a linear field.

In the hourglass control of [6],

$$\underline{\chi} = \underline{h} \quad (28)$$

so

$$\underline{k}^e = \frac{1}{A} \underline{b}_i \underline{b}_i^T + \epsilon \underline{h} \underline{h}^T \quad (29)$$

Repeating the same procedure, we find r_1 contains the same term as Eq. (27) plus an additional term which does not vanish and is given by

$$r_1 = 4\epsilon (a\Delta x + b\Delta y) \quad (30)$$

where, as can be seen from Fig. 1, Δx and Δy are the displacement of the node 1 from the center of the domain. Thus, for rectangular elements, where $\Delta x = \Delta y = 0$, this hourglass procedure meets the patch test, but for more irregularly shaped elements, it fails the patch test.

This result is not surprising once the characteristics which are required for an

hourglass control to satisfy the patch test are examined. Since the one-point quadrature of the element stiffness gives a matrix which satisfies the patch test, the stabilization matrix and hence the hourglass projection operator should not be affected by linear fields, i.e., all linear (and constant) fields must be in the kernel of γ . These conditions then make the form of χ which meets the patch test uniquely that given by Eq. (16), and any other form will not meet the patch test. This applies to the hourglass operators of both References [6] and [8].

While these arguments for simplicity have been given with the Laplace equation as a model, the developments of the previous section show that in two-dimensional solid mechanics impose identical requirements are imposed on χ , and it can easily be shown that the same conclusions follow. Therefore, these alternative hourglass control procedures should be used with great care in Lagrangian codes, since it is impossible to maintain rectangular configurations for the zones or elements.

Acknowledgement

The support of the National Science Foundation under Grant CEE-8211862 is gratefully acknowledged.

References

1. J. Zukas, "Numerical Simulation of Impact Phenomena" in Impact Dynamics, ed. by J. Zukas et al., Wiley Interscience, New York, 1982.
2. G.R. Johnson, D.J.Vavrick, and D.D. Colby, EPIC-3, Ballistic Research Laboratory, ARBRL-CR-00429, 1980.
3. B. Irons and S. Ahmad, Techniques of Finite Elements, Ellis Horwood, Chichester, England, 1980.
4. M.L. Wilkins, R.E. Blum, E. Cronshagen and P. Grantham, "A Method for Computer Simulation of Problems in Solids Mechanics and Gas Dynamics in Three Dimensions and Time" Lawrence Livermore Laboratory, Report UCRL-51574, Revision 1, May 1975.
5. T. Belytschko, J.M. Kennedy and D.F. Schoeblerle, "On Finite Element and Difference Formulations of Fluid Structure Problems", Proc. of the Conf. on Computer Methods in Nuclear Engineering, Charleston, S.C., 4:39-51, 1975.
6. G. Maenchen and S. Sack, "The TENSOR Code", in Methods in Computational Physics, Vol. 3, Ed. by B. Alder et al., Academic Press, 1964, pp. 181-210.
7. T. Belytschko and J.M. Kennedy, "Computer Models for Subassembly Simulation", Nuclear Engineering and Design, Vol. 49, July 1978, pp. 17-38.
8. G.L. Goudreau and J.O. Hallquist, "Recent Developments in Large Scale Finite Elements Lagrangian Hydrocode Technology", Report UCRL-86460, Lawrence Livermore Laboratory, October 1981, to be published in the Computer Methods in Applied Mechanics and Engineering, 1982.

9. S.W. Key, "A finite element procedure for the large deformation dynamics response of axisymmetric solids", Computer Methods in Applied Mechanics and Engineering, 4, 195-218, 1974.
10. D. Kosloff and G.A. Frazier, "Treatment of hourglass patterns in low order finite element codes", International Journal for Numerical and Analytical Methods in Geomechanics, 2, 57-72, 1978.
11. D.P. Flanagan and T. Belytschko, "A Uniform Strain Hexahedron and Quadrilateral with Orthogonal Hourglass Control", International Journal for Numerical Methods in Engineering, Vol. 17, pp. 679-706, 1981.
12. B.M. Irons and A. Razzaque, "Experience with the Patch Test for Convergence of Finite Elements in the Mathematical Foundations of the Finite Element Method with Applications to Partial Differential Equations", Ed. by A.K. Aziz, Academic Press, 1972, pp. 589-602.
13. G. Strang, "Variational Crimes in the Finite Element Method", ibid, pp. 689-710.
14. O.C. Zienkiewicz, The Finite Element Method, 3rd Edition, McGraw-Hill, 1977.
15. W.K. Liu and T. Belytschko, "Efficient Linear and Nonlinear Heat Conduction with a Quadrilateral Element", submitted for publication.
16. T. Belytschko, C.S. Tsay and W.K. Liu, "A Stabilization Matrix for the Bilinear Mindlin Plate Element", Computer Methods in Applied Mechanics and Engineering, Vol. 29, pp. 313-327, 1981.

Lecture Notes in Engineering

Edited by C. A. Brebbia and S. A. Orszag

Vol. 1: J. C. F. Telles,
The Boundary Element Method
Applied to Inelastic Problems
IX, 243 pages. 1983

Vol. 2: Bernard Amadei,
Rock Anisotropy and
the Theory of Stress Measurements
XVIII, 479 pages. 1983

Vol. 3: Computational Aspects of
Penetration Mechanics
Proceedings of the Army Research
Office Workshop on Computational
Aspects of Penetration Mechanics
held at the Ballistic Research Laboratory
at Aberdeen Proving Ground, Maryland,
27-29 April, 1982
Edited by J. Chandra and J. E. Flaherty
VII, 221 pages. 1983